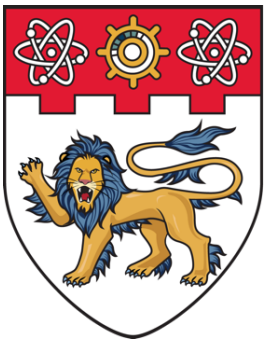

NANYANG TECHNOLOGICAL UNIVERSITY
SINGAPORE

EVALUATION AND MITIGATION OF MODELLING ERRORS IN NUMERICAL SIMULATIONS OF MOORING LINE AND SEABED CONTACT

LOW CHEE MENG

SCHOOL OF MECHANICAL AND AEROSPACE ENGINEERING

2019

EVALUATION AND MITIGATION OF MODELLING ERRORS IN NUMERICAL SIMULATIONS OF MOORING LINE AND SEABED CONTACT

LOW CHEE MENG

SCHOOL OF MECHANICAL AND AEROSPACE ENGINEERING

A thesis submitted to the Nanyang Technological University
in partial fulfillment of the requirements for the degree of
Doctor of Philosophy

2019

Statement of Originality

I hereby certify that the work embodied in this thesis is the result of original research and has not been submitted for a higher degree to any other University or Institution.

26 May 2019 .....

Date

..... Low Chee Meng

Supervisor Declaration Statement

I have reviewed the content and presentation style of this thesis and declare it is free of plagiarism and of sufficient grammatical clarity to be examined. To the best of my knowledge, the research and writing are those of the candidate except as acknowledged in the Author Attribution Statement. I confirm that the investigations were conducted in accord with the ethics policies and integrity standards of Nanyang Technological University and that the research data are presented honestly and without prejudice.

26 May 2019

....

Date Associate Professor Ng Yin Kwee

Authorship Attribution Statement

This thesis contains material from papers published in the following conferences proceedings and peer-reviewed journals where I was the first and/or corresponding author. Sections 2.1 and 2.3.2 in Chapter 2, along with Chapters 3 and 5 are published as C. M. Low, E. Y. K. Ng, S. Narasimalu, F. Lin, Y. Kim, Numerical modelling of seabed impact effects on chain and small diameter mooring cables, Applied Ocean Research 80 (2018) 248-277. doi:10.1016/ j.apor.2018.09.010. URL https://doi.org/10.1016/j.apor.2018.09.010

The contributions of the co-authors are as follows:

1. A/Prof Ng developed the scope of the paper and choices of numerical modelling methodologies together with the first author, and was the main editor of the manuscript drafts.
2. Dr Srikanth provided editorial advice on the presentation of the contents of the paper as well as its title.
3. Dr Lin provided technical advice on the mathematical models and computational techniques used in this work, and code development best practices.
4. Mr Kim provided editorial advice on the contents of the paper to highlight its contributions to existing literature.

Section 4.1.1 in Chapter 4 is published as C. M. Low, E. Y. K. Ng, S. Narasimalu, K. H. Chua, Multirate Timestepping For Mooring Line Dynamics, in: Offshore Technology Conference Brazil, 2017. doi:10.4043 /28041-MS.

1. A/Prof Ng developed the scope of the paper together with the first author, advised on stability analysis methods in general as well as the validation and verification of the code, and was the main editor of the manuscript drafts.
2. Dr Srikanth provided technical advice on dynamic modelling analysis.
3. Dr Chua provided technical advice on mooring line numerical modelling and proposed the idea of local mesh refinement.

26 May 2019

.....

Date

.....

Low Chee Meng

Acknowledgements

I would like to express my sincere gratitude to my academic supervisors Associate Professor Ng Yin Kwee and Dr Srikanth Narasimalu. Associate Professor Ng's patience, concern and continuous support in academic matters and otherwise have been pivotal for the successful completion of this thesis and for that I am very grateful. Dr Srikanth has given me invaluable advice on the direction and reporting of this research as well as my personal development. They have been my teachers and staunchest cheerleaders in this journey, and I owe them a debt of gratitude.

This project received funding from Economic Development Board of Singapore and was carried out with the support of Energy Research Institute @NTU, Lloyd's Register Singapore and Lloyd's Register Applied Technology Group; the resources and assistance provided by these organizations are duly acknowledged. I would like to thank my industrial supervisor, Mr Steve Kim, for his support and encouragement, and Dr Frank Lin for his supervision and mentorship during my overseas attachment and for developing the scope of the project. I am also very thankful to Mr David Whitehouse, with whom I have had the pleasure of running the Hypothermic Half, for helping me to get settled in at Applied Technology Group and Halifax. Mr Anand Bahuguni and Mr Krishnamoorthi Sivalingam have supported me at various stages of this journey and I am grateful for their kindness and concern for me. I would also like to especially thank Dr Kie Hian Chua for giving me plenty of valuable technical advice and suggestions, Mr Tan Hoon Kiang for his steadfast encouragement, mentorship, and belief in me, and Mr Ravi Jeeva Rathinam for his understanding, support, and advice for work and life.

I am also thankful for my friends and colleagues who have walked this journey with me. I am thankful for the projects that we did together, for the detours from our work that we took together, and for the memories we have made.

To my family, my parents and grandmothers, my grandfather who lives on in our memories, and my closest aunts, my deepest gratitude goes to you for your love and support. To 季烨, who gave me the courage to begin this adventure and stuck with me through it all, thank you, for everything that you have given to me.

Abstract

Time-domain mooring simulation is a direct and effective method of evaluating mooring line loads and floater motions, in which nonlinear effects including drag forces and seabed interaction are readily accounted for. The formulation of seabed models affects the accuracy of line loads, including maximum tension as well as fatigue results, and also floater motions in coupled simulations. The interaction between the seabed and discrete line structural models is challenging in time-domain numerical simulations and a myriad of seabed models have been proposed in the literature. However, issues such as the selection of suitable seabed force coefficients and the application of suitable line discretisations, to achieve a balance between accuracy and computational cost, remain challenging problems to be resolved. This thesis investigates the shortcomings of existing numerical methods in accurately capturing the dynamic mooring line-seabed interaction and proposes new solutions.

The line-seabed interaction problem is pertinent to catenary mooring lines which experience liftoff from and grounding on the seabed when undergoing large dynamic motions. This interaction is accounted for by various seabed models and it is known that the action of liftoff and grounding may lead to large dynamic tension fluctuations. These fluctuations may be spurious due to the inability of discretised mooring models to adequately account for the effect of the seabed on the mooring line. The effect of line discretisation and seabed model formulation on the tension fluctuations is investigated using the widely used spring-mattress approach. An in-house mooring code was developed to perform these investigations. For code validation and benchmarking, and to illustrate the existence of the tension fluctuations problem due to nodal grounding in existing mooring line simulation codes, comparisons are made to a commercial software.

This work aims to contribute to the field of numerical mooring line modelling by identifying the root cause and highlighting the conditions leading to the production of the large dynamic tension fluctuations that tend to occur due to impact loads imparted by spring-mattress type seabed models on discrete line structural models. In particular, these tension shock waves are found to be caused by strain

discontinuities manifesting in the vicinity of the touchdown zone as a result of discrete line elements and nodes coming into contact with the seabed. The likelihood of occurrence of the strain discontinuities is determined to be dependent on the impact speeds and orientations of line elements in relation to the seabed; higher impact speeds and close alignment between the seabed normal direction and the axis of line elements increase the tendency of occurrence of the strain discontinuities. In light of these findings, a novel seabed reaction force model that inhibits the production of strain discontinuities in a discrete line model is proposed.

The results from this research further show that using a suitably fine discretisation for the mooring line model, while incurring a higher computational cost, is a generally applicable approach to improve result accuracy. Specifically, the modelling of line touchdown-liftoff effects requires a finer mooring line discretisation at the touchdown point to avoid the production of spurious line tension fluctuations. The numerical experiments performed in this research demonstrate that, for the purpose of ameliorating the effects of propagating stress waves arising from rapid line grounding, a hybrid discretisation employing fine elements within a limited span of line close to the touchdown zone and coarse elements elsewhere is sufficient and preserves the accuracy of predicted peak tensions. The results of the discretisation refinement study in this work further suggest that specifying a numerical chain element size close to the physical chain link size within the locally refined zone is sufficient even under severe excitation conditions which promote the production of the tension fluctuations.

The disparity in element sizes within and outside the local refinement zone gives rise to a stiff dynamical system. This work introduces an approach for applying adaptive discretisation to the line structural model with a non-uniform mesh, and dual-rate time integration for the resultant stiff dynamic system. The results in this research suggest that a dual-rate time integration approach for the proposed hybrid spatial discretisation of the line structure significantly reduces computational times for smaller refined zone line spans as a proportion of total line length. As the touchdown point changes with time, the proposed adaptive discretisation procedure enables the locally refined zone to shift in tandem in order to limit the spatial extent of the refined domain, thereby preserving the computational efficiency gains of the dual-rate time integration scheme even as the touchdown point changes significantly. Hence, in this context, this thesis presents a method to achieve high accuracy at lower computational expense. Future studies can extend the proposed method to cable models with additional degrees of freedom such as bending and torsion.

Lay Summary

Floating structures such as oil rigs, production platforms and offshore wind turbines require a means of staying on-station for long periods of time. An effective engineering solution to fulfil this requirement is to install a system of mooring lines which anchor the floating structure to the seabed. A mooring system provides the forces required to restore a floating structure to a desired position when it is displaced from it, and also to limit the severity of motions it experiences under the myriad of environmental forces acting on it from waves, wind and currents.

Simulation software are widely used in the engineering design and analysis of mooring systems. Over the years, simulation methods have become an indispensable tool for engineers. However, these methods are based on mathematical approximations of real-world systems, and errors arise due to various assumptions and simplifications made in order to translate continuous, physical systems to their discrete, digital forms required for computer simulation.

An example of these errors is that tension fluctuations tend to arise when the digital representation of a mooring line experiences impact forces from the seabed. These fluctuations mostly do not occur in reality, and they manifest due to an inherent defect in the digital representation of a mooring line. The errors in the tension can affect the fatigue life estimation of mooring lines and the motions of a floating structure to which the line is connected in a simulation.

This research investigates the defect in present digital mooring line models which lead to the afore-mentioned errors and proposes two methods to address it. The first approach is based on the usage of a high-fidelity structural model and numerical methods to reduce required simulation time, and the second approach is an improved seabed force calculation method. This thesis aims to contribute to an improved understanding of the shortcomings in existing mooring line modelling methods pertaining to seabed interaction, and also proposes new solution ideas to shore up these shortcomings.

Contents

List of Figures

List of Tables

Nomenclatures

Acronyms

DP	Dynamic positioning
FD	Frequency domain
HF	High frequency
JONSWAP	Joint North Sea Wave Project
LF	Low/slow-drift frequency
QTF	Quadratic transfer function
RAO	Response amplitude operator
RK4	Fourth-order Runge-Kutta
TD	Time domain
TLP	Tension leg platform
WF	Wave frequency

Greek Symbols

ϵ	Element strain	
γ	Time-step fraction limit	
$\mu^{B,f}$	Seabed static friction coefficient	
ρ	Water density	$[\mathrm{kg/m^3}]$
θ	Element grounding angle	[rad]
ζ_s	Element structural damping ratio	

g	Gravitational acceleration constant, 9.81	$[\mathrm{m/s^2}]$

Roman Symbols

Δt	Time-step size	[s]
Δt_{max}	Maximum time-step size	[s]
$\dot{z}$	Nodal vertical velocity	[m/s]
$\hat{\mathbf{e}}$	Element unit direction vector	
$\hat{\mathbf{e}}^{f,A}$	Unit vector projection of the element direction unit vector on seabed surface plane	
$\hat{\mathbf{e}}^{N,A}$	Unit vector orthogonal to $\hat{\mathbf{e}}^{f,A}$ and $\hat{\mathbf{n}}_B$	
λ	Eigenvalue derived from eigenmatrix of system equations of motion	
$\ddot{\mathbf{r}}$	Nodal acceleration vector	$[\mathrm{m/s^2}]$
$\dot{\mathbf{r}}$	Nodal velocity vector	[m/s]
$\dot{\mathbf{u}}$	Fluid acceleration vector	[N]
$\hat{\mathbf{n}}_B$	Seabed normal unit vector	
$\tilde{\mathbf{K}}$	System stiffness matrix	$[\mathrm{kg \cdot m/s^2}]$
$\tilde{\mathbf{M}}$	System mass matrix	[kg]
$\mathbf{F}^A$	Hydrodynamic added mass force vector	[N]
$\mathbf{F}^{B,a}$	Seabed added mass force vector	
$\mathbf{F}^{B,d}$	Seabed vertical damping force vector	[N]
$\mathbf{F}^{B,f}$	Seabed lateral friction force vector	[N]
$\mathbf{F}^{B,r}$	Seabed reaction force vector	[N]
$\mathbf{F}^B$	Seabed force vector	[N]
$\mathbf{F}^D$	Hydrodynamic viscous drag force vector	[N]
$\mathbf{F}^{FK}$	Hydrodynamic Froude-Krylov force vector	[N]
$\mathbf{F}^H$	Total hydrodynamic force vector	[N]

$\mathbf{F}^S$	Nodal structural damping force vector	[N]
$\mathbf{F}^{tot}$	Total nodal force vector	[N]
$\mathbf{G}$	Transformation matrix from Cartesian to line element coordinate system	
$\mathbf{I}_3$	3×3 identity matrix	
$\mathbf{k}$	System state time rate-of-change vector	
$\mathbf{M}$	Nodal mass matrix	[kg]
$\mathbf{r}$	Nodal position vector	[m]
$\mathbf{r}^*$	Positions of nodes in dummy line segment S^D	[m]
$\mathbf{T}$	Tension force vector	[N]
$\mathbf{u}$	Fluid velocity vector	[N]
$\mathbf{u}_{rel}$	Relative fluid velocity vector	[N]
$\mathbf{V}$	General vector quantity	
$\mathbf{W}$	Nodal wet weight vector	[N]
$\mathbf{y}$	System state vector	
$\mathbf{y}^*$	Unperturbed system state used in linear stability analysis	
$\tilde{\mathbf{y}}_A$	Boundary conditions from active partition imposed on the latent partition	
$\tilde{\mathbf{y}}_L$	Boundary conditions from latent partition imposed on the active partition	
$\zeta^{B,d}$	Seabed vertical damping ratio	
A	Mean element displacement cross-sectional area	[m^2]
$C^{B,d}$	Seabed vertical damping force coefficient	
$C^{B,f}$	Seabed friction coefficient	
C_a	Element added mass coefficient	[m]
C_d	Element drag coefficient	

C_s	Element structural damping coefficient	
d	Discretisation index	
d_c	Current discretisation in discretisation switching procedure	
D_H	Element hydrodynamic diameter	[m]
D_S	Line structural outer diameter	[m]
d_t	Target discretisation in discretisation switching procedure	
H	Macro time-step size applied to latent partition	[s]
h	Micro time-step size applied to active partition	[s]
K	Element stiffness	$[\mathrm{kg \cdot m/s^2}]$
k^B	Seabed stiffness	[N/m]
l	Length of refined section of line in hybrid coarse/fine discretisation	[m]
L'^e	Element stretched length	[m]
L^e	Unstretched element length	[m]
L_{model}	Total unstretched line length	[m]
m	Micro time-step index for time integration of active partition	
m^e	Element mass per unit length	[kg/m]
N	System number of degrees of freedom	
n	Time-step index in single-rate and macro time-step index in dual-rate time integration schemes	
$N^{B,c}$	Seabed thickness coefficient	
N_p	Number of degrees of freedom in time integration partition p	
q	Time-step ratio between active and latent partitions	
R	Region of line where direct copying of nodal states is performed between discretisations	
R_{ramp}	Fairlead excitation ramp-up function	

S	Region of line where nodal positions are determined from requirement of satisfy interpolated strain values	
s	Static line model line coordinate system	[m]
S^A	Anchor-side strain mapping block	
S^D	Coarse region of line where dummy elements are inserted to approximate line geometry	
s^e	Element center s-coordinate	[m]
S^F	Floater-side strain mapping block	
s_{TDP}	Touchdown point s-coordinate	[m]
$s_{l,d}$	Uncorrected lower discretisation switching s-coordinate	[m]
$s_{l^*,d}$	Lower discretisation switching s-coordinate	[m]
$s_{u,d}$	Uncorrected upper discretisation switching s-coordinate	[m]
$s_{u^*,d}$	Upper discretisation switching s-coordinate	[m]
T	Element tension magnitude	[N]
t	Time	[s]
T_0	Fairlead pre-tension	[N]
T_{TDP}	Touchdown point line tension	[N]
T_H	Static line model top end horizontal force	[N]
T_{sim}	Total simulation time	[s]
$T_{V,bot}$	Static line model bottom end horizontal force	[N]
T_V	Static line model top end vertical force	[N]
W	Nodal weight	[N]
w	Wet weight per unit length in static line model	[N/m]
X_{TDP}	X-coordinate of touchdown point	[m]
X_{top}	Horizontal extent of line in Quasi-Static model	[m]
z	Nodal vertical coordinate	[m]

$z^{B,0}$	Seabed nominal seabed elevation	[m]
$z^{B,c}$	Seabed force cutoff elevation	[m]
Z_{top}	Vertical extent of line in Quasi-Static model	[m]

Superscripts

ν	Normal vector to line
τ	Tangential vector to line

Subscripts

A	Variable associated with active partition in dual-rate time integration scheme
L	Variable associated with latent partition in dual-rate time integration scheme
RK	Parameters related to the Runge-Kutta time integration scheme
X	X-component of Cartesian vector
Y	Y-component of Cartesian vector
Z	Z-component of Cartesian vector
0	Initial condition at time $t = 0$ s of a variable

Chapter 1

Introduction

One of the major challenges confronting governments and the energy industry today is that of producing and distributing enough energy to a growing and increasingly energy-hungry world. According to a report by the U.S. Energy Information Administration [6], between the year 2010 and 2040 world energy consumption is expected to grow 56% from 524 to 824 quadrillion BTU[1] while global petroleum and liquid fuel consumption is set to rise by 37% from 87 MMbbl/d[2] to 119 MMbbl/d, due to rapid urbanization and population and economic growth in developing regions [7–9].

A key challenge facing oil and gas industry today is that while existing fields are being depleted, new and viable fields are increasingly difficult to find or are situated in challenging environments such as under ice or in deep and ultra-deepwater locations offshore [10]. Meanwhile, as the wind industry faces resistance to the installation of wind farms onshore [11, 12], the prospect of harvesting the abundant and more reliable offshore wind resource [13] is enticing and the technologies required for that are being developed [14–16]. There has also been significant interest in research and development of wave and current energy devices [17, 18]. Owing to the aforementioned pressures and opportunities, the energy industry is increasingly turning towards developing offshore resources. According to a report by energy consulting firm Douglas-Westwood [19], capital expenditure on floating production systems from year 2015 to 2019 is expected to increase 73% over the previous 5 year period to reach USD $81 billion, out of which USD $55 billion

[1] British thermal unit
[2] One million barrels per day

will be committed to deepwater projects. These statistics highlight the growing importance of the offshore market particularly in deeper waters.

One of the common ways of categorizing offshore engineering developments is to use the measure of water depth as it presents challenges and constraints on the deployment and operation of offshore installations, in particular, on the type of foundations and station-keeping designs that may be used. Station-keeping refers to the task of maintaining the position of floating installations within prescribed offset limits, against environmental forces such as wind, waves, and currents. Conventionally, depths up to 300m are considered to be shallow water, while depths between 300m and 1500m is considered as deep water, and ultra-deepwater describes depths beyond 1500m [20].

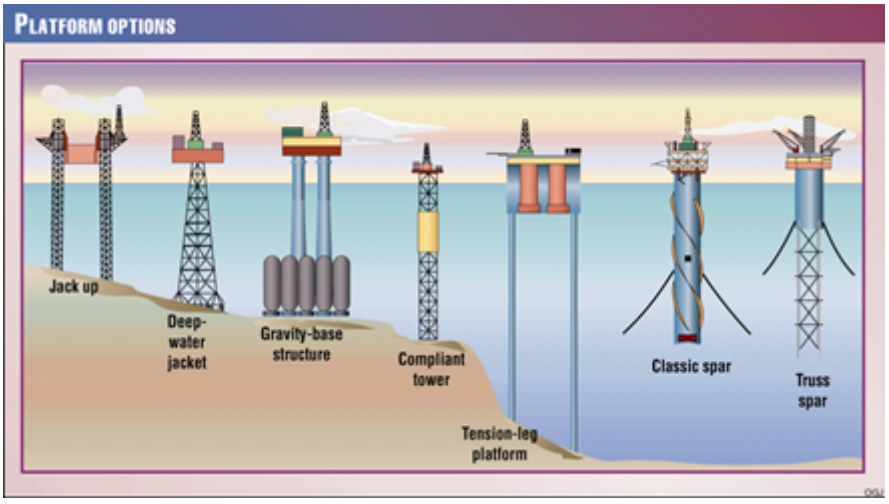

Figure 1.1: Types of Fixed and Floating Offshore Installations (Courtesy of Oil and Gas Journal).

In shallow water, fixed foundations which extend to the seabed may be used. For oil and gas platforms, fixed foundations may be jacket structures, compliant and guyed towers, or gravity-based platforms. Jacket structures are rigid truss structures resting on piles driven into the seabed and are viable up to 300m depth. Gravity based platforms are heavy structures that stay in place due to their massive weight and hence do not require the use of anchors or piles; they have been used up in water depths up to 300m. Compliant and guyed towers are structures that flex along with environmental loading and employ floats and guys to provide stability, and are used up to 600m depth. The main drawback of fixed platforms is that the cost of construction increases with water depth due to the amount

of material and structural reinforcement required, and in deep waters, it is more economically viable to use floating concepts instead, such as semisubmersibles, floating production/storage/offloading vessels, deep draught floaters or alternately known as spars, and tension leg platform (TLP). Figure 1.1 shows several of the aforementioned fixed and floating offshore installations operating at varying water depths.

Semisubmersibles typically consist of submerged pontoons which generate buoyancy and are connected to the topside via vertical columns. Floating production and storage platforms are ship-shaped vessels equipped with hydrocarbon production and processing facilities and are capable of being relocated quickly. Deep draught floaters are structures such as spars which consist of single or multiple columns that provide buoyancy and stability and have a much deeper draught than other floating concepts. TLPs have spar columns or submerged pontoons as buoyancy elements and typically have good vertical stability due to their station-keeping system. Such floater concepts have also been applied to floating wind turbines.

Offshore structures and systems are exposed to a range of environmental loads which may be severe during storms and hurricanes. Under these loads, floaters exhibit motions that need to be limited in order to prevent equipment damage and ensure crew safety and comfort. Dispensing with fixed platforms in lieu of floating concepts presents a new set of challenges, chief of which is station-keeping, which is achieved with mooring lines and dynamic positioning (DP) systems as well as hybrid systems incorporating both DP and mooring lines. Mooring line systems make use of long chains and ropes to tether the floater to the seabed. Lines may be taut or catenary, and buoys and tethers may be used to modify the geometry of the lines and thereby the restoring force characteristics. DP systems make use of dynamic control algorithms and position, motion and force sensors to control propellers and thrusters to keep the installation in place.

DP systems are preferred for exploratory drilling activities, where their comparatively short positioning times give them an advantage over mooring systems. They are also preferred as station-keeping systems for FPSOs in water depths exceeding approximately 2500 m. In such depths, if mooring lines are used their lengths and weight would be prohibitively large. This negatively impacts available payload of the floater, as well as the required size and economics of the line materials,

winches, chain jacks and connectors used [21]. While DP systems are versatile and operate varying water depths, the disadvantage is that they require more fuel to run and are typically more expensive to operate than mooring systems. Being complicated systems, failure of each crucial component may seriously compromise the operation of DP systems and there have been a number of incidents involving DP sub-systems failure and operator error which led to the loss of position [22]. In comparison, mooring lines operate most of the time as passive systems, and thus even when winches and chain jacks are non-operational, platform station-keeping ability is minimally compromised. Mooring lines are suitable for use across most water depths from shallow water up to ultra-deepwater depths of 2500 m [23]. Hybrid systems typically use its DP thrusters to support the passive mooring system and provide fine-tuning of the station-keeping characteristics [24]. In this way fuel, consumption is reduced and the overall reliability of the station-keeping system is enhanced.

Given that station-keeping systems are complex and critical systems for floating platforms, it is crucial that they are designed and maintained properly so that the risk and consequences of failure are mitigated. To that end the offshore industry has established station-keeping codes and recommended practices which describe environmental load criteria, analysis methods and procedures, design considerations and approval criteria, in-service maintenance and inspection requirements for various station-keeping systems including dynamic positioning and mooring line systems.

The aforementioned documents advocate the use of computer models and software to perform simulations of floater dynamics and mooring line responses in order to make accurate predictions of critical attributes such as platform maximum offset and line loads as well as long-term fatigue characteristics. Computer simulations are required to account for the complex environmental loading and mooring line interaction with the floater and the basis of such simulations is the mathematical model of the physical systems.

The aim of the next section is to provide a review of the methods and models used for calculation of mooring line loads, motions and dynamic interaction with the floater. The environmental loads and motions, as well as an overview of the global force and motion analysis methods typically used for moored floating structured will be discussed so as to provide a context for the development and application

numerical mooring line models. Having developed this background, the literature review focuses on existing line structure and seabed interaction models. This section is particularly pertinent to the scope of this thesis, which, as will be discussed, focuses on the problem on mooring line-seabed interaction.

1.1 Literature review

1.1.1 Environmental loads and responses of moored floating structures

A moored floating structure experiences time-varying environmental forces that are dependent on meteorological and oceanographic, or collectively known as metocean conditions. Ocean currents are caused by winds, in addition to the gravitational pull of the moon and sun, and salinity and temperature gradients in the ocean water. Current velocity varies with water depth and is dependent on the local bathymetry and underwater topographic features. Therefore velocity profile data is usually obtained from field measurements [25]. Conventionally, current velocities are treated as temporally constant for the calculation of structural loading [26], however, according to a recent ITTC[3] Specialist Committee on Deep Water Mooring report [27], current forces may be separated into mean and fluctuating components; this approach enables the assessment of vortex induced vibration loads which are relevant for risers and mooring lines with tubular cross sections such as sheathed wire ropes, in addition to the mean current which contributes to the mean drift force on the floater as well as influences the static equilibrium configuration of the mooring lines [28]. The report also highlighted that in deeper waters, where the lines are longer and spread over a large area, current velocity profiles used for analysis should ideally be spatially and temporally varying. However, because such information is usually not available, current velocities are typically specified as a spatially uniform unidirectional depth varying profile [27]. In practice, in dynamic moored floater motion analyses, vertically uniform, linear or bilinear vertically varying velocity profiles are typically used [28–30]. DNV-RP-C205 [31] provides guidance on the specification of current velocity profiles.

[3]International Towing Tank Conference

Local winds impose aerodynamic loads on the parts of the structure above the waterline. To calculate the loading, the wind speed and structural aerodynamic force coefficients are needed. Wind speeds are considered to be random Gaussian processes. The latter is usually found from wind tunnel measurements [4]. Over short time durations, the wind speed may be considered to be randomly fluctuating and statistically stationary, which implies that its statistical properties such as its mean, standard deviation, and autocorrelation of the random process, in this case, the wind speed, remain unchanged over the specified duration. The mean component is the average speed over the time duration, and a fluctuating component, known as wind gusts, is superposed on the mean speed [26]. The wind gust component can be generated by superposing multiple frequencies of varying amplitudes and phase angles relative to one another. This produces the seemingly random fluctuating wind speed component. The amplitudes corresponding to each of the frequency components can be obtained from wind spectra measurement data, such as the Davenport, Harris and NPD wind spectra [32].

Wave loads are transmitted to the submerged parts of floating structures and their attached slender structures such as risers, pipelines and mooring lines. Due to the large size of floaters such as ships, FPSOs and semi-submersibles, the dominant loads are usually inviscid loads. Figure 1.2 shows the different regimes where diffraction, inertia and viscous effects are important for a generic cylindrical structure exposed to waves. This is directly relevant for structures such as the cylindrical columns of a semi-submersible floater, but the concept may be applied to any floating structure in general. In the regime where both the wave height to characteristic structural dimension ratio and the wavelength to characteristic dimension ratios are low, in the region under 5, the large size of the structure will modify the direction of propagation of the waves and diffraction loading becomes dominant. In the regime where the wave height to characteristic dimension ratio is low, under 10, and the wavelength to characteristic dimension ratio is above 5, diffraction and viscous forces are less important whereas the forces arising from fluid acceleration due to the passing of the unperturbed waves are dominant. For cylindrical structures, this refers to the Froude-Krylov force. The viscous forces are dominant in the regime where the wave height and wavelength to characteristic dimension ratios are high, in effect, where the structural dimension is small relative to the characteristic wave dimensions. Linear wave theory implies that the instantaneous wave elevation of a long-crested random sea is considered to be a linear summation of regular wave

components and is assumed to adhere to the Gaussian distribution while the wave amplitudes, however, are Rayleigh distributed [1]. Hence, the instantaneous wave forces on an offshore structure can be considered to be Gaussian distribution while the peak loads are considered to be Rayleigh distributed.

For many floaters, which typically have small wave height to characteristic structural dimension ratios, viscous loads are less important compared to the inertia and diffraction loads. Hence, Figure 1.2 shows simply the relative importance of the different types of loads corresponding to different flow conditions. References [1] and [33] are sources for a more detailed explanation of the physics corresponding to the different flow regimes. The wave conditions, like wind conditions, is considered to be a random Gaussian process. Wave spectra may then be used to generate the wave conditions. The water surface elevation can be prescribed by the superposition of different frequency components extracted from a chosen wave spectrum.

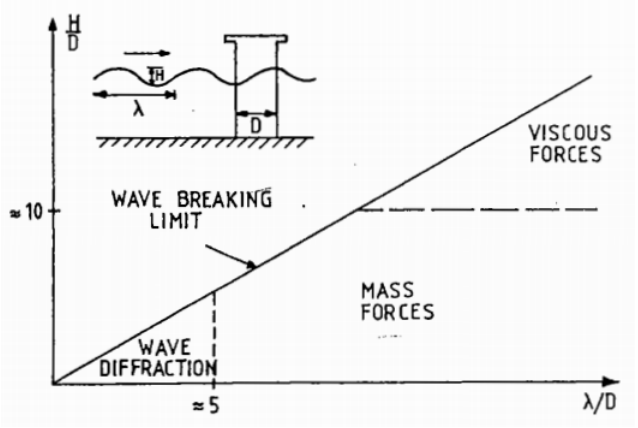

Figure 1.2: Flow regimes where diffraction, inertia and viscous forces dominate (Adapted from Ref. [1]).

Examples of wave spectra include the JONSWAP and Pierson-Moskowitz spectra [26]. Superposition of the various wave components follows the process for wind gusts, and gives rise to a steady, mean wave load, in addition to time-varying loads due to nonlinear interactions between the structural motions and wave frequency (WF) components.

Floating structures experience six degrees of freedom motions. The three translational motions are the surge, sway and heave motions, while the rotational motions are the roll, pitch and yaw motions. Being exposed to current, wind and wave

loads, moored floaters experience oscillatory motions across a range of frequencies. Because the wave loading is usually the dominant environmental load source on moored floaters, it is conventional to classify the different range of motion frequencies with respect to the wave frequencies or periods. Typically, a random sea state is composed of wave components with frequencies within the range of 0.04 and 0.2 Hz, or equivalently 5 and 25 s. Hence, this band of frequencies is known as WF range. Oscillatory motions of the floater within this frequency range are excited by first-order wave forces and are correspondingly known as WF motions. Floaters also experience motions at frequencies lower than 0.04 Hz, and motions within this frequency range are known as the low frequency (LF) motions. Certain floaters also experience motions at frequencies above the WF frequencies, and these motions are called high frequency (HF) motions.

The LF and HF motions are excited by the second-order LF and HF loads respectively. The LF second-order loads are also known as the difference frequency loads because they occur at the frequencies corresponding to the difference between the frequencies of the excitation force component pairs that gave rise to them. Similarly, the HF second-order loads are alternately known as the sum frequency loads because they occur at the frequencies equivalent to the sum of the frequencies of the source excitation force component pairs.

The first-order motions of the floater are excited by the first-order incoming waves, and the motion amplitudes are assumed to be linearly varying with the incoming wave amplitudes. This assumption allows the computation and usage of force and motion response amplitude operators (RAO) for floater dynamics computations. The LF and HF motions occur due to second-order forces, as shown in References [2] and [34]. The LF motions induced by the LF forces are also known as drift motions. In addition to the LF and HF motions, floaters also experience a mean, steady load from the environmental forces which give rise to a mean offset. Using perturbation theory, Pinkster [34] showed that the second-order pressure forces can be accounted for by considering the interaction between the first-order wave induced motions and first-order wave potential as well as the second-order wave potential. With such a formulation for the second-order force, and using a panel code and diffraction analysis to compute and integrate the pressure over the specified hull geometry, the quadratic transfer functions (QTF) relating the second-order force and the amplitudes of pairs of incident waves of different frequencies may be calculated.

For floater dynamics calculations, the usage of the QTFs to compute the second-order forces for a given seastate is convenient, but requires a preprocessing step in which the QTFs are generated by the use of a panel code such as WAMIT [35]. The LF or drift effect are accounted for by the difference frequency QTFs, while the HF effects are accounted for by the sum frequency QTFs [4]. RAOs are also calculated using diffraction analysis. Some examples of the usage of QTFs to compute second-order loads can be found in References [36–38]. This approach is also adopted by several commercial floater dynamics computer programs such as Orcaflex, Ariane, and DeepC.

Table 1.1 shows the typical natural periods in each of the six degrees of freedom for various floater types. The heave, roll and pitch motion natural periods are generally related to the hydrostatic restoring force while the surge sway and yaw natural periods are related to the restoring force of the mooring system. The exception among the floaters is the TLP, where the heave, roll and pitch motions are also largely dependent on the tension in the tendon members tethering the floater to the seabed. It is noted that the natural periods of the degrees of freedom related to the mooring forces are typically an order of magnitude larger than those related to the hydrostatic restoring force. Furthermore, the surge, sway, and yaw natural periods are outside of the range of the wave component frequencies. Despite this, moored floaters have been observed to exhibit large amplitude oscillatory motions in the LF range close to the resonance frequencies [39].

	Natural Periods (s)			
	FPSO	Spar	TLP	Semisub
Surge	> 100	> 100	> 100	> 100
Sway	> 100	> 100	> 100	> 100
Heave	5-12	20-35	< 5	20-50
Roll	5-30	50-90	< 5	30-60
Pitch	5-12	50-90	< 5	30-60
Yaw	> 100	> 100	> 100	> 100

Table 1.1: Typical natural periods of floaters in deep water (Adapted from Ref. [4]).

The LF motions, occurring close to the resonance frequencies, have amplitudes that are larger than the WF motions, as shown in Figure 1.3 even though the magnitude

of the second-order slow drift forces are small [34]. However, the frequencies of LF forces are close to the resonance frequencies of the surge, sway, and yaw motions. Furthermore, because the velocities of the LF motions are slow, the viscous and wave-making damping attributed to such motions are small. Therefore, the magnitude of the LF motions have been found to be highly dependent on the damping provided by the mooring lines [21, 40, 41].

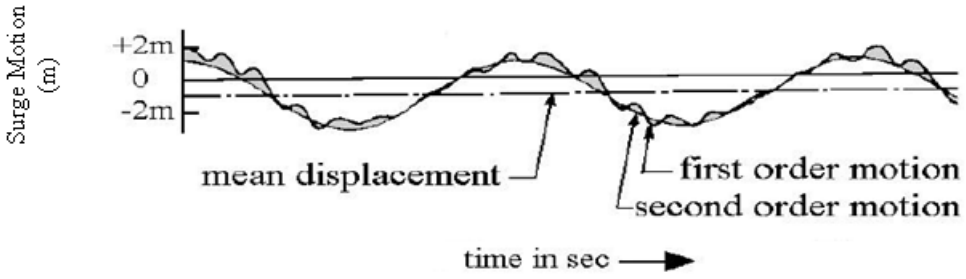

Figure 1.3: Typical mean, low and wave frequency motions of a barge (Adapted from Ref. [2]).

1.1.2 Time and frequency domain analysis

In frequency domain (FD) analysis, the motion response of the floater is calculated by solving the equations of motion for each frequency component of the environmental excitation force spectrum. Thus the first-order responses may be obtained from the force and motion RAOs and the force spectrum. For the second-order responses, the LF response is obtained by solving the equation of motion with each combination pair of the difference frequency loads, while the HF response is obtained in a similar manner using the sum frequency loads.

In time domain (TD), the environmental forces prescribed typically from the wind and wave spectra have to be converted from frequency to time domain. As shown in Reference [42], this can be accomplished by converting the force RAOs for the first-order wave forces and the QTF for the second-order forces into their respective impulse response functions by taking their inverse Fourier transforms. Then a convolution of the impulse response functions and the components of the incident waves will produce the total first and second-order wave forces in the time domain. The first and second-order wave forces are not differentiated in the time domain and their combined effects are represented as a single time signal. The equations

of motions can then be marched forward in time while imposing the time signal of the forces on the system.

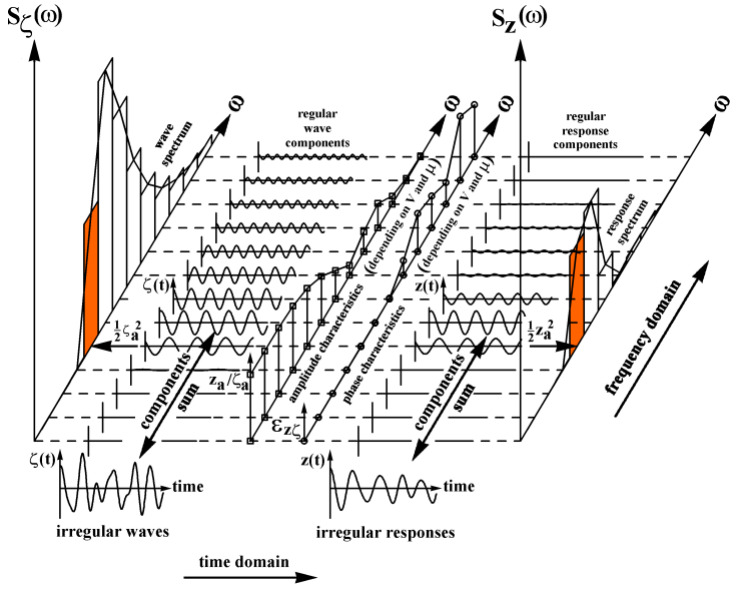

Figure 1.4: Superposition of regular wave components to form an irregular wave (Adapted from Ref. [2]).

Figure 1.4 shows graphically both the TD and FD approaches. It can be noted that the outputs for motion response arising from an FD analysis are spectral density data. For TD analysis, a time signal for the motions is obtained. A key advantage of the FD approach is its efficiency [43–45]. However, the FD approach assumes a linear or linearized system. For a typical floating structure dynamics problem, the possible sources of nonlinearities in the equations of motions include structural material nonlinearities, seabed contact and friction, geometric nonlinearity of the slender structures due to large displacements, and slender structure drag force which is calculated typically using Morison equation and hence scales quadratically with respect to relative fluid velocity [45]. These nonlinearities have to be linearized to apply FD analysis. For periodic nonlinear loadings, the method of equivalent linearization can be applied [46]. This technique is based on substituting a nonlinear model with linear one, and determining the linearized model coefficients by equating the energy dissipation of both models over one oscillation period. For stochastic loadings, the method of stochastic linearization, which is based on minimizing the least square error between the time average of the nonlinear and linearized models, may be used [47–49]. The methods may be applied to linearize the quadratic drag force as in References [50] and nonlinear seabed effects

[51]. TD analyses are able to accommodate the nonlinearities mentioned, but the computational cost is typically much higher.

In cases where the nonlinearities are weak, FD analysis has been found to provide good results comparable to TD analysis. Liu and Bergdahl [52] compared the energy dissipation, related to the fairlead line tension, from the TD and FD calculations, and found that the agreement was good even taking into consideration that the seabed friction forces had to be linearized. Ran et al. [44] similarly compared the motion responses of a Spar exposed to random waves calculated from TD and FD simulations, and found that the motion responses calculated by the FD method tends to underpredict that of the TD approach. They attributed this to the tendency of statistical linearization method, used to linearize the quadratic drag forces on the moorings, to be overestimated.

Low and Langley [50] performed both TD and FD analysis of a floater coupled to an array of mooring lines. The system is exposed to random waves and thus undergoes both WF and LF motions. From FD analysis, the motion response spectra was directly obtained. From TD analysis, the time series results for the motions were converted to frequency space and compared to the FD results. They reported that the agreement between both types of analysis methods was good. They attributed this to the good performance of the statistical linearization method applied for drag force linearization, and the weak geometric nonlinearity of the mooring lines arising from structural displacement, due to the fact that the system considered is in deep water and the line geometry changes due to floater displacement are small compared to the length of the lines. In a continuation of this work, Low and Langley [53] assessed the suitability of FD analysis to shallower water depths and found that in this case, the geometric nonlinearities arising from geometry change of the mooring lines resulted in the poor agreement between the TD and FD results.

1.1.3 Uncoupled analysis

The uncoupled approach for calculating moored floater motions is currently the most efficient method to calculate the floater motions and line responses. In the uncoupled approach, floater motion and line response are calculated separately.

First, the vessel motion is calculated, and then these calculated motions are imposed on the mooring line model to calculate the structural response of the lines [4, 54].

In the first step to obtain the vessel motions, a simplified model of the mooring system is included in the vessel equation of motion. The most basic description of a mooring system is to model it as linear or nonlinear springs. To generate the coefficients for the restoring force of the springs used to represent the mooring lines, a common approach has been to apply a discretized line model such as a finite element model may be used to calculate the fairlead static tension force across a range of offsets [28, 54]. This description neglects the dynamic effects of the lines namely the inertial and damping loads. For small floaters such as catenary anchor leg mooring buoys, the line inertia loads have significant effect on their dynamics [54]. For large floaters, however due to their large mass and size, the inertia loads from the lines is a small fraction of the total environmental loads and has a small effect on the motions.

In addition to the static restoring forces, the damping effect of the mooring lines may be included with the addition of a damping term in the equations of motions typically in the yaw, surge and sway motions in the horizontal plane which are most affected by mooring line forces. Ormberg and Larsen [28] described a process in which the damping coefficient is estimated from experimental data or calculated top end line tension from static spring forces. From the time trace of line tensions and floater displacements obtained from experiments, the LF floater dynamics and line tension fluctuations can be extracted which are equated, from which the linear damping coefficient are derived. It should be noted however that this method ignores wave drift damping and hydrodynamic drag forces on the floater hull and assumes that the floater motions are due to the line tensions acting through the fairlead. The authors commented that a linear damping coefficient is usually sufficient to represent line damping. This approach of using top end line tension to calculate a linear damping coefficient was also described by Brown and Mavrakos [5] and Webster [55].

Another approach is based on calculating the work done by hydrodynamic drag on the lines over an LF oscillation period. In this approach, assumed LF motions of the floater on the horizontal plane, such as surge, sway and yaw, are imposed on

the top end node of the lines which induces the lines to undergo corresponding displacements. The relative velocities arising from those motions are then integrated over an LF oscillation period, which amounts to the kinetic energy of the floater dissipated through the hydrodynamic drag on the lines. Integrating the equation of motion of the floater over one LF period, it may be proved that the inertial and restoring force components do not dissipate energy, which leaves the damping term as the contributor to energy dissipation. The linear damping coefficient can then be found by equating the line and floater energy dissipation terms. Huse and Matsumoto [56] proposed a method which accounts for the vertical in-plane motion of the line. This method was modified by Liu and Bergdahl [57] to improve on the evaluated in-plane relative velocities. Bauduin and Naciri [58] proposed a method that accounts for the out-of-plane displacement of the lines, further improving on the estimation of the relative fluid velocities, drag forces, and energy dissipation. However, it should be noted that WF line oscillations contribute significantly to energy dissipation and floater motion damping [53, 59, 60] and it has been neglected in this approach. This approach has, however, been used in various applications [61–63].

To account for the effect of WF motions on line energy dissipation and LF floater motion damping, Lie et al. [30] proposed a method in which the relative fluid velocities induced by WF motions are evaluated with a statistical analysis approach. From the expected value of the drag force on the line, the linearised damping coefficient is found. Low and Langley [50] also found that as the line stiffnesses change significantly due to LF floater motions, the natural frequency of the lines under increased tension moves closer to the WF range. The convergence of the modal and excitation frequencies lead to increased oscillation amplitude and relative fluid velocities over the lines, amplifying the hydrodynamic drag forces, energy dissipation and floater motion damping.

The uncoupled approaches achieve computational efficiency by simplifying the representation of the mooring line forces on the floater and separating the analysis of the line and floater responses, thus reducing the degrees of freedom of the individual systems. However, applying this method requires judgement in the specification of suitable static restoring force and in particular the damping coefficients, which is not straightforward because of the need to account for stochastic loads on the line as well as the nonlinear LF line responses.

1.1.4 Comparison of coupled and uncoupled mooring system and floating structure analysis

API RP 2SK [54] describes two variants of this approach. In the semi-coupled approach, one solves the equation of motion of the floater coupled to the static stiffness of the lines, thus neglecting the inertia and damping effects. In the fully-coupled approach, the line inertia and damping are taken into account and the motions of the line and floater are calculated simultaneously. The coupling between the lines and the floater is achieved by establishing a common node between the two representing the fairlead.

Ormberg and Larsen [28] compared the responses of a turret-moored vessel using coupled and uncoupled approaches and stated that the main drawback of this approach is that the effects of current and WF oscillations are not taken into account. The former affects the line geometry, restoring line forces and thus the calculated mean offset significantly, while WF oscillations affect the line damping and thus has a strong influence on the LF motion amplitude. They used a finite element model of the mooring lines and potential flow theory to calculate the hydrodynamic forces on the floater and found that as water depth increases and in the presence of current, the coupled approach is required in order to capture the influence of the current on the mean line shape as well as hydrodynamic line damping in order to obtain good estimates of the mean and LF offsets.

Similar conclusions were drawn by Heurtier et al. [64], who used one of the tests cases reported by Ormberg and Larsen [28]. By setting the drag coefficient of the lines to zero, they found that the LF response predicted by the uncoupled and coupled approaches were very similar, which led them to conclude that line inertial loads have little effect on the calculated surge motion while a good estimation of the relative velocities between the fluid and lines is critical to calculating LF responses affected by line damping. These results show that while motions in the horizontal plane such as the surge motion are characterized by the dominance of the LF motion amplitudes over the WF motion amplitudes, both the wave and LF oscillations contribute significantly to the amplitude of the line tensions. Further, a fully coupled approach taking into consideration the dynamical line loads across the low and WF range is required to accurately capture line tension fluctuations. This has also been reported by various other researchers [65].

Vendhan [45] describes a method frequently used in industry in which relatively coarse discrete line models are used for coupled simulations to obtain nodal accelerations and velocities, which are then inserted into the refined line model with higher nodal densities to achieve detailed line stresses.

A coupled analysis is computationally demanding and this fuels the development of techniques to reduce computational effort while still achieving acceptable accuracy.

1.1.5 Mooring line structural models

For the calculation of the mooring line forces on the floating structure dynamics, the most important factor is the mooring line axial tension. For chain-link type lines, in numerical modelling of line dynamics usually only axial tension is taken into account, and torsion and bending are neglected [65–67]. This is often a good approximation for chains [1] because the axial stiffness is typically uncoupled from the twist of the lines unless the axial rotation angles are large. However, out-of-plane bending fatigue damage of chains has been identified as a significant cause of failure for mooring lines [67]. For wire ropes made of steel or synthetic materials such as polyester, torsional loads and axial tension are coupled [68], and for such materials, this effect may have to be taken into account in floater structure dynamics analysis.

Mooring line models can be static or dynamic. The latter includes the inertial and damping loads while the former does not. Jonkman [15] formulated a quasi-static mooring model that takes into consideration seabed contact and friction and calculates the anchor and fairlead vertical and horizontal forces based on the line material properties and the anchor and fairlead positions. This static model was subsequently extended to be able to consider multisegment lines consisting of different branches and line materials [69]. Chai et al. [70] also formulated a quasi-static model that can account for inclined seabeds and external attachments such as buoys. The main drawback of the static line models is that dynamic loads cannot be taken into consideration.

Dynamic line models are able to account for the unsteady loads from the environment. They apply discretization in space and time to capture the dynamic

effects along the line. Broadly, the presently available models can fall within three categories, lumped mass, finite element rod, and finite difference models.

The lumped mass (LM) model considers the line structural masses to be lumped at regular intervals along the mooring line. The structural mass along the line is assumed to be concentrated at the lumped mass nodes and each node is attached to its neighbours via a massless spring. In the original formulation of the LM approach by Walton and Polachek [71], the nodes are linked via inextensible elements, which provided the constraint conditions for the calculation of line tensions. The application of a massless elastic spring model to describe the line tension force between adjacent nodes was then discussed in a follow-up paper by Polachek et al. [72]. In addition to the line tension, other forces including line weight, buoyancy, hydrodynamic forces and other imposed forces are applied to the nodes. The structural mass matrix is a diagonal matrix. Structural damping is often excluded as in References [50, 66, 73–75], but may also be included [65, 76] to improve numerical stability. For chain-link mooring lines, usually bending and torsion effects are excluded. For low tension or zero tension cases, the line response is nonlinear and requires the inclusion of bending stiffness effects in order to capture the line dynamics [40]. Hence, for lines consisting of steel wire or synthetic ropes, and when cables may be slack or when line tensions are low, bending effects should be included [77, 78]. To this end, Buckham [78] formulated a higher order lumped mass model that incorporates torsional and bending effects using a cubic spline to calculate the line curvature between nodes.

For lines which may undergo taut-slack transitions, instead of a linear line stiffness, a bilinear line tension may be specified [79]. In this formulation, the tension of each element in the discrete model is assumed to be zero when the separation distance between two adjacent nodes is lower than the unstretched length of the element. A linear line stiffness is adequate for lines that are predominantly under tension. Huang and Vassalos [80] found that for severe fairlead excitations, the lines undergo alternating slack-taut transitions, resulting in snap loadings and amplified maximum tension loads, necessitating the use of a bilinear line stiffness. Buckham [78] noted that the lumped mass approach is simple, versatile and facilitates the assembly of multisegment, multicomponent line assemblies. Kurian et al. [75] demonstrated this by generating a lumped mass discretization for a multicomponent line that includes buoys and clump weights for imposed fairlead motions at

the fairlead.

Finite element mooring line models, in comparison to lumped mass models, make use of shape functions to decompose the distributed forces along the line into discrete forces imposed at the nodes. The structural mass matrices in finite element models are consistent matrices, and discretization is performed using one-dimensional shape functions. An example of the finite element mooring model is that developed by Garrett [81], which uses cubic spline shape functions. Using Galerkin's weighted residual method [82], the governing equations for a continuous line can be discretized. This formulation takes into consideration bending effects and is able to accommodate torsion as well, but the latter effect is deemed to be less important and is usually neglected [44, 83–86]. Leonard and Nath [87] compared the finite element and lumped mass approaches and concluded that for the same spatial discretization the finite element method is more accurate, but the two approaches should be equivalent when higher nodal densities are used in the lumped mass approach. The advantage of the lumped mass method is that having a diagonal mass matrix removes the need for solving a system of equations, thus saving on computational expense. The applicability of the lumped mass approach to mooring line modelling has been proven in many implementations [65, 78, 88].

Another line discretization approach is via the finite difference formulation. In such an approach, the governing equations of motions are spatially and temporally discretized using Taylor series expansion, as detailed in [89–91]. This is the approach adopted in the WHOI Cable software [92]. However, the selection of a suitable time step and spatial discretization requires mesh sensitivity studies the solutions tend to be susceptible to numerical errors [76]. As noted by Masciola [76] and Gobat and Grosenbaugh [92], the selection of suitable time-step sizes for the time-integration of the equations of motion is challenging and might be limited by numerical stability requirements rather than results accuracy. However, it should be noted that finite element and lumped mass models, regardless of the choice of time-integration schemes, have to address the issue of numerical stability during time integration, and furthermore Gobat and Grosenbaugh [92] have developed an adaptive time-stepping method to address this difficulty. Nonetheless, the finite difference approach has proven its applicability to a wide range of mooring line and riser simulation problems considering seabed contact [93, 94], current loads [95], and low tension conditions [93, 96].

1.1.6 Seabed interaction models

There are uncertainties pertaining to the soil material, stiffness and damping, as well as the time-varying aspect of its properties with progressive grounding, sliding and lifting of the lines [97], which complicates analysis efforts. For example, the soil forces resisting the motions of the slender structures are typically anisotropic. The forces also vary with the depth of penetration of the line into the soil [97]. Trenching effects, in addition to affecting riser pipelines [94, 98], also affect mooring lines [91] and the holding capacity of suction anchors used in conjunction with taut mooring lines [99]. Soil remoulding effects and water entrainment due to repeated pipeline penetration affects the shear strength of soils and has an influence on soil stiffness [100, 101] the breakout resistance of the soil, which then affects pipeline dynamics [102]. Soil behaviour thus varies over time, loading conditions, and with soil material. The Randolph and Quiggins model [103] model is an example of a sophisticated soil-constitutive model which describes the vertical soil stiffness as a nonlinear resistance accounting for trenching, suction, uplift and hysteretic effects of repeated cycles of these penetrative motions. Modelling the lateral motions of slender structures can similarly take the complex, high fidelity approach by using nonlinear models such as that proposed by White and Cheuk [104], which considers the kinematic hardening of soil due to the build up of berms.

One description of the seabed forces is the spring-mattress model, or variously referred to as the elastic seabed model, such as that proposed by Webster [55]. In this model, the seabed is modelled as a flat or undulating surface which provides a vertical support force to the mooring line. This model is described in detail in Section 3.1.2. Similar variations of this approach are used in Refs. [65, 88, 105, 106] and is implemented in commercial codes such as Orcaflex [107] and aNyMOOR [108]. In contrast to the high fidelity soil-consitutive models, this approach greatly simplified and mainly aims to capture the mooring line dynamics at a resolution relevant to fulfilling the purpose of predicting the mooring line forces, in particular, the tension restoring forces. The main advantage of this simplified approach is that the entire line length remains active over a simulation. Hence, the effect of the grounded section on the suspended part, and vice versa is fully accounted for. In contrast to the spring-mattress model, in which the dynamics of the grounded section are calculated, Chatjigeorgiou and Mavrakos [109] proposed a model which calculates

the touchdown point from a quasi-static solution, and truncating it from the touchdown point onwards. A further simplification is to represent the touchdown point as a static location which is the approach taken by Goodman and Breslin [110] as well as Mavrakos et al. [111]. Under the assumption of a static and quasi-static touchdown point, the effects of the line liftoff and touchdown forces are neglected.

Thomas [112] proposed a seabed model in which the mass of the first two suspended nodes adjacent to the seabed are gradually reduced as they approach the sea-bed. The motivation for the development of this model was to eradicate the fluctuations in the line tensions associated with nodal grounding. However, a limitation of the method is that the mass modifier coefficients used to perform the nodal mass reduction have to be determined, by trial and error, for individual grounding nodes and recalibrated for each specific fairlead excitation time history.

Wang et al. [113] used the lumped mass approach to model a mooring line in conjunction with a seabed model based on rigid body collision analysis. It was noted by the authors that, upon line impact with the seabed, there were fluctuations in the fairlead tension which they attributed to the spatially discrete nature of the line structural model. Triantafyllou et al. [114] showed analytically that tension shocks may occur during both the loading and unloading phases of a dynamic mooring cable motion period and derived a condition for its occurrence. Gobat and Grosenbaugh [115] experimentally verified the condition, noting however that the occurrence of unloading shocks may not affect the fairlead tension.

Nakajima et al. [116] proposed a method in which the masses of line nodes are reduced to zero as they approach the seabed, thus avoiding the line tension shocks from the impact loading associated with deceleration of the line mass. The effect of seabed impact using a discrete lumped mass line model was investigated in detail by Thomas [112], who concluded that the nodal momentum is the main contributor to the vertical dynamic impact force on the lumped mass nodes upon contact with the seabed, with line stiffness being a secondary contributor. Other findings from this research are that nodal density and timestep size are parameters that affect the manifestation of the oscillations. Following Nakajima [116], Thomas [112, 117] proposed prescribing mass modifiers that adapted the weight of the grounding nodes such that the tension fluctuation history is optimized for reduction of the tension fluctuations that appear due to nodal grounding. However, the parameters that are used to tune the mass modifier coefficients can only be determined via

postmortem analysis. Hence, in order to apply this technique, the same calculation may need to be done repeatedly.

For time domain analyses, nonlinearities associated with line-seabed friction and hysteresis can be accounted for directly. Liu and Bergdahl [57] used a Coulomb friction model for time domain line calculations and concluded that seabed friction greatly contributes to energy dissipation and is proportional to excitation amplitude. This implies that the damping of LF floater motions will particularly be influenced by the representation of seabed friction. Chang et al. [74] also used a Coulomb friction model to represent lateral soil-line interaction forces, while the vertical force is represented with critically damped spring-dampers. In some time-domain simulations [50, 53] only the vertical forces are accounted for while the lateral friction forces are neglected, with the justification being that the influence of the soil-line interaction on floater dynamics and line tensions is small compared to other effects such as hydrodynamic damping when the suspended line length is much greater than grounded length.

Liu and Bergdahl [57] also linearized their Coulomb friction model using the stochastic linearization method for frequency domain calculations. They concluded that frequency domain results with their linearized seabed model compare well with time domain results. Another frequency domain approach, adopted by Ong and Pellegrino [118], involves linearization of the static catenary line equation to obtain linear spring coefficients. In their study prescribed fairlead motions were imposed on linearized spring as well as pinned support models and the fairlead tensions from these two models obtained from frequency domain analysis were compared with time domain analyses in Orcaflex. They concluded that modelling the touchdown point as a pinned support leads to large overestimation of the dynamic tensions even for small fairlead motions, and that for high pretensions catenary action is subdued and a horizontal spring model will suffice while for low pretensions catenary action is significant necessitating the use of a system of coupled vertical and horizontal springs.

Brown and Mavrakos [5] stated for seabed forces acting on mooring lines, out-of-plane friction and suction forces are not significant, whereas in-plane forces can have an effect on the dynamic peak line tensions. Further, seabed friction has an effect on reducing the tension fluctuations experienced by the line segments on the seafloor. This is because friction limits the nodal movements due to the tension

forces transmitted from the suspended segments, thereby limiting line elongation and compression, which manifests as an increased line stiffness.

Yu and Tan [119] used a simple elastic spring as well as sophisticated elastic-plastic soil constitutive models, namely the Mohr-Coulomb and Drucker-Prager models to calculate soil-line friction and slip. They concluded that the simple elastic spring model gave similar results for line stresses and fairlead offsets compared to the complex elastic-plastic models.

1.2 Discussion

From the literature review, it is clear that there are numerous seabed modelling approaches of varying levels of fidelity developed to address various application difficulties and shortcomings of prior methods. At one end of the spectrum is the static touchdown point model in which the grounded line span is excluded from consideration. At the other end are complex, nonlinear soil constitutive models, such as that proposed by Randolph and Quiggin [103] and White and Cheuk [104]. The tradeoff between these two ends of the spectrum is simplicity and non-reliance on model coefficients. Model coefficients typically provide a simplified means of describing the bulk effects of one medium on another, with the inherent sacrifice of model fidelity and general applicability.

For time-domain mooring cable analysis, effects such as trenching and soil hysteresis effects are less important compared to an accurate representation of tension, especially close to the fairlead, because it is where mooring line failures frequently occur due to overload or fatigue [120, 121]. The fairlead force also provides the net effect of mooring line dynamics on floater motions. The spring-mattress method is the most widely used due to its flexibility, simplicity, and completeness of analysis for the entire mooring line. It is less restricted in its applicability compared to static touchdown point models, and requires lower data storage and computational effort compared to high fidelity seabed models. However, previous studies have suggested that the spring mattress model is prone to discretisation errors associated with line contact with the seabed, particularly spurious tension fluctuations as noted by Refs. [112, 113]. The dependence of these models on force coefficients

which are difficult to define and calibrate for various seabed and case-specific environmental excitation conditions is an area where further work is required.

Among the candidate line structural models, the finite element and lumped mass approaches, in comparison to the finite difference approach, are more widely adopted, perhaps due to the sensitivity to numerical issues experienced with a finite difference based approach. Between the lumped mass and finite element approaches, the former inherently makes simplifications including the assumption of a diagonal mass matrix which, when paired with suitable time-integration schemes, removes the need to solve a linear system of coupled equations. While its accuracy is generally lower than a finite element based system, this can be improved by increasing the density of the discrete elements within a given spatial domain.

1.3 Research Hypotheses

Following the literature review, several research hypotheses are constructed:

- The numerical errors generated by line-seabed impact is due to the interaction between the seabed model and the discrete nature of the lumped-mass mooring line structural model. If proven to be true, this leads to the construction of the following hypotheses for solution methods.
- The discretisation errors generated by line-seabed impact may simply be ameliorated by modifying the line structural model, in effect, via mesh refinement.
- The discretisation errors generated by line-seabed impact may be ameliorated with the use of a higher-order seabed force model which accounts for the discrete nature of the line structural model.

1.4 Objectives of this work

Based on the review of the literature, the main goals of this research are:

- Investigate the cause of the potentially spurious tension fluctuations that are experienced due to seabed contact when the variants of the spring-mattress model is used.
- Develop a generally applicable modelling approach, which is not reliant on uncertain model force coefficients, and also minimizes the occurrence of spurious tension fluctuations caused by seabed impact when the spring-mattress model is used.
- Develop an improved spring-mattress type seabed model which is resistant to the irregularities caused by seabed impact forces.

1.5 Research approach

The approach taken in this research work consists of the following steps:

1. In order to have adequate control over modelling techniques and parameters, and fully expose the pertinent issues related to the investigative problem at hand, a numerical mooring line model is developed from the ground up. The accuracy of the in-house line model will be validated against analytical results as well as results from commercial software.
2. A detailed analysis of the line dynamics at the touchdown point and the influence on the rest of the line will be performed in order to understand the circumstances which lead to the development of undesired effects such as tension fluctuations.
3. Develop a technique that allows a spring-mattress type seabed model, with generic force coefficients, to be used under general environment excitation conditions and is free of tension fluctuations.
4. Develop an improved spring-mattress model which is resistant to the production of tension fluctuations due to seabed impact loads.

The contributions of this research are an improved understanding of the deficiencies of existing spring-mattress type seabed models, as mentioned in point 2 above, and two different approaches to address the identified deficiencies.

1.6 Thesis structure

The background, literature review, and research objectives, approaches and contributions of this research are presented in this chapter.

Chapter 2 presents the development of the mathematical models required for the line internal structure, fluid-structure interaction as well as the time integration algorithm. The results of a series of model validation tests are then presented.

Chapter 3 introduces the basic spring-mattress seabed model. The effects of line-seabed impact are evaluated and the causes of the afore-mentioned numerical errors are identified. The root cause and conditions that lead to the production of the large dynamic tension fluctuations is determined. The factors which have an influence on the severity of the numerical errors such as line discretisation are also analysed.

Chapter 4 presents the development of a adaptive meshing strategy to reduce the numerical errors associated with line-seabed impact and a compatible time integration scheme for efficient computation of line dynamics. The purposes for the development of the time integration scheme and adaptive discretisation strategy are explained, and the effectiveness and improvements over present methods are illustrated.

Chapter 5 presents the development of a modified spring-mattress model. The effectiveness in addressing the shortcomings of the conventional spring-mattress model is presented.

Finally, Chapter 6 provides a summary of the present work and discusses potential areas for further research.

Chapter 2

Numerical Mooring Line Model Development and Validation

The first phase of this project is concerned with the development and validation of a time domain numerical mooring line model, as stated in Section 1.5. Several types of dynamic mooring line models were described in Section 1.1.5, along with their relative strengths and drawbacks. The differences between them lie in their spatial and temporal discretisation approaches. In this work, the line structural model will be developed based on the lumped mass methodology due to the advantages it possesses over the other classes of line structural models as discussed in Section 1.1.5.

In this chapter, the theoretical aspects of the line structural model are described in Section 2.1 and aspects of the time integration schemes for dynamic simulation will be described in Section 2.2. The basic line model developed in this work is validated against analytical results for static cases, and against the results of the commercial software Orcaflex [107] for dynamic cases. The validation results are presented in Section 2.3.

2.1 Mooring line structural dynamics model

In a lumped mass model, a mooring line is discretised into nodes and elements, and a typical configuration of a discretised catenary line is presented in Figure 2.1a.

Figure 2.1b shows the connectivity between nodes and elements in the present model. The Orcaflex theory manual [107] documents the force calculation procedures used in that software, while the methods in the current in-house code are presented in this section.

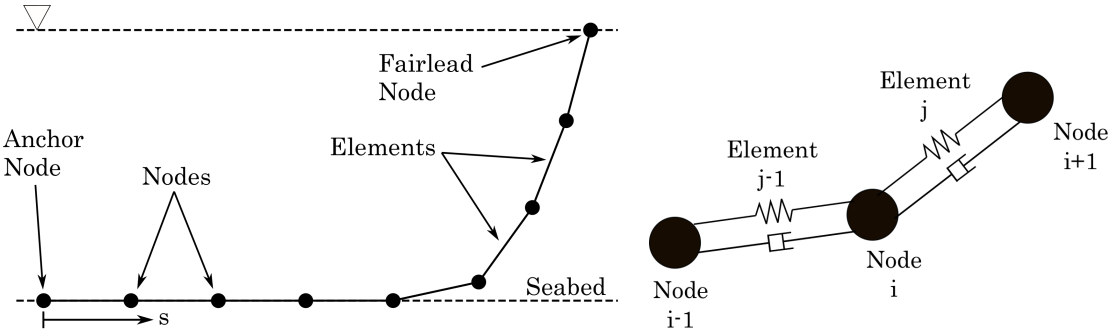

(a) Discretised catenary mooring line. (b) Node and element connectivity.

Figure 2.1: Typical lumped mass mooring line discretisation.

2.1.1 Distribution of mass

The equations of motion are solved for the nodes. The mass of each element is distributed equally to the adjacent nodes by way of a diagonal mass matrix.

$$\mathbf{M}_i = \frac{m^e_{j-1} L^e_{j-1}}{2}\mathbf{I}_3 + \frac{m^e_j L^e_j}{2}\mathbf{I}_3 = \sum_{\xi=j,j-1} \frac{m^e_\xi L^e_\xi}{2}\mathbf{I}_3 \tag{2.1}$$

where m^e_ξ and L^e_ξ, $\xi = \{j,\, j-1\}$ are the mass per unit length and lengths of the elements j and $j-1$, and $\mathbf{I}_3$ is a 3x3 identity matrix.

2.1.2 Internal strain and tension

The tension in a section of the line is represented as the tension, T_j, in the associated element j given by,

$$T_j = \begin{cases} K_j \epsilon_j, & \epsilon_j > 0 \\ 0, & \epsilon_j \leq 0 \end{cases} \tag{2.2}$$

where ϵ_j is the strain and K_j is the linear stiffness of the element. The element strain is given by,

$$\epsilon_j = \frac{|\mathbf{r}_{i+1} - \mathbf{r}_i|}{L_j^e} - 1 \tag{2.3}$$

where $\mathbf{r}_{i+1}$ and $\mathbf{r}_i$ are the positions of the nodes bounding element j, and L_j is the unstretched element length. With reference to Figure 2.1b, the resultant tension force vector acting on node i, $\mathbf{T}_i$, is the sum of the tension forces from its connected elements given by,

$$\mathbf{T}_i = K_j \epsilon_j \hat{\mathbf{e}}_j - K_{j-1} \epsilon_{j-1} \hat{\mathbf{e}}_{j-1} \tag{2.4}$$

where the element unit direction vectors $\hat{\mathbf{e}}_j$ and $\hat{\mathbf{e}}_{j-1}$ are given by,

$$\hat{\mathbf{e}}_j = \frac{\mathbf{r}_{i+1} - \mathbf{r}_i}{L_j^e} \tag{2.5a}$$

$$\hat{\mathbf{e}}_{j-1} = \frac{\mathbf{r}_i - \mathbf{r}_{i-1}}{L_{j-1}^e} \tag{2.5b}$$

2.1.3 Structural damping

With reference to Figure 2.1b, the material damping force in an element i is given by,

$$\mathbf{F}_i^S = C_{s,j} \left[(\dot{\mathbf{r}}_{i+1} - \dot{\mathbf{r}}_i) \cdot \hat{\mathbf{e}}_j \right] \hat{\mathbf{e}}_j + C_{s,j-1} \left[(\dot{\mathbf{r}}_i - \dot{\mathbf{r}}_{i-1}) \cdot \hat{\mathbf{e}}_{j-1} \right] \hat{\mathbf{e}}_{j-1} \tag{2.6}$$

where the structural damping coefficient $C_{s,\xi}$, $\xi \in [j, j-1]$, is given by,

$$C_{s,\xi} = 2\zeta_{s,\xi} \sqrt{K_\xi m_\xi^e L_\xi^e} \tag{2.7}$$

and $\zeta_{s,\xi}$ is the structural damping coefficient for element ξ, and $\dot{\mathbf{r}}$ denotes nodal velocity.

2.1.4 Weight and buoyancy

The present mooring line model also takes into consideration the weight, buoyancy and hydrodynamic forces on the line. The weight of a line section submerged in water is given by,

$$\mathbf{W}_i = \sum_{\xi=j,j-1} \frac{\left(m_\xi^e - \rho A_\xi\right) L_\xi^e g}{2} \hat{z} \tag{2.8}$$

where $\hat{z}$ is the vertical direction unit vector, g is the gravitational acceleration constant, and A_ξ is the mean cross section of an element which gives the result that $A_\xi L_\xi$ is the displaced volume of water for element ξ.

2.1.5 Hydrodynamic forces

The hydrodynamic forces are evaluated using Morison's equation [122], which consists of the added mass, Froude-Krylov and viscous drag components. For a unit length line section, the Morison force is given by,

$$\begin{aligned}
\mathbf{F}^H &= \mathbf{F}^{H,\tau} + \mathbf{F}^{H,\nu} \\
&= \mathbf{F}^{FK,\tau} + \mathbf{F}^{FK,\nu} + \mathbf{F}^{A,\tau} + \mathbf{F}^{A,\nu} + \mathbf{F}^{D,\tau} + \mathbf{F}^{D,\nu} \\
&= \rho\frac{\pi}{4} D_H^2 \left[(C_a^\tau + 1)\dot{\mathbf{u}}^\tau - C_a^\tau \ddot{\mathbf{r}}^\tau\right] + \frac{1}{2}\rho D_H C_d^\tau \left|\mathbf{u}_{rel}^\tau\right| \mathbf{u}_{rel}^\tau \\
&+ \rho\frac{\pi}{4} D_H^2 \left[(C_a^\nu + 1)\dot{\mathbf{u}}^\nu - C_a^\nu \ddot{\mathbf{r}}^\nu\right] + \frac{1}{2}\rho D_H C_d^\nu \left|\mathbf{u}_{rel}^\nu\right| \mathbf{u}_{rel}^\nu
\end{aligned} \tag{2.9}$$

where $\mathbf{F}^{A,\tau}$ and $\mathbf{F}^{A,\nu}$ are the added mass, $\mathbf{F}^{I,\tau}$ and $\mathbf{F}^{I,\nu}$ are the Froude-Krylov and $\mathbf{F}^{D,\tau}$ and $\mathbf{F}^{D,\nu}$ are the drag forces in the line tangential and normal directions. C_a^τ, C_a^ν and C_d^τ, and C_d^ν are the sectional tangential and normal added mass and drag coefficients, D_H is the hydrodynamic diameter of the line section, ρ is the water density, $\ddot{\mathbf{r}}$ is the nodal acceleration vector, $\dot{\mathbf{u}}$ is the acceleration vector of the water, and $\mathbf{u}_{rel}$ is the relative velocity between the water and the line structure as given by,

$$\mathbf{u}_{rel} = \mathbf{u} - \dot{\mathbf{r}} \tag{2.10}$$

For a general vector quantity $\mathbf{V}$, its components tangent and normal to the line segment with unit vector $\hat{\mathbf{e}}$ are given as in Equations (2.11) and (2.12) respectively.

$$\mathbf{V}^{\tau} = (\mathbf{V} \cdot \mathbf{e})\,\mathbf{e} = \begin{bmatrix} e_X^2 & e_Y e_X & e_Z e_X \\ e_X e_Y & e_Y^2 & e_Z e_Y \\ e_X e_Z & e_Y e_Z & e_Z^2 \end{bmatrix} \begin{bmatrix} V_X \\ V_Y \\ V_Z \end{bmatrix} = \mathbf{G}^{\tau}\mathbf{V} \tag{2.11}$$

$$\mathbf{V}^{\nu} = \mathbf{V} - \mathbf{V}^{\tau} = (\mathbf{I} - \mathbf{L}^{\tau})\,\mathbf{V} = \begin{bmatrix} 1 - e_X^2 & e_Y e_X & e_Z e_X \\ e_X e_Y & 1 - e_Y^2 & e_Z e_Y \\ e_X e_Z & e_Y e_Z & 1 - e_Z^2 \end{bmatrix} \begin{bmatrix} V_X \\ V_Y \\ V_Z \end{bmatrix} = \mathbf{G}^{\nu}\mathbf{V} \tag{2.12}$$

$\mathbf{G}^{\tau}$ and $\mathbf{G}^{\nu}$ are the transformation matrices to obtain the components of $\mathbf{V}$ that are tangent and normal to the line segment with orientation $\hat{\mathbf{e}}$, respectively. Therefore, the tangential and normal components for $\ddot{\mathbf{r}}$, $\dot{\mathbf{u}}$, and $\mathbf{u}_{rel}$, which are required in Equation (2.9), are given by,

$$\dot{\mathbf{u}}^{\tau} = \mathbf{G}^{\tau}\dot{\mathbf{u}} \tag{2.13a}$$

$$\dot{\mathbf{u}}^{\nu} = \mathbf{G}^{\nu}\dot{\mathbf{u}} \tag{2.13b}$$

$$\mathbf{u}_{rel}^{\tau} = \mathbf{G}^{\tau}\mathbf{u}_{rel} \tag{2.14a}$$

$$\mathbf{u}_{rel}^{\nu} = \mathbf{G}^{\nu}\mathbf{u}_{rel} \tag{2.14b}$$

$$\ddot{\mathbf{r}}^{\tau} = \mathbf{G}^{\tau}\ddot{\mathbf{r}} \tag{2.15a}$$

$$\ddot{\mathbf{r}}^{\nu} = \mathbf{G}^{\nu}\ddot{\mathbf{r}}_{rel} \tag{2.15b}$$

With reference to Figure 2.1b, the Morison force acting on node i is thus given by the sum of the hydrodynamic forces acting on the half-lengths of the elements j and $j-1$, and is given by,

$$\mathbf{F}_i^H = \sum_{\xi=j,j-1} \rho\frac{\pi}{8} D_{H,\xi}^2 L_\xi^e \Big\{ \left[(C_{a,\xi}^\tau + 1)\mathbf{G}_\xi^\tau + (C_{a,\xi}^\nu + 1)\mathbf{G}_\xi^\nu\right] \dot{\mathbf{u}}_i - \left(C_{a,\xi}^\tau \mathbf{G}_\xi^\tau + C_{a,\xi}^\nu \mathbf{G}_\xi^\nu\right) \ddot{\mathbf{r}}_i \Big\} + \frac{1}{4}\rho D_{H,\xi} L_\xi^e \left[C_{d,\xi}^\tau \left|\mathbf{G}_\xi^\tau \mathbf{u}_{i,rel}\right| \mathbf{G}_\xi^\tau + C_{d,\xi}^\nu \left|\mathbf{G}^\nu{}_\xi \mathbf{u}_{i,rel}\right| \mathbf{G}_\xi^\nu\right] \mathbf{u}_{i,rel} \tag{2.16}$$

2.1.6 Equation of motion

The equations of motion are assembled as,

$$\mathbf{M}_i \ddot{\mathbf{r}}_i = \mathbf{T}_i + \mathbf{F}_i^S + \mathbf{F}_i^B + \mathbf{W}_i + \mathbf{F}_i^H = \mathbf{F}_i^{tot} \tag{2.17}$$

where $\mathbf{F}_i^B$ and $\mathbf{F}_i^{tot}$ are the seabed and total force vectors acting on node i. There are two seabed force formulations used in this work; firstly, the spring-mattress model proposed by Webster [55] is be discussed in Section 3.1, and a modified spring-mattress model developed in this work to address the shortcomings of the original model. The modified spring-mattress model is presented in Section 5.1.

2.2 Time integration schemes

There are two time integration schemes used in this work, namely, the fourth-order Runge-Kutta [123] (RK4) and Modified Euler [124] integration schemes. The fourth-order Runge-Kutta scheme is used in the single-rate time-integration cases and in the context of this research includes the investigation of the effects on nodal grounding (Section 3.2) and the application of a modified spring-mattress model in a number of test cases (Section 5.2). The Modified Euler integration scheme is is used as the base integration scheme in the dual-rate time-integration procedure developed and evaluated in Chapter 4.

A state vector, $\mathbf{y}$, containing the nodal positions and velocities, $\mathbf{r}$ and $\dot{\mathbf{r}}$, is defined and its time derivative can be written as,

$$\frac{\mathrm{d}\mathbf{y}}{\mathrm{d}t} = \mathbf{k}\left(\mathbf{y}\right) = \begin{bmatrix} \dot{\mathbf{y}}_1 \\ \dot{\mathbf{y}}_2 \end{bmatrix} = \begin{bmatrix} \dot{\mathbf{r}} \\ \ddot{\mathbf{r}} \end{bmatrix} = \begin{bmatrix} \dot{\mathbf{r}} \\ \tilde{\mathbf{M}}^{-1}(\mathbf{r})\mathbf{F}^{tot}(\mathbf{r}, \dot{\mathbf{r}}) \end{bmatrix} \tag{2.18}$$

where $\mathbf{k}$ is the time rate of change of the state vector.

2.2.1 Fourth-order Runge-Kutta integration scheme

According to the RK4 algorithm, the state vector at the next time-step, $\mathbf{y}_{n+1}$, is given by,

$$\mathbf{y}_{n+1} = \mathbf{y}_n + \sum_{i_{RK}=1}^{4} b_{i_{RK}} \mathbf{k}_{i_{RK}} \tag{2.19}$$

where the values for $\mathbf{k}_{i_{RK}}$, $i_{RK} \in [1, 4]$ at each stage of intermediate time integration stages are given by,

$$\mathbf{k}_{i_{RK}} = \mathbf{k}\big(t_n + c_{i_{RK}} \Delta t, \mathbf{y}_n + a_{i_{RK}} \mathbf{k}_{i_{RK}}\big) \tag{2.20}$$

where Δt is the time-step, and the coefficients $a_{i,j,RK}$, $b_{i,RK}$, and $c_{i,RK}$ corresponding to the classical RK4 form are given by,

$$\begin{array}{c|c} c_{i,RK} & a_{i,j,RK} \\ \hline & b_{i,RK} \end{array} = \begin{array}{c|cccc} 0 & 0 & 0 & 0 & 0 \\ 1/2 & 1/2 & 0 & 0 & 0 \\ 1/2 & 0 & 1/2 & 0 & 0 \\ 1 & 0 & 0 & 1 & 0 \\ \hline & 1/6 & 1/3 & 1/3 & 1/6 \end{array} \tag{2.21}$$

The linear stability assessment function [123] for the RK4 scheme is given by,

$$\left|Q(\Delta t \lambda_j)\right| = \left|1 + \Delta t \lambda_j + \frac{1}{2}(\Delta t \lambda_j)^2 + \frac{1}{6}(\Delta t \lambda_j)^3 + \frac{1}{24}(\Delta t \lambda_j)^4\right| \leq 1 \tag{2.22}$$

where λ_j refer to the eigenvalues of the system of ordinary differential equations to which the stability function is applied. Before the linear stability criterion can

be applied, the nonlinear state representation of the equations of motion, Equation (2.18), has to be linearized as,

$$\mathbf{k}(\mathbf{y}) = \mathbf{k}(\mathbf{y}^*) + \frac{\partial \mathbf{k}}{\partial \mathbf{y}} \delta \mathbf{y} \tag{2.23}$$

where $\mathbf{y}^*$ is an arbitrary state of the system, and $\delta \mathbf{y} = \mathbf{y} - \mathbf{y}^*$ is a perturbation from that state. The quantity $\partial \mathbf{k}/\partial \mathbf{y}$ is the Jacobian matrix of $\mathbf{k}$ with respect to the state vector $\mathbf{y}$, and is given by,

$$\frac{\partial \mathbf{k}}{\partial \mathbf{y}} = \begin{bmatrix} 0 & \mathbf{I} \\ \dfrac{\partial \dot{\mathbf{y}}_2}{\partial \mathbf{r}} & \dfrac{\partial \dot{\mathbf{y}}_2}{\partial \dot{\mathbf{r}}} \end{bmatrix} \tag{2.24}$$

Following Ref. [125], a fourth-order approximation of the Jacobian or equivalently the gradient of $\mathbf{k}$ with respect to $\mathbf{y}$, via a centered difference formula, is given by,

$$\begin{aligned} \left.\frac{\partial \mathbf{k}}{\partial \mathbf{y}}\right|_{\mathbf{y}^*} \approx \Big[& -\mathbf{k}^{1,-2} + 8\mathbf{k}^{1,1} - 8\mathbf{k}^{1,-1} + \mathbf{k}^{1,-2}, \dots, \\ & -\mathbf{k}^{2N,-2} + 8\mathbf{k}^{2N,1} - 8\mathbf{k}^{2N,-1} + \mathbf{k}^{2N,-2} \Big] \frac{1}{12\,\delta \mathbf{y}} \end{aligned} \tag{2.25}$$

where N if the number of degrees of freedom of the system, and the notation $\mathbf{k}^{j,d}$ is defined as,

$$\mathbf{k}^{j,d} = \mathbf{k}\left(\dots, y_j^* + d\,\delta y_j, \dots \right) \tag{2.26}$$

where $j \in [1, 2N]$. An eigenvalues, λ_j, of the Jacobian of $\mathbf{k}$ can then be inserted into Equation (2.22), along with a desired time-step h to determine if the stability criterion is breached. The maximum stable time-step is one that satisfies Equation (2.27).

$$max\Big(\big|Q(\Delta t, \lambda_j)\big|, \dots, \big|Q(\Delta t_{max}, \lambda_{2N})\big| \Big) = 1 \tag{2.27}$$

To find Δt_{max}, Equation (2.27) is reformulated as Equation (2.28) and solved using the Nelder-Mead optimization scheme [126].

$$Q'(\Delta t_{max}) = \left| max\Big(\big|Q(\Delta t_{max}, \lambda_j)\big|, \dots, \big|Q(\Delta t_{max}, \lambda_{2N})\big|\Big) - 1 \right| \tag{2.28}$$

The applied time-step, Δt, is then the maximum time-step scaled by a factor lower than one. This is to account for the limitation that the maximum timestep is determined at the start of the simulation using the initial line geometry. However, as the line geometry changes over the course of the simulation, the maximum time-step which is dependent on the state vector $\mathbf{y}$, changes in tandem. Therefore, a scaling factor C_{time}, to account for the fact that the maximum time-step at some point during a simulation may be lower than what was determined with the initial line state, as illustrated in Equation 2.29.

$$\Delta t = C_{time} \Delta t_{max} \tag{2.29}$$

2.2.2 Modified Euler integration scheme

In the Modified Euler integration scheme [124], the nodal positions and velocities at each successive time-step as,

$$\mathbf{r}_{n+1} = \mathbf{r}_n + \dot{\mathbf{r}}_{n+1} \Delta t \tag{2.30a}$$

$$\dot{\mathbf{r}}_{n+1} = \dot{\mathbf{r}}_n + \left[\mathbf{M}_n(\mathbf{r})\right]^{-1} \mathbf{F}^{tot}\left(t_n,\, \mathbf{r}_n,\, \dot{\mathbf{r}}_n\right) \Delta t \tag{2.30b}$$

To determine the maximum time step for the Modified Euler algorithm, the undamped, homogeneous form of the equation of motion, as shown in Equation (2.31), is considered.

$$\tilde{\mathbf{M}}(\mathbf{r})\ddot{\mathbf{r}} + \tilde{\mathbf{K}}(\mathbf{r})\mathbf{r} = 0 \tag{2.31}$$

The maximum time-step for each partition is evaluated following the procedure described by Hahn [124], and re-arranging Equation (2.31) as follows,

$$\ddot{\mathbf{r}} + \left(\tilde{\mathbf{M}}^{-1}\tilde{\mathbf{K}}\right)\mathbf{r} = \ddot{\mathbf{r}} + \mathbf{E}\mathbf{r} = 0 \tag{2.32}$$

where λ_{max}, the largest eigenvalue of the $\mathbf{E}$ matrix is then used to determine the maximum stable time-step for the partition using the condition derived by Hahn [124],

$$\Delta t_{max} = \frac{2}{\sqrt{\lambda_{max}}} \tag{2.33}$$

The applied time-step is scaled by C_{time}, following Equation 2.29.

2.3 Validation of mooring line model

2.3.1 Static line model validation

2.3.1.1 Comparison of static configuration with analytical solution

Validation of the line model begins with the validation of the static configuration of the line. For this purpose, comparisons can be made between the analytical catenary line model and that given by the static lumped mass model. Following Ref. [1], the catenary line shape for a two dimensional freely hanging line is given in Equation (2.34),

$$\begin{aligned} X(s) =& \frac{T_H}{w}\left[\ln\left(\frac{T_{V,bot}+ws}{T_H}+\sqrt{1+\left(\frac{T_V+ws}{T_H}\right)^2}\right)-\right. \\ & \left.\ln\left(\frac{T_{V,bot}}{T_H}+\sqrt{1+\left(\frac{T_{V,bot}}{T_H}\right)^2}\right)\right]+\frac{T_H s}{K} \end{aligned} \tag{2.34a}$$

$$\begin{aligned} X(s) =& \frac{T_H}{w}\left[\sqrt{1+\left(\frac{T_{V,bot}+ws}{T_H}\right)^2}-\sqrt{1+\left(\frac{T_{V,bot}}{T_H}\right)^2}\right]+ \\ & \frac{1}{K}\left(T_{V,bot}s+\frac{ws^2}{2}\right) \end{aligned} \tag{2.34b}$$

$$T_{V,bot} = T_V - w\,L_{model} \tag{2.34c}$$

where T_H and T_V are the horizontal and vertical forces at the elevated line end, while $T_{V,bot}$ is the vertical force at the lower end, as is calculated as shown in Equation (2.34c), K is the line stiffness and w is the wet weight per unit length

of the line which takes buoyancy into consideration. Figure 2.2 illustrates the positions and orientations of the forces on a suspended line.

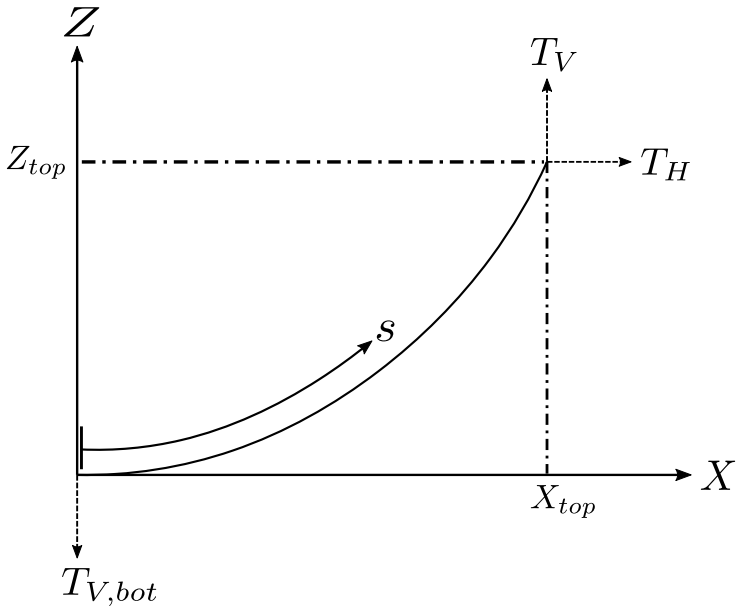

Figure 2.2: Coordinate system and forces for catenary line model.

Equation (2.34) can be modified by setting s equal to the length of the line, from which horizontal and vertical extent of the line can be set, as shown in Equation (2.35). These two equations can be solved simultaneously for the horizontal and vertical fairlead forces, T_H and T_V, which can then be inserted into Equation (2.34) to find the analytical line shape. For different fairlead positions, the line geometry generated by the analytical model is then compared to that given by the lumped mass model.

$$X_{top} = \frac{T_H}{w}\left[\ln\left(\frac{T_V}{T_H} + \sqrt{1+\left(\frac{T_V}{T_H}\right)^2}\right) - \ln\left(\frac{T_V - wL_{model}}{T_H} + \sqrt{1+\left(\frac{T_V - wL_{model}}{T_H}\right)^2}\right)\right] + \frac{T_H L_{model}}{K} \tag{2.35a}$$

$$Z_{top} = \frac{T_H}{w}\left[\sqrt{1+\left(\frac{T_V}{T_H}\right)^2} - \sqrt{1+\left(\frac{T_V - wL_{model}}{T_H}\right)^2}\right] + \frac{1}{K}\left(T_V L_{model} - \frac{wL_{model}^2}{2}\right) \tag{2.35b}$$

The mooring line used in the static configuration validation process is a chain type with the parameters as shown in Table A.1. The same mooring line material will be used in the dynamic model validation process. The static configuration for two different fairlead positions were generated by the analytical and lumped mass numerical models and shown in Figure 2.3. There is close agreement between the analytical and lumped mass models in the line geometries.

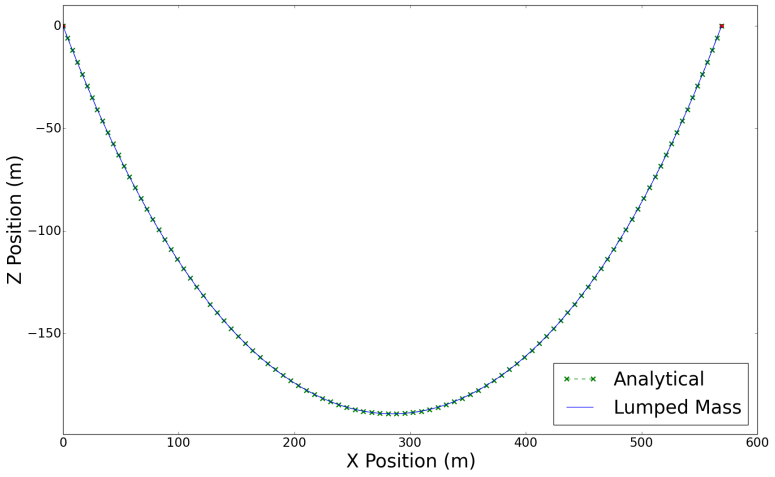

(a) Configuration 1: Fairlead position at x = 569.04 m, z = 0.0 m.

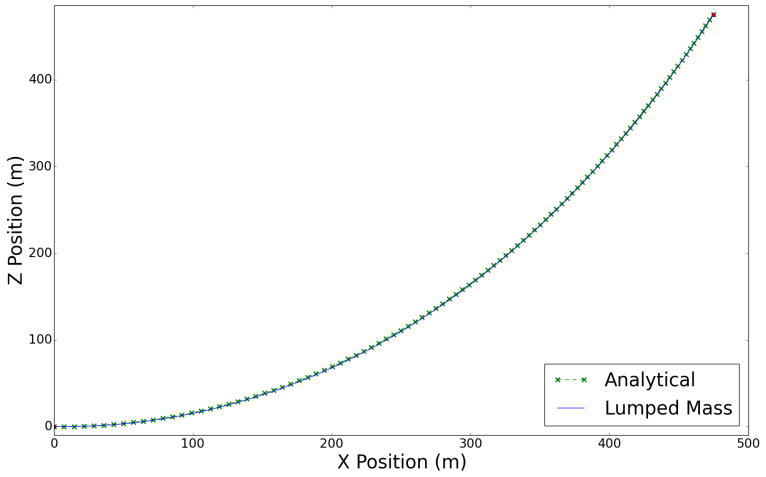

(b) Configuration 2: Fairlead at x = 474.68 m, z = 474.68 m.

Figure 2.3: Static line configurations for two fairlead positions using analytical and lumped mass models.

Table 2.1 shows the line end tensions, T_H, T_V and $T_{V,bot}$, calculated with the lumped mass and analytical solutions, and it can be noted that the deviation between the

two models is negligible. The close agreement between the line geometries and calculated end tensions indicates that the static behavior of the lumped mass model is correct.

Table 2.1: Line end tensions for static configurations by lumped mass and analytical models.

Tension	Lumped Mass	Analytical	Percentage Deviation
Configuration 1			
T_H (N)	7.68E+05	7.69E+05	0.06%
T_V (N)	1.14E+06	1.14E+06	0.01%
$T_{V,bot}$ (N)	1.12E+06	1.12E+06	0.00%
Configuration 2			
T_H (N)	9.20E+05	9.26E+05	0.62%
T_V (N)	2.26E+06	2.27E+06	0.39%
$T_{V,bot}$ (N)	6.76E+03	6.76E+03	0.00%

2.3.1.2 Comparison of static configuration with commercial software

To further validate the static response of the line model, the tension results from the commercial software Orcaflex [107] and the current in-house code are compared without considering seabed contact so as to compare the results from the two codes involving all other forces including weight, buoyancy, hydrodynamic and tension forces. The two test configurations consisting of fully suspended mooring chains, one with a fixed end and the other a free end, are shown in Figure 2.4.

The line is assumed to be fully submerged in water for the entire duration of the simulation. The water density is 1025 kg/m^3. The structural parameters of the mooring line are listed in Table A.1. For static analysis, there are no external loads except for weight, hence in both configurations, the entire line is in the X-Z plane. The static line tensions for both configurations are shown in Table 2.2. For Configuration 3, the line end tensions at both ends of the line are in agreement up to 6 significant figures. For Configuration 4, the discrepancy in the fixed and fairlead end tensions are both 0.021%.

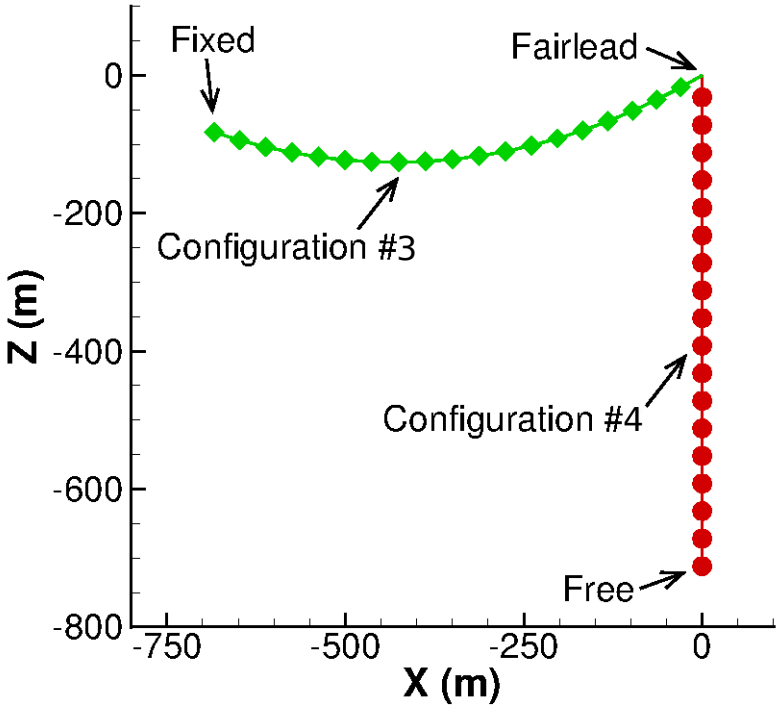

Figure 2.4: Suspended line configurations for validation by comparison to Orcaflex.

Table 2.2: Initial position and tension at line ends.

Config	Line End	(X,Y,Z)-coordinates	Tension-Orcaflex (kN)	Tension-Inhouse (kN)
3	Free	(0.0, 0.0, 711.3)	0.00	0.00
	Fairlead	(0.0, 0.0, 0.0)	2275.58	2275.58
4	Fixed	(-683.74, 0.0, -82.5)	2542.82	2542.28
	Fairlead	(0.0, 0.0, 0.0)	2806.61	2806.01

2.3.2 Dynamic line model validation

To validate the dynamic response of the mooring line, prescribed position and velocity are imposed at the fairlead position according to the functions presented in Equations (B.1) and (B.2).

where the index $i = \{1, 2, 3\}$, refers to the surge (X), sway (Y) and heave (Z) directions, and $(.)^{WF}$ and $(.)^{LF}$ refer to the wave and slow-drift frequency fairlead components for the quantity in $(.)$, r_i are the motion amplitudes, T_i are the motion periods, and ϕ_i are the phase angles. $R_{ramp}(t)$ is a ramp-up function implemented in Orcaflex [107]. Three prescribed motions profiles, as presented in Table B.1, are used for validation of dynamic line response. The line discretisation used is a

homogeneous mesh consisting of 2.50 m length elements. The time-step size was set to 0.0012 s, which was 0.72 times of the maximum stable time-step evaluated by Section 2.2.1.

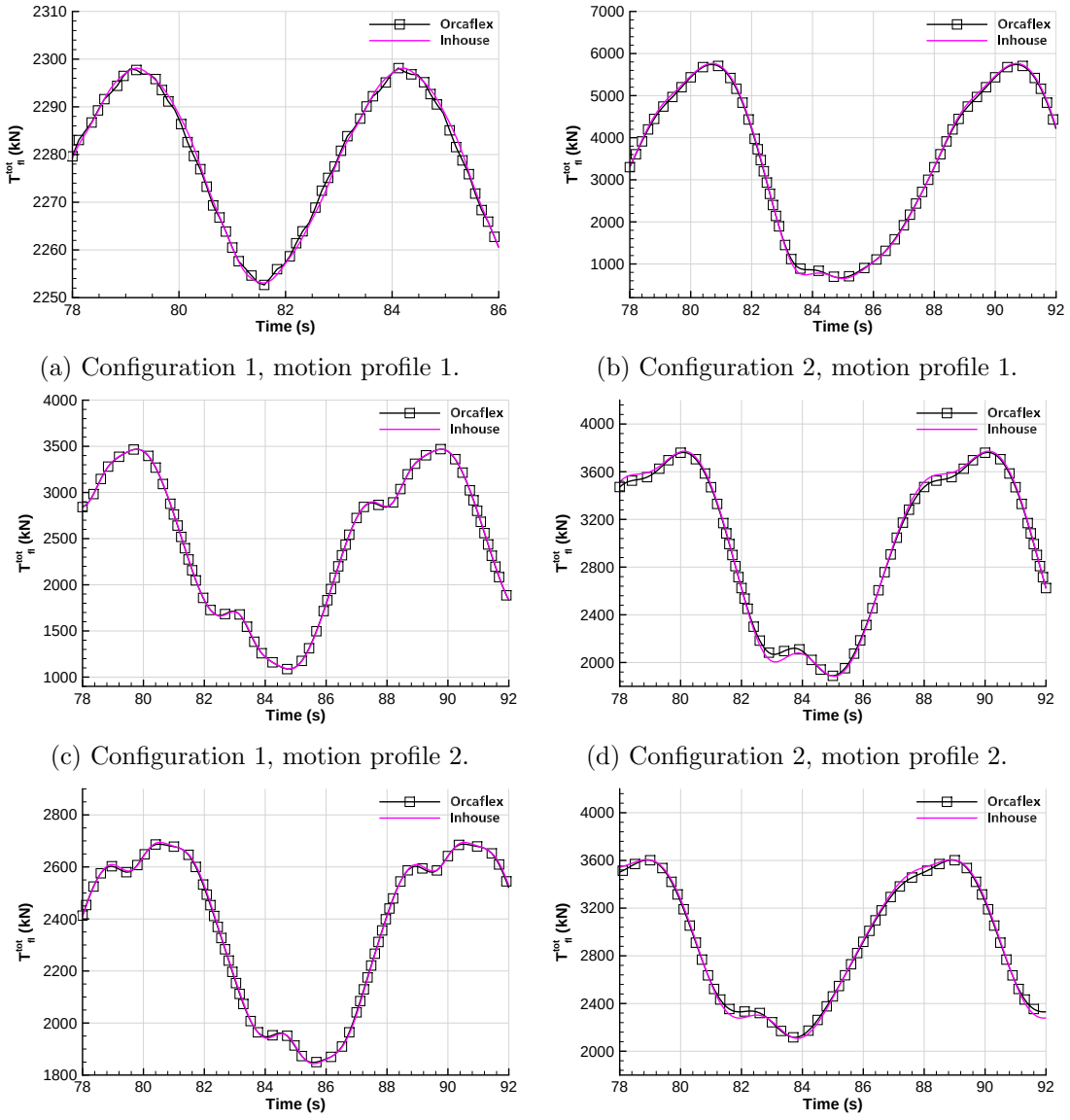

(a) Configuration 1, motion profile 1.

(b) Configuration 2, motion profile 1.

(c) Configuration 1, motion profile 2.

(d) Configuration 2, motion profile 2.

(e) Configuration 1, motion profile 3.

(f) Configuration 2, motion profile 3.

Figure 2.5: Fairlead tensions for fully suspended line from Orcaflex and current in-house code.

Figure 2.5 presents the fairlead tensions time histories for Configurations 3 and 4 with the imposed fairlead motions included in Table B.1. The results are shown for time windows that are slightly wider than one period of the tension fluctuations, and when the fluctuations are fully developed; the ramp-up time region is excluded. sespite the difference in the time integration methods used for the two

codes, the implicit Generalized-α scheme in Orcaflex and the fourth-order Runge-Kutta scheme is used in the in-house code, The results show that the time histories of the fairlead tensions from both codes are in good agreement. In particular, the tension peaks and troughs predicted are consistent.

2.4 Chapter closure

In this chapter, the basic line structural dynamics model was developed. The effects that are taken into consideration include material weight and inertia, buoyancy, internal tension, hydrodynamic drag, and added mass, and were presented in Section 2.1. For time integration, two schemes were implemented, namely the fourth-order Runge-Kutta and Modified Euler schemes. As these are explicit methods, the time-step stability assessment procedures are important and they were presented in Section 2.2. Static and dynamic validation of the line model without seabed contact was performed via comparison with an analytical model and results from the commercial software Orcaflex in Section 2.3 and show that the present line model gives accurate results and can be applied to investigate the effects of seabed contact.

Chapter 3

Analysis of Seabed Impact Effects

In this chapter, the seabed force components that contribute to the total seabed force, $\mathbf{F}^B$, in Equation (2.17) is presented. The spring mattress seabed model refers to the vertical reaction force component of $\mathbf{F}^B$ and is presented in Section 3.1.2. The effects of the mooring line lifting off from and grounding on the seabed, as well as the root cause of the tension fluctuations arising from seabed impact forces is also examined in Section 3.2.

3.1 Spring mattress seabed model

3.1.1 Seabed coordinate system and force components

Figure 3.1 shows the seabed coordinate system and an element j in contact with the seabed. The seabed nominal elevation is $z^{B,0}$, while the seabed force cutoff elevation is $z_{B,c}$; the elevation at which the element section is not in contact with the seabed. The unit vector normal to the seabed is $\hat{\mathbf{n}}_B$. The unit vector $\hat{\mathbf{e}}^{f,A}$ is a unit vector that is the projection of the element direction unit vector $\hat{\mathbf{e}}_j$ on the seabed tangent plane, while the unit vector $\hat{\mathbf{e}}^{f,N}$ is the unit vector orthogonal to both $\hat{\mathbf{e}}^{f,A}$ and $\hat{\mathbf{n}}_B$.

$$\hat{\mathbf{e}}_j^{f,A} = \frac{\hat{\mathbf{e}}_j - (\hat{\mathbf{e}}_j - \hat{\mathbf{e}}_j \cdot \hat{\mathbf{n}}_B)}{|\hat{\mathbf{e}}_j - (\hat{\mathbf{e}}_j - \hat{\mathbf{e}}_j \cdot \hat{\mathbf{n}}_B)|} \tag{3.1}$$

$$\hat{\mathbf{e}}_j^{f,N} = \frac{\hat{\mathbf{e}}_j^{f,A} \times \hat{\mathbf{n}}_B}{\left|\hat{\mathbf{e}}_j^{f,A} \times \hat{\mathbf{n}}_B\right|} \tag{3.2}$$

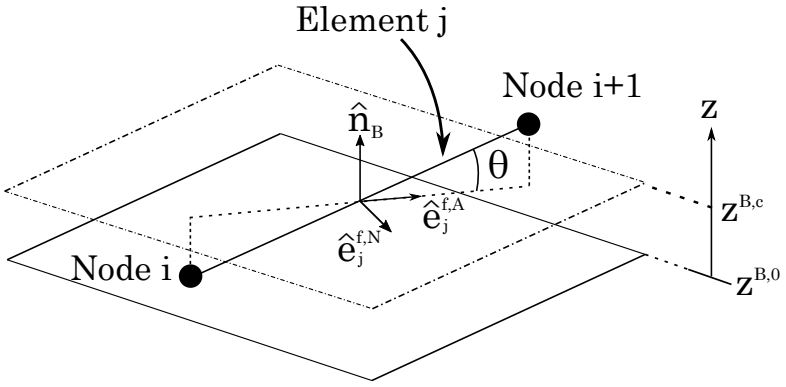

Figure 3.1: Seabed coordinate system definitions.

With this coordinate system, the total seabed force on node i is then given by,

$$\mathbf{F}_i^B = \mathbf{F}_i^{B,r} + \mathbf{F}_i^{B,f} + \mathbf{F}_i^{B,d} \tag{3.3}$$

where $\mathbf{F}_i^{B,r}$, $\mathbf{F}_i^{B,d}$ and $\mathbf{F}_i^{B,f}$ are respectively the seabed normal reaction and damping and lateral friction force components.

3.1.2 Spring mattress reaction force model

In the usual seabed spring mattress model as described by Webster [55] and Gobat and Grosenbaugh [106]. Figure 3.2 shows the schematic of the spring mattress model, in which the cylindrical object represents a slender structure such as a pipeline or the outer envelope diameter of a mooring line.

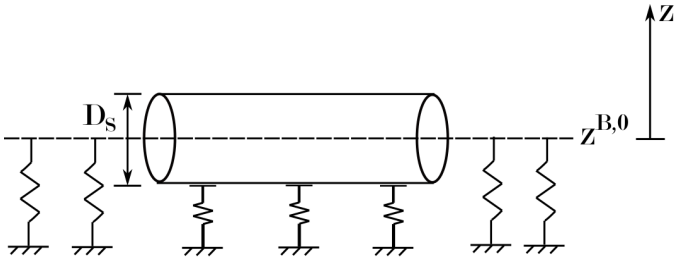

Figure 3.2: Schematic of the spring mattress model.

A seabed reaction force is directly applied on a node as a function of its own vertical elevation,

$$\mathbf{F}_i^{B,r} = k_i^B \left(z_i^{B,c} - z_i \right) \hat{\mathbf{n}}_B \tag{3.4}$$

where k_i^B is the spring constant, z_i is the nodal elevation and $z_i^{B,c}$ is the seabed force cutoff elevation, defined as

$$z_i^{B,c} = z^{B,0} + N^{B,c} D_{S,i} \tag{3.5}$$

where $z^{B,0}$ is the nominal seabed elevation, $N^{B,c}$ is the seabed thickness coefficient and $D_{S,i}$ is the line structural outer diameter at the s-coordinate of Node i.The nodal seabed stiffness coefficient k_i^B is given by

$$k_i^B = \frac{W_i}{N^{B,c} D_{S,i}} \tag{3.6}$$

where W_i is the nodal weight. Notice that when Equations 3.5 and 3.6 are inserted into Equation 3.4, the seabed reaction force reduces to the nodal weight, W_i. Thus the term $N^{B,c} D_{S,i}$ is the distance over which the seabed reaction force linearly increases from zero to the nodal weight.

3.1.3 Seabed friction force model

The friction force formulation is based on the Coulomb friction model. First, the lateral velocity of Node i is first calculated as,

$$\dot{\mathbf{r}}_{lat,i} = \dot{\mathbf{r}}_i - \dot{\mathbf{r}}_i \cdot \hat{\mathbf{n}}_B \tag{3.7}$$

Next, $\dot{\mathbf{r}}_{lat,i}$ is projected onto its adjacent elements as,

$$\dot{\mathbf{r}}_\xi^{f,\kappa} = \dot{\mathbf{r}}_{lat,i} \cdot \hat{\mathbf{e}}_\xi^{f,\kappa} \tag{3.8}$$

where $\xi \in j, j-1$. The unlimited friction force on Node i, $\tilde{\mathbf{F}}_i^{B,f,\kappa}$, is then calculated as,

$$\tilde{\mathbf{F}}_i^{B,f} = \sum_{\kappa=A,N} \sum_{\xi=j,j-1} -C^{B,f,\kappa} \dot{\mathbf{r}}_\xi^{f,\kappa} \tag{3.9}$$

where $C^{B,f,\kappa}$, $\kappa \in A, N$ are the seabed friction coefficients in the element axial, A, and normal, N, directions. The unit direction vector of the friction force, $\hat{\mathbf{e}}^f$, can be calculated as,

$$\hat{\mathbf{e}}^f = \frac{\tilde{\mathbf{F}}_\xi^{B,f,\kappa}}{\left|\tilde{\mathbf{F}}_\xi^{B,f,\kappa}\right|} \tag{3.10}$$

The nodal friction force magnitude is limited by the static friction limit, $\mu^{B,f} \left|\mathbf{F}_i^{B,r}\right|$,

$$\mathbf{F}_i^{B,f} = \begin{cases} \tilde{\mathbf{F}}_i^{B,f,\kappa}, & \left|\tilde{\mathbf{F}}_i^{B,f,\kappa}\right| < \mu^{B,f} \left|\mathbf{F}_i^{B,r}\right| \\ \mu^{B,f} \left|\mathbf{F}_i^{B,r}\right| \hat{\mathbf{e}}^f, & \left|\tilde{\mathbf{F}}_i^{B,f,\kappa}\right| \geq \mu^{B,f} \left|\mathbf{F}_i^{B,r}\right| \end{cases} \tag{3.11}$$

3.1.4 Seabed normal damping force

The seabed normal damping force on node i, $\mathbf{F}_i^{B,d}$, is given by

$$\mathbf{F}_i^{B,d} = \mathbf{F}_j^{B,d} + \mathbf{F}_{j-1}^{B,d} = \sum_{\xi=j,j-1} \mathbf{F}_\xi^{B,d} \tag{3.12}$$

with the contributions from elements j and $j-1$ as given by

$$\mathbf{F}_\xi^{B,d} = \begin{cases} -C_\xi^{B,d} \dot{z}_i \ \hat{\mathbf{n}}_B, & \dot{z}_i < 0, \ \ |\mathbf{F}_\xi^{B,r}| > 0 \\ 0, & \text{otherwise} \end{cases} \tag{3.13}$$

where $\dot{z}$ is the vertical velocity of node i. The damping force is active only when a node has downward velocity and is experiencing a reaction force from the seabed contributed by the elements attached to it. The damping force coefficient, $C_\xi^{B,d}$,

following the theory of vibrations [127], is given by $C_{\xi}^{B,d} = 2\zeta^{B,d}\sqrt{k_{\xi}^{B} m_{\xi}}$, where m_{ξ} are the masses per unit length of their respective elements, and $\zeta^{B,d}$ is the damping ratio [127].

3.2 Effects of nodal grounding

Having validated the fairlead tension response for a fully suspended line without considering seabed model effects in Section 2.3, in this section we examine the effects of nodal grounding on line tensions with different fairlead excitations and line spatial discretisations. As the line material specified is a studlink mooring chain, the axial length of a chain link is typically six times that of its diameter. For the line specified in Table A.1, the length of one of its chain links is therefore 0.84 m. However, for numerical simulations element sizes are typically much larger than the size of a discrete chain link. For a catenary mooring line, the grounding and liftoff of the individual chain links is the primary factor that determines the fairlead tension. When element sizes that are much larger than the physical chain links are used, a discretisation error is introduced.

3.2.1 Test parameters

Two single-harmonic fairlead motion profiles from Ref. [5], respectively surge motions in the wave frequency and slow-drift frequency ranges, are used as test cases. The water depth is 82.5 m. The fairlead excitation functions for position and velocity follow Equations (B.1) and (B.2) in which t refers to the time in the time series, $(.)^{WF}$ and $(.)^{LF}$ denote wave- and low-frequency components of the fairlead excitation, T_i, r_i and ϕ_i are the motion periods, amplitudes, and phase angles respectively, and the indices $i \in \{1, 2, 3\}$ here, respectively refer to the surge, sway, and heave directions as shown in Figure 3.3, which portrays the initial line geometry of the test cases. The values for the input parameters Cases 1 and 2 are shown in Table B.2. The initial line geometry is shown in Figure 3.3.

The seabed parameters used in Orcaflex are presented in the shallow water coefficient set shown in Table C.1. The spring mattress (SM) seabed model described in Section 3.1.2, using the SM seabed force coefficient set presented in Table C.2,

was used to define the seabed forces. The fourth-order Runge-Kutta scheme used for time-integration in the studies presented in the present chapter.

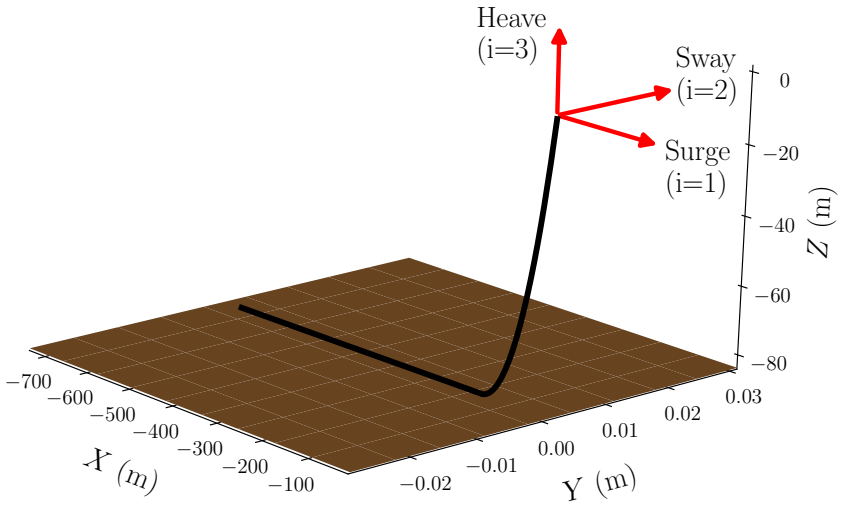

Figure 3.3: Initial line geometry of test cases.

3.2.2 Influence of element size

Eight uniform line discretisations with element sizes of 11.86 m, 9.48 m, 8.0 m, 7.11 m, 4.74 m, 2.85 m, 2.03 m and 0.84 m are used for each test case. The finest discretisation using an element size of 0.84 m, equivalent to the size of a chain link for the present model, most closely represents physical reality. For all the test cases used in this study a uniform timestep size of 0.00025 s was applied to satisfy the stability limits of the time integration scheme applied to the 0.84 m-element discretization.

3.2.2.1 Case 1: Pure surge motion at wave frequency

The following discussion focuses on a time window for one period of fairlead tension oscillation in Case 1 during which a segment of the line undergoes grounding and liftoff from the seabed. Figure 3.4 shows the location of the touchdown point, s_{TDP}, as a function of the s-coordinate (see Figure 2.1a) and indicates that the line is experiencing grounding in the time period from 82.25 s to 87.0 s and the length

of line in contact with the seabed increases from approximately 520 m to 560 m. Between 81.0 s to 82.25 s and 87.0 s to 91.0 s, the line is lifting off from the seabed. The instantaneous locations of the touchdown point tracked by all discretisations are in reasonably close agreement.

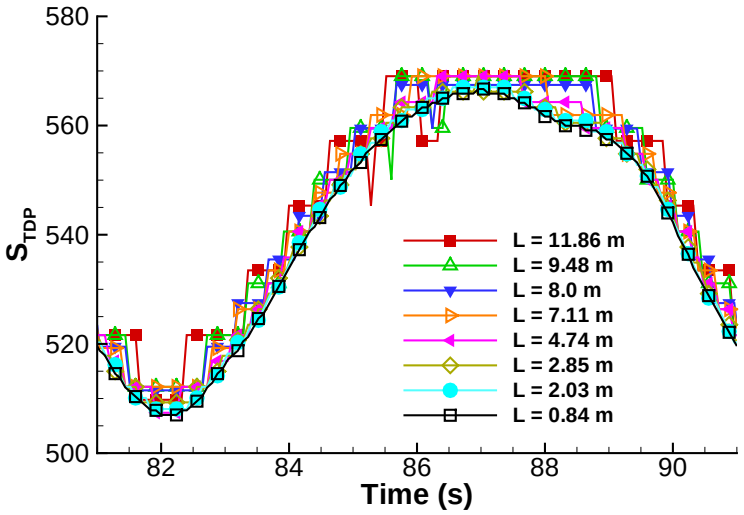

Figure 3.4: Time history of touchdown point location, s_{TDP}, for Case 1 from in-house code.

Figures 3.5 and 3.6 present the fairlead tension time histories for Case 1, from the in-house code and Orcaflex respectively, using the eight element lengths mentioned and show that the tension time series from both codes are smoothly varying and in good mutual agreement from 81.0 s up to approximately 83.5 s and from 87.0 s to 91.0 s. Between 83.5 s and 87.0 s, significant fluctuations develop, coinciding with the line grounding time period as shown in Figure 3.4.

Figures 3.8 and 3.7 present the frequency spectra plots for the fairlead tension time histories from the in-house code and Orcaflex respectively, and show that at lower frequencies of approximately 1 Hz and below, the magnitude of the frequency components in the tension time histories generated by both codes, for the varying element sizes, are in good mutual agreement. However, the frequency spectra begin to diverge at frequencies above 1 Hz. Figures 3.8 and 3.7 further illustrate that as the element size is reduced, the magnitudes of the higher frequency components are correspondingly reduced as well; the tension time histories for the 0.84 m-element discretization are smoothly varying.

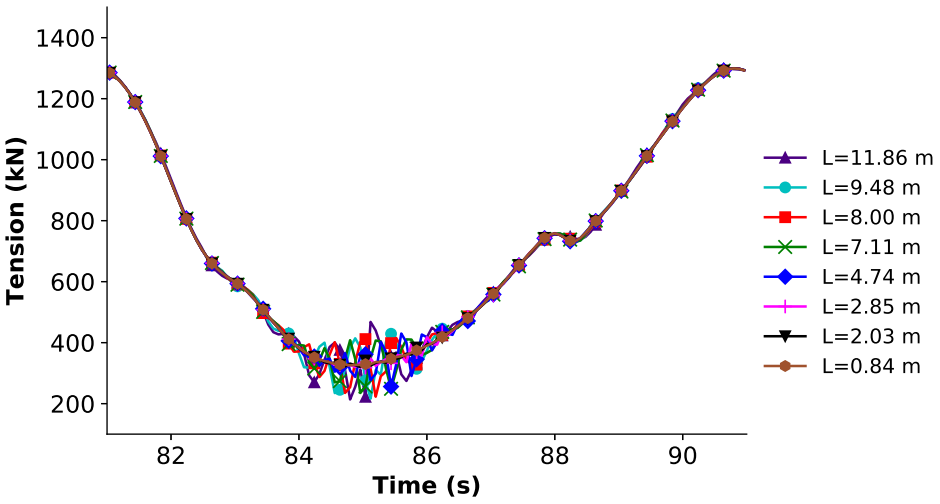

Figure 3.5: Fairlead tension time histories for Case 1 from current in-house code during nodal grounding.

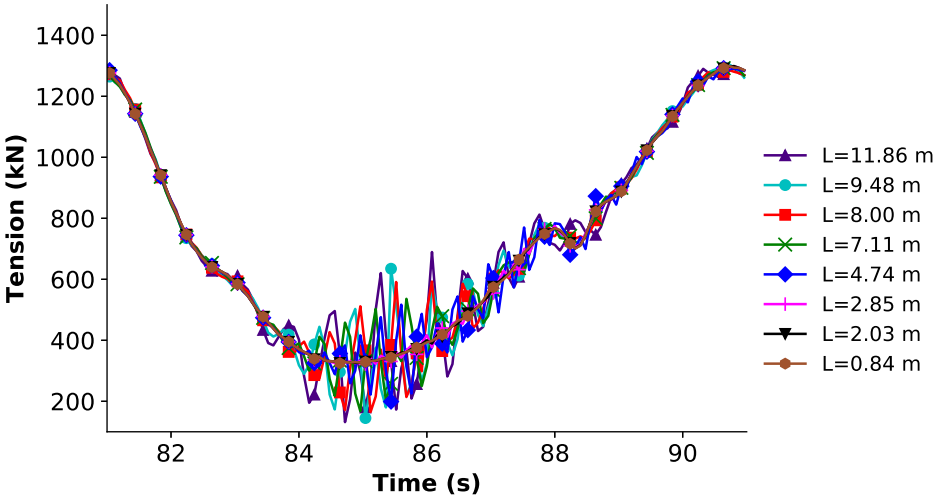

Figure 3.6: Fairlead tension time history for Case 1 from Orcaflex during nodal grounding.

Using the results for the 0.84 m-element size as a baseline and defining the deviation from this benchmark as the magnitude of the fluctuations, the maximum peak-to-peak tension fluctuation amplitude for each discretisation can be quantified and are plotted in Figure 3.9a, where it is illustrated again that the fluctuation amplitudes are reduced along with a reduction in the element size. The peak tensions from both Orcaflex and the in-house code with the various element sizes are presented in Figure 3.9a and show that as element size is reduced the peak tension converges towards to the benchmark values of the 0.84 m-element discretisation.

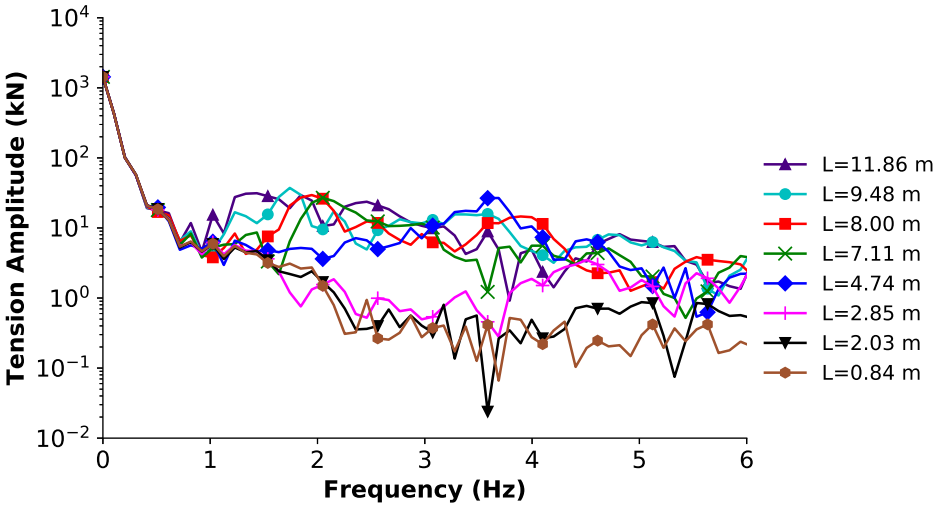

Figure 3.7: Fairlead tension frequency spectra for Case 1 from Orcaflex during nodal grounding.

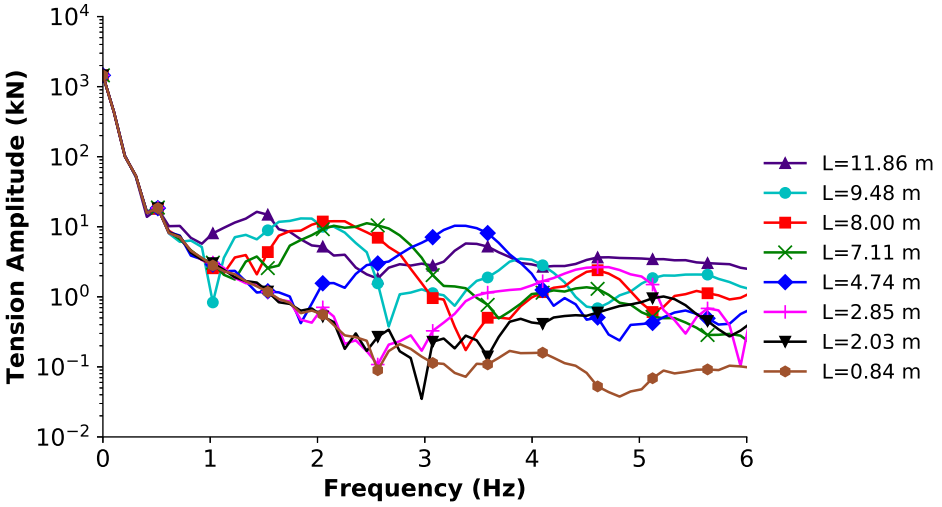

Figure 3.8: Fairlead tension frequency spectra for Case 1 from current in-house code during nodal grounding.

The deviation of the peak tension values given by the various discretisations, from their respective benchmark peak tension values of the 0.84 m-element discretisation, are generally small. In contrast, the amplitudes of the tension fluctuations, particularly for the coarser discretisations, are large in comparison to the smoothly varying tension benchmark results and degrade the quality of the solution.

To investigate the cause of the tension fluctuations, the discussion is now focused on the results for the 8.0 m and 0.84 m discretisations. The 0.84 m discretisation

is chosen because the tension oscillations in this discretisation are the most subdued among all the discretisations and thus provides the conditions of the desired outcome to compare against. The 8.0 m discretisation is chosen because the magnitude of the tension fluctuations, as shown in Figure 3.9b, are significant and thus facilitates ease of identification of the onset of the tension fluctuations while, as will be discussed, the nodal density is sufficiently high such that the case provides a mixture of nodal grounding occurrences that do and do not generate tension fluctuations.

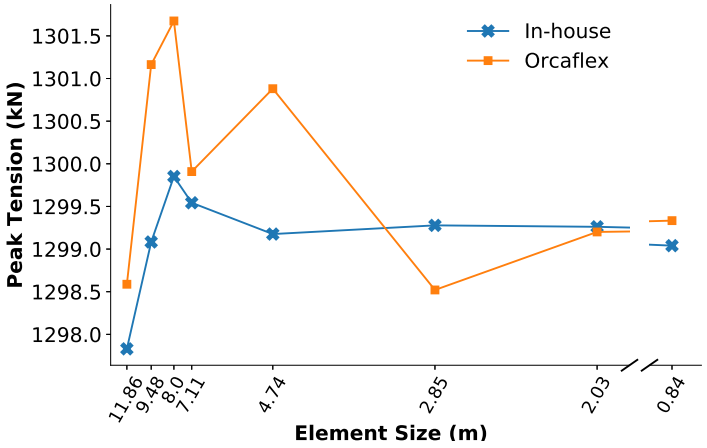

(a) Peak fairlead tension with varying discretisations.

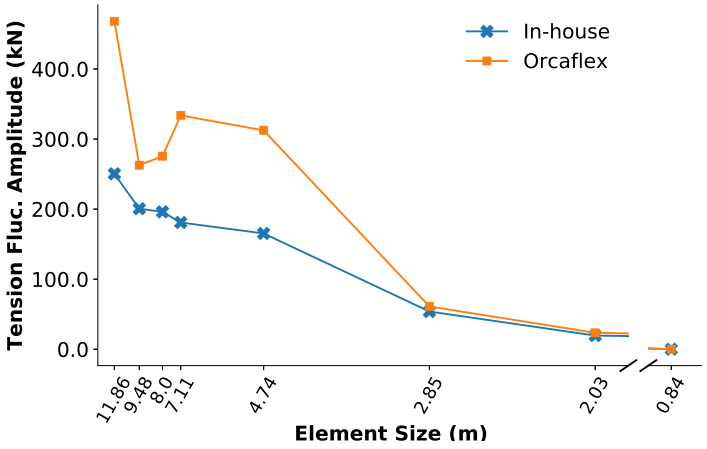

(b) Fairlead tension fluctuation amplitude with varying discretisations.

Figure 3.9: Peak fairlead tension and fairlead tension fluctuation amplitudes for Case 1 with uniform line element sizes ranging from 11.86 m to 0.84 m.

Figure 3.4 shows that line grounding starts at approximately 83.1 s. However, the tension fluctuations appear at approximately 84.0 s, coinciding with the grounding of Node 68. The grounding of Nodes 66 and 67, at 83.12 s and 83.64 s respectively, do not cause any tension fluctuations. The strain, ϵ, and strain spatial gradient,

$\mathrm{d}\epsilon/\mathrm{d}s$, within the associated time window are shown in Figures 3.10a and 3.10b respectively. It is noted the temporal and spatial gradients of strain are smoothly varying.

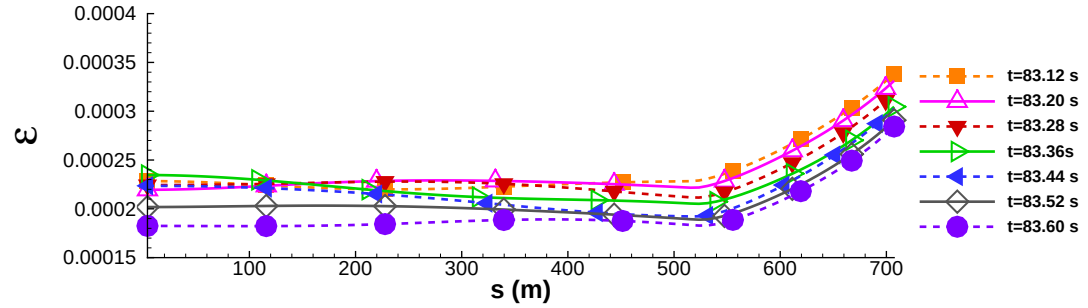

(a) Strain during grounding of Nodes 66 and 67 (Case 1) with 8.0 m-element line.

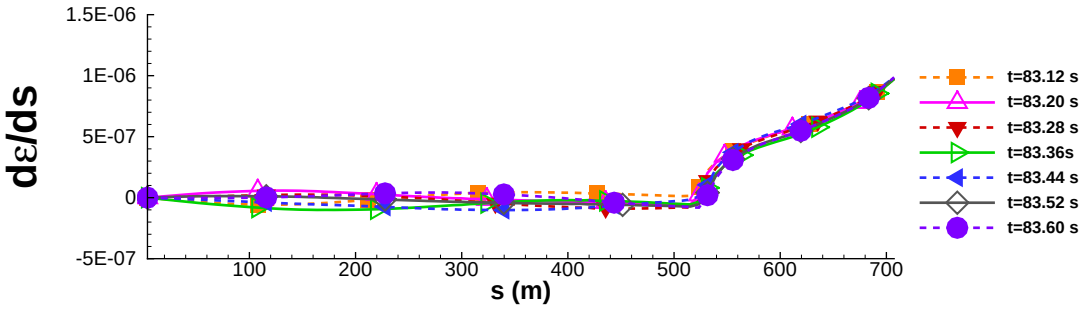

(b) Strain spatial gradient during grounding of Nodes 66 and 67 (Case 1) with 8.0 m-element line.

Figure 3.10: Strain and strain spatial gradient distribution with nodal grounding time window (83.12 s $\leq t \leq$ 83.60 s) for Case 1 with 8.0 m-element line.

In contrast, as Nodes 68, 69 and 70 are grounded between 84.08 s and 84.97 s, Figure 3.11a illustrates that within the time window 84.88 s $\leq t \leq$ 85.52 s the strain curves are highly irregular and large spatial gradients are observed in Figure 3.11b. Figure 3.11a also reveals the formation of localised low and negative strain zones in the strain curves of 84.20 s, 85.28 s, and 85.36 s at locations close to the touchdown point ($s \approx 500$ m). As shown in Equation (2.2), a mooring cable does not support compressive loading hence negative strain indicates a slack region where the line is slack. Equation (2.3) shows that element strain is determined from the distance between its two bounding nodes, hence, a low strain region is a compression zone where the separation distances between nodes are low. Conversely, a high strain region is a rarefaction zone where the nodes are spaced further apart.

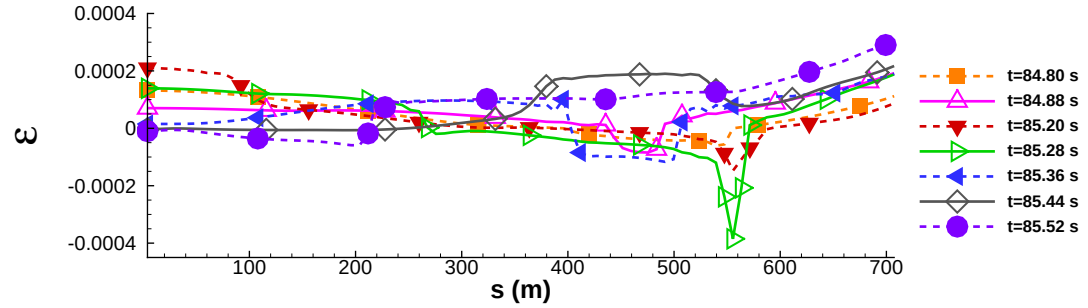

(a) Strain during grounding of Nodes 68, 69, 70 and 71 in Case 1 with 8.0 m-element line.

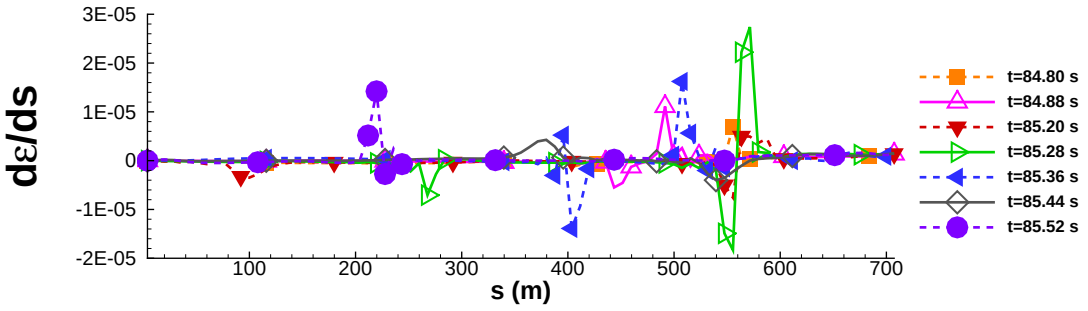

(b) Strain spatial gradient during grounding of Nodes 68, 69, 70 and 71 in Case 1 with 8.0 m-element line.

Figure 3.11: Strain, strain spatial gradient during nodal grounding time window (84.80 s $\leq t \leq$ 85.60 s) for Case 1 with 8.0 m-element line.

Figure 3.12 provides a closer look at the development and time evolution of the compression and rarefaction zones. Figure 3.12a presents the strain curves of the 8.0 m-element line after the grounding of Node 69 at 84.48 s, and illustrates the development of a slack region in the region of 400 m $\leq s \leq$ 550 m. The spatial extent of the slack zone is time-varying. At 84.96 s, the slack zone has become a high-strain, rarefaction region. Similarly, Figure 3.12b illustrates that after the grounding of Node 70 at 84.97 s, at 85.20 s a slack region spanning 390 m $\leq s \leq$ 590 m develops in the vicinity of the touchdown point ($s \approx 560$ m). At 85.28 s, the elements in the vicinity of the touchdown point have undergone further compression and the maximum negative strain has increased further. At 85.44 s, the slack span has become a high tension zone. The high tension zone then expands, as shown by an enlarged high strain region in the strain curve at 85.48 s relative to 85.44 s.

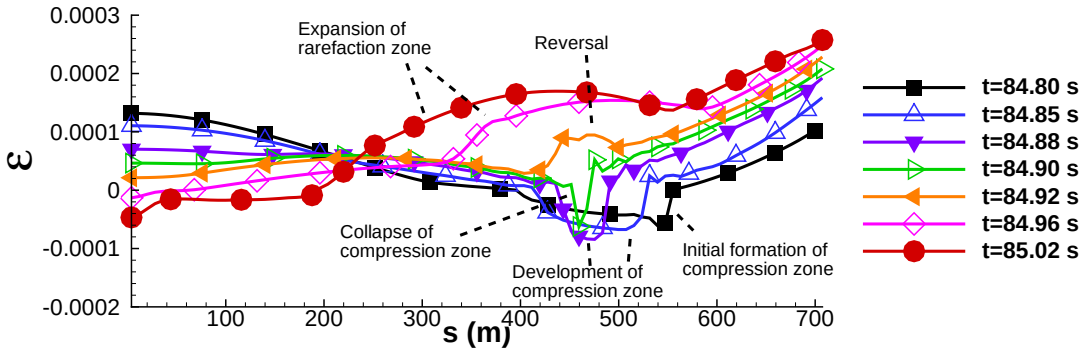

(a) Development and reversal of low strain zone after grounding of Node 69 with 8.0 m-element line.

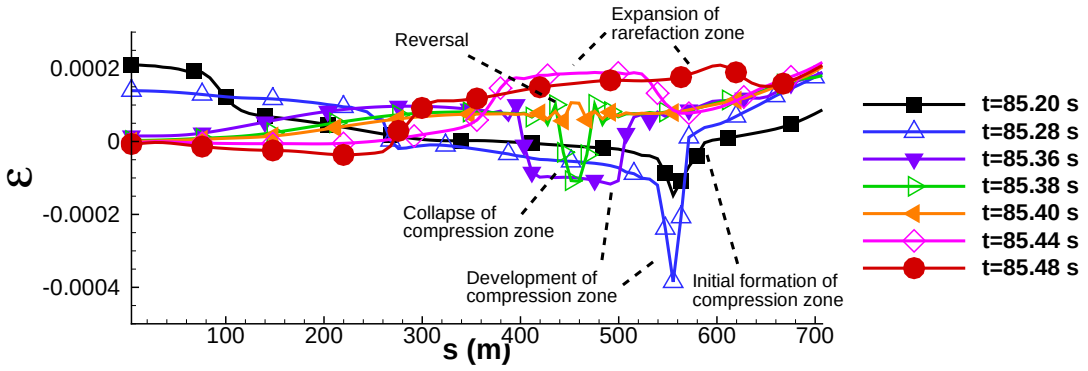

(b) Development and reversal of low strain zone after grounding of Node 70 with 8.0 m-element line.

Figure 3.12: Development and reversal of low strain zones post-nodal grounding (Case 1) with 8.0 m-element line.

The ϵ and $\mathrm{d}\epsilon/\mathrm{d}s$ curves for the 0.84 m-element line are shown in Figures 3.13a and 3.13b respectively. The time period shown in these plots span the period prior to ($t < 84.08$ s) and during ($84.08 \text{ s} \leq t \leq 85.60$ s) the development of the tension fluctuations presented in Figure 3.11. Figure 3.13b illustrates that the $\mathrm{d}\epsilon/\mathrm{d}s$ curves during the period of occurrence of tension fluctuations are smoothly varying with the exception of a kink that occurs consistently in the vicinity of the touchdown point.

During the grounding of Nodes 66 and 67, the $\mathrm{d}\epsilon/\mathrm{d}s$ curves presented in Figure 3.10b have similar profiles compared to the $\mathrm{d}\epsilon/\mathrm{d}s$ curves for 0.84 m-element line presented in Figure 3.13b. Both situations were free of tension fluctuations. In contrast, the $\mathrm{d}\epsilon/\mathrm{d}s$ curves during the grounding of Nodes 68 to 70 for the 8.0 m-element line, presented in Figure 3.11b, exhibit large gradients which are up to an

order of magnitude larger than in Figures 3.10b and Figure 3.13b at s-coordinates that vary widely in time.

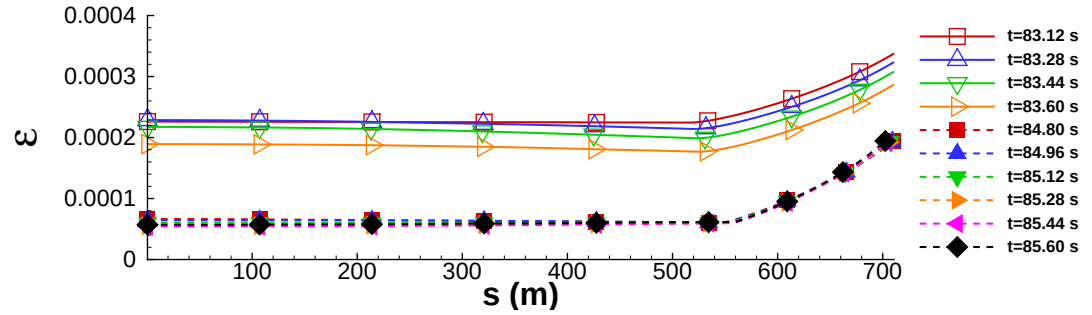

(a) Strain during nodal grounding time window (83.12 s $\leq t \leq$ 85.60 s) in Case 1 with 0.84 m-element line.

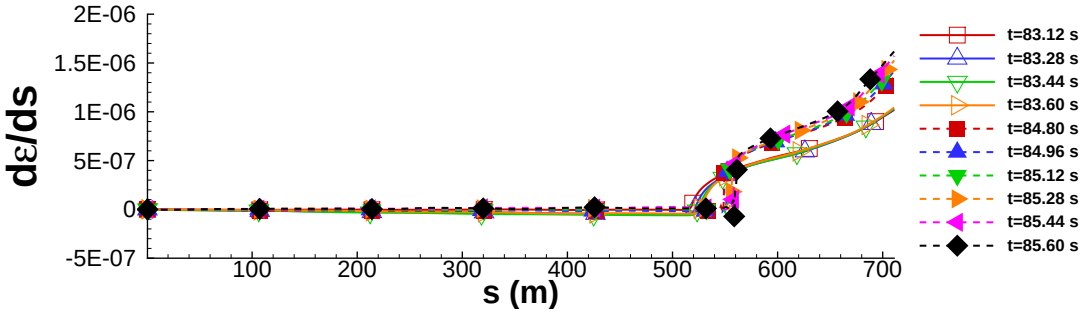

(b) Strain spatial gradient during nodal grounding time window (83.12 s $\leq t \leq$ 85.60 s) in Case 1 with 0.84 m-element line.

Figure 3.13: Strain, strainrate and strain spatial gradient distribution during nodal grounding time window (83.12 s $\leq t \leq$ 85.60 s) for Case 1 with 0.84 m-element line.

The ϵ and dϵ/ds curves for the 0.84 m-element line are shown in Figures 3.13a and 3.13b respectively. The time period shown in these plots span the period prior to ($t <$ 84.08 s) and during (84.08 s $\leq t \leq$ 85.60 s) the development of the tension fluctuations presented in Figure 3.11. Figure 3.13b illustrates that the dϵ/ds curves during the period of occurrence of tension fluctuations are smoothly varying with the exception of a kink that occurs consistently in the vicinity of the touchdown point.

During the grounding of Nodes 66 and 67, the dϵ/ds curves presented in Figure 3.10b have similar profiles compared to the dϵ/ds curves for 0.84 m-element line presented in Figure 3.13b. Both situations were free of tension fluctuations. In

contrast, the $d\epsilon/ds$ curves during the grounding of Nodes 68 to 70 for the 8.0 m-element line, presented in Figure 3.11b, exhibit large gradients which are up to an order of magnitude larger than in Figures 3.10b and Figure 3.13b at s-coordinates that vary widely in time.

The nodal vertical and horizontal velocities as well as the vertical coordinate for the 8.0 m and 0.84 m-element lines are shown in Figures 3.14 and 3.15 respectively. The times of grounding of each node are also shown to demarcate the pre and post-grounding time regions for each node. The selected grounding nodes shown in Figure 3.15 for the 0.84 m-element line were chosen at s-coordinates similar to the grounding nodes for the 8.0 m-element line, as shown in Table 3.1, in order to compare the grounding velocities at the same s-coordinates with different discretisations. The fairlead forcing of Case 1 is a single-harmonic surge motion in the X (surge) direction, and a negative v_X at the fairlead corresponds to the unloading phase of the motion.

Table 3.1: Grounding nodal indices and s-coordinates (Case 1.)

Node index	8.0 m	66	67	68	69	70	71
	0.84 m	619	629	639	648	658	667
TDP s-coord (m)	8.0 m	519.48	527.48	535.47	543.47	551.46	559.45
	0.84 m	519.60	528.00	536.41	543.98	552.39	559.95

As the fairlead velocity magnitude increased from 1.289 m/s to 3.088 m/s, the vertical velocities of the grounding nodes in the 8.0 m-element and 0.84 m-element discretisations respectively increased from 1.127 m/s to 3.348 m/s and 1.085 m/s to 3.227 m/s. Comparing the grounding velocities shown in Figures 3.14b and 3.15b with the corresponding fairlead velocities shown in Figures 3.14a and 3.15a respectively, it is observed that the magnitudes of the nodal vertical grounding velocities are positively correlated with the fairlead velocity.

Comparing Figure 3.14b with 3.15b, Figure 3.14c with 3.15c, and Figure 3.14d and 3.15d, it is noted that the post-grounding velocity and positional fluctuations for the 8.0 m-element line are more pronounced than that of the 0.84 m-element line. Figures 3.14b, 3.14c, 3.15b, and 3.15c illustrate that the post-grounding nodal velocities in Case 1 eventually settle at magnitudes close to zero. Comparing Figures 3.14b with 3.15b, and 3.14c with 3.15c, and 3.14a with 3.15a, it is observed that

the post-grounding velocities and vertical positions of the 8.0 m-element disretisation are underdamped and experience several periods of oscillations, while the post-grounding velocities and vertical positions are critically damped.

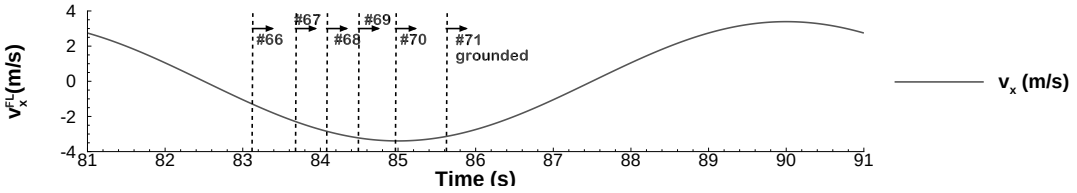

(a) Fairlead horizontal velocity v_X in Case 1 for 8.0 m-element line.

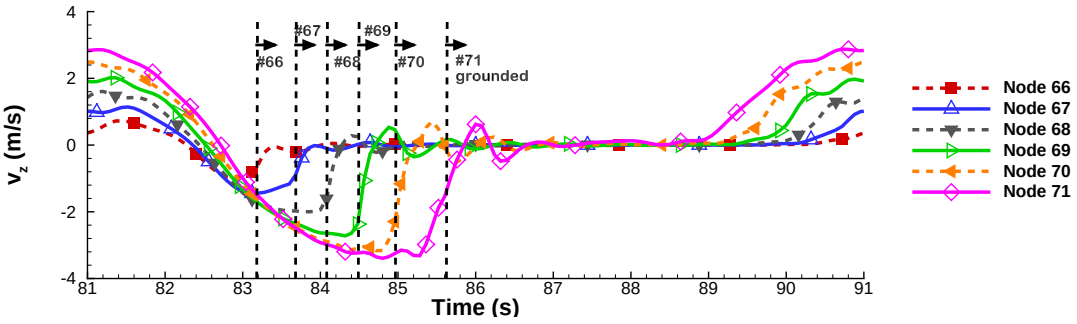

(b) Nodal vertical velocities, v_Z, in Case 1 for 8.0 m-element line.

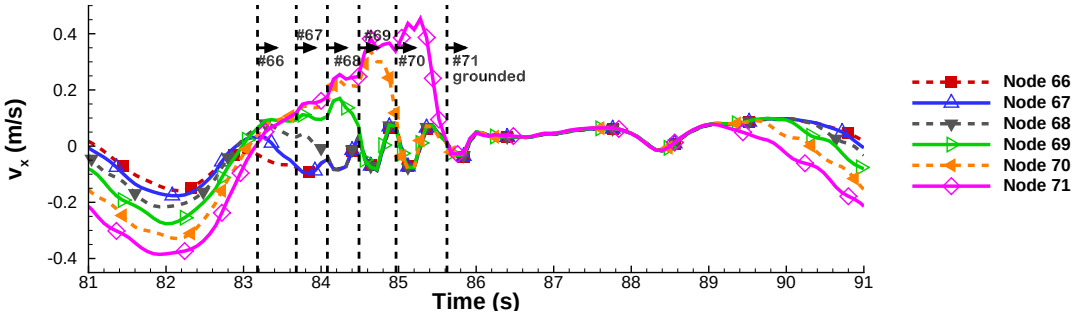

(c) Nodal horizontal velocities, v_X, in Case 1 for 8.0 m-element line.

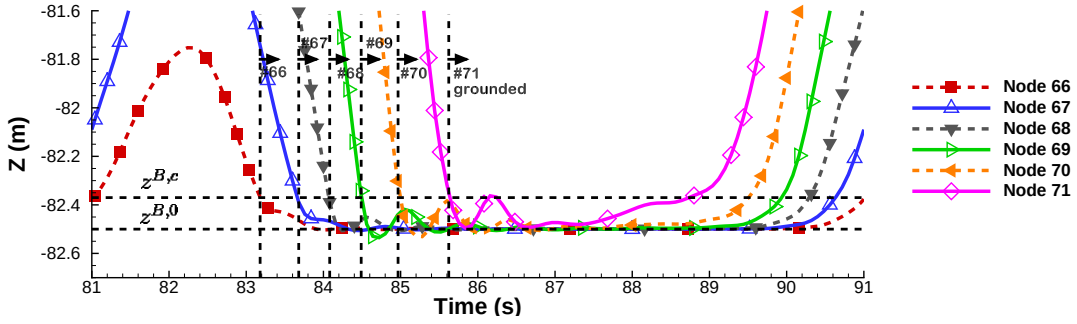

(d) Nodal vertical coordinate, Z, in Case 1 for 8.0 m-element line.

Figure 3.14: Nodal vertical coordinate and velocities in Z and X directions of grounding nodes in Case 1 with element length of 8.0 m.

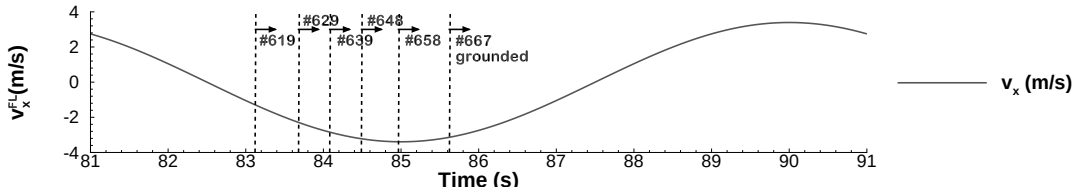

(a) Fairlead and horizontal velocity v_x in Case 1 for 0.84 m-element line.

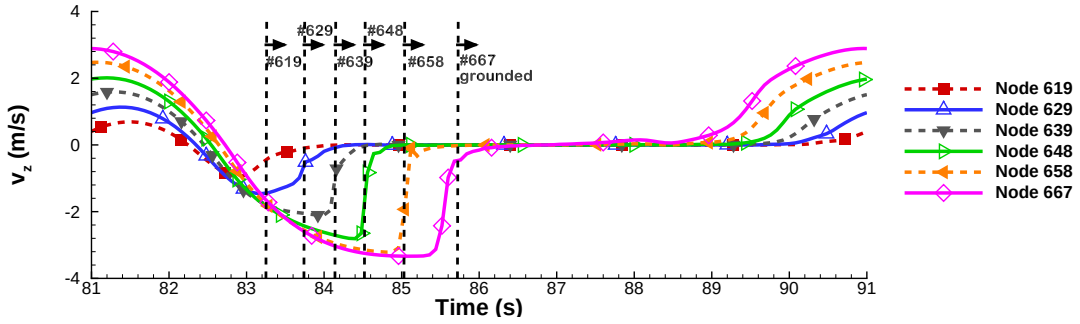

(b) Nodal vertical velocities, v_z, in Case 1 for 0.84 m-element line.

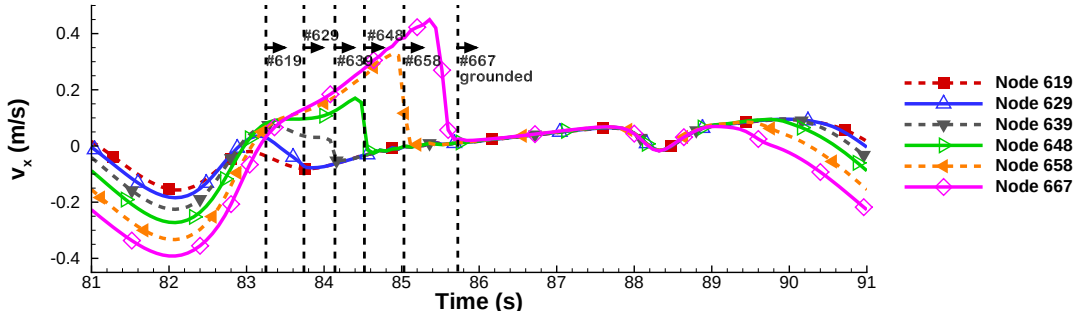

(c) Nodal horizontal velocities, v_x, in Case 1 for 0.84 m-element line.

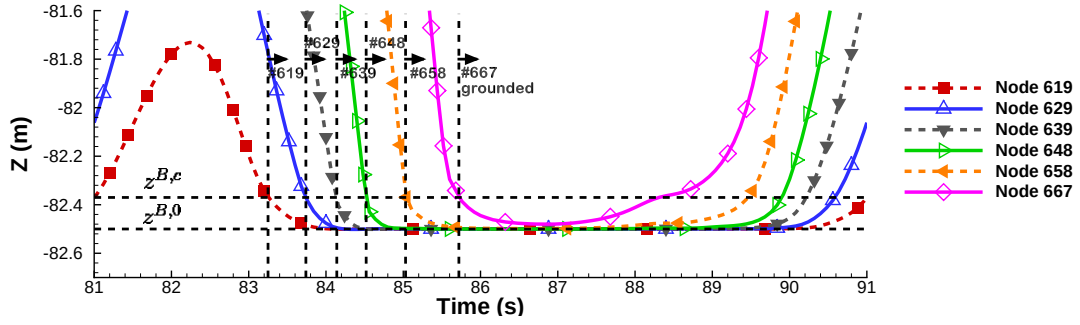

(d) Nodal vertical coordinates, Z, in Case 1 for 0.84 m-element line.

Figure 3.15: Nodal vertical coordinate and velocities in Z and X directions of grounding nodes in Case 1 with element length of 0.84 m.

An interesting observation of the oscillatory behavior of the horizontal nodal velocities v_X in the vicinity of the touchdown zone is observed in Figure 3.14c. After a node in the 8.0 m-element discretization is grounded, for a short period of time the slope of the horizontal velocity curves ($\mathrm{d}v_X/\mathrm{d}t$), or equivalently the horizontal acceleration, for that node and the nearby nodes on the side of the line that is grounded is negative, while that of the nodes that are suspended are positive.

For example, when Node 67 is grounded at 83.68 s, the slopes of the v_X curves for itself and Node 66, which is on the grounded side of the line, are negative, while slopes of the v_X curves for Nodes 68 to 71 on the suspended side of the line are positive. When Node 68 grounded at 84.08 s, the slopes of the v_X curves for the grounded Nodes 66 and 68 are negative, while the slopes of the v_X curves for the suspended Nodes 69 to 71 are positive. Similarly, when Node 69 grounded at 84.48 s, the slopes of the v_X curves for the grounded Nodes 66 to 69 are negative, while the slopes of the v_X curves for the suspended Nodes 70 and 71 are positive. Finally, when Node 70 grounded at 84.97 s, the slopes of the v_X curves for grounded Nodes 66 to 70 are negative, while the slope of the v_X curve for the suspended Node 71 is positive. This behavior suggests that after a node is grounded, the nodes on the grounded side of the line as well as the recently grounded node itself, accelerate towards the anchor node while the nodes on the suspended side accelerate towards the fairlead node. However, as the horizontal velocities are oscillating, the accelerations of the grounded nodes are soon reversed until the grounding of the next node.

3.2.2.2 Case 2: Pure surge motion at slow-drift frequency

Figure 3.16a presents the peak tensions for Case 2 with the range of element sizes and shows that the variation in the peak tension associated with varying element size is small compared to the peak tension value. Figure 3.16b presents the peak-to-peak tension fluctuation amplitude for each discretisation and reveals that the tension fluctuations, in the range between 3 kN to 41.5 kN, are an order of magnitude smaller than in Case 1 as presented in Figure 3.9b.

The grounding time window for Case 2 is 650 s $\leq t \leq$ 740 s, as shown in Figure 3.17, during which the length of line in contact with the seabed increases from approximately 250 m to 600 m. The number of nodes on the seabed resting on

the seabed from 32 to 77 for the 8.0 m-element line, and 291 to 720 for the 0.84 m-element line.

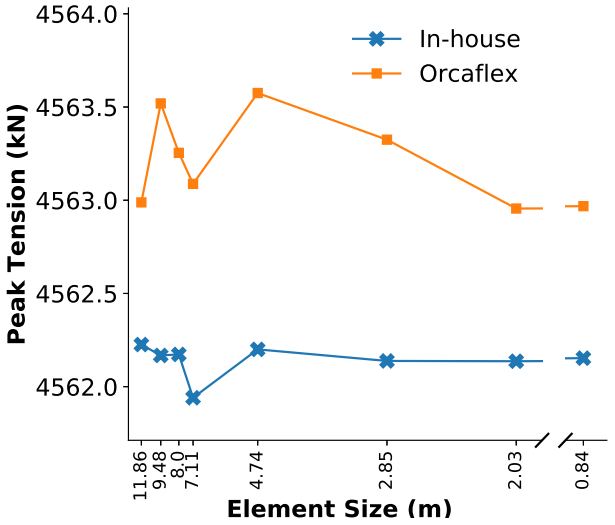

(a) Peak fairlead tension with varying discretisations.

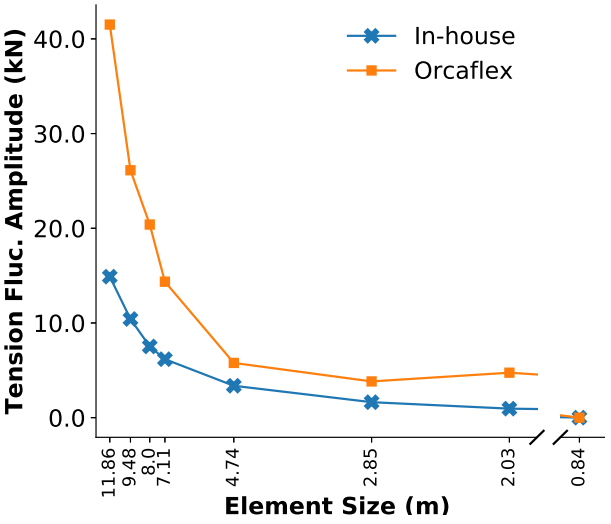

(b) Fairlead tension fluctuation amplitude with varying discretisations.

Figure 3.16: Peak fairlead tension and fairlead tension fluctuation amplitudes for Case 2 with uniform line element sizes ranging from 11.86 m to 0.84 m.

Figures 3.18 and 3.20 respectively present the fairlead tension histories and frequency spectra for Case 2 from the current in-house code, while Figures 3.19 and 3.21 show the fairlead tension history and frequency spectra for Case 2 from Orcaflex. Figures 3.20 and 3.21 confirm that the frequency contents of the tension time histories are dominated by the lower frequencies below approximately 0.1 Hz, which are in good agreement.

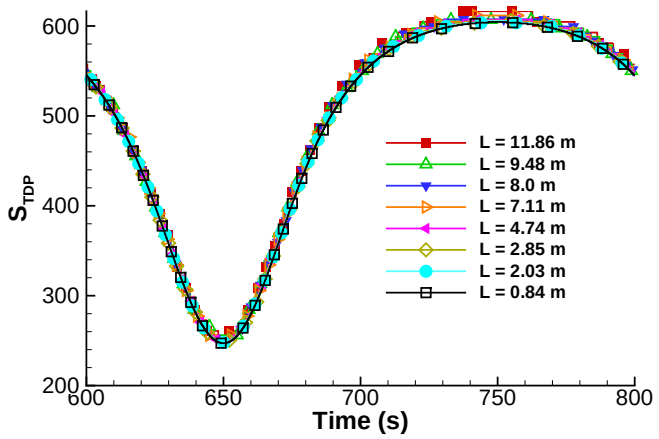

Figure 3.17: Time history of touchdown point location for Case 2 from in-house code.

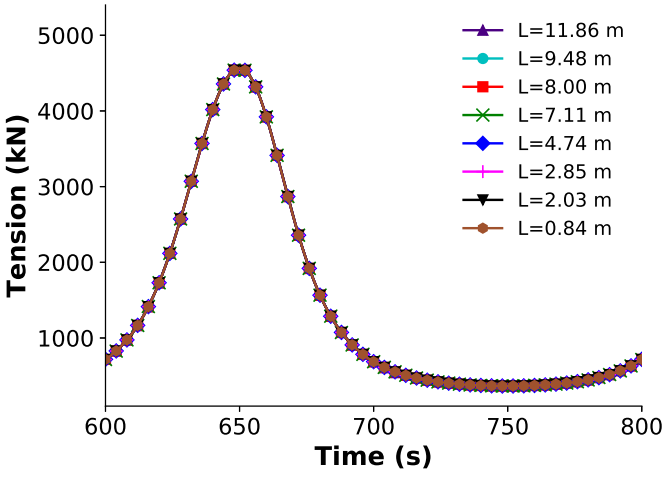

Figure 3.18: Fairlead tension time history for Case 2 from current in-house code during nodal grounding.

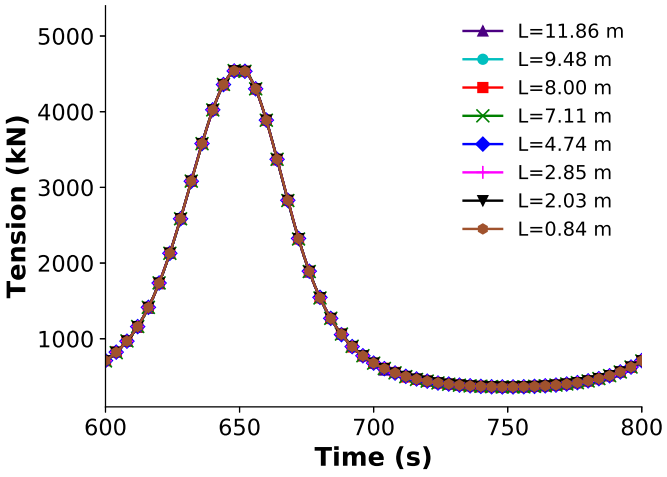

Figure 3.19: Fairlead tension time history for Case 2 from Orcaflex during nodal grounding.

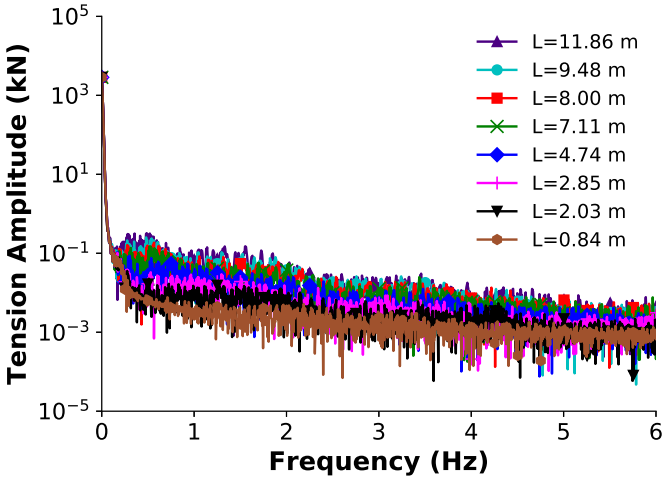

Figure 3.20: Fairlead tension frequency spectra for Case 2 from current in-house code during nodal grounding.

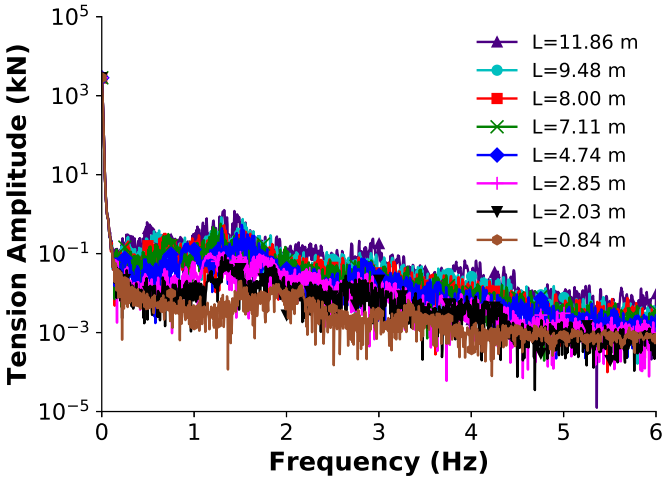

Figure 3.21: Fairlead tension frequency spectra for Case 2 from Orcaflex during nodal grounding.

Table 3.2 shows the s-coordinates of the selected nodes whose velocities and vertical coordinates within the grounding time window are illustrated in Figure 3.22 and shows that the maximum vertical grounding velocity magnitudes in Case 2 are 1.12 m/s and 1.11 m/s for the 0.84 m-element and 8.0 m-element discretisation respectively, which are lower than the grounding velocities in Case 1. The maximum fairlead velocity magnitude in Case 2 is 0.628 m/s compared to 3.392 m/s in Case 1.

Table 3.2: Grounding nodal indices and s-coordinates (Case 2.)

Node index	8.0 m 0.84 m	39 358	45 417	51 477	57 536	64 596	70 655
TDP s-coord (m)	8.0 m	303.70	351.65	399.61	447.56	503.50	551.46
	0.84 m	300.15	349.76	400.21	449.81	500.26	549.87

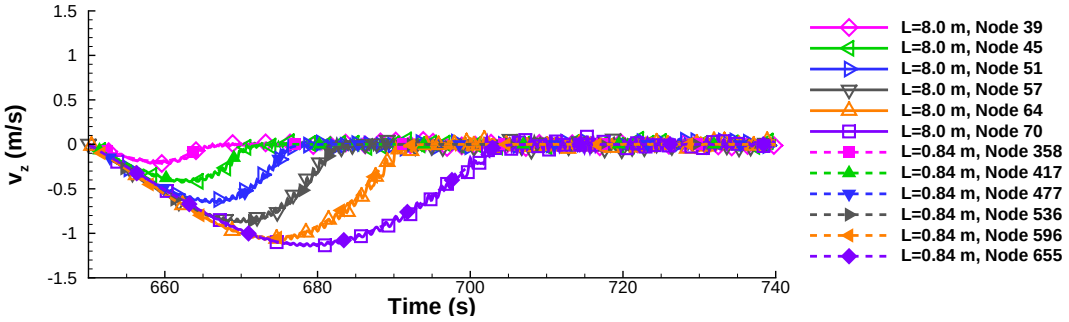

(a) Nodal vertical velocities, v_Z for 8.0 m-element and 0.84 m-element line.

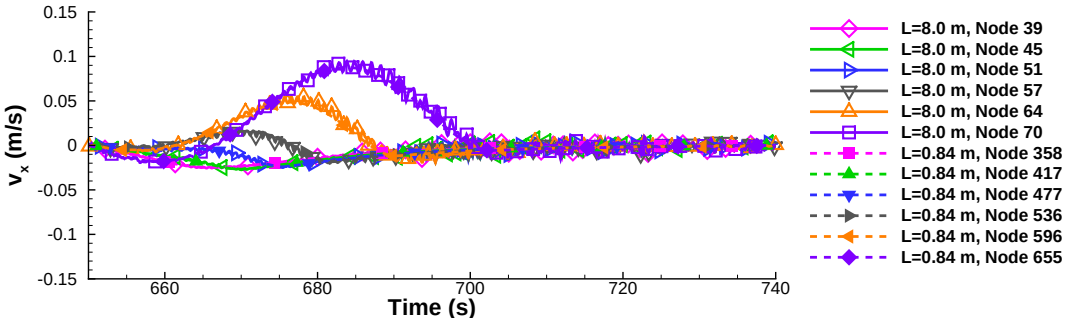

(b) Nodal horizontal velocities, v_X for 8.0 m-element and 0.84 m-element line.

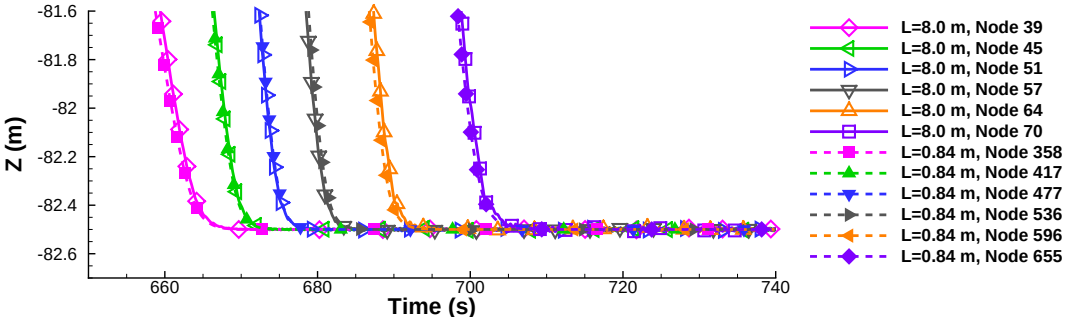

(c) Nodal vertical coordinate, Z for 8.0 m-element and 0.84 m-element line.

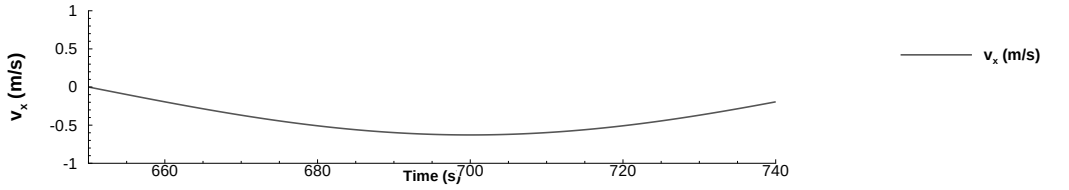

(d) Fairlead and horizontal velocity v_X.

Figure 3.22: Nodal vertical coordinate and velocities in Z and X directions of grounding nodes in Case 2 with element lengths of 8.0 m and 0.84 m.

Figures 3.23a and 3.23b respectively present the ϵ and $\mathrm{d}\epsilon/\mathrm{d}s$ curves of the 8.0 m-element and 0.84 m-element lines within the period of nodal grounding (660.0 s $\leq$ t $\leq$ 720.0 s) for Case 2, and confirm that the strain distributions for the two discretisations are in good agreement at all the presented time-steps, and that there are no large strain spatial gradients.

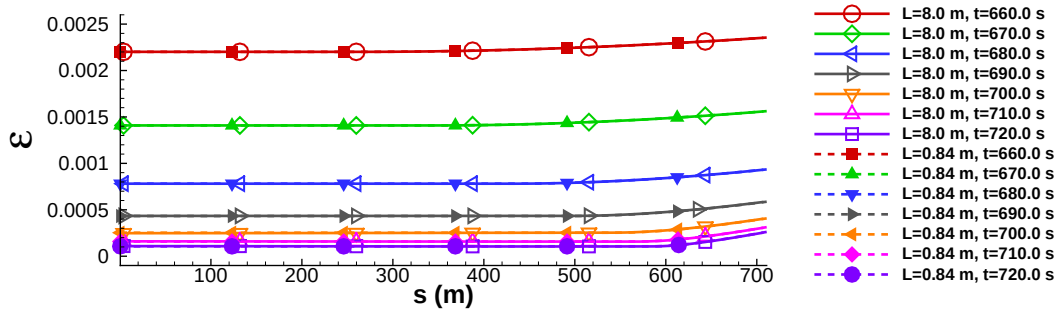

(a) Strain for 8.0 m-element and 0.84 m-element lines with time window 660.0 s $\leq$ t $\leq$ 720.0 s.

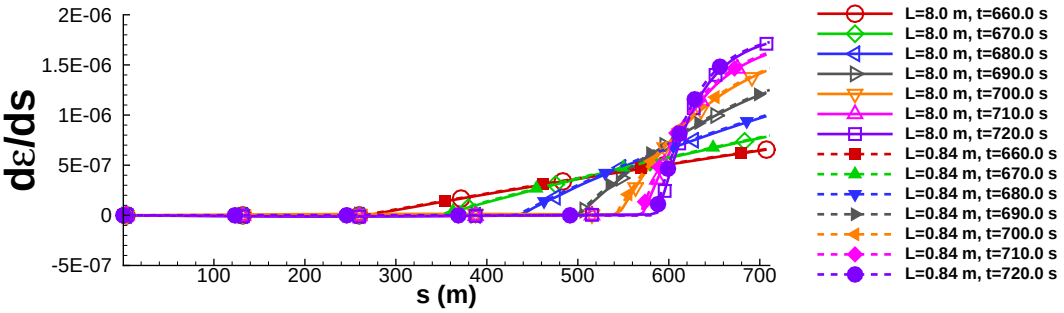

(b) Strain spatial gradient for 8.0 m-element and 0.84 m-element lines with time window 660.0 s $\leq$ t $\leq$ 720.0 s.

Figure 3.23: Strain, strain rate and strain gradient distribution for 8.0 m-element and 0.84 m-element lines for Case 2 between 660.0 s and 720.0 s.

3.2.3 Effects of varying seabed force coefficients

The choice of seabed force coefficients is arbitrary and selected to reduce the nodal penetration depth on the seabed, and post-grounding positional fluctuations [65, 88]. This section examines the effects of varying the coefficients of the spring-mattress model on line tension in Case 1. This section examines the effects of applying different seabed force coefficients sets presented in Table C.2 with the 4.74 m-element discretisation. The attention is focused on the coefficients for the

vertical reaction and damping forces in the spring-mattress model, respectively $N^{B,c}$ (see Equation (3.6)) and vertical damping $\zeta^{B,d}$ (see Section 3.1.4).

The 4.74 m-element discretisation is chosen because no significant change in the peak tension result is achieved with further refinement of the nodal density; the difference in the peak tension result between the 4.74 m and 2.85 m-element discretisations is 0.0015% and thus the solution for peak tension is considered to be converged. The applied time step, 0.00025 s, is significantly smaller than the maximum stable time step of 0.00328 s, and is sufficient for time step convergence for Case 1.

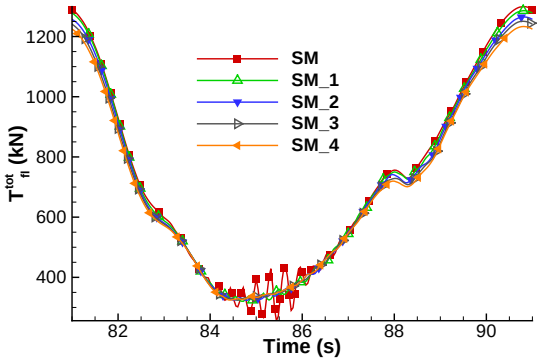

(a) Fairlead tensions with SM, SM_1, SM_2, SM_3, and SM_4 coefficients sets.

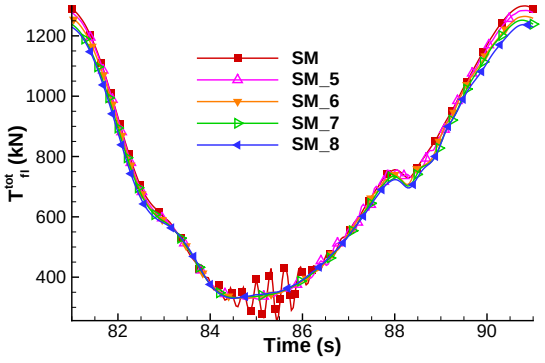

(b) Fairlead tensions with SM, SM_5, SM_6, SM_7, and SM_8 coefficients sets.

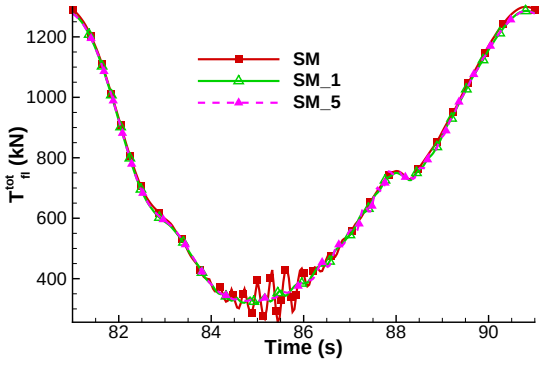

(c) Fairlead tensions with SM, SM_1, and SM_5 coefficients sets.

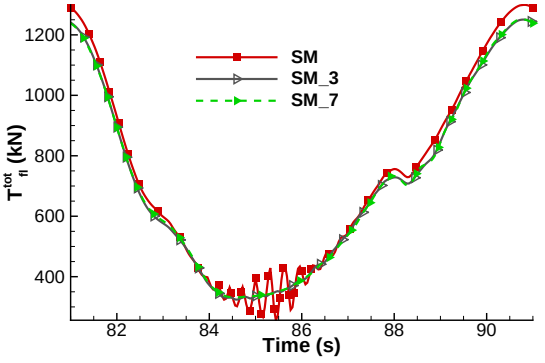

(d) Fairlead tensions with SM, SM_3, SM_7 coefficients sets.

Figure 3.24: Fairlead tensions for Case 1 with spring-mattress seabed model and SM, SM_1, SM_2, SM_3, SM_4, SM_5, SM_6, SM_7 and SM_8 coefficient sets.

Figure 3.24a shows the fairlead tension time history for Case 1 with the SM coefficient set, which produced the tension fluctuations discussed in Section 3.2.2.1, compared with the tension time histories using a $\zeta^{B,d}$ value of 1.0 and $N^{B,c}$ values of 5 (SM_1), 10 (SM_2), 15 (SM_3), and 20 (SM_4). The effect of increasing $N^{B,c}$ is

that the seabed vertical spring stiffness, k^B, is reduced and the seabed reaction force cutoff elevation, $z^{B,c}$ (see Figure 3.1), is increased. It is evident from Figures 3.24a that the tension fluctuations are progressively reduced as $N^{B,c}$ is increased. However, the peak tensions for the SM_1, SM_2, SM_3, and SM_4 coefficient sets, at 1285.18 kN, 1264.57 kN, 1250.44 kN, and 1232.86 kN respectively, are lower than the 1298.69 kN peak tension for the SM coefficient set.

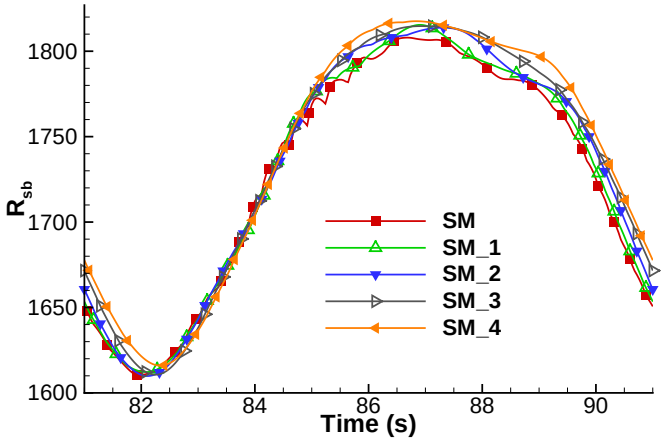

(a) Seabed reaction force with SM, SM_1, SM_2, SM_3, and SM_4 coefficients sets.

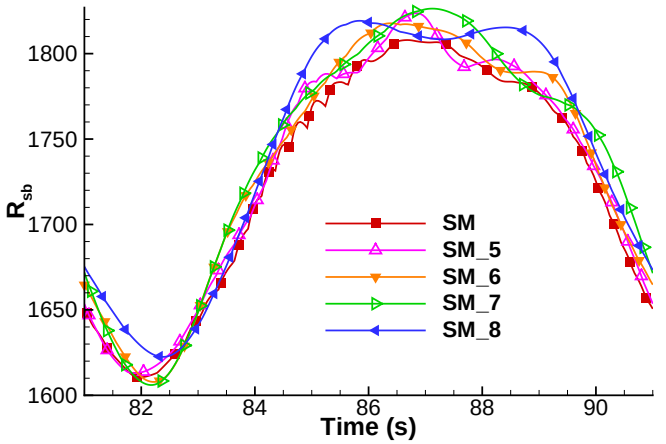

(b) Seabed reaction force with SM, SM_5, SM_6, SM_7, and SM_8 coefficients sets.

Figure 3.25: Seabed reaction force for Case 1 with spring-mattress seabed model and SM, SM_1, SM_2, SM_3, SM_4, SM_5, SM_6, SM_7 and SM_8 coefficient sets.

Figure 3.24b shows the fairlead tension time history using the SM coefficient set compared with the fairlead tension time histories using a $\zeta^{B,d}$ value of 0 and the same $N^{B,c}$ values of 5, 10, 15 and 20, corresponding to the SM_5, SM_6, SM_7, and SM_8 coefficient sets respectively, and illustrates that the tension fluctuations are progressively reduced as $N^{B,c}$ is increased. The peak tensions are 1283.81 kN, 1264.29 kN, 1251.66 kN and 1237.44 kN respectively for the SM_5, SM_6, SM_7, and

SM_8 coefficient sets. Figure 3.24c presents the fairlead tension results that with a $N^{B,c}$ value of 5, and shows that the magnitude of the tension fluctuations are reduced as the value of $\zeta^{B,d}$ was changed from 1.0 to 0.0, however, the peak tension was also lowered slightly by 1.1%. Figure 3.24d illustrates that with a value of 15 for $N^{B,c}$, the tension fluctuations are further reduced slightly as the value of $\zeta^{B,d}$ was changed from 1.0 to 0.0, while the peak tension experienced a small increase of 0.1%.

The cause for the reduction in fairlead tension is the increased seabed reaction force on the line as a result of increasing $N^{B,c}$. Figures 3.25a and 3.25b respectively present, for $\zeta^{B,d}$ values of 1.0 and 0.0, the total seabed reaction force on the grounded line section for $N^{B,c}$ values of 5, 10, 15 and 20, as well as the seabed reaction force for the SM coefficient set, and illustrate that the seabed reaction force on the line, which reduces the suspended line weight, generally increases together with $N^{B,c}$ over a period of oscillation.

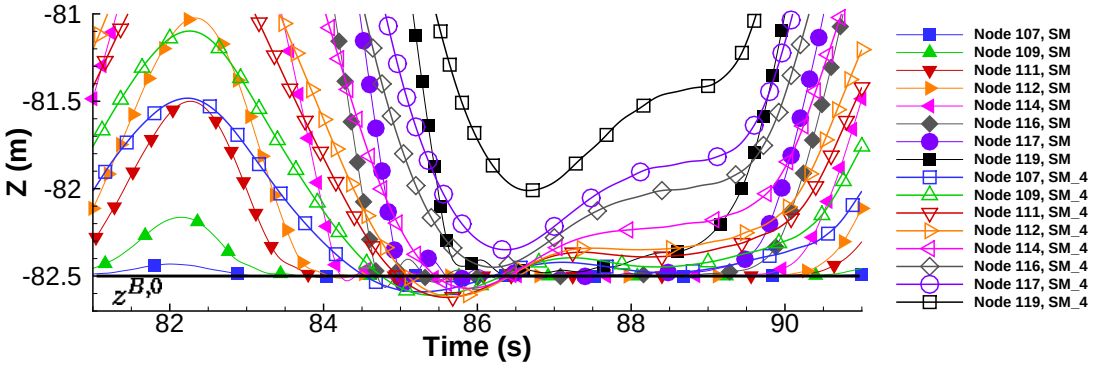

(a) Nodal vertical positions, Z, with SM and SM_4 coefficients sets for Case 1.

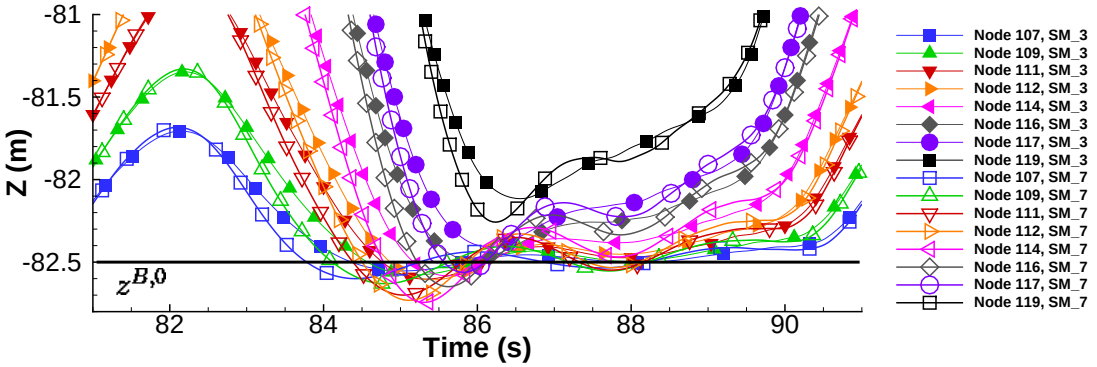

(b) Nodal vertical positions, Z, with SM_3 and SM_7 coefficients sets for Case 1.

Figure 3.26: Nodal vertical positions, Z, with SM, SM_3, SM_4 and SM_7 coefficients sets for Case 1.

Figure 3.26b also illustrates that for different values of $\zeta^{B,d}$, the vertical nodal coordinates begin to deviate at elevations closer to the seabed due to the increasing downward velocities of the grounding nodes as they approach the seabed (see Figure 3.14b) and leads to a larger disparity in the vertical damping force arising from differing values of $\zeta^{B,d}$.

Figure 3.26a shows the Z-coordinate of the grounding nodes when the SM and SM_4 coefficients are used, and it is evident that the penetration depths of the grounding nodes below $z^{B,0}$ increased with a larger $N^{B,c}$ value and, correspondingly, a lower seabed spring stiffness. Figure 3.26b presents the Z-coordinate of the grounding nodes when the SM_3 and SM_7 coefficients are used, which respectively apply the values of 1.0 and 0.0 for $\zeta^{B,d}$ and the same value of 15 for $N^{B,c}$, and illustrates that the nodal penetration depth increases with a reduction in the value of $\zeta^{B,d}$.

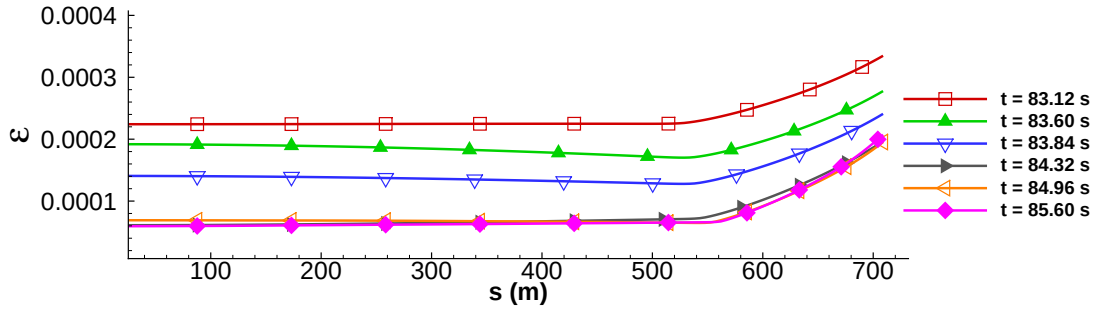

(a) Strain with 4.74 m-element line, SM_7 coefficient set.

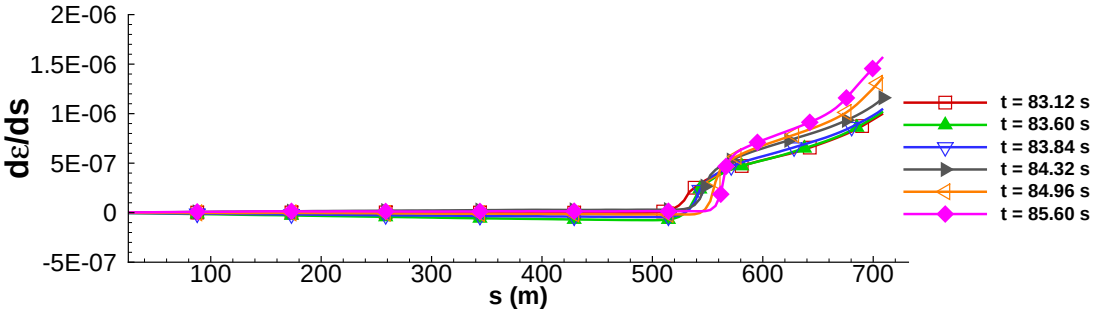

(b) Strain spatial gradient with 4.74 m-element line, SM_7 coefficient set.

Figure 3.27: Strain and spatial gradient of strain with 4.74 m-element line, SM_7 coefficient set and time window (83.12 s $\leq t \leq$ 85.60 s) for Case 1.

Figures 3.27a and 3.27b respectively present the strain and strain spatial gradient distributions with the 4.74 m-element discretisation and the SM_7 coefficient set during the nodal grounding time window, 83.12 s $\leq t \leq$ 85.60 s, and illustrates that the both the strain and strain gradient curves are free of the large spatial gradients that are observed in Figures 3.11a and 3.11b. In relation to the fairlead tension time

histories, the smoothly varying strain curves and strain gradient curves, presented in Figures 3.27a and 3.27b respectively, correspond to the SM_7 fairlead tension time history presented in Figure 3.24d, while the undulating strain and strain gradient curves in Figures 3.11a and 3.27b respectively correspond to the irregular fairlead tension time series for the 8.0 m-element line shown in Figure 3.8.

The key findings from this series of test cases are, firstly, the seabed spring stiffness has a significant effect on the fairlead peak tension and increasing it, while beneficial from the standpoint of reducing tension fluctuations, leads to the underestimation of the peak tension results. Secondly, the effect of the vertical damping coefficient is mainly on the tension fluctuations and its effect on peak tension is small, and that a lower damping coefficient has the effect of reducing the fluctuations.

3.2.4 Effect of grounding element orientation

Figure 3.1 shows an element that is in the grounding state, with the vertical angle between the element axis and the seabed defined as θ, the grounding angle of an element. For a catenary line, the θ of an element closer to the anchor is usually lower than for an element closer to the fairlead. Hence, to investigate the effect of θ on the production of the tension fluctuations, the 4.74 m-element line in a water depth of 82.5 m is specified together with three pretension values, respectively 706.9 kN, 1248.4 kN, and 3136.5 kN; henceforth referred to as the low, mid-range and high pretension cases. The pretension value changes the s_{TDP} range, as shown in Figure 3.28. The fairlead excitation amplitude and frequency of 5.4 m and 10 s (Case 1) is uniformly applied for all three lines.

Figure 3.29 presents the location of the touchdown point s_{TDP} for the lines with three pretension values in the time period for three oscillation cycles from 61 s to 91 s. As pretension is increased, s_{TDP} is shifted towards the anchor as a longer segment of the line is suspended. For the low, mid-range and high pretension value cases, the s_{TDP} range for the same fairlead excitation specified here are 161.23 m to 396.53 m, 346.16 m to 497.91 m, and 507.39 m to 569.04 m respectively.

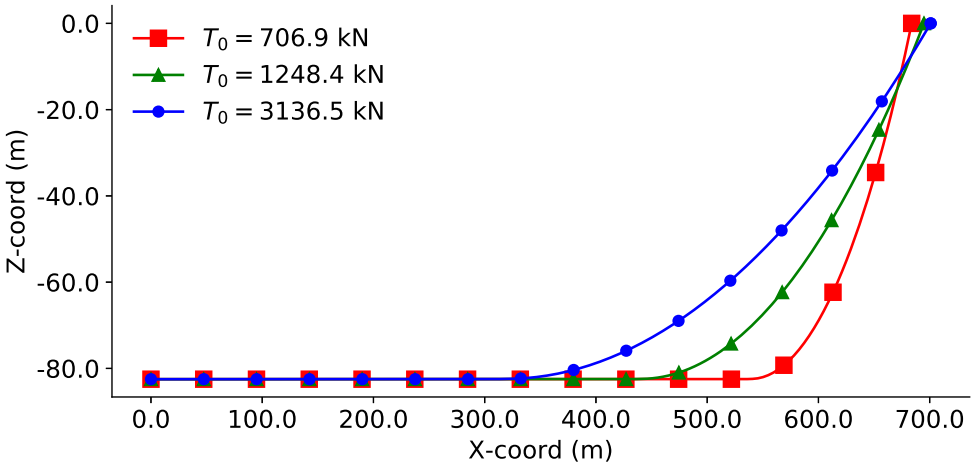

Figure 3.28: Initial line geometries of 4.74 m-element discretisation with pretension values, T_0 , of 706.9 kN, 1248.4 kN and 3136.5 kN.

The fairlead tension time histories are shown in Figure 3.30, where the disparities in the magnitudes of the tension fluctuations between the tension time histories for the three pretension cases are clearly presented. The fluctuation magnitude is largest for the low pretension case, which also experienced the highest s_{TDP} range, and smallest for the high pretension case, with the lowest s_{TDP} range. The magnitude of the tension fluctuations for mid-range pretension case lies in between the high and low pretension cases.

The velocity of the grounding node, which is the first suspended node of a grounding element (Node i+1 in Figure 3.1), for the three pretension cases, are presented in Figure 3.31. The grounding node velocities for the two higher pretension cases are similar, and attained a maximum value of approximately 3.8 m/s, whereas that for the lowest pretension case achieved a maximum of 2.96 m/s.

The grounding angle θ time histories are presented in Figure 3.32. Comparing Figures 3.32 and 3.30, it is evident that the onsets of the tension fluctuations appear in tandem with higher grounding θ angles during the unloading phase of the fairlead excitation motion. The magnitude of the grounding angles achieved by the three pretension cases vary in the same order of the pretension values. The highest pretension case experienced the highest grounding angles, followed by the mid-range and low pretension cases. This variation in the grounding angles is due to the geometry of the catenary cable, and is also evident in the static line geometries, as seen in Figure 3.28.

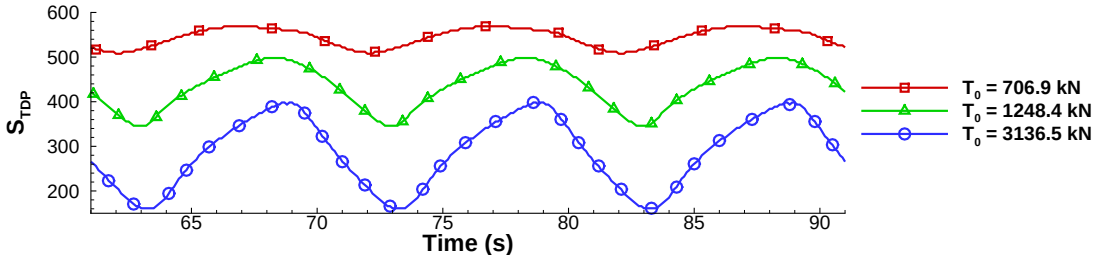

Figure 3.29: Touchdown location s_{TDP} of 4.74 m-element line with pretension values, T_0, of 706.9 kN, 1248.4 kN and 3136.5 kN for Case 1 fairlead excitation parameters.

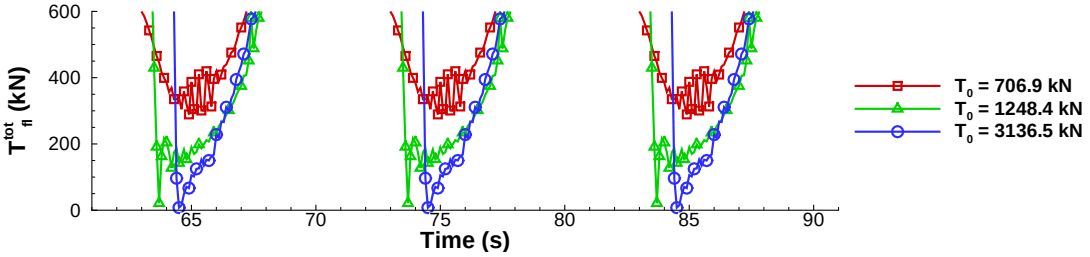

Figure 3.30: Fairlead tension time histories of 4.74 m-element line with pretension values, T_0, of 706.9 kN, 1248.4 kN and 3136.5 kN for Case 1 fairlead excitation parameters.

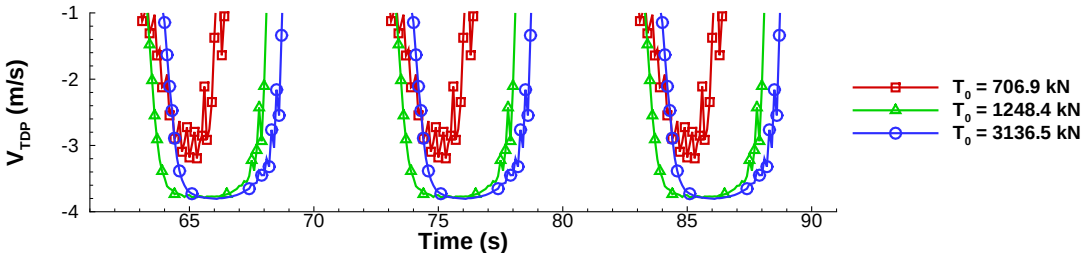

Figure 3.31: Vertical velocity of touchdown node of 4.74 m-element line with pretension values, T_0, of 706.9 kN, 1248.4 kN and 3136.5 kN for Case 1 fairlead excitation parameters.

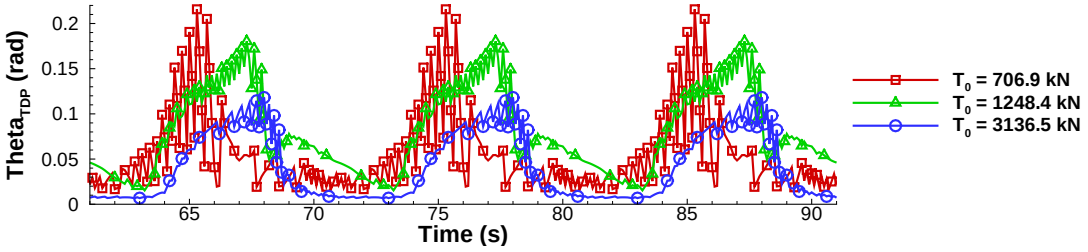

Figure 3.32: Grounding element angle θ of 4.74 m-element line with pretension values of 706.9 kN, 1248.4 kN and 3136.5 kN for Case 1 fairlead excitation parameters.

With the same dynamic excitation applied to the three pretension cases, the difference between them are in the pretension values and the s_{TDP} ranges. A s_{TDP} range close to the anchor generally leads to lower θ angles, due to the natural geometry of the catenary. Comparing the grounding velocities and θ angle profiles of the mid-range and high pretension cases, it is noted that the tension fluctuations are more significant in the mid-range case, even though the grounding velocity profiles in the two cases are similar. Furthermore, the grounding velocities in the low-pretension case is the lowest among the three cases, while also experiencing the highest θ angles, and it is notable that the tension fluctuation magnitude experienced in this case is larger than in the mid-range and high pretension cases. Therefore, the magnitudes of the tension fluctuations are positively correlated with θ.

Consider a grounding element with the asymptotic values of θ at 0 and $\pi/2$, corresponding to the perfectly vertical and horizontal orientations, as shown in Figure 3.33. The seabed reaction force acting in the axial direction of the element is thus $\left(\mathbf{F}_j^{B,r} \cdot \hat{\mathbf{e}}_j\right) \hat{\mathbf{e}}_j = F_j^{B,r} \sin\theta \, \hat{\mathbf{e}}_j$. Hence the maximum value of the seabed reaction force acting in the axial direction of the grounding element is $F_j^{B,r}$ when θ is $\pi/2$ and the element is vertical and acts to compress the element. Conversely, when the grounding element is horizontal and θ is 0, an isolated element will not experience compression due to seabed contact.

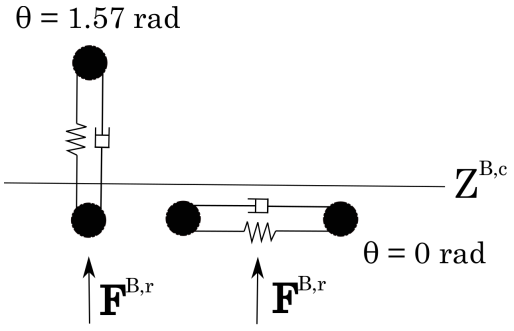

Figure 3.33: Grounding element with angle θ of 0 and $\pi/2$ rad.

It was evident in Section 3.2.2.1 that the effect of compression on a particular segment of the line gives rise to large strain gradients which in turn lead to the production and propagation of stress waves. High θ values lead to a larger effective seabed force component in the grounding element axial direction, which compresses the grounding element and leads to the rapid creation of a low strain region and large strain gradients in the line, and is therefore associated with the creation of the propagating stress waves.

3.3 Discussion

Reducing the element size leads to a reduction of the magnitude of the tension fluctuations. Taking Case 1 as an example, Figure 3.9b shows that for the in-house code an element size of 2.03 m is required to reduce the amplitude of the spurious tension fluctuations to approximately 20 kN or 1.5% of peak tension. However, the peak tension value achieved convergence with a coarser discretisation comprising of 4.74 m length elements. The use of a finer discretisation necessarily entails longer computing times, and for the in-house code, the increase was approximately 1.93 times comparing the 4.74 m (150 elements) to the 2.03 m (350 elements) discretisations. Presently, the same time step was used for both discretisations, and considering that a larger time step may be applied for the coarser discretisation, the disparity in computing times can potentially be wider.

Higher grounding velocities are associated with the development of tension fluctuations. In Case 2, the maximum fairlead velocity attained was lower than Case 1. When considering only the grounding velocities in Case 1, Figures 3.14b and 3.15b show that the grounding velocities of Nodes 66 and 67 for the 8.0 m line and Nodes 619 and 629 for the 0.84 m-element line were lower than that for Nodes 68 to 71 and Nodes 639 to 667 for the two discretisations respectively. The same is observed in Case 2, where a comparison of Figure 3.22a and Figure 3.22d shows that the grounding velocities of the nodes increase in tandem with fairlead velocity. In Case 1, the grounding of Nodes 66 and 67 in Case 1 with the 8.0 m-element line did not lead to the development of tension oscillations, while the grounding of Nodes 68 to 71 did, due to comparatively higher grounding velocities. The relatively low grounding velocities in Case 2 also did not lead to tension fluctuations. The cause of the tension fluctuations is the formation of localised low strain or slack regions in the vicinity of the touchdown point, as illustrated in Figures 3.11 and 3.12. The process is initiated by high-speed nodal grounding situations and the formation of a localised low tension or compression zone, followed by the development and expansion of the compression zone. The compression zones are transient and eventually collapse, to be replaced by a local rarefaction, high strain zone, which then expands.

High strain gradients are generated due to the presence of the compression and rarefaction zones. The large strain gradients represent unbalanced tension forces

and are responsible for driving the propagation of stress waves which travel along the length of the line. The transition from a compression to a rarefaction zone is due solely to the nodal motions. When the grounding of Node 70 produced a low tension zone at the vicinity of the touchdown point, this resulted in a net acceleration of the nodes outwards relative to the low strain region. The contraction and collapse of the compression zone is a result of the outward motion of the nodes relative to it; as the nodes at the high strain gradient interfaces experience an increase in the resultant tension force due to the high strain gradient (see Equation (2.4)), they begin to accelerate in the direction of the resultant tension forces. As the nodes move outwards from the compression zone, the separation between the nodes within it and consequently the strain increases again. At the boundaries, namely the anchor and fairlead nodes, the stress waves are reflected back into the line, as shown by Yang et. al [128]. The inertial and tension forces on the nodes give rise to oscillatory motions. Successive nodal groundings may occur and contribute to the creation of multiple stress waves that propagate back and forth along the length of the line, as was observed in Case 1.

To accurately resolve high strain gradients close to the touchdown zone, the discretisation has to be sufficiently high. If the number of elements is equivalent to that would be present in a physical line, the strain spatial gradient can be expected to follow that shown in Figure 3.13b. The kinks in the strain and strain gradient curves close to the touchdown point are characteristic of static catenary lines. In contrast, when the discretisation is insufficiently refined to capture a smooth spatial strain variation, localised strain discontinuities and low strain regions may form due to rapid nodal grounding. Of particular importance is the $\mathrm{d}\epsilon/\mathrm{d}s$ curve, because large spatial strain gradients deviating from the smoothly varying profiles as shown in Figures 3.13b and 3.10b indicate that there are large resultant nodal tension forces. This leads to the creation and propagation of stress waves following large nodal accelerations, velocities, and motions; manifesting at the fairlead as tension fluctuations.

In addition to the grounding velocity, the grounding element angle θ has an effect on the production of the tension fluctuations and higher vertical element orientations tend to increase the likelihood of the creation of low strain regions and large strain gradients, particularly if the grounding velocities are significant. Locally refining the element size in such regions is expected to be helpful in reducing the effects of

the propagating stress waves created due to large strain gradients. Larger elements can be used in regions where θ is expected to be lower.

Reducing the seabed spring stiffness and damping coefficients, as discussed in Section 3.2.3, have the effect of reducing the magnitude of the fairlead tension fluctuations. The mechanisms that produce this effect is the increased seabed penetration depths and the higher seabed force cutoff elevation, $z^{B,c}$. Consider the motion of two successive grounding nodes, as the first node is allowed to penetrate deeper into the seabed and the downwards vertical speed of the second node is reduced due to a higher $z^{B,c}$, the separation between the two nodes, which determines the element strain (see Equation (2.3)) is less likely to transition rapidly into a slack state, causing the large strain gradients that subsequently produce the propagating stress waves. However, reducing the linear spring stiffness and damping tends to lower the peak tensions in an oscillation period.

3.4 Chapter closure

This chapter has presented an investigation into the cause of the spurious tension fluctuations that affect lumped mass mooring line models due to line-seabed interactions. It was shown that both the commercial code Orcaflex as well as an in-house code may experience the tension fluctuations under moderately severe line-seabed impact conditions.

The typical strain and spatial strain gradient profiles of situations which would lead to or preclude the development of tension fluctuations were presented in Section 3.2.2. The tension fluctuations develop due to the formation of low strain regions close to the touchdown point when nodal grounding velocities are relatively high. The rapid formation of the localised low strain regions after nodal grounding leads to the creation of large strain gradients close to the touchdown point. The strain gradients represent unbalanced tension forces and lead to the propagation of the elastic stress waves along the length of the line.

Chapter 4

Development of Dual-rate, Adaptive Discretisation Dynamic Mooring Line Model

Chapter 3 illustrated that tension shock waves arising from large strain gradients along the length of the mooring line are directly attributed to impact loads from seabed contact, and can be mitigated by reducing the element size in a numerical mooring line model. The drawback of this approach is the higher computational effort required due to the increased degrees of freedom in the numerical model. For explicit time-domain mooring codes such as those described in Refs. [88, 129, 130], the usage of smaller elements also necessitates the use of smaller time-steps to satisfy the stability limit of the time integration scheme.

In multisegmented mooring lines, the usage of different line materials may give rise different time constants in separate segments of the discretized numerical line model. The application of local mesh refinement techniques such as described in Refs. [91] and [130], for the purposes of capturing high curvature and snap loads respectively, will also lead to stiffness in the discrete line model due to a wide separation between the largest and smallest element sizes. A constant time-step was applied for the entire line structure in both aforementioned adaptive mesh refinement implementations. Implicit time integration algorithms allow the use of larger time-steps for such stiff systems but are computationally expensive for

systems with a large number of degrees-of-freedom. Alternatively, a mixed implicit-explicit integration approach with a single time-step is used for the entire system in conjunction with the application of implicit and explicit time-stepping algorithms in the stiff and non-stiff components respectively; examples of the application of this approach in structural dynamics include Refs. [131–134].

In contrast to the implicit-explicit approach, Multi-Rate time integration methods allow the use of different time-steps sizes for the components in a coupled system. The impetus for using Multi-Rate integration is to reduce computational expense by applying appropriate time-step sizes, from considerations of stability and accuracy, for each component in a system. Multi-Rate algorithms have been built upon linear multi-step integration schemes including the implicit backward differentiation methods [135], as well as single-step explicit Runge-Kutta [136, 137], semi-implicit Rosenbrock-Wanner [138**?**], and Richardson extrapolation [139] schemes. Arnold [140] presented several examples in the area of multibody dynamics where Multi-Rate methods are advantageous. Shome et al. [141] devised a partitioned Runge-Kutta method involving base Runge-Kutta integrators of different orders applied to a vehicle dynamics problem. Chang et al. [142] presented a Multi-Rate linear multistep scheme applied to spacecraft dynamics using the Adams-Bashforth and Adams-Moulton methods as base integration schemes. Grote et al. [143] derived a Multi-Rate Runge-Kutta scheme based on explicit fourth-order and low storage Runge-Kutta integrators and applied it to finite element wave propagation simulations.

To mitigate the production of fairlead tension fluctuations arising from line-seabed impact, a straightforward solution is to apply a higher element density in a limited region enveloping the touchdown point. However, due to potentially large displacements of the fairlead, the region of a mooring line which will experience liftoff/grounding will be correspondingly large. Using a reduced element size for the full extent of the line segment expected to experience liftoff/grounding increases the computational costs unnecessarily because the undesirable effects of nodal grounding may be circumvented by having a locally refined region in the vicinity of the touchdown zone.

This chapter presents an adaptive discretisation method applied to a lumped-mass mooring line model, limiting the refined region close to the touchdown zone where nodal grounding and liftoff occurs. Depending on the change in the touchdown

zone location relative to the axial coordinate along a mooring line, the appropriate discretisation, prepared prior to the start of computations, is selected. The mapping algorithm from one discretisation to another is presented, with the focus on ensuring that fairlead tensions are accurate. An approach to Multi-Rate time integration, as well as the determination of the optimal time-steps to apply in the different zones, is also proposed. The quality of the results obtained and the computational cost of the solution using the proposed Multi-Rate-adaptive discretisation method, in comparison with uniformly coarse and fine element density meshes are presented.

4.1 Dual-rate time integration

4.1.1 Temporal synchronization and spatial coupling of partitions

The base integration algorithm of the dual-rate integration method is the Modified Euler scheme. Equations (2.30a) and (2.30b) can be merged to produce a first order differential equation,

$$\mathbf{y}_{n+1} = \mathbf{A}\left(\mathbf{y}_n + \mathbf{B}_n \Delta t\right) \tag{4.1}$$

in which $\mathbf{y}$ is the state vector, $[\mathbf{r}, \dot{\mathbf{r}}]^{\mathrm{T}}$, $\mathbf{y} \in \mathbb{R}^{2N}$, and N is the number of degrees of freedom in the system. The matrix $\mathbf{A}$ and vector $\mathbf{B}$ are defined in Equations (4.2) and (4.3).

$$\mathbf{A}\left(\Delta t\right) = \begin{bmatrix} 1 & \Delta t \\ 0 & 1 \end{bmatrix} \tag{4.2}$$

$$\mathbf{B}\left(\mathbf{y}(t)\right) = \begin{bmatrix} 0 \\ \left(\mathbf{M}_n\right)^{-1} \mathbf{F}_n^{tot} \end{bmatrix} \tag{4.3}$$

For the purposes of Multi-Rate time integration, the system $\mathbf{y}$ can be separated into k partitions, for which the time rate of change of state in each partition is given by,

$$\dot{\mathbf{y}}_p = \mathbf{f}_p(t, \mathbf{y}_1, ..., \mathbf{y}_k) \tag{4.4}$$

where $\mathbf{y}_p \in \mathbb{R}^{2N_p}$, $p \in [1, k]$, and $\sum_{p=1}^{k} N_p = N$. A different time-step can be applied in each partition. This requires that the larger time-step for any two coupled partitions must be an integer multiple of the smaller time-step. This is illustrated in Figure 4.1 for two coupled partitions, where the macro (larger) time-step, H, is q times that of the micro (smaller) time-step, h. Synchronization of the partitions are performed at each macro time-step and involves the exchange of the data of the coupled variables, $\mathbf{y}_p$.

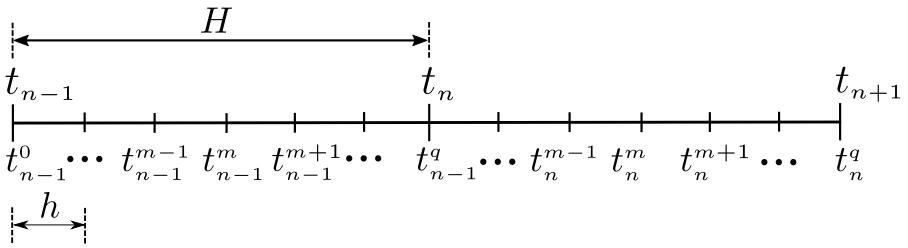

Figure 4.1: Macro and micro time-steps. Adapted from Ref. [3].

In the lexicon of Multi-Rate time integration, the partitions using the macro and micro time-steps are referred to as the latent and active partitions respectively, and the time rates of change of each partition are given by,

$$\dot{\mathbf{y}}_L = \mathbf{f}_L\left(\mathbf{y}_L, \tilde{\mathbf{y}}_A\right), \qquad \mathbf{y}_L\left(t_0\right) = \mathbf{y}_{L,0} \tag{4.5a}$$

$$\dot{\mathbf{y}}_A = \mathbf{f}_A\left(\mathbf{y}_A, \tilde{\mathbf{y}}_L\right), \qquad \mathbf{y}_A\left(t_0\right) = \mathbf{y}_{A,0} \tag{4.5b}$$

where $\mathbf{y}_L$ and $\mathbf{y}_A$ refer to a pair of coupled latent and active partitions, $\mathbf{y}_{L,0}$ and $\mathbf{y}_{A,0}$ are their initial conditions, and $\tilde{\mathbf{y}}_A$ and $\tilde{\mathbf{y}}_L$ are the values of the variables from the coupled partition which can be obtained from interpolation or extrapolation procedures or function evaluations of $\mathbf{f}_L$ and $\mathbf{f}_A$.

The sequence of time integration of the latent and active partitions affects the choice of Multi-Rate algorithms. In a slowest-first approach, the latent partition, $\mathbf{y}_L$, is first advanced in time with macro time-step H, and subsequently the active partition, $\mathbf{y}_A$, is marched forward in time with q steps of micro time-step h. The relationship between h and H is,

$$H = qh \tag{4.6}$$

Synchronization is done when both partitions have advanced in time by the interval H. In a slowest-first approach, $\mathbf{y}_A$ is advanced in time first with q steps of time-step h, and is followed by the integration of $\mathbf{y}_L$ with the time-step H. Gear and Wells [135] proposed that the fastest-first method is suitable for fixed time-steps while the slowest-first approach is appropriate for adaptive time-stepping in order to reduce the number of potential rejected steps, following the evaluation of the error between the extrapolated values of the active component used to integrate the latent partition (see Equation (4.5a)), and the actual values of the active component after q steps. This argument holds if extrapolated values of $\mathbf{y}_A$ are needed for the integration of $\mathbf{y}_L$; for example, if Adams-Moulton or Runge-Kutta methods of second-order of higher is used as the base integration scheme for $\mathbf{y}_L$. Another Multi-Rate integration approach is to concurrently advance both $\mathbf{y}_A$ and $\mathbf{y}_L$ through the use of coupling coefficients, examples of which can be found in Refs. [144] and [145].

Following Low et al. [146], for the present in-house code, the Modified Euler integration scheme is used for monolithic time integration and is modified for Multi-Rate integration. According to Gear and Wells [135], the sources of errors from a Multi-Rate integration procedure are the truncation error of the base integration scheme, and interpolation and extrapolation errors of the fast and slow components. Therefore, the slowest-first strategy is compatible with the choice of the base integration scheme because no extrapolation procedure is required, thereby eliminating one of the sources of approximation errors in a Multi-Rate procedure.

1 Calculate $\mathbf{y}_L\left(t_n + H\right)$ with Equation (4.7);
2 Interpolate values for $\tilde{\mathbf{y}}_L(t_n^m)$, where $1 \leq m \leq q$, with Equation (4.8);
3 **for** $m = 0 \rightarrow q - 1$ **do**
4 | Calculate $\mathbf{y}_A\left(t_n^{m+1}\right)$ with Equation (4.9);
5 **end**

Algorithm 1: Multi-Rate Modified Euler time integration procedure.

To demonstrate the veracity of this statement, and illustrate the integration procedure, consider the proposed dual-rate integration procedure shown in Algorithm 1. To advance the latent partition $\mathbf{y}_L$ from t_n to $t_{n+1} = t_n + H$, only $\mathbf{y}_A\left(t_n\right)$ and $\mathbf{y}_L\left(t_n\right)$ are needed as shown in Equation (4.7). Furthermore, as shown in Equation (4.9),

for the time marching of $\mathbf{y}_A$ from t_n^m to $t_n^{m+1} = t_n^m + h$, the linearly interpolated value of the coupled active partition variable, $\tilde{\mathbf{y}}_L$, obtained using Equation (4.8), is required.

$$\mathbf{y}_L\left(t_{n+1}\right) = \mathbf{A}\left(H\right)\left[\mathbf{y}_L(t_n) + H\mathbf{B}_n\left(\mathbf{y}_A\left(t_n\right), \mathbf{y}_L\left(t_n\right)\right)\right] \tag{4.7}$$

$$\tilde{\mathbf{y}}_L\left(t_n^m\right) = \mathbf{y}_L\left(t_n\right) + mh\frac{\mathbf{y}_L\left(t_{n+1}\right) - \mathbf{y}_L\left(t_n\right)}{H} \tag{4.8}$$

$$\mathbf{y}_A\left(t_n^{m+1}\right) = \mathbf{A}\left(h\right)\left[\mathbf{y}_L(t_n^m) + h\mathbf{B}_n\left(\mathbf{y}_A\left(t_n^m\right), \tilde{\mathbf{y}}_L\left(t_n^m\right)\right)\right] \tag{4.9}$$

The coupling between the latent and active partitions is illustrated in Figure 4.2. Smaller elements are concentrated around the touchdown zone while coarser elements are used in the segments adjacent to the refined zone, in a hybrid coarse/fine discretisation. The boundary conditions for the active partition are imposed with $\mathbf{y}_{L*}$, which are equivalent to the values for $\tilde{\mathbf{y}}_L(t_n^m)$ obtained from Equation (4.8). The boundary conditions for the latent partition, $\mathbf{y}_{A*}$, is obtained from the active partition during synchronization at the start of a macro time step, i.e. $\mathbf{y}_{A*} = \mathbf{y}_A(t_n^0)$.

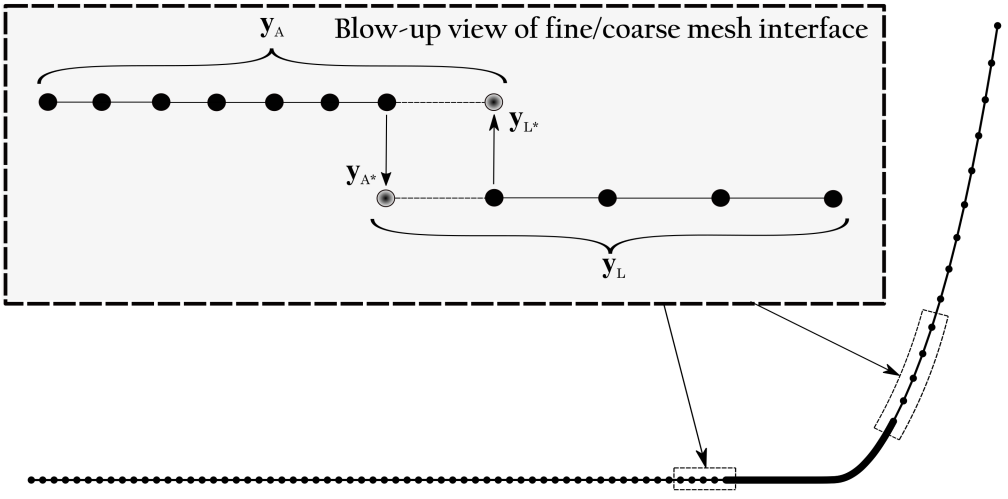

Figure 4.2: Partition spatial boundary conditions.

4.1.2 Selection of time-step sizes

Following the procedure described by Grote et al. [143], a diagonal matrix $\mathbf{Q}$, whose diagonal entries contain ones when referring to degrees-of-freedom belonging to the active component and zero otherwise, can be used to separate the system position vector,

$$\mathbf{r} = (\mathbf{I} - \mathbf{Q})\,\mathbf{r} + \mathbf{Q}\mathbf{r} = \mathbf{r}_L + \mathbf{r}_A \tag{4.10}$$

The same can be done for the system velocity and acceleration vectors but is not shown here for brevity. Inserting Equation (4.10) into Equation (2.31), the equation of motion for the system can be separated into its component partitions,

$$[\mathbf{M}_A\ddot{\mathbf{r}}_A + \mathbf{K}_A\mathbf{r}_A] + [\mathbf{M}_L\ddot{\mathbf{r}}_L + \mathbf{K}_L\mathbf{r}_L] = 0 \tag{4.11}$$

The maximum time-step for each partition can then be evaluated separately following the procedure described by Hahn [124], and re-arranging Equation (2.31) for each of the partitions as shown in Equation (2.32). The maximum time-steps for each partition can then be obtained following the procedure described in Section 2.2.2.

With the maximum stable time-steps of each partition available, the optimum time-step sizes of the latent and active partition can be determined. For the purposes of this paper, which is concerned with the single-line simulation using fixed time-steps for a prescribed duration of simulation, I_1, the total number of nodal time integration operations in one macro time-step for a mooring line split into two partitions, one active and the other latent, is given by,

$$I_1 = N_L + N_A q \tag{4.12}$$

where N_L and N_A are the numbers of degrees of freedom in the latent and active partitions. Denoting T_{sim} as the total simulation duration, the total number of nodal time integration operations, I_{sim}, is described by,

$$I_{sim} = \frac{T_{sim} I_1}{H} \tag{4.13}$$

Considering that the current problem is nonlinear and that the time-step stability criterion (see Equation (2.33)) described by Hahn [124] is valid for linear problems, the applied time-step for each partition is scaled by a reduction factor, γ_p, where p refers to the latent or active partition. Inserting γ_p into Equation (4.13) and expanding the term I_1,

$$I_{sim}\left(\gamma_L,\, \gamma_A\right) = \frac{T_{sim}}{\gamma_L \Delta t_{L,max}} \left(N_L + N_A \frac{\gamma_L \Delta t_{L,max}}{\gamma_A \Delta t_{A,max}} \right) \tag{4.14}$$

To reduce the total number of nodal time integration operations, I_{sim} is set as the objective function to be minimized with constraints on γ_A and γ_L,

$$\begin{aligned} &\text{minimize} && I_{sim}\left(\gamma_L,\, \gamma_A\right) \\ &\text{subject to} && 1 : \gamma_{min} \leq \gamma_A \leq \gamma_{max} \\ & && 2 : \gamma_{min} \leq \gamma_L \leq \gamma_{max} \\ & && 3 : \quad \text{mod} \left(\frac{\gamma_L \Delta t_{L,max}}{\gamma_A \Delta t_{A,max}} \right) = 0 \end{aligned} \tag{4.15}$$

where γ_{max} and γ_{min} are the partition maximum and minimum time-step fraction constraints. The constant γ_{max} is arbitrarily set to a conservative value lower than 1 to account for the effect of nonlinearities on the calculated stable time-step sizes, and γ_{min} provides an arbitrary lower bound on the scaling parameter and should be a positive real number. The third constraint ensures that the applied time-step size for the latent partition is an integer multiple of the time-step size of the active partition, i.e. $q \in \mathbb{Z}^+$. The solver applied to the optimization problem stated in Equation (4.15) is the COBYLA scheme by Powell [147], and implemented in Fortran 90 by Miller [148]. The time-step sizes for the active and latent partitions can then be determined as,

$$h = \gamma_A \Delta t_{A,max} \tag{4.16a}$$

$$H = \gamma_L \Delta t_{L,max} \tag{4.16b}$$

4.2 Line discretisation preparation, selection and mapping

4.2.1 Discretisation preparation

Figure 2.1a shows that the origin of the line axial coordinate, s, coincides with the anchor position. In this work, the discretisations (meshes) of a mooring line are prepared and saved in advance. This reduces the computational load of generating new discretisations during the course of a simulation run. The coarse and fine-element regions of the line, consisting of elements of lengths L_L and L_A and designated as the latent and active partitions respectively, are therefore pre-determined, as presented in Figure 4.3.

The procedure of preparing the mooring line discretisations in advance of dynamic simulations begin by obtaining the initial static line geometry and determining $s_{TDP,0}$, the initial static touchdown point s-coordinate, which should be close to s_0, the s-coordinate of the midpoint of the fine-element segment of the starting discretisation, so that the length of the refined region is approximately evenly split on each side of s_0. The separation $\epsilon_{TDP,0}$ between $s_{TDP,0}$ and s_0 of the initial discretisation, as shown in Figure 4.3, is used to correct the upper and lower switching s-coordinates of all discretisations,

$$s_{u^*,d} = s_{u,d} + \epsilon_{TDP,0} \tag{4.17a}$$

$$s_{l^*,d} = s_{l,d} + \epsilon_{TDP,0} \tag{4.17b}$$

where $d \in [1, N_d]$, and N_d is the total number of discretisations prepared. The location $s_{u^*,d}$ is the midpoint between $s_{l^*,d}$ and $s_{u^*,d}$, as shown in Figure 4.4. The element lengths in the coarse and refined regions, $L_{L,d}$ and $L_{A,d}$, are equivalent in all discretisations, i.e. $L_{A,1} = L_{A,2} = ... = L_{A,N_d}$ and $L_{L,1} = L_{L,2} = ... = L_{L,N_d}$.

The lengths of the refined regions, $l_{A,d}$, is arbitrary, and are equivalent in all prepared discretisations, i.e. $l_{A,1} = l_{A,2} = ... = l_{A,N_d}$. The length of the refined region affects its effectiveness in suppressing the propagation of the stress waves generated by the creation of large localized strain gradients due to nodal grounding. There is also a trade-off between reducing the computational load for each macro

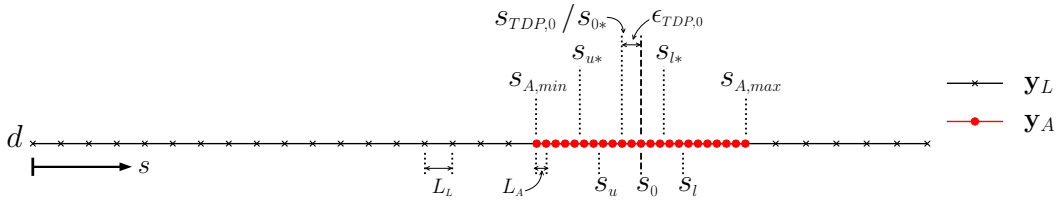

Figure 4.3: Schematic relationship between $s_{TDP,0}$, the initial static touchdown point, and s_0, the initial discretisation refined zone midpoint s-coordinate.

time-step by reducing the length of the refined region and increasing the frequency of discretisation switches which incurs an additional computational expense. This is because reducing the length of the refined region of a particular discretisation will reduce its range of applicable s_{TDP}, i.e. $s_{l^*} \leq s_{TDP}(t) \leq s_{u^*}$. Hence, when s_{TDP} changes significantly, more discretisation switches will be performed when the lengths of $l_{A,d}$ are shorter.

The number of discretisations to be prepared depends on the expected range of $s_{TDP}(t)$ over the full simulation duration. In the present work, the available discretisations meet the following condition,

$$\min\left\{s_{l,1},...,s_{l,N_d}\right\} \leq s_{TDP}(t) \leq \max\left\{s_{u,1},...,s_{u,N_d}\right\}, \quad 0 \leq t \leq T_{sim} \tag{4.18}$$

which states that the touchdown point location will be within the lower and upper switching s-coordinates of the appropriate discretisation. A switch will be made to the suitable discretisation when the instantaneous $s_{TDP}(t)$ moves beyond the switching s-coordinates of the active discretisation.

4.2.2 Discretisation switching

The s-range of the active partition of each discretisation, $s_{A,min} \leq s \leq s_{A,max}$, is necessarily different from others so that each discretisation covers a staggered and overlapping range of $s_{TDP}(t)$. During the course of a simulation run, the occurrence of exceedance of s_{TDP} beyond s_u or s_l will trigger a switch to the adjacent discretisation. Using Figure 4.4 as an example, which shows discretisation d as the current discretisation along with two adjacent discretisations, a check of s_{TDP} is performed at fixed time intervals Δt_c.

Figure 4.4: Prepared line discretisations with staggered refined segments.

If $s_{TDP}(t)$ exceeds $s_{u,d}$, the upper switching s-coordinate for discretisation d, then a switch will be made to discretisation $d-1$. Similarly, if $s_{TDP}(t)$ exceeds $s_{l,d}$, the lower switching s-coordinate for discretisation d, a switch will be made to discretisation $d+1$. The switch from d to $d-1$ corresponds to a refinement of the discretisation on the fairlead-side end of the refined region, and simultaneously a coarsening of the discretisation on the anchor-side end. Conversely, the switch from d to $d+1$ is a refinement of the anchor-side, and corresponding coarsening of the fairlead-side of the refined region. The procedure is shown in Algorithm 2.

if $t = t_c$ **then**
  if $s_{TDP}(t) < s_{l,d}$ **then**
    Switch to Discretisation $d+1$;
  else if $s_{TDP}(t) > s_{u,d}$ **then**
    Switch to Discretisation $d-1$;
  $t_c \leftarrow t_c + \Delta t_c$

Algorithm 2: Discretisation checking and switching procedure.

The s-coordinate range of the refined segment of each discretisation overlaps with and is staggered with respect to its adjacent discretisations as shown in Figure 4.4. Presently, the separation between adjacent discretisations is set such that $s_{u,d} = s_{0,d+1}$ and $s_{l,d} = s_{0,d-1}$, and therefore the following relationships, $s_{A,min,d} = s_{A,min,d+1} + (s_{0,d-1} - s_{l,d-1})$ and $s_{A,min,d+1} = s_{A,min,d} + (s_{0,d} - s_{l,d})$, hold. Further, the length of the refined region is a constant $l_{A,d}$, therefore $s_{A,max,d} = s_{A,min,d} + l_{A,d}$.

4.2.3 Discretisation mapping

The transition from the current to the next active discretisation, hereafter referred to as d_c and d_t respectively, involves the mapping of the nodal positions, velocity, and accelerations. It is essential that the strain and curvature distributions, $\epsilon(s)$ and $\kappa(s)$ respectively, in the next discretisation matches that in the current discretisation as closely as possible. This is because, firstly, it provides a smoother

transition in the data record for these variables, and secondly, the occurrence of discontinuities and large gradients due to imperfect line mapping, particularly in $\epsilon(s)$ and $\kappa(s)$, gives rise to force imbalances and instability.

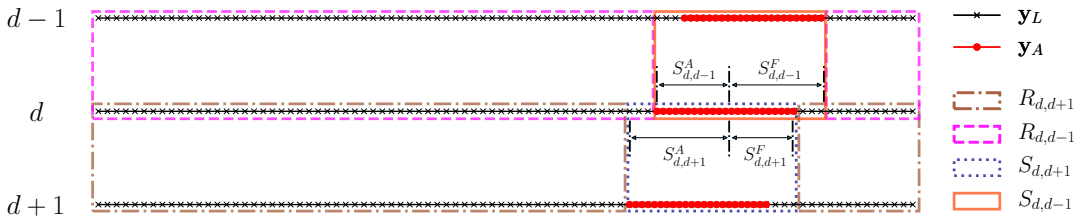

Figure 4.5: Discretisation line spans containing direct mapping nodal pairs, $R_{d,d_{+1}}$ and $R_{d,d_{-1}}$, and strain mapping zones, $S_{d,d_{d+1}}$ and $S_{d,d_{d-1}}$.

The first step in the transition from d_c to d is to directly map the positions, velocity and accelerations of the nodes in d_t with common s-coordinates with d_c. The direct mapping nodes for every discretisation d with its adjacent discretisations, $d+1$ and $d-1$, have been identified at the discretisation preparation phase. For each d_c-d_t pair, there is a set, R_{d_t,d_c}, containing N_{R,d_t,d_c} pairs of nodal indices, (i,j), for which the s-coordinates of node i in d_c and node j in d_t are equivalent. The discretisation spans containing the direct mapping pairs in adjacent discretisations is shown schematically in Figure 4.5. Thus, direct mapping of the state for each pair of nodes in R_{d_t,d_c} is given by,

$$\mathbf{r}_{i,d_t} = \mathbf{r}_{j,d_c} \tag{4.19a}$$

$$\dot{\mathbf{r}}_{i,d_t} = \dot{\mathbf{r}}_{j,d_c} \tag{4.19b}$$

$$\ddot{\mathbf{r}}_{i,d_t} = \ddot{\mathbf{r}}_{j,d_c} \tag{4.19c}$$

The nodes in d_t that are not in R_{d_t,d_c} do not have a neighbour node in d_c from which the nodal state can be directly copied. These regions, denoted as S_{d_t,d_c}, where these nodes are located, are presented as $S_{d,d+1}$ and $S_{d,d-1}$ in Figure 4.5 if the target discretisations are $d+1$ and $d-1$ respectively. For these nodes, the nodal velocity and acceleration are obtained from piecewise cubic Hermitian spline interpolation [149], for which the prototype interpolation function and function derivative are,

$$f_l(s) = c_{0,l} + c_{1,l}\left(s - s_j^{d_c}\right) + c_{2,l}\left(s - s_j^{d_c}\right)^2 + c_{3,l}\left(s - s_j^{d_c}\right)^2\left(s - s_{j+1}^{d_c}\right) \tag{4.20a}$$

$$\frac{\mathrm{d}f_l}{\mathrm{d}s} = c_{1,l} + 2c_{2,l}\left(s - s_j^{d_c}\right) + c_{3,l}\left[2\left(s - s_j^{d_c}\right)\left(s - s_{j+1}^{d_c}\right) + \left(s - s_j^{d_c}\right)^2\right] \tag{4.20b}$$

where $f_l(s)$ and $\mathrm{d}f_l/\mathrm{d}s$, valid for the range $s_j^{d_c} \leq s \leq s_{j+1}^{d_c}$, and for $l \in [1,3]$ and $l \in [4,6]$ respectively, represent the interpolating functions for the individual components of the vectors $\dot{\mathbf{r}}$ and $\ddot{\mathbf{r}}$. The following boundary conditions apply,

$$f_l\left(s_j^{d_c}\right) = g_k\left(s_j^{d_c}\right) \tag{4.21a}$$

$$f_l\left(s_{j+1}^{d_c}\right) = g_k\left(s_{j+1}^{d_c}\right) \tag{4.21b}$$

$$\left.\frac{\mathrm{d}f_l}{\mathrm{d}s}\right|_{s=s_j^{d_c}} = \left.\frac{\mathrm{d}g_l}{\mathrm{d}s}\right|_{s=s_j^{d_c}} \tag{4.21c}$$

$$\left.\frac{\mathrm{d}f_l}{\mathrm{d}s}\right|_{s=s_{j+1}^{d_c}} = \left.\frac{\mathrm{d}g_l}{\mathrm{d}s}\right|_{s=s_{j+1}^{d_c}} \tag{4.21d}$$

where g_l and $\mathrm{d}g_l/\mathrm{d}s$, $l \in [1,6]$, provide the scalar function and function derivative values for the individual components of the vectors $\dot{\mathbf{r}}$ and $\ddot{\mathbf{r}}$ in d_c at $s_j^{d_c}$ and $s_{j+1}^{d_c}$. Inserting $s = s_j^{d_c}$ and $s = s_{j+1}^{d_c}$ into Equations (4.20a) and (4.20b) and applying the boundary conditions, Equations (4.21a) to (4.21d), the values for coefficients $c_{0,l}$, $c_{1,l}$, $c_{2,l}$ and $c_{3,l}$ can be obtained for each interval $[s_j^{d_c}, s_{j+1}^{d_c}]$. The scalar values for the components of the vectors $\dot{\mathbf{r}}\left(s_i^{d_t}\right)$ and $\ddot{\mathbf{r}}\left(s_i^{d_t}\right)$ in d_t, valid for the range $s_j^{d_c} \leq s_i^{d_t} \leq s_{j+1}^{d_c}$, are then be obtained from $f_l\left(s_i^{d_t}\right)$, $l \in [1,6]$.

The mapping of the nodal positions in S_{d_t,d_c} affects the local strain and curvature, both of which strongly influence the resultant nodal tension force. The procedure starts with obtaining the element strains in the region S_{d_t,d_c} in d_t via piecewise linear interpolation,

$$\epsilon^{d_t}(s_i^e) = \epsilon^{d_c}(s_j^e) + \frac{s_i^e - s_j^e}{s_{j+1}^e - s_j^e}\left[\epsilon^{d_c}(s_{j+1}^e) - \epsilon^{d_c}(s_j^e)\right] \tag{4.22}$$

where $\epsilon^{d_t}(s_i^e)$ is the strain of element i in d_t with the s-coordinate of the element midpoint at s_i^e, and $s_j^e \leq s_i^e \leq s_{j+1}^e$, and $\epsilon^{d_c}(s_j^e)$ and $\epsilon^{d_c}(s_{j+1}^e)$ are the strains of the elements in d_c that are closest in proximity in terms of the s-coordinate to element i in d_t. The stretched length of element i is then given by,

$$L_i^{'e,d_t} = L_i^{e,d_t}\left[1 + \epsilon^{d_t}(s_i^e)\right] \tag{4.23}$$

where L_i^{e,d_t} is the unstretched length of element i.

The S_{d_t,d_c} region is further split into two zones, denoted as $S^F_{d_t,d_c}$ and $S^A_{d_t,d_c}$ as illustrated in Figure 4.5. The interface between these two zones is at the midpoint of the fine-element segment of d_t. The size of the two zones changes depending on whether d_c is $d+1$ or $d-1$. The two possible modes of the discretisation transition from d_c to d_t, as discussed in Section 4.2.2 as mappings from d to $d+1$ in which the element size is refined on the floater-side and coarsened on the anchor-side ends, and from d to $d-1$, in which the nodal density is coarsened on the floater-side and refined on the anchor-side ends. The example of pre- and post-mapping nodal positions are presented in Figure 4.6. The indices of the nodes at the ends of the R_{d_t,d_c} region from the anchor and fairlead-sides, as illustrated in Figures 4.6a and 4.6b, are denoted as i_0^{A,d_t} and i_0^{F,d_t} respectively. The nodal position mapping begins from Nodes i_0^{A,d_t} and i_0^{F,d_t}, moves towards the interior of S_{d_t,d_c}, and stops at the interface of the $S^F_{d_t,d_c}$ and $S^A_{d_t,d_c}$ regions.

The nodal positions in d_t have to closely trace the line geometry in d_c as illustrated in Figure 4.6. During the mapping process, the nodes in d_t may be mapped to a region on d_c that is in the fine or coarse regions. The states of the nodes in the R_{d_t,d_c} segment, which within the coarse-element segments of d_c to d_t, are directly copied over.

For a node in the $S^F_{d_t,d_c}$ and $S^A_{d_t,d_c}$ blocks of d_t that maps to a fine-element region of d_c, the procedure to determine its position is illustrated in Figures 4.7 and 4.8 respectively, where $\mathbf{r}_m^{d_t}$ is a node in d_t that already has its position defined and $\mathbf{r}_{m+1}^{d_t}$ is the next node in the nodal mapping sequence, and $L_{m+1}^{'e,d_t}$ is the stretched length of the element $m+1$ in d_t between nodes m and the next node in the sequence, $m+1$, the strain of which is calculated using Equation (4.22). The nodal positions and element unit vectors in d_c are indicated by $\mathbf{r}^{d_c}$, and $\hat{\mathbf{e}}^{d_c}$.

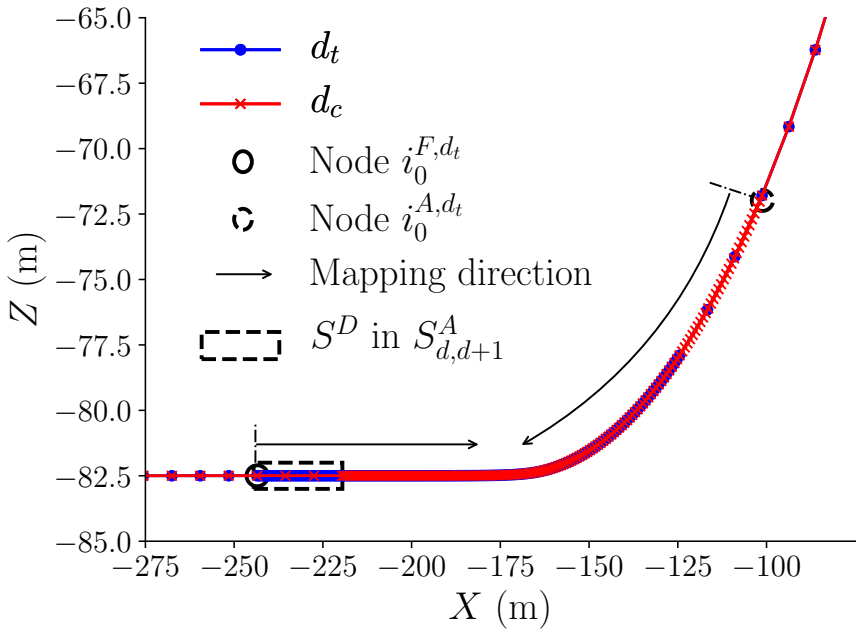

(a) Coarsening and refinement of discretisation on fairlead-side and anchor-side respectively.

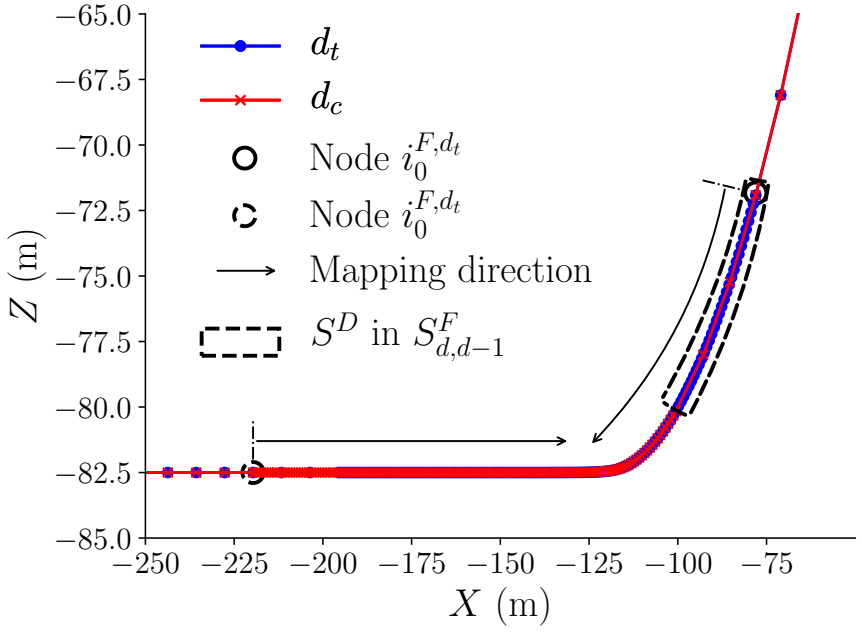

(b) Refinement and coarsening of discretisation on fairlead-side and anchor-side respectively.

Figure 4.6: Examples of transition from d_c to d_t with refinement and coarsening of discretisation at fairlead and anchor-sides.

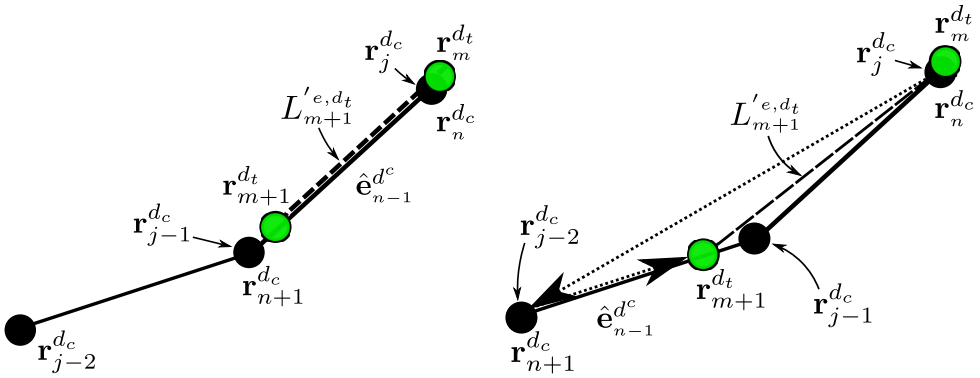

(a) Nodal position mapping with $L_{m+1}^{'e,d_t} < \left|\mathbf{r}_{n+1}^{d_c} - \mathbf{r}_m^{d_t}\right|$.

(b) Nodal position mapping with $L_{m+1}^{'e,d_t} \geq \left|\mathbf{r}_{n+1}^{d_c} - \mathbf{r}_m^{d_t}\right|$.

Figure 4.7: Nodal position mapping from d_c to d_t in S_{d_t,d_c}^F.

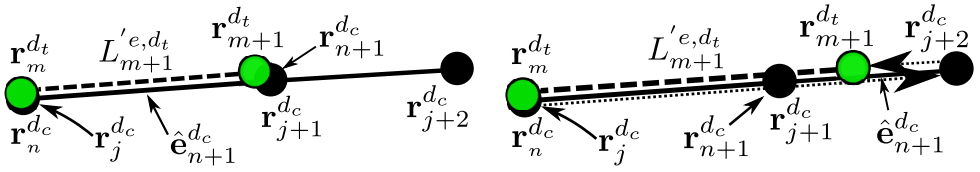

(a) Nodal position mapping with $L_{m+1}^{'e,d_t} < \left|\mathbf{r}_{n+1}^{d_c} - \mathbf{r}_m^{d_t}\right|$.

(b) Nodal position mapping with $L_{m+1}^{'e,d_t} \geq \left|\mathbf{r}_{n+1}^{d_c} - \mathbf{r}_m^{d_t}\right|$.

Figure 4.8: Nodal position mapping from d_c to d_t in S_{d_t,d_c}^A.

Figure 4.7a illustrates schematically the mapping procedure in S_{d_t,d_c}^F when $L_{m+1}^{'e,d_t} < \left|\mathbf{r}_{n+1}^{d_c} - \mathbf{r}_m^{d_t}\right|$, while Figure 4.7b presents the procedure when $L_{m+1}^{'e,d_t} \geq \left|\mathbf{r}_{n+1}^{d_c} - \mathbf{r}_m^{d_t}\right|$. Similarly, Figures 4.8a and 4.8b illustrate the nodal position mapping procedures in S_{d_t,d_c}^A when the conditions $L_{m+1}^{'e,d_t} < \left|\mathbf{r}_{n+1}^{d_c} - \mathbf{r}_m^{d_t}\right|$ or $L_{m+1}^{'e,d_t} \geq \left|\mathbf{r}_{n+1}^{d_c} - \mathbf{r}_m^{d_t}\right|$ are met respectively. The procedure illustrated in Figures 4.7 and 4.8 is detailed in Algorithm 3, and is used to determine the position of a single node. The position of each node in S_{d_t,d_c}^F and S_{d_t,d_c}^A is determined sequentially starting from Node i_0^{A,d_t} and moving in the positive s-direction for the nodes in S_{d_t,d_c}^A, and starts from Node i_0^{F,d_t}, moving in the negative s-direction for the nodes in S_{d_t,d_c}^F.

Equation (4.24) is used in Algorithm 3 to determine $\mathbf{r}_{m+1}^{d_t}$ when the condition $L_{m+1}^{'e,d_t} < \left|\mathbf{r}_{n+1}^{d_c} - \mathbf{r}_m^{d_t}\right|$ is met. The nonlinear equation is subjected to a constraint condition so that the calculated position of $\mathbf{r}_{m+1}^{d_t}$ is consistent with the intended spatial direction of mapping, $\beta\hat{\mathbf{e}}_{n+1}^{d_c}$, and does not deviate from $\beta\hat{\mathbf{e}}_{n+1}^{d_c}$ by an angle of more than $\pi/2$.

$k = j + \beta$ ▷ β accounts for direction of mapping with Equation (4.25) ;
$\mathbf{r}_{n+1}^{d_c} \leftarrow \mathbf{r}_k^{d_c}$;
$L_{m+1}^{'e,d_t} \leftarrow L_{m+1}^{e,d_t} \epsilon_{m+1}$ ▷ ϵ_{m-1} calculated with Equation (4.22) ;
if $L_{m+1}^{'e,d_t} < \left|\mathbf{r}_{n+1}^{d_c} - \mathbf{r}_m^{d_t}\right|$ **then**
  while $L_{m+1}^{'e,d_t} < \left|\mathbf{r}_{n+1}^{d_c} - \mathbf{r}_m^{d_t}\right|$ **do**
    $k \leftarrow k + \beta$;
    $\mathbf{r}_{n+1}^{d_c} \leftarrow \mathbf{r}_k^{d_c}$;
  end
  $\mathbf{r}_{m+1}^{d_t} \leftarrow \mathbf{r}_{n+1}^{d_c} - \beta \tilde{L}_{m+1}^{'e,d_t} \hat{\mathbf{e}}_{n+1}^{d_c}$ ▷ Solve for $\tilde{L}_{m-1}^{e,d_t}$ with Equation (4.24);
else
  $\mathbf{r}_{m+1}^{d_t} \leftarrow \mathbf{r}_m^{d_t} + \beta L_{m+1}^{'e,d_t} \hat{\mathbf{e}}_{n+1}^{d_c}$
end

Algorithm 3: Nodal position search algorithm.

$$\begin{aligned} &\text{Solve} \quad f\left(\tilde{L}_{m+1}^{'e,d_t}\right) = \left|\left(\mathbf{r}_{n+1}^{d_c} + \beta \tilde{L}_{m+1}^{'e,d_t} \cdot \hat{\mathbf{e}}_{n+1}^{d_c}\right) - \mathbf{r}_m^{d_t}\right| - L_{m+1}^{'e,d_t} = 0 \\ &\text{subject to} \quad \beta \hat{\mathbf{e}}_{n+1}^{d_c} \cdot \left[\left(\mathbf{r}_{n+1}^{d_c} + \beta \tilde{L}_{m+1}^{'e,d_t} \cdot \hat{\mathbf{e}}_{n+1}^{d_c}\right) - \mathbf{r}_m^{d_t}\right] > 0 \end{aligned} \tag{4.24}$$

where

$$\beta = \begin{cases} -1, & \text{Node } m+1 \in S_{d_t,d_c}^F \\ 1, & \text{Node } m+1 \in S_{d_t,d_c}^A \end{cases} \tag{4.25}$$

Applying Algorithm 3 to the mapping of fine-element nodes in d_t to a coarse segment of d_c will lead to the creation of alternating line segments of zero and high curvature. This is because blocks of fine elements in d_t will be aligned with a coarse element in d_c. Since the element unit direction vectors of these elements are equal, the line curvature will be zero. Using node $j-1$ in Figures 4.7 as an example, the curvature at node $j-1$ is given by,

$$\kappa_{j-1} = \left.\frac{\mathrm{d}T}{\mathrm{d}s}\right|_{s_{j-1}} \approx \frac{2\,|\hat{\mathbf{e}}_{j-1} - \hat{\mathbf{e}}_{j-2}|}{L_{j-1}^{'e} + L_{j-2}^{'e}} \tag{4.26}$$

At the interface of adjacent coarse elements in d_c, there may be an abrupt change of the element unit direction vectors. Hence, for the nodes in d_t that are mapped to locations close to the element interfaces in d_c, the changes in the element direction unit vectors are large relative to the fine element lengths in d_t, leading to localised

high line curvature, which is undesirable because it leads to large resultant nodal tension forces on affected nodes.

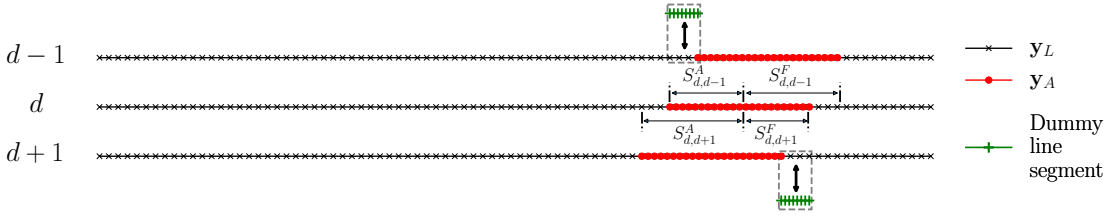

Figure 4.9: Specification and insertion of dummy fine-element line segments into d_c to replace selected coarse segments.

To ameliorate the tendency of Algorithm 3 to generate zones of high line curvature due to the transition from d_c to d_t, a dummy line segment consisting of fine-elements is generated to supplant the coarse segment in d_c for the purpose of providing a smoothened line geometry in d_c for the application of Algorithm 3 to determine the nodal positions in d_t. Figure 4.9 shows the location of along the line where the dummy segment will be inserted, replacing the original coarse elements, for the mapping from discretisation $d-1$ and $d+1$ to d. The spatial extent of the dummy segment is denoted as S^D and, for the mapping of $d-1$ to d, begins at the start of the $S^A_{d,d-1}$ zone to the start of the fine element segment in d, while that for the mapping of $d+1$ to d is from the end of the fine-element segment in d_c to the end of the $S^F_{d,d+1}$ segment. The element lengths in the dummy segment are set to be equivalent to the length of the fine elements in d_c.

The nodal positions in S^D are calculated using the spline interpolation method presented in Equations (4.20a) and (4.20b), where the boundary conditions are the positions of the nodes in the original line that are within the same s-coordinate span of S^D, and applied at $s_j^{d_c}$ and $s_{j+1}^{d_c}$, to determine the position interpolation coefficients for each node at the s-coordinate, s_i^*. The positions of the dummy nodes, $\mathbf{r}^*(s_i^*)$, are then calculated using Equation (4.27), where $s_j^{d_c} \leq s_i^* \leq s_{j+1}^{d_c}$. The interpolated nodal positions in S^D replace the original coarse-segment nodal positions in d_c, $\mathbf{r}^{d_c}$, in Algorithm 3 to determine the mapped nodal positions in d_t, $\mathbf{r}^{d_t}$. The element strains in S^D are not explicitly specified or used in other calculations.

$$\mathbf{r}^*(s_i^*) = \mathbf{c}_0 + \mathbf{c}_1\left(s_i^* - s_j^{d_c}\right) + \mathbf{c}_2\left(s_i^* - s_j^{d_c}\right)^2 + \mathbf{c}_3\left(s_i^* - s_j^{d_c}\right)^2\left(s_i^* - s_{j+1}^{d_c}\right) \tag{4.27}$$

where $\mathbf{c}_0$, $\mathbf{c}_1$, $\mathbf{c}_2$ and $\mathbf{c}_3$ are three-element coefficient vectors, i.e. $c_{i,l}$, $i \in [0,3]$, $l \in [1,3]$, where the index l corresponds to a direction in the Cartesian coordinate system.

4.2.4 Curvature correction

A curvature control procedure is implemented to augment the fine-element dummy line segment geometry in reducing occurrences of curvature spikes during the transition from d_c to d_t. The line curvature at the nodes in d_c, κ^{d_c}, provides a comparison baseline for the curvature in d_t as the nodal positions are prescribed. Linear interpolation is then used to obtain the desired curvature at the s-coordinates in d_t, $\tilde{\kappa}^{d_t}$, as given by,

$$\tilde{\kappa}_m^{d_t} = \kappa_j^{d_c} + \frac{s_m^{d_t} - s_j^{d_c}}{s_{j+1}^{d_c} - s_j^{d_c}}\left[\kappa_{j+1}^{d_c} - \kappa_j^{d_c}\right] \tag{4.28}$$

where the $s_j^{d_c} \leq s_m^{d_t} \leq s_{j+1}^{d_c}$. The κ adjustment procedure is active for the line segment in the span S^D in d_t, and is executed for the nodes in this segment at the end of Algorithm 3. The procedure begins by checking the line curvature at node m in d_t, $\kappa_m^{d_t}$, if the position of the node to be determined is $m+1$. The exceedance of the curvature at node m, $\kappa_m^{d_t}$, beyond $\tilde{\kappa}_m^{d_t}$ is given by,

$$\delta\kappa = \kappa_m^{d_t} - \tilde{\kappa}_m^{d_t} \tag{4.29}$$

The conditions that are evaluated and must be met for the curvature correction procedure to be performed are given by,

$$\kappa_m^{d_t} > \kappa_{min} \tag{4.30a}$$

$$\delta\kappa > \delta\kappa_{max} \tag{4.30b}$$

In this work, κ_{min} and $\delta\kappa_{max}$ are set to 1×10^{-3} and $\tilde{\kappa}_m^{d_t}$ respectively. A lower curvature limit, κ_{min}, is set because points of low curvature do not create the problem of unbalanced resultant tension forces. The value for $\delta\kappa_{max}$ is set such that the correction is performed when the curvature in the target discretisation exceeds double of the curvature in the previous discretisation. From the numerical experiments performed in this work, the aforementioned values for κ_{min} and $\delta\kappa_{max}$ are suitable.

The position of node $m+1$ was previously prescribed per Algorithm 3 prior to the curvature check. If curvature correction at node m is required, the position of node $m+1$ is then adjusted. This is accomplished by rotating the element direction unit vector $\hat{\mathbf{e}}_{m+1}^{d_t}$ about the binormal vector, $\widehat{\mathbf{B}}$, as shown in Figure 4.10, thereby modifying the position of node $m+1$ in d_t. The calculation of the unit binormal vector at node m, $\widehat{\mathbf{B}}_m$, requires the unit normal vector, $\widehat{\mathbf{N}}_m$, which was determined as part of obtaining the line curvature, and unit tangent vector, $\widehat{\mathbf{T}}_m$.

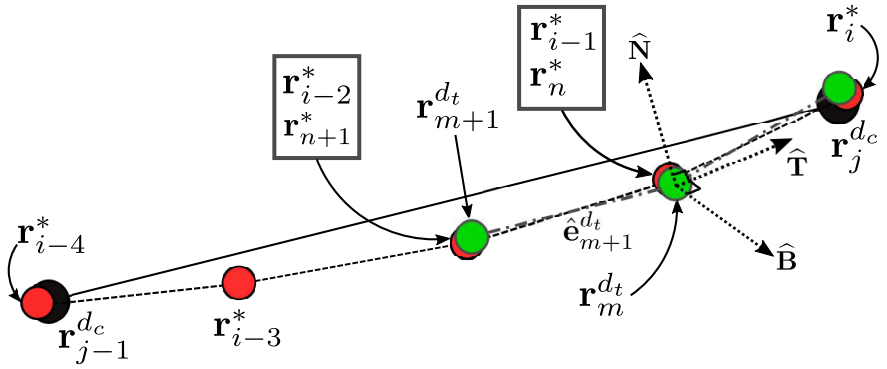

Figure 4.10: Nodal position mapping with dummy line segment replacement of coarse elements and curvature correction.

The unit direction vectors $\widehat{\mathbf{N}}_m$, $\widehat{\mathbf{T}}_m$, and binormal vector $\widehat{\mathbf{B}}_m$, are calculated as presented in Equations 4.31, 4.32 and 4.33, respectively.

$$\widehat{\mathbf{N}}_m = \frac{1}{\kappa_m^{d_t}} \left[\frac{2\left(\hat{\mathbf{e}}_m - \hat{\mathbf{e}}_{m+1}\right)}{L_m'^e + L_{m+1}'^e} \right] \tag{4.31}$$

$$\widehat{\mathbf{T}}_m = \frac{\left(L_{m+1}'^e \hat{\mathbf{e}}_m + L_m'^e \hat{\mathbf{e}}_{m+1}\right)}{\left|L_{m+1}'^e \hat{\mathbf{e}}_m + L_m'^e \hat{\mathbf{e}}_{m+1}\right|} \tag{4.32}$$

$$\widehat{\mathbf{B}}_m = \widehat{\mathbf{T}}_m \times \widehat{\mathbf{N}}_m \tag{4.33}$$

$$\mathbf{R}(\theta) = \begin{bmatrix} \cos\theta + \mathrm{B}_{m,1}^2\,(1-\cos\theta) & \mathrm{B}_{m,1}\mathrm{B}_{m,2}\,(1-\cos\theta) - \mathrm{B}_{m,3}\sin\theta & \mathrm{B}_{m,1}\mathrm{B}_{m,3}\,(1-\cos\theta) + \mathrm{B}_{m,2}\sin\theta \\ \mathrm{B}_{m,1}\mathrm{B}_{m,2}\,(1-\cos\theta) + \mathrm{B}_{m,3}\sin\theta & \cos\theta + \mathrm{B}_{m,2}^2\,(1-\cos\theta) & \mathrm{B}_{m,2}\mathrm{B}_{m,3}\,(1-\cos\theta) - \mathrm{B}_{m,1}\sin\theta \\ \mathrm{B}_{m,1}\mathrm{B}_{m,3}\,(1-\cos\theta) - \mathrm{B}_{m,2}\sin\theta & \mathrm{B}_{m,2}\mathrm{B}_{m,3}\,(1-\cos\theta) + \mathrm{B}_{m,1}\sin\theta & \cos\theta + \mathrm{B}_{m,3}^2\,(1-\cos\theta) \end{bmatrix} \tag{4.34}$$

The rotation matrix used to modify the direction unit vector of element $m+1$ by an angle θ requires the input of the elements in $\widehat{\mathbf{B}}_m$, and is given by Equation 4.34, where $B_{m,l}$, $l \in [1,3]$ are the elements in $\widehat{\mathbf{B}}_m$. The rotation matrix $\mathbf{R}(\theta)$ is multiplied with $\hat{\mathbf{e}}_{m+1}$ to obtain $\hat{\mathbf{e}}'_{m+1}$, the rotated direction unit vector of element $m+1$,

$$\hat{\mathbf{e}}'_{m+1} = \mathbf{R}(\theta)\,\hat{\mathbf{e}}_{m+1} \tag{4.35}$$

An objective function for minimizing the magnitude difference between the pre- and post-mapping line curvature for elements in S^D is written as,

$$\text{minimize} \qquad f(\theta) = |\kappa'_m(\theta) - \kappa_m| \tag{4.36}$$

where $\kappa'_{m+1}(\theta)$ is obtained from inserting the value for θ into Equation 4.35 to calculate an updated $\hat{\mathbf{e}}'_{m+1}$ and substituting the latter into Equation 4.26 to obtain the curvature at Node m. The Nelder-Mead optimization scheme [126] implemented in Fortran 90 by Burkardt [150] is applied to the optimization problem stated in Equation 4.36. The final updated value for $\hat{\mathbf{e}}'_{m+1}$ then replaces the original $\hat{\mathbf{e}}_{m+1}$, and the position of node $m+1$ is updated as,

$$\mathbf{r}_{m+1}^{d_t} = \mathbf{r}_m^{d_t} + \beta L'^e_{m+1}\hat{\mathbf{e}}'_{m+1} \tag{4.37}$$

Figures 4.6a and 4.6b are examples of the mapped nodal positions from discretisations $d+1$ and $d-1$, and highlight the S^D zones in $S^A_{d_t,d_c}$ and $S^F_{d_t,d_c}$, respectively. The element bounded by the last two nodes in the nodal mapping procedure of the $S^F_{d_t,d_c}$ and $S^A_{d_t,d_c}$ zones is at the midpoint of the S_{d_t,d_c} region.

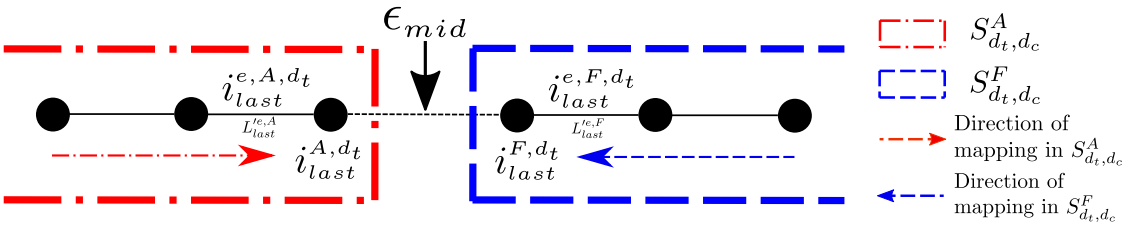

Figure 4.11: Illustration of directions of nodal position mapping and last nodes to be mapped in $S^F_{d_t,d_c}$ and $S^A_{d_t,d_c}$.

for $S^{\xi}_{d,\eta} \in \{S^F_{d,\eta}, S^A_{d,\eta}\}$ **do**
  if S^D *is present in* $S^{\xi}_{d,\eta}$ **then**
    Generate dummy line segment for S^D in $S^{\xi}_{d,\eta}$ ▷ η is either $d+1$ or $d-1$;
    Calculate $\tilde{\kappa}_i^{d_t}$ at $s_i^{d_t}$ for node i, $i \in \{$*nodal indices in* $S^D\}$;
    for *node* $i \in [i_0^{\xi,d_t}$, *number of nodes in* $S^{\xi}_{d,\eta}]$ **do**
      if *node* i *is in* S^D *of* $S^{\xi}_{d,\eta}$ **then**
        Determine $\mathbf{r}_i$ with Algorithm 3;
        Calculate $\kappa_{i-1}^{d_t}$;
        if $\kappa_{i-1}^{d_t} - \tilde{\kappa}_{i-1}^{d_t} > \delta$ **then**
          Calculate θ and $\hat{\mathbf{e}}'_i$ using Equations 4.36 and 4.35 respectively;
          Correct $\mathbf{r}_i$ with Equation 4.37;
        else
          Determine $\mathbf{r}_i$ with Algorithm 3;
        end
      end
  else
    for *node* $i \in [i_0^{\xi,d_t}$, *number of nodes in* $S^{\xi}_{d,\eta}]$ **do**
      Determine $\mathbf{r}_i$ with Algorithm 3;
    end
end

Algorithm 4: Position search algorithm with curvature correction for nodes in S_{d_t,d_c}.

Figure 4.11 illustrates the directions of mapping in $S^F_{d_t,d_c}$ and $S^A_{d_t,d_c}$, and the last nodes to be mapped in both zones, i_{last}^{F,d_t} and i_{last}^{A,d_t} respectively, which are determined according to Algorithm 4, the complete nodal position search algorithm with curvature correction for the nodes in S^D.

The nodal mapping procedure starts from the outer boundaries of the S_{d_t,d_c} region at nodes i_0^{F,d_t} and i_0^{A,d_t} and proceeds inwards, as shown in Figure 4.6. The stretched lengths, $L_{last}^{\prime e,F}$ and $L_{last}^{\prime e,A}$, of the elements adjacent to the nodes, $i_{last}^{e,F}$ and $i_{last}^{e,A}$ respectively, and by extension the line strains (see Equations 4.22 and 4.23), are taken into consideration in the mapping procedure (Line 9 or 11 in Algorithm 3) but the strain in the midpoint element, denoted as ϵ_{mid} in Figure 4.11, is not considered the determination of the positions of nodes i_{last}^{F,d_t} and i_{last}^{A,d_t} in Algorithm 4. Hence, the post-mapping strain in the midpoint element in d_t, $\epsilon_{mid}^{d_t}$, with an s-coordinate s_{mid}, may differ significantly from that of d_c, $\epsilon_{mid}^{d_c}$, and result in large strain gradients which create tension shocks that propagate through the line.

4.2.5 Line midpoint strain correction

To reduce the effects of the tension shocks on the fairlead tension results, large spanwise gradients in the element strains have to be mitigated using a strain correction procedure with the main objective of preserving the accuracy of the fairlead tension result. After running the nodal position mapping procedure in Algorithm 4, the strain at the midpoint element of the new line geometry d_t is determined and compared to that at the same location in d_c.

The strain correction algorithm is executed if the disparity in the midpoint element strain magnitude exceeds a threshold value, $\delta\epsilon_{max}$, evaluated as,

$$\delta\epsilon_{mid} = \left|\epsilon_{mid}^{d_t} - \epsilon_{mid}^{d_c}\right| > \delta\epsilon_{max} \tag{4.38}$$

where $\epsilon_{mid}^{d_t}$ and $\epsilon_{mid}^{d_c}$ are the midpoint element strains in d_t and d_c respectively. The midpoint element length difference, $\left|\epsilon_{mid}^{d_t} - \epsilon_{mid}^{d_c}\right|$, is made up by scaling the lengths of the elements from the anchor up to the last element in S_{d_t,d_c}^{A}, adjacent to i_{last}^{A}, as shown in Figure 4.11. The strain in these elements will be modified as a result of the adjustment and hence will not be accurate for a period of time after a transition from d_c to d_t. This trade-off is made in order to avoid the production of significant spatial strain gradients and tension shocks so that the fairlead tension results remain accurate. The inaccuracies introduced in the correction are transient and diminish rapidly as the simulation progresses after a transition.

The augmentation lengths, $\mathrm{d}L_i'^e$, to be added to the stretched lengths of the elements from the anchor up to the midpoint are defined as,

$$\mathrm{d}L_i'^e = \alpha L_i^e \mathrm{d}\epsilon_{i,base}, \qquad i_{anchor}^{e,d_t} \leq i \leq i_{last}^{e,A,d_t} \tag{4.39}$$

where $i_{anchor}^{e,A,dt}$ and $i_{last}^{e,A,dt}$ are the indices of the element adjacent to the anchor node and the last element in S_{d_t,d_c}^A zone (see Figure 4.11), $\mathrm{d}\epsilon_{i,base}$ is the base strain adjustment to element i, and α is a scaling factor. The sign of α, and correspondingly $\mathrm{d}L_i'^e$, can be positive or negative and corresponds to the elongation and shortening of element lengths respectively.

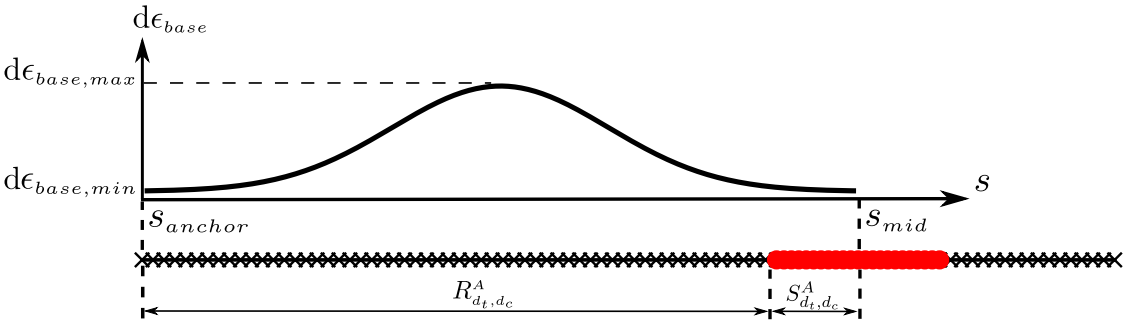

Figure 4.12: Strain modification distribution profile, $\mathrm{d}\epsilon$, in the line span from the anchor location, s_{anchor}, to the line midpoint, s_{mid}.

The base strain adjustment profile for the elements affected by the length augmentation defines the distribution of the length modification magnitude for the selected elements from s_{anchor} to s_{mid} and is presently set to follow a Gaussian profile, as depicted in Figure 4.12. The shape of the Gaussian profile is defined by the parameters μ and σ, as expressed in Equation 4.40,

$$\mathrm{d}\epsilon_{base}(s) = \frac{1}{\sqrt{2\pi}\sigma} \exp\left[-\frac{(s-\mu)^2}{2\sigma^2}\right] \tag{4.40}$$

where μ is set to $(s_{mid} + s_{anchor})/2$, and σ is determined by setting a value for the ratio between $\mathrm{d}\epsilon_{base}(\mu)$ and $\mathrm{d}\epsilon_{base}(s_{anchor})$ and solving Equation 4.41 for σ,

$$\frac{\mathrm{d}\epsilon_{base}(\mu)}{\mathrm{d}\epsilon_{base}(s_{anchor})} = \frac{\mathrm{d}\epsilon_{base,max}}{\mathrm{d}\epsilon_{base,min}} = \frac{1}{\exp\left[-\frac{1}{2}\left(\frac{\mu}{\sigma}\right)^2\right]} \tag{4.41}$$

For each discretisation,the value for μ varies with s_{mid}, and the ratio $\mathrm{d}\epsilon_{base,max}/\mathrm{d}\epsilon_{base,min}$ is set to 5. This value affects the distribution of element augmentation lengths. A high value concentrates the distribution of the augmentation lengths to a smaller number of element and increases in the strain gradients in the vicinity of $s = \mu$, while a low value may lead to a high strain gradient at s_{mid}. The numerical experiments in this work suggest that a value of 5 is suitable. The base augmentation lengths can then be determined from Equation 4.40 by inserting the s-coordinates for the center of the selected elements i, $i^e_{anchor} \leq i \leq i^{e,A}_{last}$, for each discretisation. By setting a value for α, the augmented element lengths are then calculated as,

$$L'^e_i = L'^e_{i,orig} + \alpha L^e_i \mathrm{d}\epsilon_{i,base} \tag{4.42}$$

where $L'^e_{i,orig}$ refers to the stretched lengths of the elements prior to augmentation.

The nodal mapping procedure, Algorithm 4, is executed with the updated element lengths for the line span represented as $R^A_{dt,dc}$ and $S^A_{dt,dc}$ in Figure 4.12. After the mapping is performed, the strain at the midpoint element is evaluated again with the midpoint element strain exceedance criteria, Equation 4.38. Hence, the value of α determines if the exceedance critera is met. The procedure is summarised in Algorithm 5.

1 Set a value for α;
2 Calculate augmentation lengths $\mathrm{d}L'^e_i$ with Equation 4.39;
3 Calculate augmented element lengths L'^e_i with Equation 4.42;
4 Execute Algorithm 4 with $S^\xi_{d,\eta} \in \{R^A_{d,\eta}, S^A_{d,\eta}\}$ where $R^A_{d,\eta}$ refers to the line section that extends from the anchor to the start of the $S^A_{d,\eta}$ section as shown in Figure 4.12;
5 Evaluate $\delta\epsilon_{mid}$, the midpoint element strain exceedance magnitude;

Algorithm 5: Nodal position re-mapping with augmented elements.

The Nelder-Mead [126] optimization procedure is used in conjunction with Algorithm 5 to determine the value of α that minimizes $\left|\epsilon^{d_t}_{mid} - \epsilon^{d_c}_{mid}\right|$ during each discretisation transition. The initial value for α, α_0, to be optimized by the Nelder-Mead algorithm, is given by,

$$\alpha_0 = \frac{L^e_{mid}\,\delta\epsilon_{mid}}{\sum_{i=1}^{i^{e,A}_{last}} L^e_i \mathrm{d}\epsilon_{i,base}} \tag{4.43}$$

where L^e_{mid} is the unstretched length of the midpoint element.

4.3 Numerical model settings and test cases

4.3.1 Environmental conditions and line structural properties

A set of test cases in a shallow water environment selected from Brown and Mavrakos [5] are used for the evaluation of the proposed time integration and discretisation adaptation strategy. The fairlead position and velocity prescribed in the test cases are the boundary conditions and are described by the functions presented in Equation (B.1) and Equation (B.2).

The parameters for the fairlead excitations are test Cases 1, 3 and 4 specified in Table B.2 and include harmonic and biharmonic fairlead excitations sufficient to induce significant line liftoff and grounding. Comparisons will be made between the in-house code and the commercial software Orcaflex [151], and the seabed parameters for the in-house code is the SM coefficient set presented in Table C.2 while those for Orcaflex are the shallow water coefficient set presented in Table C.1.

The water depth is 82.5 m, and no current or wave velocities are prescribed. The mooring line material consists of homogeneous chain-links along its entire length and the structural parameters are presented in Table A.1.

4.3.2 Dual-rate integration settings, prepared discretisations and switching s-coordinates

The prepared discretisations to exercise the mapping algorithm proposed in Section 4.2 and the Multi-Rate time integration scheme described in Section 4.1 are presented in Figure 4.13. The segments designated as $\mathbf{y}_A$ refer to the fine-element segment and the active partition in each discretisation, while the segments designated as $\mathbf{y}_L$ are the coarse-element segment and latent partition in the respective discretisation.

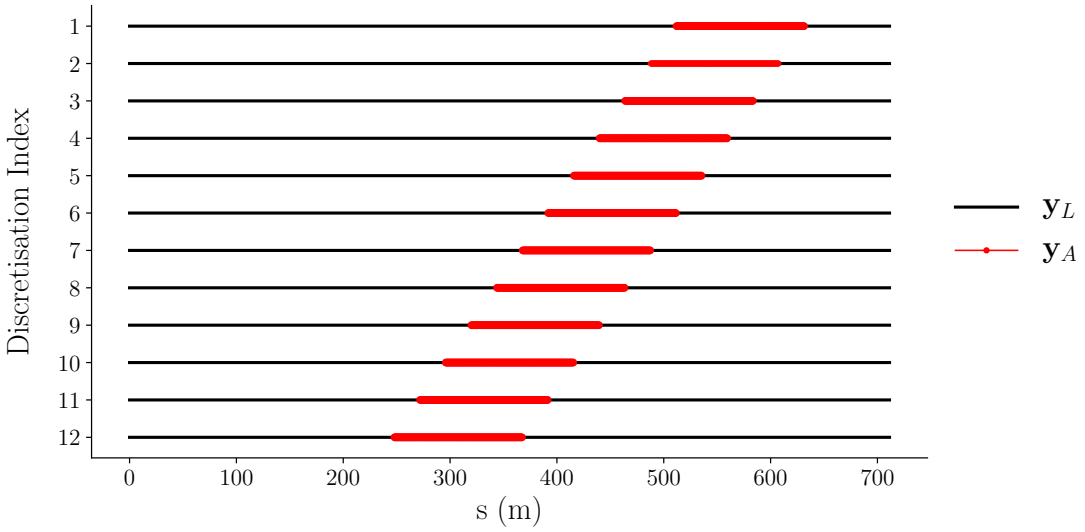

Figure 4.13: Prepared discretisations for switching.

Discretisation Index	s_l	s_u
1	$s_{TDP,0} + 24.0$ m	-
2	$s_{TDP,0}$	$s_{TDP,0} + 48.0$ m
3	$s_{TDP,0} - 24.0$ m	$s_{TDP,0} + 24.0$ m
4	$s_{TDP,0} - 48.0$ m	$s_{TDP,0}$
5	$s_{TDP,0} - 72.0$ m	$s_{TDP,0} - 24.0$ m
6	$s_{TDP,0} - 96.0$ m	$s_{TDP,0} - 48.0$ m
7	$s_{TDP,0} - 120.0$ m	$s_{TDP,0} - 72.0$ m
8	$s_{TDP,0} - 144.0$ m	$s_{TDP,0} - 96.0$ m
9	$s_{TDP,0} - 168.0$ m	$s_{TDP,0} - 120.0$ m
10	$s_{TDP,0} - 192.0$ m	$s_{TDP,0} - 144.0$ m
11	$s_{TDP,0} - 216.0$ m	$s_{TDP,0} - 168.0$ m
12	-	$s_{TDP,0} - 192.0$ m

Table 4.1: Discretisation switching s-coordinates.

The element sizes used in dual-rate integration are 8.0 m and 0.751 m in the coarse and fine-element sections respectively. The suitability of the element sizes is examined in Section 4.4.1. Due to stability limits of the Modified Euler time integration scheme and the need for temporal synchronization between the latent and active partitions, the time-step ratio between the partitions is 10, when the

value for the partition maximum and minimum time-step fraction constraints, γ_{max} and γ_{min}, are set to 0.95 and 0.1 in this work.

The length span of $\mathbf{y}_A$ in each discretisation is 119.3 m, and is staggered in their locations along the s-coordinate by 24 m between two adjacent discretisations. With the initial touchdown point s-coordinate denoted as $s_{TDP,0}$, the discretisation switching s-coordinates (see Algorithm 2) are determined at the start of each test case and presented in Table 4.1.

4.4 Evaluation of fairlead tension results

4.4.1 Case 1: harmonic surge motion

Test case 1 prescribes a harmonic fairlead excitation at wave frequency (see Table B.2). The maximum fairlead velocity and displacement from the original position are 3.4 m/s and 5.4 m respectively, which induces a nodal grounding velocity of approximately 3.2 m/s [152]. Figure 4.14 shows the s-coordinate variation tracked by 7 homogeneous line discretisations with element sizes ranging from 11.86 m to 0.60 m, and a hybrid coarse/fine discretisation corresponding to that presented in Figure 4.13. The hybrid discretisation consists of a refined region close to the touchdown zone and coarse elements elsewhere. Due to the initial line geometry at $t = 0$ s, the initial discretisation is set to d_3 as shown in Figure 4.13. As the touchdown point changes, the selected discretisation changes in tandem. The fairlead excitation profile for Case 1, with a maximum displacement of the fairlead position by 5.4 m, induces the touchdown point s-coordinate, s_{TDP}, to vary between approximately 505 m and 565 m over one period of fairlead excitation between 81 s and 91 s of simulation time, as shown in Figure 4.14, after initial transient effects have passed and line motion and forces are fully developed. Presently, s_{TDP} is tracked to first order accuracy equivalent to the s-coordinate of the node furthest along the s-axis that is in contact with the seabed. As the nodal density is increased, s_{TDP} is tracked to the higher accuracy with the homogeneous discretisation lines, and similarly in the hybrid coarse/fine discretisation line because of the high density of nodes locally around the touchdown zone.

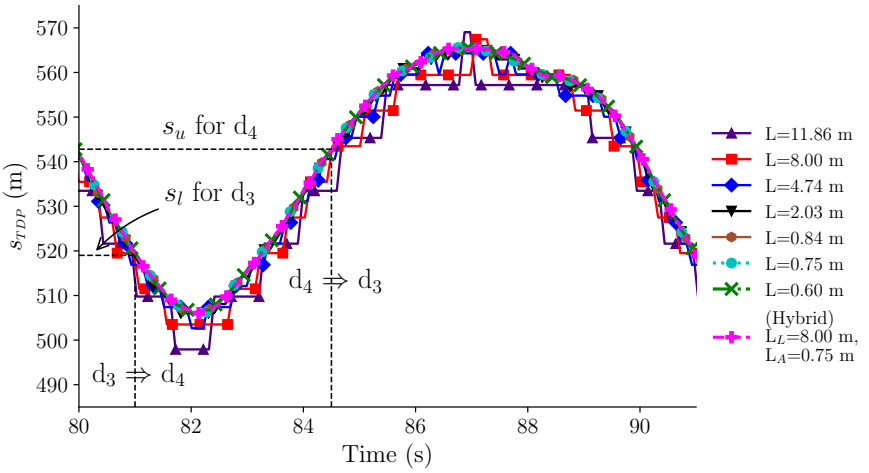

Figure 4.14: Touchdown point variation over one period of fairlead excitation for Case 1.

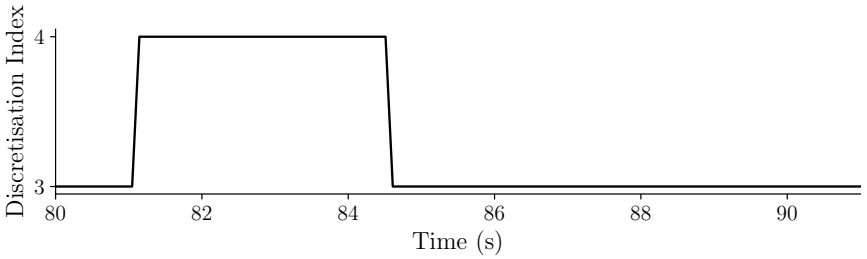

Figure 4.15: Discretisation switches for Case 1.

The variation in the touchdown point over 60 m induces the adaptive discretisation line to switch between discretisations 3 and 4, as presented in Figure 4.15. Over the time period shown, a switch from discretisation 3 to 4 was made at 81.0 s and another from 4 back to 3 was made at 84.5 s. The $s_{TDP,0}$ is 542.8 m, hence according to Table 4.1 and depicted in Figure 4.14, the switching s-coordinate from discretisation 3 to 4, s_l for d_3, was 518.8 m, while the switching s-coordinate from discretisation 4 to 3, s_u for d_4, was 542.8 m.

Figures 4.16a and 4.16b show the strain distributions in a line prior to the discretisation transition, as well as the strain distributions before and after performing the strain correction at 81.0 s and 84.5 s respectively. In Figure 4.16a, which depicts the case where $\delta\epsilon_{mid} < 0$ prior to correction, a spike in the strain curve is present at approximately s=500.0 m because the initial nodal position mapping using Algorithm 4 does not consider the strain in the midpoint element. The correction applied in this situation is to prescribe a negative value for α, and apply a negative

adjustment to the lengths, and consequently the strains, of the elements in the $R^A_{d_t,d_c}$ and $S^A_{d_t,d_c}$ regions of d_t with the Gaussian-shaped strain modification profile presented in Figure 4.12. The reduction of the element strains is observable in the post-correction strain curve, essentially introducing an error of the magnitude $\alpha \mathrm{d}\epsilon_{i,base}$. Figure 4.16b shows a contrary situation where $\delta\epsilon_{mid} > 0$ at approximately at 84.5 s and s=525.0 m, a positive value is prescribed for α, in which a positive adjustment is required for the lengths of the elements in the $R^A_{d_t,d_c}$ and $S^A_{d_t,d_c}$ regions of d_t. The maximum error introduced into the strain occurs at $s = \mu$ of the post-transition active discretisation, with the magnitude $\alpha/(\sigma\sqrt{2\pi})$, which corresponds to 0.9% and 2.65% respectively for the switches from discretisation 3 to 4 at 81.0 s and 4 back to 3 at 84.5 s.

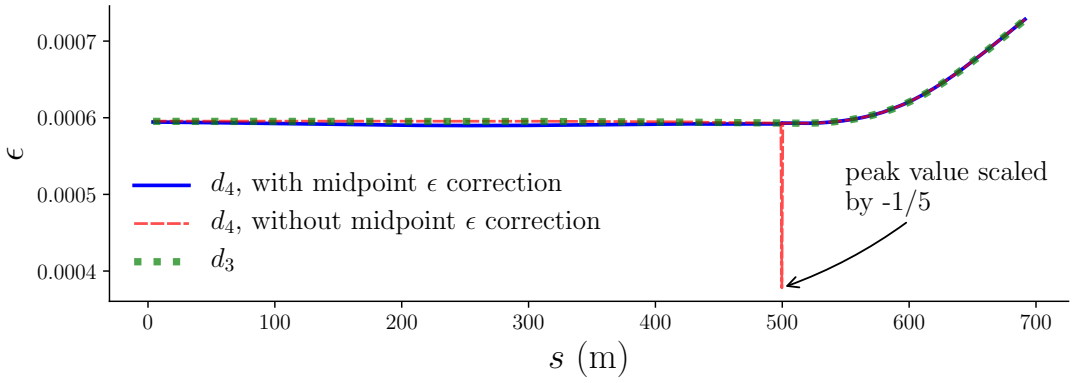

(a) Pre- and post-nodal position mapping strain distributions with and without midpoint strain correction for Case 1 at 81.0 s.

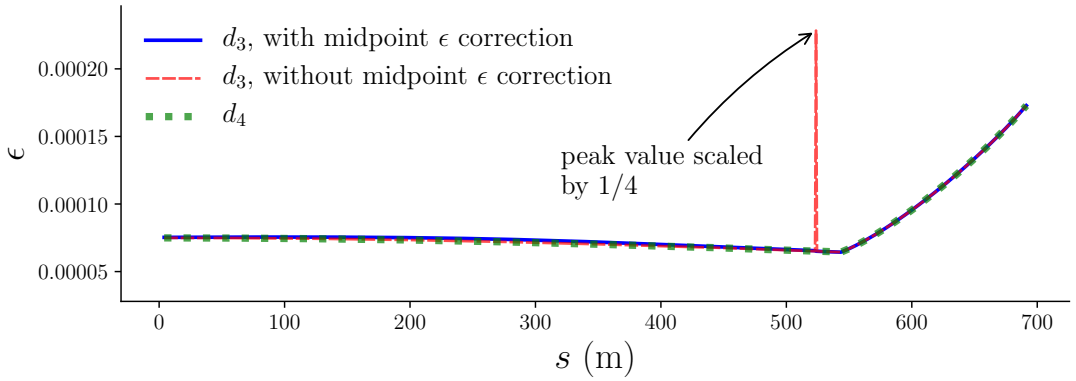

(b) Pre- and post-nodal position mapping strain distributions with and without midpoint strain correction for Case 1 at 84.5 s.

Figure 4.16: Pre- and post-nodal position mapping strain distributions, switching between discretisations 3 and 4, with and without midpoint strain correction for Case 1.

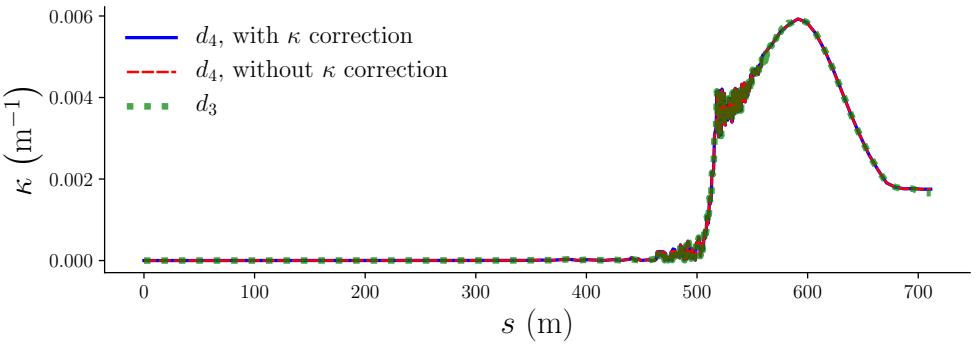

(a) Pre- and post-nodal position mapping curvature distributions with and without curvature correction for Case 1 at 81.0 s.

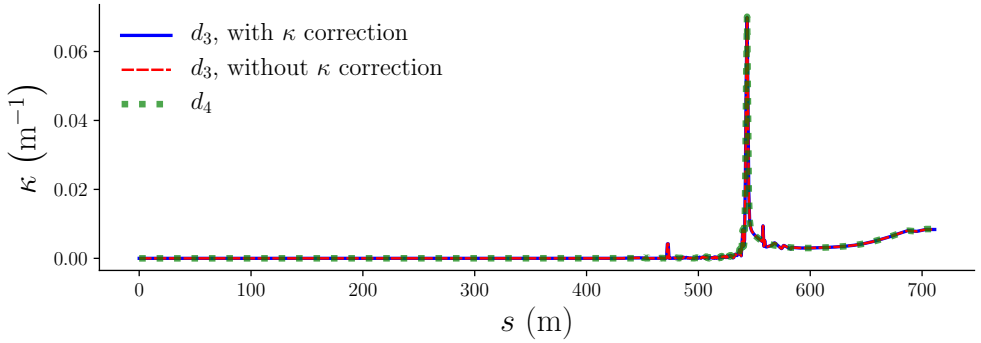

(b) Pre- and post-nodal position mapping curvature distributions with and without curvature correction for Case 1 at 84.5 s.

Figure 4.17: Pre- and post-nodal position mapping curvature distributions, switching between discretisations 3 and 4, with and without curvature correction for Case 1.

Figures 4.17a and 4.17b present the pre- and post-mapping curvature distributions with the curvature correction feature active and inactive at the discretisation transitions at 81.0 s and 84.5 s. The curvature profiles with and without correction are identical because the curvature exceedance condition (Equations 4.30a and Equation (4.30b)) were not met during the transitions in Case 1.

The fairlead tension time histories from the in-house code with the seven homogeneous and single hybrid coarse/fine size discretisations, and the frequency spectra of the same tension time histories, are presented in Figures 4.18a and 4.18b respectively. Irregular oscillations are observed in the tension time histories between 83.5 s and 87 s for the homogeneous discretisation of element lengths ranging from 11.86 m to 2.03 m.

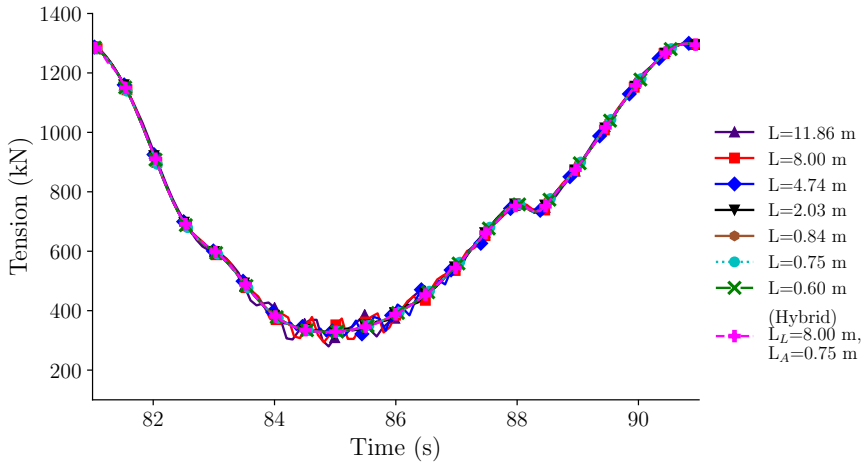

(a) Fairlead tension time history for Case 1 from in-house code.

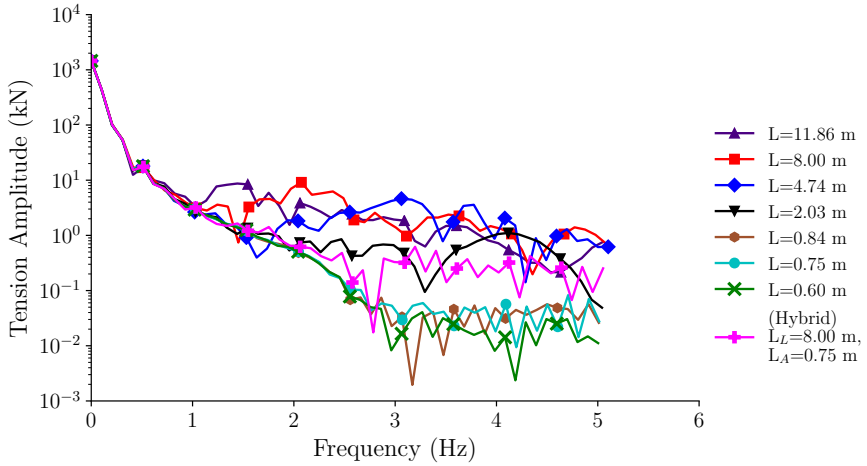

(b) Fairlead tension frequency spectra for Case 1 from in-house code.

Figure 4.18: Fairlead tension time history and frequency spectra for Case 1 from in-house code with homogeneous and hybrid coarse/fine line discretisations.

The frequency spectra presented in Figure 4.18b indicates that at frequencies of approximately 1 Hz and below, the magnitudes of the frequency components of the tension time series with varying element sizes are in good mutual agreement. However, the frequency spectra of the various time histories begin to diverge at frequencies above 1 Hz, above which the frequency components in the time histories associated with element sizes of 0.84 m and smaller are lower than those present in the time series generated with larger element sizes.

Figures 4.19a and 4.19b present the tension time histories and frequency spectra of the tension for Case 1, using the commercial software Orcaflex, for the range of homogeneous line discretisations. The tension fluctuations associated with nodal

grounding there were observed in the results in the in-house code are also present in the results generated by Orcaflex. Similarly, the magnitudes of the fluctuations are also reduced as element sizes are reduced and are largely eliminated from the tension results for element sizes of 0.84 m or smaller. The results in Figures 4.18 and 4.19 suggest that reducing element sizes is an effective means of ameliorating the undesirable effects of nodal grounding on the tension results.

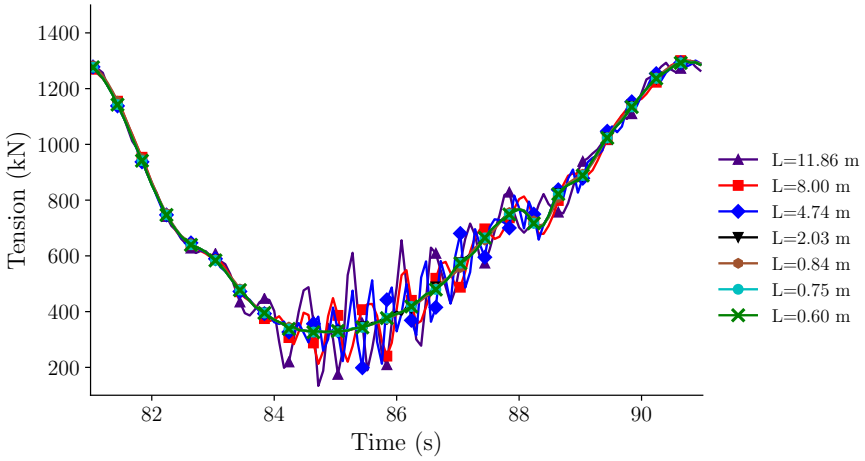

(a) Fairlead tension time history for Case 1 from Orcaflex.

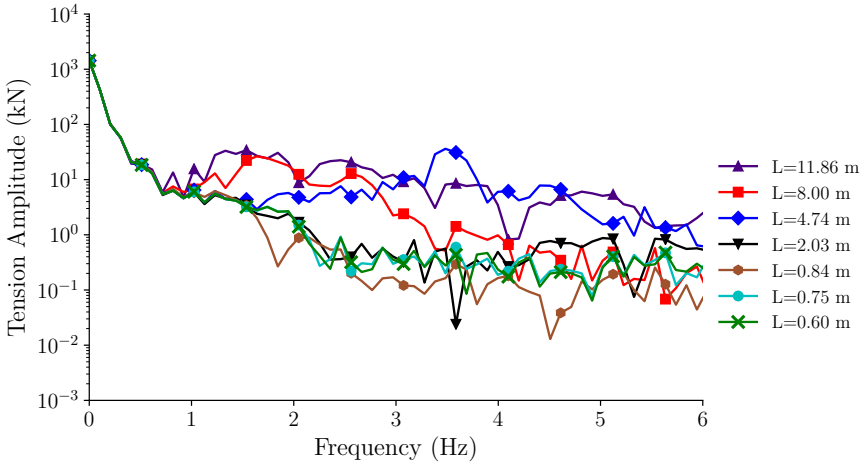

(b) Fairlead tension frequency spectra for Case 1 from Orcaflex.

Figure 4.19: Fairlead tension time history and frequency spectra for Case 1 from Orcaflex with homogeneous line discretisations.

The higher frequency components in the frequency spectra plots are associated with the tension fluctuations. Figures 4.18a and 4.19a show that periods of the tension fluctuations are typically lower than 0.5 s or higher than 2 Hz. A qualitative assessment of Figures 4.18a and 4.18b suggests that the tension fluctuations

are largely absent in the tension results for the discretisations of element lengths of 0.84 m or smaller. Figure 4.18b shows that the higher range frequency components above 2.5 Hz, is lowest for the results for the smallest element size of 0.6 m. However, the results for the 0.75 m element size are assessed to be sufficiently close to that of the finest discretisation used in this series of tests, thus is the required element refinement necessary to provide converged tension results when the intent is to remove the spurious tension fluctuations.

The tension time history for the hybrid coarse/fine size discretisation shows good agreement with the converged results, as shown in Figure 4.18a. The frequency spectra of the time series for this discretisation also reveals good agreement at frequencies lower than 2 Hz with the frequency spectra of the converged results given by the 0.75 m and 0.6 m element discretisations. The magnitudes of the frequency components above 2 Hz deviate from the converged results but are generally lower when compared with those of the coarser homogeneous discretisations.

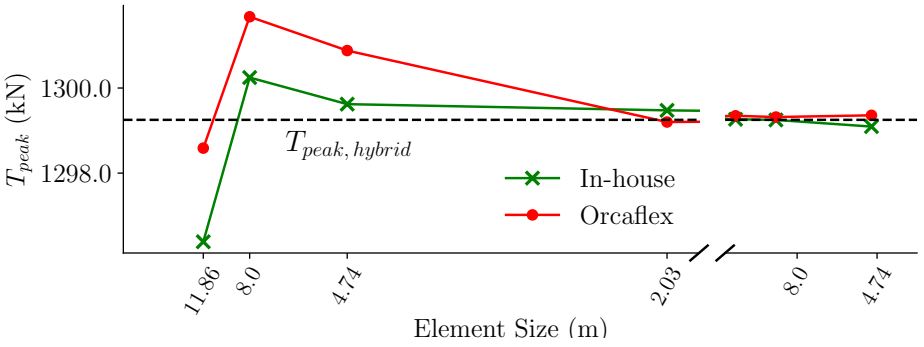

Figure 4.20: Peak tension values for Case 1 with homogeneous and hybrid coarse/fine discretisations.

The peak tensions for Case 1 using the various element sizes discussed are presented in Figure 4.20 for both Orcaflex and the in-house code, and show that as element size is reduced the peak tension converges to the value of approximately 1299.30 kN for both codes. The peak tension using the hybrid coarse/fine discretisation, at 1299.26 kN, is in good agreement with the converged peak tension results and is comparable to that provided by the 0.84 m and 0.75 m homogeneous line discretisations. Hence, in addition to providing converged peak tension results, the tension fluctuations are also significantly reduced using the hybrid coarse/fine discretisation. This suggests that the hybrid coarse/fine discretisation, with a higher nodal density in the vicinity of the touchdown zone and lower densities elsewhere

is able to mitigate the negative effects of nodal grounding, without refining the discretisation for the entire length of the line structure.

4.4.2 Case 3: biharmonic surge and heave motion

Test Case 3 prescribes a biharmonic fairlead excitation in the surge and heave directions. In Case 3, the maximum fairlead velocity and displacement from the initial position are 3.45 m/s and 20.71 m respectively, which induces a maximum nodal grounding velocity of 3.9 m/s [152], which is 21% larger than in Case 1, and thus represents a more severe test case.

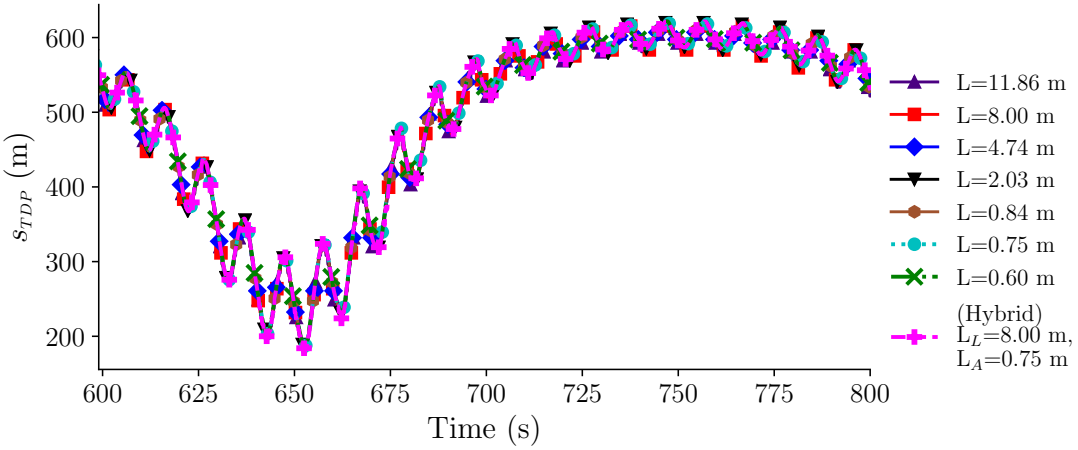

Figure 4.21: Touchdown point variation over one period of fairlead excitation for Case 3.

Figure 4.21 shows that the s_{TDP} variation range of the homogeneous and hybrid coarse/fine discretisations over one period of the fairlead motion for Case 3 is between approximately s =177 m and 622 m over one low-frequency fairlead excitation period between the time window of 600 s and 800 s. This variation in the touchdown point induced the adaptive, hybrid coarse/fine discretisation line, choosing from the prepared discretisations presented in Figure 4.13, to make a total of 52 discretisation switches within the time span of one low-frequency fairlead excitation period and to switch between all of the prepared discretisations from 1 through 12, as presented in Figure 4.22.

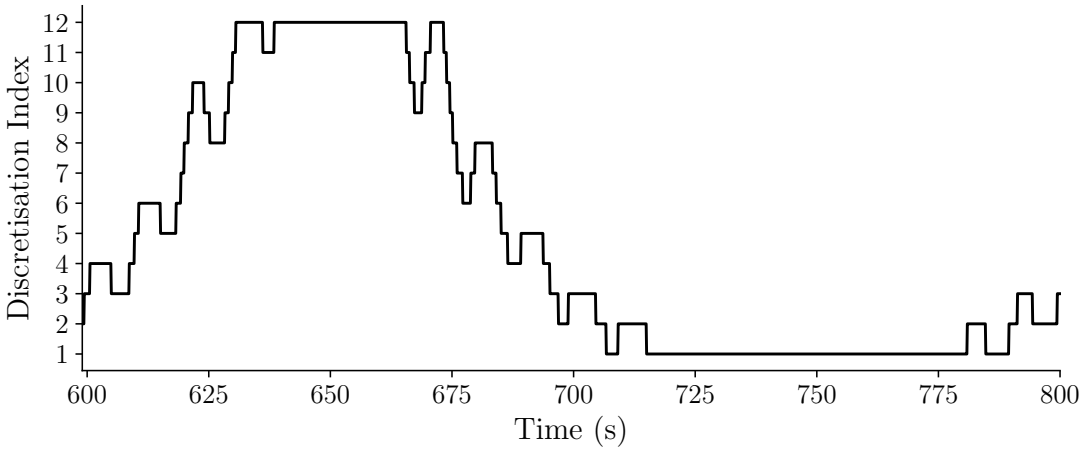

Figure 4.22: Discretisation switches for Case 3.

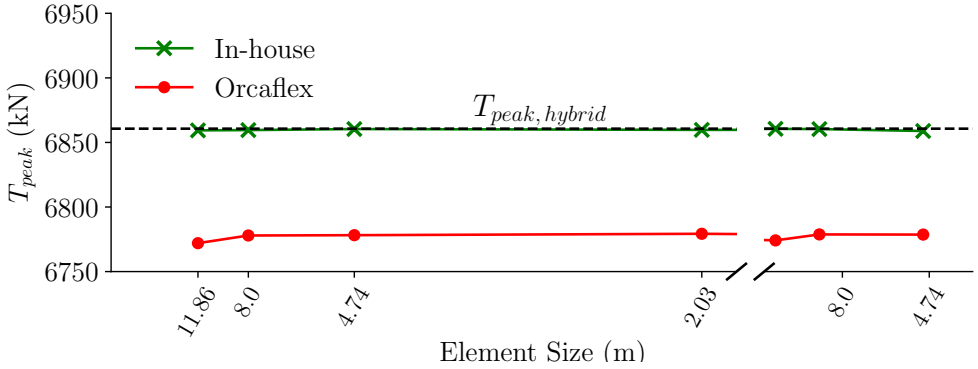

Figure 4.23: Peak tension values for Case 3 with homogeneous and hybrid coarse/fine discretisations.

Figure 4.23 shows the peak tensions, from Orcaflex and the in-house code, produced by the various discretisations. The peak tensions from the in-house code and Orcaflex reach convergence quickly as element sizes are reduced and the peak tension values do not change significantly with the application of smaller element sizes. The peak tension result by the hybrid coarse/fine discretisation is in close agreement with the converged tension magnitude.

Figure 4.24 shows the fairlead tension time series for Case 3 generated by the in-house code for the various discretisations. The time window revealed corresponds to one period of the low-frequency excitation. The results suggest that between 600 s and 674 s, the agreement between the various discretisation is very good, and the tension results are free of spurious fluctuations.

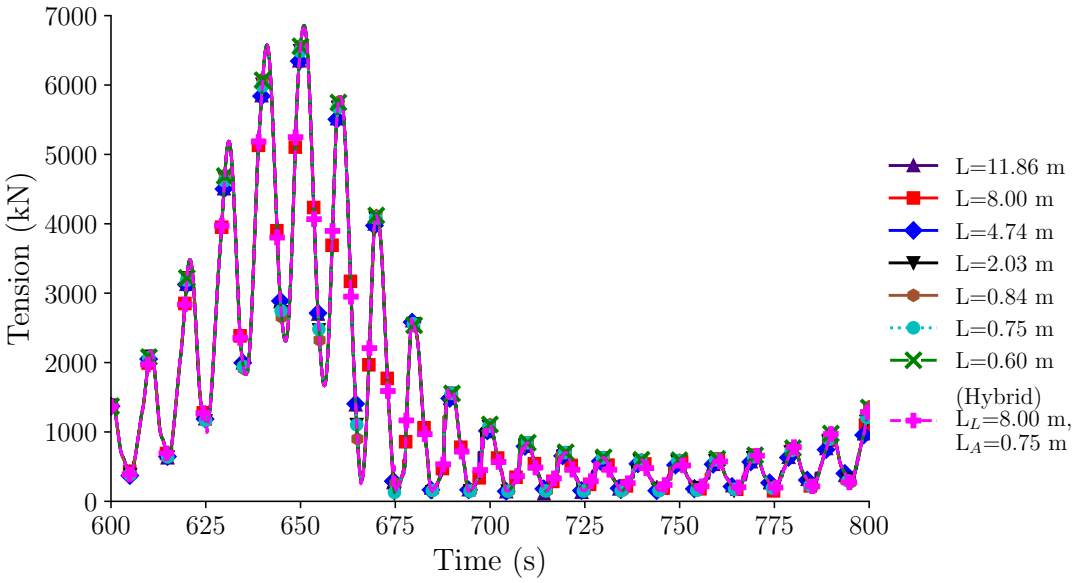

Figure 4.24: Fairlead tension time history for Case 3 from in-house code.

In contrast, between 674 s and 700 s, the results produced by the various discretisations differ in the severity of the irregular tension fluctuations, as presented in Figure 4.25. The fluctuations occur close to the troughs of the wave frequency tension loading/unloading cycle at 705 s, 715 s, 725 s, 735 s, 745 s, 765 s, 775 s, 785 s, and 795 s. Fluctuations also occur in some situations, during the loading phase as well at 707.5 s, 735.5 s, 727.5 s, 737.5 s, 747.5 s, 757.5 s, and 767.5 s. The fluctuations occurring at the troughs in Figure 4.25 are due to travelling tension waves that originate from the touchdown point due to the initial creation of local spatial strain gradients at the touchdown zone as grounding nodes make contact with the seabed at high speeds. The fluctuations that appear during the loading phase are snap loading shocks which occur due to the rapid transition of the strain state of line section at the touchdown zone from being in a negative strain, unloaded state due to nodal grounding to a positive strain and loaded state, as discussed in Ref. [152].

Figures 4.24 and 4.25 illustrate that as element sizes are reduced, the severity of the irregularities in the tension time series, which are generated by nodal grounding and liftoff, is reduced. Additionally, the results produced by the hybrid coarse/fine discretisation can qualitatively be assessed to contain less severe irregularities compared to the coarser discretisations of larger than 0.84 m, and are comparable to the results generated by the finer discretisations of 0.84 m, 0.75 m and 0.6 m.

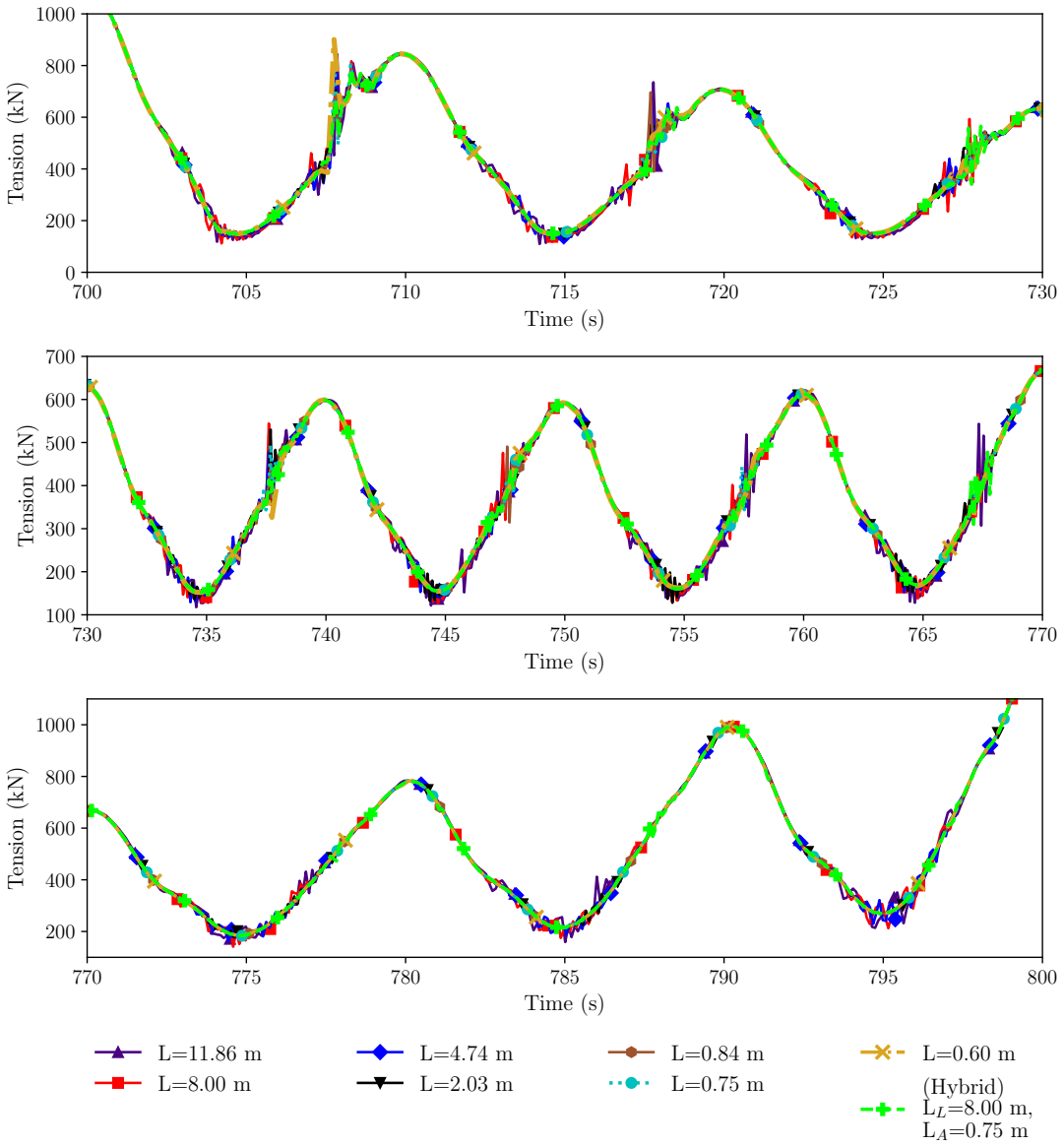

Figure 4.25: Close-up view of fairlead tension fluctuations due to nodal grounding in the time window 700 s $\leq t \leq$ 800 s for Case 3.

Due to the large and rapid line motions and shifts in the touchdown zone induced by the fairlead motions, the frequency and number of changes in the selected discretisation were relatively high compared to Case 1, as shown in Figure 4.22. The strain and curvature correction procedures were exercised frequently for this case, and Figure 4.26 provides an example of a discretisation switch, which occurs at 624 s, in which both correction procedures were active.

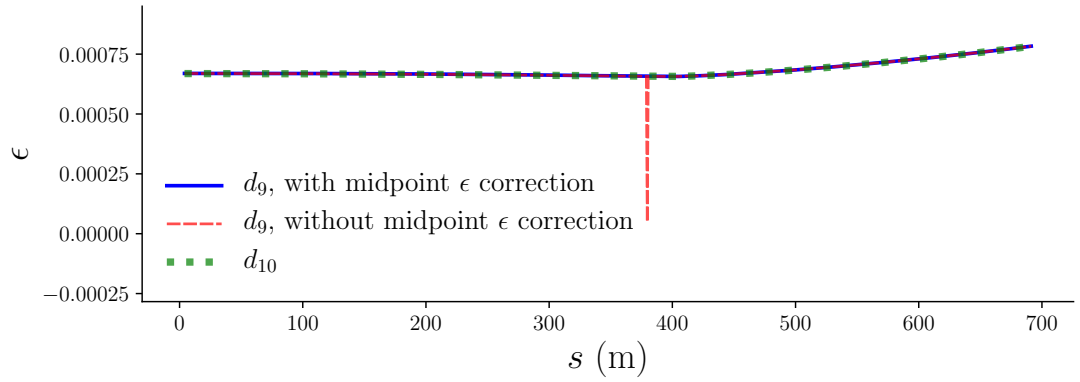

(a) Pre- and post-nodal position mapping strain distributions with and without midpoint strain correction for Case 3 at 624 s.

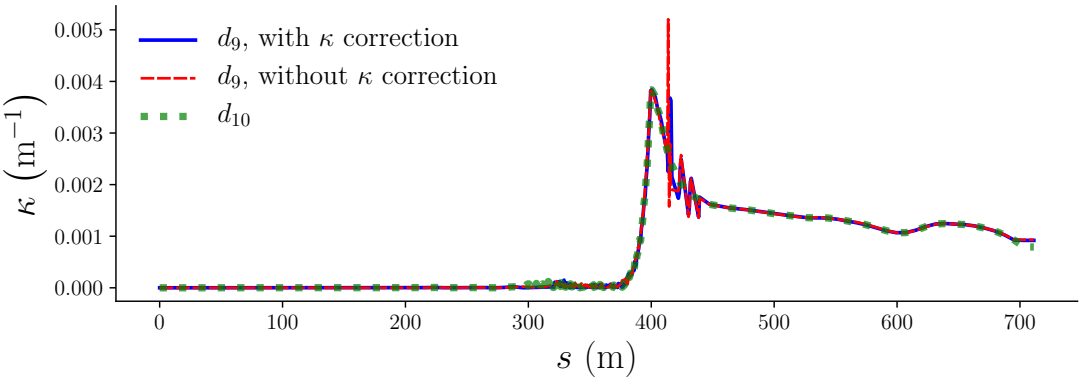

(b) Pre- and post-nodal position mapping curvature distributions with and without curvature correction for Case 3 at 624 s.

Figure 4.26: Pre- and post-nodal position mapping strain and curvature distributions, for Case 4 at 624 s, switching between discretisations 9 and 10.

Figure 4.26a illustrates that the prior to performing the strain correction, a large spike in the strain value was present at the midpoint element at $s = 380$ m, which creates a large local strain discontinuity. The strain value in the midpoint element of the target discretisation, #9, prior to and after strain correction were 5×10^{-5} and 6.5×10^{-4} respectively. Figure 4.26b shows the curvature profile of the line prior to and after curvature correction during the discretisation switch at 624 s, and illustrates that a spike in the curvature at $s = 413.8$ m was reduced from 5.25×10^{-3} to 3.69×10^{-3} m^{-1}.

4.4.3 Case 4: biharmonic surge motion

Case 4 prescribes a biharmonic fairlead excitation in the surge directions. The maximum fairlead velocity and displacement from the initial position are 5.65 m/s and 12.8 m respectively, which induces a maximum nodal grounding velocity of 3.9 m/s, comparable to that of Case 3.

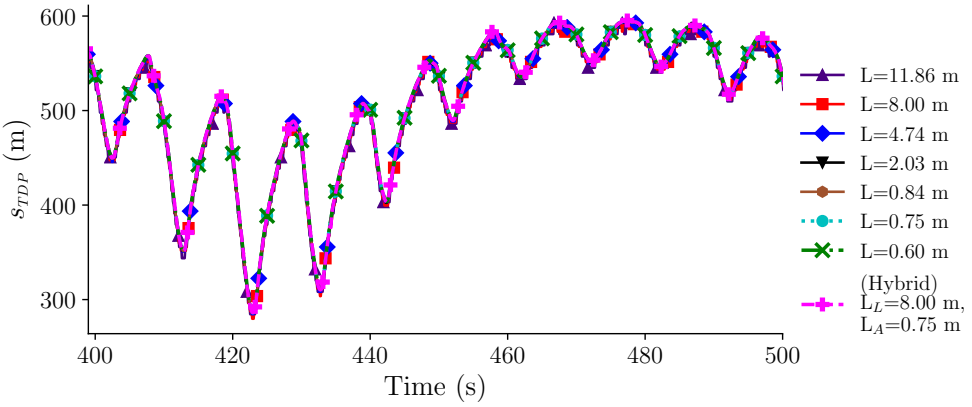

Figure 4.27: Touchdown point variation over one period of fairlead excitation for Case 4.

Figure 4.27 shows the variation s_{TDP} over one low-frequency oscillation period for Case 4. The time-varying touchdown point location tracked by the various discretisations are in close agreement, especially so for the finer homogeneous discretisation of 0.84 m and smaller and the hybrid coarse/fine discretisation, which is chosen from the prepared discretisations illustrated in Figure 4.13 and changes dynamically with the touchdown point. The s_{TDP} varies between 284.6 m and 595.6 m for Case 4.

Figure 4.28 presents the active line discretisations over one low-frequency oscillation period of fairlead motion, during which 70 discretisation switches over all the prescribed 12 prepared line discretisations took place. Comparing Figures 4.27 and 4.28, it can be observed that the switching between suitable discretisations is directly related to the location of s_{TDP}.

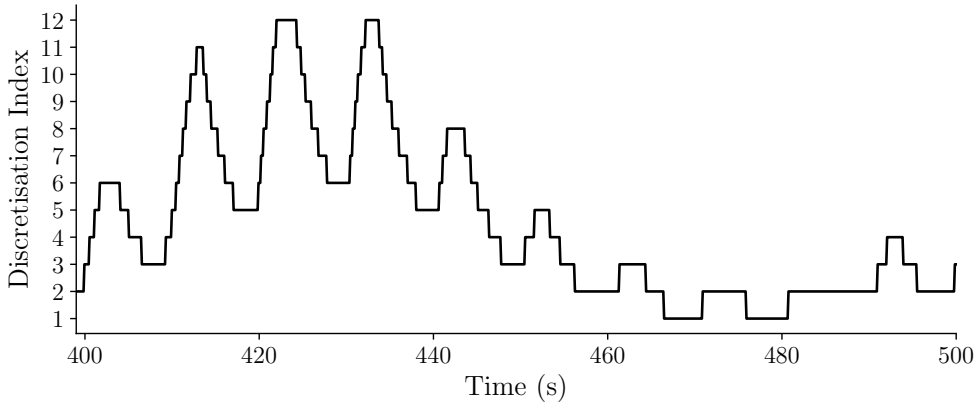

Figure 4.28: Discretisation switches for Case 4.

Figure 4.29 compares the peak tensions from Orcaflex and the in-house code for various discretisations for Case 4. The peak tensions from the in-house code are not modified by more than 0.02% with successive refinements of the element size while the peak tensions from Orcaflex are not modified by more than 0.4% with the same element size refinements. Hence the results for the peak tension are considered converged for all the discretisations used, which, for the in-house code is 7419.20 kN. The peak tension result by the hybrid coarse/fine discretisation, at 7425.92 kN, exceeds the converged peak tension result from the homogeneous discretisations by a small value of 0.09%.

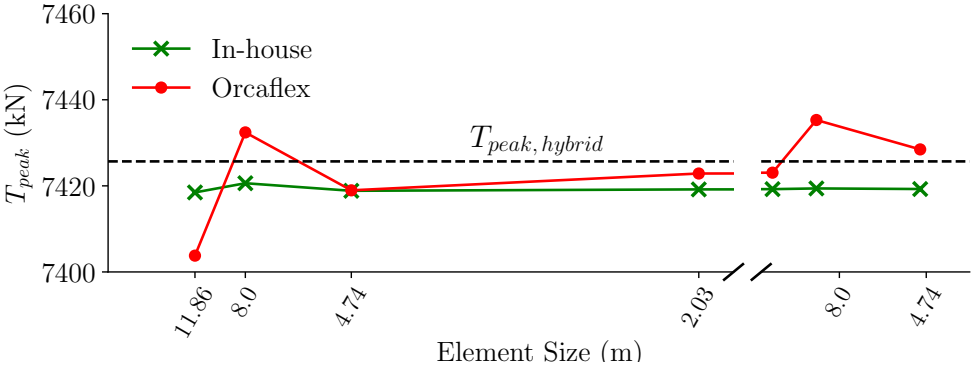

Figure 4.29: Peak tension values for Case 4 with homogeneous and hybrid coarse/fine discretisations.

Figure 4.30 shows the fairlead tension time series for Case 4 generated by the in-house code for the various discretisations over one period of the low-frequency excitation. The peaks of the tension time series given by the various discretisations, including the hybrid coarse/fine discretisation, are in good agreement. The

difference between the time series is in the small, irregular and high frequency fluctuations which occur due to nodal grounding and liftoff.

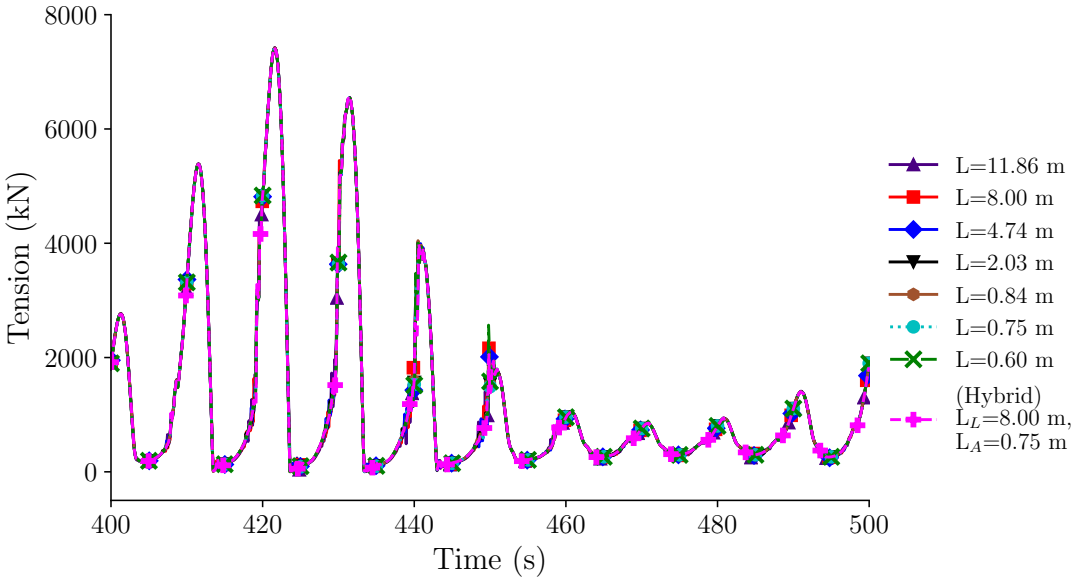

Figure 4.30: Fairlead tension time history for Case 4 from in-house code.

The fluctuations are seen in greater visual detail in the close up view of the tension time series in Figure 4.31. The irregularities observed are similar to those manifested in the results for Case 2. At 418.0 s, 428.0 s, 438.0 s and 448.0 s, the cause of the irregularities is attributed to snap loads due to a line section returning to tensioned state after becoming slack with rapid nodal grounding during the previous unloading cycle. The fluctuations observed at 475 s, 485 s, and 495 s are due to the rapid creation of a local low or negative strain section at the touchdown zone due to nodal grounding, and a large spatial strain gradient between the elements further away from and in close proximity to the touchdown zone, which creates propagating stress waves that are reflected back and forth between the touchdown zone and the line boundaries, namely the anchor and fairlead nodes. Figure 4.32 shows that the fluctuations due to both snap loading and the initial creation of low strain zones and propagating stress waves are significantly reduced, in particular the latter type, with nodal density refinement. The tension time series of the hybrid coarse/fine discretisation indicate that the fluctuations can be substantially attentuated with the usage of a locally refined nodal density at the touchdown zone and coarse elements elsewhere.

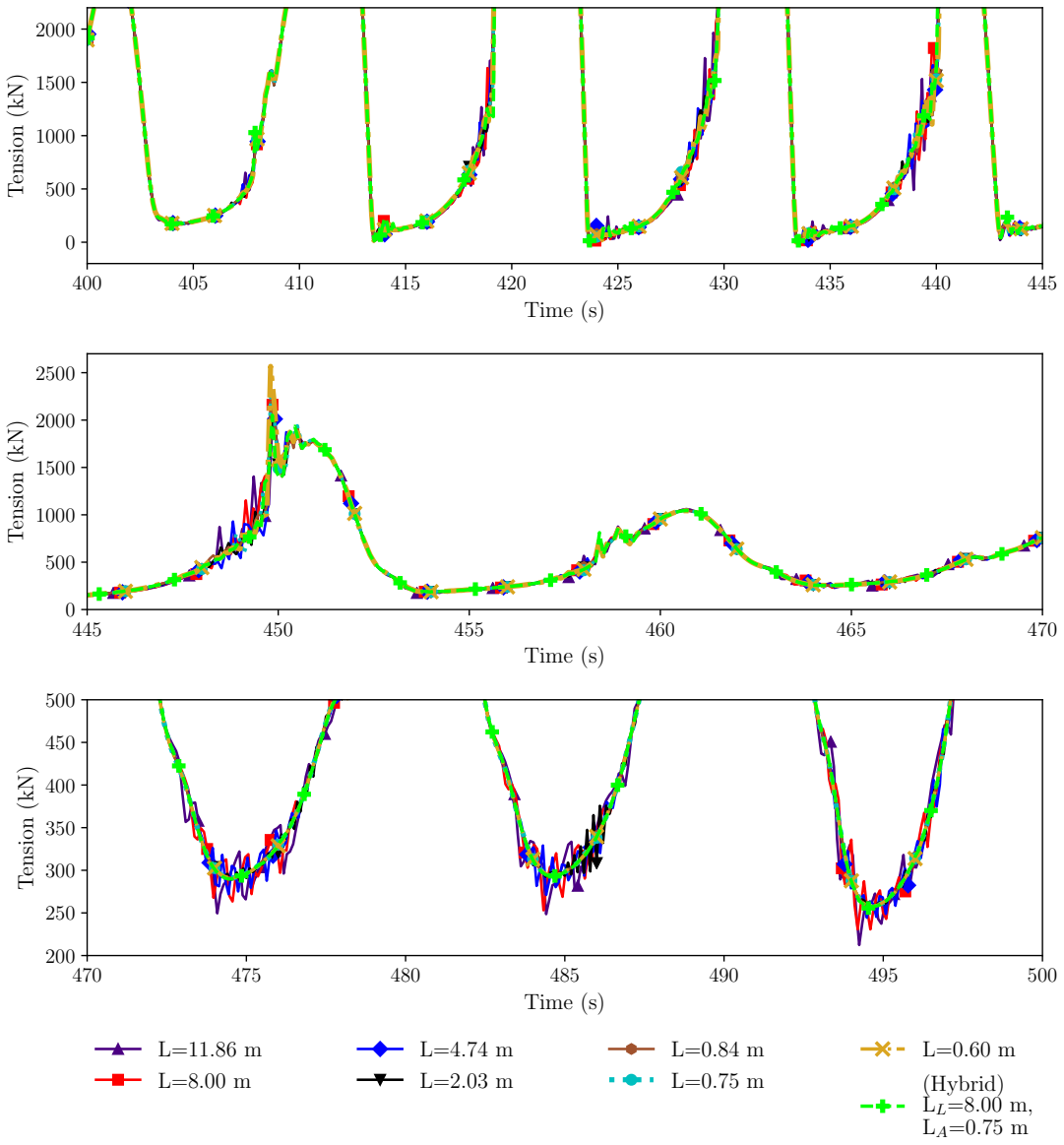

Figure 4.31: Close-up view of fairlead tension fluctuations due to nodal grounding in the time window 400 s $\leq t \leq$ 500 s for Case 4.

To illustrate the action of the nodal position mapping, and strain and curvature correction procedures, Figure 4.32 shows the strain and curvature distributions with and without peforming the corrections during the discretisation transition which took place at 426.80 s. Figure 4.32a demonstrates that the strain distribution without correction contains multiple spikes in the range of 380 m $\leq s \leq$ 425 m. The strain gradients at the locations of these spikes are high and persist due to successive and rapid discretisation switches without sufficient time for the strain discontinuities to dissipate as nonequilibrium tension forces lead to nodal motions that tend to dampen strain discontinuities.

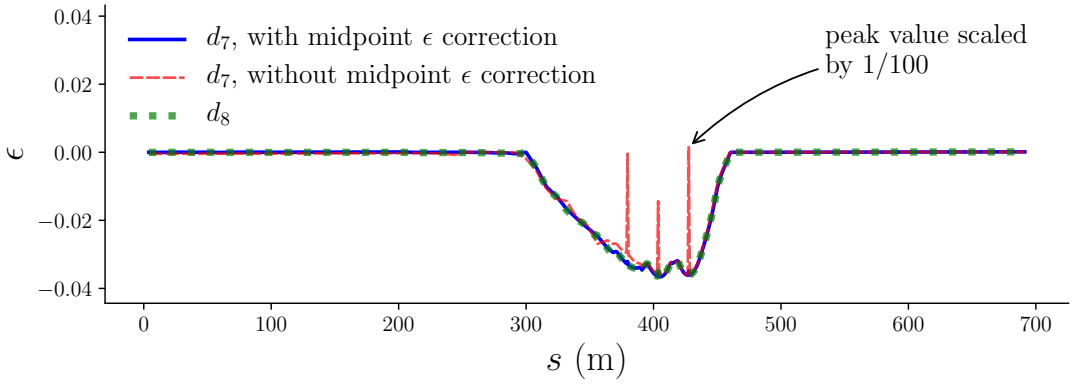

(a) Pre- and post-nodal position mapping strain distributions with and without midpoint strain correction for Case 4 at 426.80 s.

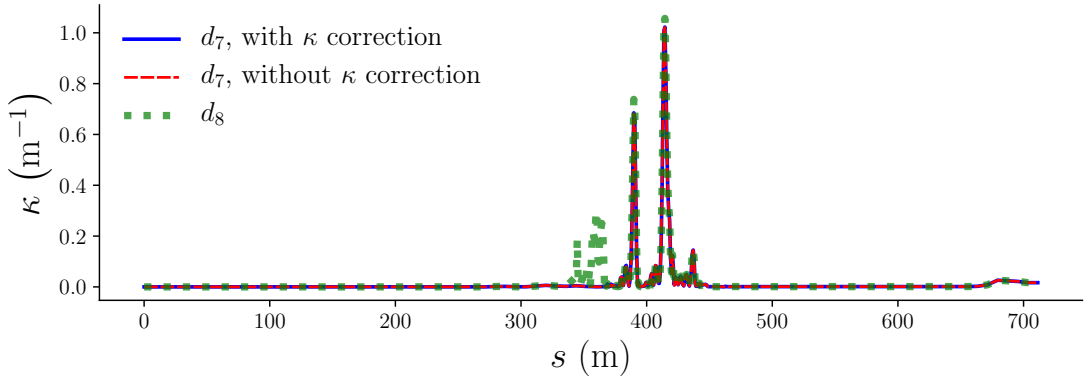

(b) Pre- and post-nodal position mapping curvature distributions with and without curvature correction for Case 4 at 426.80 s.

Figure 4.32: Pre- and post-nodal position mapping strain and curvature distributions, for Case 4 at 426.80 s, switching between discretisations 7 and 8.

The occurrence of very large strain discontinuities, particularly when the spikes are positive in magnitude and represent large tension forces, leads to numerical instabilities. When the spikes are negative in magnitude, their eventual dissipation is accompanied by tension shock waves. The magnitude of the largest spike shown in Figure 4.32a is scaled down by a factor of 100, and illustrates an occurrence of a large positive strain discontinuity.

Figure 4.32b shows the curvature distributions during the transition from discretisation 8 to 7 executed at 426.80 s, which corresponds to the coarsening and refinement of the elements on the anchor-side and floater-side ends respectively of the refined zone as shown in Figure 4.13. Between 344.0 m $\leq s \leq$ 368.0 m, the refined elements on the anchor-side end of d_8 are replaced by coarse elements on

the anchorside-end of d_7. The undulations in the curvature curve of d_8 in the range 344.0 m $\leq s \leq$ 368.0 m, which are due to the local unevenness in the orientation of refined elements, do not exist in the curvature curve of d_7 after coarse elements replace the refined elements of d_8 in-situ and the bulk geometry of the line is reflected in the curvature curve.

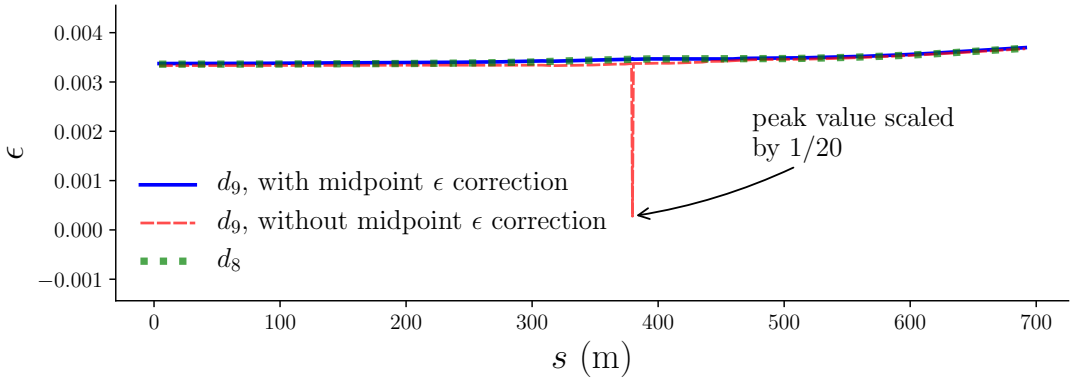

(a) Pre- and post-nodal position mapping strain distributions with and without midpoint strain correction for Case 4 at 430.97 s.

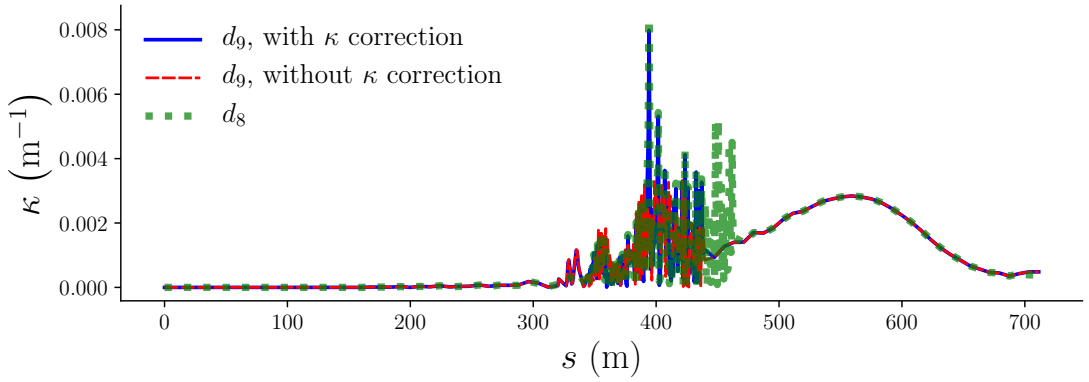

(b) Pre- and post-nodal position mapping curvature distributions with and without curvature correction for Case 4 at 430.97 s.

Figure 4.33: Pre- and post-nodal position mapping strain and curvature distributions, for Case 4 at 430.97 s, switching between discretisations 8 and 9.

Figure 4.33a shows the strain distributions during the discretisation switch from d_8 to d_9 that took place at 430.97 s. The strain discontinuity peak at $s = 379.6$ m during this transition was negative in magnitude and was scaled by a factor of 20 to better illustrate the strain distribution for the entire line. The strain correction procedure was required to eliminate the discontinuity produced during the nodal mapping step. Figure 4.33b displays the curvature distributions during the same

transition step, and presents a case in which fine elements on the fairlead-side end of the refined section of d_8 are replaced by coarse elements in d_9. As with the transition from d_8 to d_7, the replacement of fine elements with coarse elements is accompanied by a smoothening of the curvature curve as coarse elements are less sensitive to local curvature variations.

4.4.4 Summary of the evaluation of fairlead tension results

The three test cases prescribed in Table B.2 involve surge and heave motions which induce line liftoff and grounding, and large changes in s_{TDP} for Cases 3 and 4. The fairlead tension results show that the in-house code produces converged results for peak tension as element sizes for the homogeneous discretisations are refined. The peak tension results for the hybrid coarse/fine discretisation were in very good agreement with the converged tension results for each of the test cases, which indicates that such a discretisation is capable of producing accurate peak tension results.

Fluctuations were observed in the tension time series and were shown to be typically larger in the results produced by coarser discretisations. Using smaller elements was proven to be an effective approach to reduce the fluctuations which occur due to the discrete nature of the numerical model and the effects of nodal grounding and liftoff. It was concluded that a locally refined line segment close to the touchdown zone was as effective as a globally refined discretisation with respect to the reduction of the fluctuations.

The proposed discretisation switching procedure was exercised in the test cases, particularly in Cases 2 and 3 that involved successive and rapid switches. The tendency of the proposed nodal mapping procedure to produce strain and curvature discontinuities was addressed and the effectiveness of the correction procedures were demonstrated in the test cases. Finally, the accuracy and stability of the dual-rate time-stepping scheme, which is suitable for application with a hybrid coarse/fine discretisation, were also demonstrated.

4.5 Assessment of computational efficiency

From the fairlead tension results presented in Section 4.4, the element size required to effectively attenuate the nodal grounding and liftoff fluctuations for the prescribed test cases is 0.75 m. Three different discretisations are used to assess the efficiency gains of the dual-rate and discretisation switching methods presented in this work. The first is a homogeneous discretisation, henceforth referred to as type M-1, consisting of 0.75 m-length elements, provides the baseline benchmark for comparison. The second meshing scheme, type M-2, is illustrated in Figure 4.34, is a static, hybrid coarse/fine discretisation which consists of fine elements of 0.75 m length within the grounding span of each case and coarse elements of 8.0 m elsewhere. The third discretisation scheme was presented in Figure 4.13, henceforth referred to as type M-3, and is applicable to the dual-rate, adaptive discretisation approach.

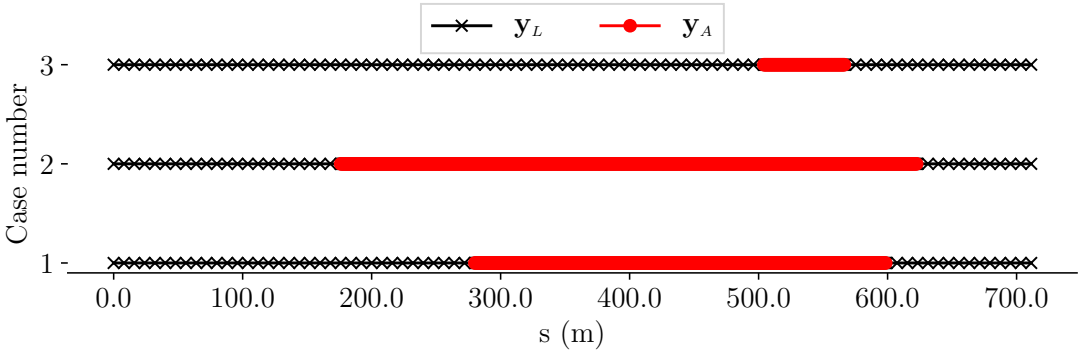

Figure 4.34: Hybrid coarse/fine static discretisations for test Cases 1, 3 and 4.

Case	Grounding s span, s_l (m) $\leq s \leq s_u$ (m)	Grounding span length, L_g (m)	L_g/L_{model}
1	$504.0 \leq s \leq 567.3$	63.3	0.089
3	$176.0 \leq s \leq 623.6$	447.3	0.629
4	$280.0 \leq s \leq 599.3$	319.3	0.449

Table 4.2: Grounding-span lengths, s-coordinates and grounding-span length to line length ratios for test Cases 1, 3 and 4.

The s-coordinate span of the grounding spans for each case, their lengths, L_g, and the ratio between L_g and the total line length L_{model}, L_g/L_{model}, are included in

Table 4.2. The L_g/L_{model} ratio indicates the proportion of the line consisting of fine elements.

The time integration approaches evaluated for the computational efficiencies are the single-rate and dual-rate methods, henceforth referred to as type TI-1 and TI-2 respectively. The expended calculation time per second of simulation time, $\Delta\overline{T}$, for each case is presented in Table 4.3. Each result is the average of five runs. The computations were performed serially on an Intel Core i7, 2.6 GHz CPU.

TI and M codes	Case 1	Case 3	Case 4
TI-1, M-1	0.953	0.976	0.977
TI-2, M-3	0.179	0.185	0.249
TI-1, M-2	0.154	0.591	0.439
TI-2, M-2	0.084	0.563	0.403

Table 4.3: Calculation expended time per second of simulation time for test Cases 1, 3 and 4.

The results in Table 4.3 highlight that, naturally, the fully refined discretisation with single-rate time integration approach is the slowest, giving calculation to simulation time ratios of close to unity. By using the partially refined, M-2 discretisation, the time ratios are reduced to the ranges of 0.18, 0.59 and 0.44 and below for cases 1, 2 and 3 respectively. Switching from the TI-1 to TI-2 (single-rate to dual-rate) integration approach further reduced the computational times for all the cases, and, as it will be shown, the reduction is dependent on the L_g/L_{model} ratio.

The L_g/L_{model} ratio is an important factor influencing the efficiency of the computational schemes applied in this work. It determines the length span of the section using refined elements in the M-2 discretisation. The efficiency gain, $\eta_{a,b}$, of a particular computational approach, (TI-a, M-b), is defined in this work as,

$$\eta_{a,b} = \frac{\Delta\overline{T}_{TI-1,M-1}}{\Delta\overline{T}_{TI-a,M-b}} \tag{4.44}$$

where $a \in [1,2]$ and $b \in [1,2,3]$ and denote the choice of time integration and discretisation methods respectively. The efficiency gain as a function of L_g/L_{model}

ratio for the (TI-1, M-2), (TI-2, M-2), and (TI-2, M-3) integration and discretisation scheme combinations are presented in Figure 4.35.

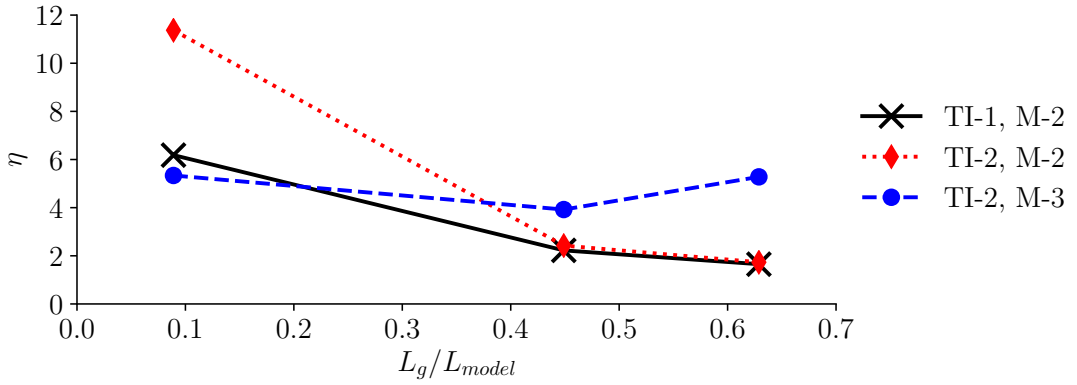

Figure 4.35: Computational efficiency gains of combinations of single and dual-rate time integration with static and adapting discretisations.

A few general conclusions that can be drawn from the results presented in Figure 4.35. Firstly, applying the dual-rate integration approach allowed efficiencies to be reaped ($\eta > 1$) when a significant line span, up to 44.9%, or L_g/L_{model}=0.449, uses fine elements. This result is deduced from a comparison of the (TI-1,M-2) and (TI-2,M-2) curves, where the difference in η values represents the relative efficiencies of the approaches. Both approaches apply the static, partially refined discretisation (M-2), differing only in the time integration method.

It is observed that the η curve for the (TI-2, M-2) approach is higher than that of (TI-1,M-2) up to the L_g/L_{model} ratio of 0.63. At the L_g/L_{model} ratio of 0.09, the η values of the (TI-1, M-2) and (TI-2, M-2) approaches were 6.2 and 11.4 respectively, while at the L_g/L_{model} ratio of 0.45, the η values for the respective methods were 2.22 and 2.42. This indicates that the computational time saving afforded by the dual-rate strategy is inversely proportional to L_g/L_{model} ratio, and suggests that the line span using refined elements should be limited in order to extract higher efficiencies from the dual time-step integration method. It is expected that at some point with higher L_g/L_{model} ratios, the TI-2 approach will give lower η values than that of TI-1 due to the necessary overheads associated with data interpolation and saving inherent in the dual-rate approach. It should be noted that this result is also sensitive to the relative time-step sizes used for the latent and active partitions. In this work, the line material stiffness, element sizes in the coarse and fine sections (8.0 m and 0.75 m respectively) required for effective reduction of seabed contact

tension fluctuations, and γ_{max} and γ_{min} (see Equation (4.15)) values of 0.9 and 0.1 respectively, result in a time-step ratio of 10 between the latent and active partitions. It can be expected that the efficiency gains of the dual-rate integration scheme over the single-rate method is proportionately higher with larger time-step ratios.

The second observation is that the η curve of the (TI-2, M-3) is relatively flat, which suggests that the discretisation adaptation strategy allows the dual-rate approach to maintain its efficiency gains over a range of L_g/L_{model} ratios. This is to be expected because the line span using fine elements is fixed. At a low L_g/L_{model} ratio of 0.09, the (TI-2, M-3) strategy gives the lowest η value compared with the (TI-1, M-2) and (TI-2, M-2) approaches, due to the overheads of nodal positions, velocities, and accelerations mapping in the discretisation switching procedure. At L_g/L_{model} ratios of above 0.38, the η values for the (TI-2, M-3) approach exceeds that for (TI-2, M-2), which indicates that the discretisation adaptation strategy is suited for higher L_g/L_{model} ratios, or equivalently, when liftoff and grounding are experienced by larger spans of the line.

In summary, the dual-rate, static disretisation (TI-2, M-2) approach provides the highest efficiency gains up to a L_g/L_{model} ratio of 0.38, beyond which the discretisation adaptation strategy has to be applied to augment the dual-rate time integration strategy in order to sustain the efficiency gains.

4.6 Chapter closure

A novel dual-rate time integration and adaptive discretisation strategy for dynamic mooring line simulation was presented in this chapter. This approach is developed for the application of a hybrid coarse/fine discretisation using fine elements in the vicinity of touchdown zone and coarse elements elsewhere to attenuate tension fluctuations created by line-seabed contact. It was shown that a hybrid discretisation approach was able to provide good results for peak tensions while also effectively reducing the spurious tension fluctuations.

A method was presented to determine the optimal time-step ratio between the latent (coarse mesh) and active partitions (fine mesh), based on the evaluation of numerical stability requirements of the base integration scheme and the total

simulation time. A procedure for the mapping of nodal positions, velocities and accelerations between discretisations was presented. The requirement to eliminate strain discontinuities and reduce high line curvatures was explained and the procedures to implement these control measures were demonstrated.

The efficiency gains of the proposed dual-rate time integration and adaptive discretisation schemes over a standard monolithic time integration, static discretisation approach were evaluated. It was proven that the dual-rate time integration method afforded good computational efficiency improvements over a monolithic time integration scheme for moderate line liftoff/ grounding spans as a proportion of total line length. The discretisation adaptation approach is applicable to cases experiencing larger line liftoff/grounding spans, where it is needed to sustain the computational efficiency gains of the dual-rate time integration method.

Chapter 5

Development of Modified Spring Mattress Seabed Contact Model

The cause of the tension fluctuations due to nodal grounding was discussed in Chapter 3. Mesh refinement was determined to be an effective solution to mitigating the production of large strain gradients which create the tension shock waves that propagate through the line, manifesting as tension fluctuations and an efficient and accurate method to implement this solution was developed in Chapter 4. However, the method of local mesh refinement proposed in Chapter 4 nonetheless incurs additional computational costs.

In this chapter, a different approach to the problem is proposed. The widely used spring mattress seabed model is modified and improved upon so as to reduce its susceptibility to tension shocks due to nodal grounding. The new seabed model formulation is presented in Section 5.1, and the evaluation of its effectiveness is presented in Section 5.2.

5.1 Modified Spring Mattress model

In the Modified spring mattress model, the total seabed force is given by

$$\mathbf{F}_i^B = \mathbf{F}_i^{B,r} + \mathbf{F}_i^{B,a} + \mathbf{F}_i^{B,\tau} + \mathbf{F}_i^{B,d} \tag{5.1}$$

where the lateral friction and vertical damping components, $\mathbf{F}_i^{B,\tau}$ and $\mathbf{F}_i^{B,d}$, have been defined in Sections 3.1.3 and 3.1.4 respectively. The formulation for the vertical reaction force component in the modified spring mattress model is presented in Section 5.1.1, while that for the added mass force component is presented in Section 5.1.2.

5.1.1 Seabed reaction force formulation

In the modified seabed spring mattress model an element can be in four states with respect to the seabed, as shown in Equation (5.1). States I and IV respectively describe the element in fully embedded and suspended states with respect to the seabed. State II refers to an element in the state of partial embedment with the center of the element below the seabed force cutoff elevation, $z^{B,c}$. State III describes a partially embedded element with the element center above $z^{B,c}$. The four states determine how the seabed forces are calculated and distributed to the bounding nodes.

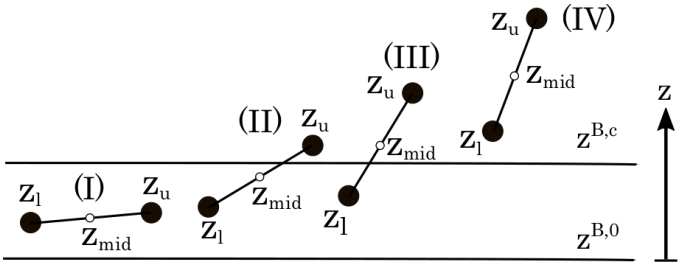

Figure 5.1: Element embedment states.

The seabed forces acting on an element, $\mathbf{F}^B$, are comprised of forces that are tangential and normal to the seabed surface, $\mathbf{F}^{B,\tau}$ and $\mathbf{F}^{B,\nu}$,

$$\mathbf{F}^B = \mathbf{F}^{B,\tau} + \mathbf{F}^{B,\nu} \tag{5.2}$$

In the present model, the forces that are normal to the seabed surface are comprised of the seabed reaction, damping, and added mass components, respectively represented as $\mathbf{F}^{B,r}$, $\mathbf{F}^{B,d}$ and $\mathbf{F}^{B,a}$, in Equation 5.3.

$$\mathbf{F}^{B,\nu} = \mathbf{F}^{B,r} + \mathbf{F}^{B,d} + \mathbf{F}^{B,a} \tag{5.3}$$

The seabed reaction force on element j, $\mathbf{F}_j^{B,r}$, is given by,

$$\mathbf{F}_j^{B,r} = \left(\int_{s_{1,j}}^{s_{2,j}} k_j^B \left[z_j^{B,c} - z_j(s) \right] \ \mathrm{d}s \right) \hat{\mathbf{n}}_B \tag{5.4}$$

where $\hat{\mathbf{n}}_B$ is the seabed normal direction unit vector, s is the line axial coordinate, as shown in Equation (2.1a), and z is the vertical coordinate, as shown in Equation (5.1). The quantity, $z_j^{B,c} - z_j(s)$, in Equation (5.4) is the per unit length embedment depth.

The element seabed spring stiffness is given by

$$k_j^B = \frac{W_j / L_j^e}{z_j^{B,c} - z^{B,0}} \tag{5.5}$$

where W_j and L_j are the element weight and unstretched lengths respectively. The relationship between the seabed force cutoff elevation $z_j^{B,c}$ and $z^{B,0}$ is given by

$$z_j^{B,c} = N_j^{B,c} D_{S,j} + z^{B,0} \tag{5.6}$$

where $N_j^{B,c}$ is the seabed thickness coefficient and $D_{S,j}$ is the diameter of the element, or equivalently taken to be the physical outer diameter of the line section. The parameter $N_j^{B,c} D_{S,j}$ denotes the distance over which the seabed force is increased linearly from zero to the element weight per unit length.

Equation (5.7) shows that when the entire element is resting on the seabed at the seabed nominal elevation, $z^{B,0}$, the seabed reaction force on element j is equivalent to its weight.

$$\begin{aligned} \mathbf{F}_j^{B,r} &= \left(\int_{s_{1,j}}^{s_{2,j}} \frac{W_j / L_j^e}{z_j^{B,c} - z^{B,0}} \left[z_j^{B,c} - z^{B,0} \right] \ \mathrm{d}s \right) \hat{\mathbf{n}}_B \\ &= \left(\int_{s_{1,j}}^{s_{2,j}} \frac{W_j}{L_j^e} \ \mathrm{d}s \right) \hat{\mathbf{n}}_B = W_j \ \hat{\mathbf{n}}_B \end{aligned} \tag{5.7}$$

Since each element is bounded by two nodes, with reference to Equation (5.1), the elevation of any point along an element is described with a linear interpolation between the elevations of its bounding nodes,

$$z_j(s) = z_{l,j} + \frac{z_{u,j} - z_{l,j}}{L_j^e} s = z_{l,j} + \frac{\Delta z_j}{L_j^e} s \tag{5.8}$$

where z_u and z_l refer to the z-coordinates of the upper and lower nodes. Differentiating Equation (5.8) with respect to z allows a change of integration variable from s to z in Equation (5.4),

$$\mathbf{F}_j^{B,r} = \frac{k_j^B L_j^e}{\Delta z_j} \int_{z_{1,j}}^{z_{2,j}} \left(z_j^{B,c} - z_j \right) \mathrm{d}z \tag{5.9}$$

Each element can be split into two half-elements of equal lengths, and the force on each half-element is assigned to its adjoining node. With reference to Equation (5.1), for an element in State I, fully embedded in the seabed, the seabed reaction force contribution of element j on the adjoining node of lower elevation can be calculated by integrating Equation (5.9) with the limits of integration $z_{l,j} = z_l$ and $z_{2,j} = z_{mid,j} = (z_{l,j} + z_{u,j})/2$, which gives

$$\mathbf{F}_l^{B,r} = \frac{k_j^B L_j^e}{\Delta z_j} \left[\left(z_j^{B,c} (z_{mid,j} - z_{l,j}) \right) + \frac{z_{l,j}^2 - \left(z_j^{B,c} \right)^2}{2} \right] \tag{5.10}$$

For the node with the higher elevation, the limits of integration are $z_{1,j} = z_{mid,j}$ and $z_{2,j} = z_u$. Integrating Equation (5.9) with these limits leads to the reaction force on the upper node being given by

$$\mathbf{F}_u^{B,r} = \frac{k_j^B L_j^e}{\Delta z_j} \left[\left(z_j^{B,c} (z_{u,j} - z_{mid,j}) \right) + \frac{z_{mid,j}^2 - z_{u,j}^2}{2} \right] \tag{5.11}$$

For a partially embedded element in State II, the seabed reaction force on the lower node is as shown in Equation (5.10). To obtain the seabed reaction force on the upper node, Equation (5.9) is integrated with the limits $z_{1,j} = z_{mid,j}$ and $z_{2,j} = z_j^{B,c}$, which leads to

$$\mathbf{F}_u^{B,r} = \frac{k_j^B L_j^e}{\Delta z_j} \left[\frac{\left(z_j^{B,c} \right)^2 + z_{mid,j}^2}{2} - z_j^{B,c} z_{mid,j} \right] \tag{5.12}$$

For a partially embedded element in State III, the seabed reaction force on the upper node is taken to be zero as $z_{mid,j} > z_j^{B,c}$. For the lower node, using the integration limits $z_{1,j} = z_{l,j}$ and $z_{2,j} = z_j^{B,c}$ in Equation (5.9) leads to

$$\mathbf{F}_l^{B,r} = \frac{k_j^B L_j^e}{\Delta z_j} \left[\frac{\left(z_j^{B,c}\right)^2 + z_{l,j}^2}{2} - z_j^{B,c} z_{l,j} \right] \tag{5.13}$$

An element in State IV is fully suspended and does not experience any seabed forces. For Node i, the total seabed reaction force, as with all other forces, are contributed by elements j and $j-1$,

$$\mathbf{F}_i^{B,r} = \mathbf{F}_j^{B,r}(\chi_j, z_i, z_{i+1}) + \mathbf{F}_{j-1}^{B,r}(\chi_{j-1}, z_{i-1}, z_i) \tag{5.14}$$

where the contributions from the elements are dependent on the elemental grounding state, $\chi = \{I,\ II,\ III,\ IV\}$, and the relative elevations of nodes $i+1$, i and $i-1$. In this modified spring mattress model, a node experiences a seabed reaction force when either of the half elements adjacent to it is in contact with the seabed, when $z_{mid,j} \leq z_j^{B,c}$ or $z_{mid,j-1} \leq z_{j-1}^{B,c}$.

5.1.2 Seabed added mass formulation

Borrowing from the theory of hydrodynamic added mass, in addition to the reaction and damping forces, an added mass force is introduced as a vertical seabed force. A thorough search of the relevant literature reveals that existing time domain seabed models typically model the seabed normal forces on a mooring line as a spring and damper system. The seabed added mass force on node i is given by

$$\mathbf{F}_i^{B,a} = \mathbf{F}_j^{B,a} + \mathbf{F}_{j-1}^{B,a} = \sum_{\xi=j,j-1} \mathbf{F}_\xi^{B,a} \tag{5.15}$$

where the force contribution from the adjacent elements are

$$\mathbf{F}_\xi^{B,a} = \begin{cases} -C_\xi^{B,a} \left(\ddot{\mathbf{r}}_i \cdot \hat{\mathbf{n}}_B\right) \ \hat{\mathbf{n}}_B, & |\mathbf{F}_\xi^{B,r}| > 0 \\ 0, & \text{otherwise} \end{cases} \tag{5.16}$$

and where $C_{\xi}^{B,a}$, $\xi = \{j,\, j-1\}$ represent the added mass coefficients of elements j and $j-1$. The added mass force is active only when the acceleration of the node $\ddot{z}_i$ is downwards, and the node experiences a seabed reaction force. The added mass coefficients are prescribed as $C_{\xi}^{B,a} = (\zeta^{B,a} m_{\xi} L_{\xi})/2$, where $\zeta^{B,a}$ is the added mass coefficient, and m_{ξ} and L_{ξ}, $\xi = \{j,\, j-1\}$ represent the structural masses per unit length and lengths of the elements j and $j-1$.

5.2 Application of Modified Spring Mattress model

In this section the effectiveness of the modified spring mattress (MSM) model in mitigating the fairlead tension fluctuations is evaluated for the shallow and deep water depths of 82.5 m and 914.0 m respectively. The features of the MSM model that differ from the spring mattress (SM) model are the modified reaction force and added mass force models described in Sections 5.1.1 and 5.1.2.

5.2.1 Shallow water environment

A single segment mooring line with structural parameters enumerated in Table A.1 is used for the shallow water environment. Test cases 1, 3 and 4, as shown in Table B.2, provide the fairlead excitation profiles. Comparisons are made between the results from the SM, SM_7 and Modified Spring-Mattress (MSM) seabed models using the relevant coefficient sets shown in Table C.2. Comparisons are made between the results from the SM, SM_7 and Modified Spring-Mattress (MSM) seabed models using the relevant coefficient sets shown in Table C.2. The SM_7 coefficient set is chosen because it was shown to be effective at reducing the tension fluctuations in Case 1 (see Section 3.2.3).

The maximum tension results from the present code are compared to that from Ref. [5], shown in Table 5.1 as $\overline{T}$ [5], as a means of benchmarking. A second qualitative indicator for the quality of the results is the existence of spurious oscillations, which can be evaluated from the tension time series plots for Cases 1, 3 and 4 as shown in Figures 5.2, 5.5 and 5.12 respectively.

For Case 1, the peak tension results, presented in Table 5.1, using the SM, SM_7 and MSM seabed models with the two line discretisations agree well with $\overline{T}$ [5]

in general. The SM model with the 4.74 m and 0.84 m-element discretisations ($SM^{4.74}$ and $SM^{0.84}$) respectively underpredict $\overline{T}$ [5] by 0.08% and 0.09%, while the MSM ($MSM^{4.74}$) and SM_7 ($SM_7^{4.74}$) coefficient sets, both using the 4.74 m-element discretisation, respectively underpredict $\overline{T}$ [5] by 0.43% and 3.72%.

Table 5.1: Fairlead peak tensions with SM, SM_7 and MSM models compared to benchmark tension $\overline{T}$ [5] for Cases 1 to 4.

Model	Case 1	Case 3	Case 4
	Fairlead Tension (kN)		
$\overline{T}$ [5]	1300	6777	7488
$\overline{T}^{SM}_{4.74m}$	1298.98	6876.02	7384.98
$\overline{T}^{SM}_{0.84m}$	1298.87	6860.27	7414.92
$\overline{T}^{SM_7}_{4.74m}$	1251.68	6752.64	7337.61
$\overline{T}^{MSM}_{4.74m}$	1294.38	6858.60	7355.22
	Percentage deviation of tension from $\overline{T}$ [5]		
$\overline{T}^{SM}_{4.74m}$	-0.079%	1.461%	-0.975%
$\overline{T}^{SM}_{0.84m}$	-0.087%	1.229%	-1.376%
$\overline{T}^{SM_7}_{4.74m}$	-3.717%	-0.359%	-2.008%
$\overline{T}^{MSM}_{4.74m}$	-0.432%	1.204%	-1.773%

The tension time series in Table 5.2 show that the tension fluctuations are significantly reduced in the results for $SM^{0.84}$, $MSM^{4.74}$ and $SM_7^{4.74}$. The ϵ and $d\epsilon/ds$ distributions in a line with 4.74 m elements and applying the MSM model are presented in Figures 5.3a and 5.3b and illustrate that the MSM model is effective in preventing severe strain gradients from occurring during nodal grounding.

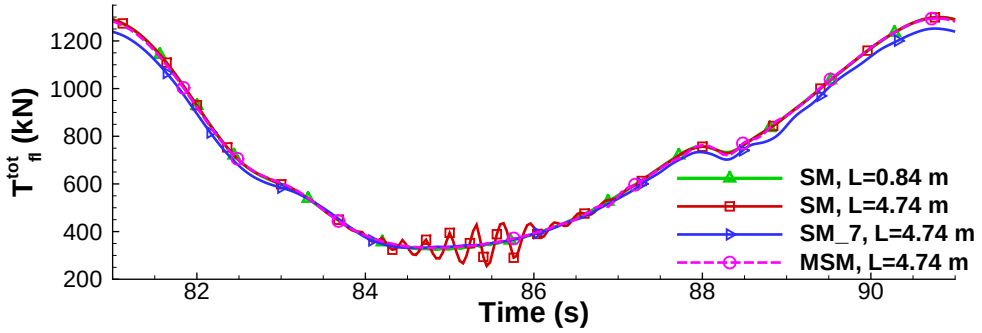

Figure 5.2: Fairlead tension time history for Case 1 with 0.84 m and 8.0 m-element lines and SM, SM_7 and MSM models.

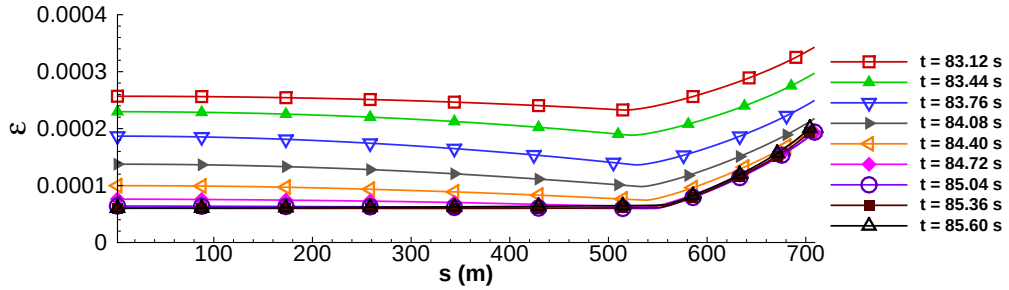

(a) Strain distributions for 8.0 m-element line using MSM model.

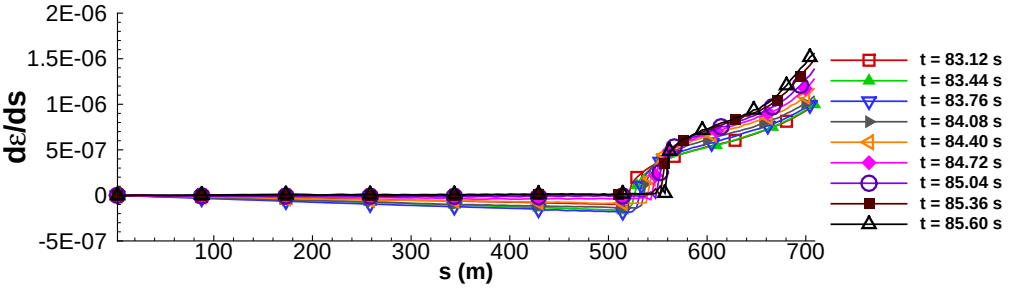

(b) Strain spatial gradient distributions for 8.0 m-element line using MSM model.

Figure 5.3: Strain and strain gradient distribution for Case 1 during nodal grounding time window (8.12 s $\leq t \leq$ 85.52 s).

Table 5.4 illustrates that the penetration depth of the nodes has increased when the MSM model is applied, compared to the nodal penetration depths of the SM model, due to a more gradual application of the vertical seabed force by the MSM model as well as the addition of the artificial grounding added mass force which increases the mass of the nodes when they make contact with the seabed. The maximum penetration elevation in Case 1 with the MSM model is -82.84 m compared to that of -82.74 m with the SM_7 coefficient set.

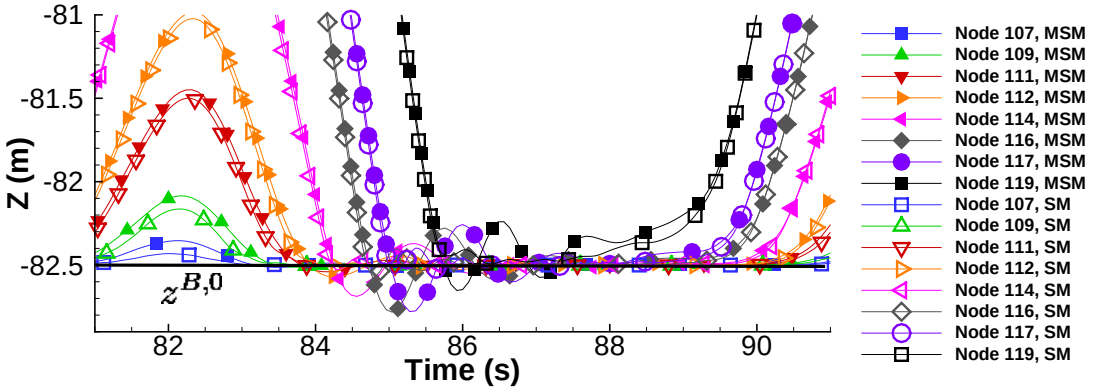

Figure 5.4: Nodal vertical coordinate, Z, results for 8.0 m-element line using SM and MSM models during nodal grounding time window (8.12 s $\leq t \leq$ 85.52 s).

Case 3 is a biharmonic fairlead excitation in the surge and heave directions with a maximum displacement of 25.4 m of the fairlead node from the initial position. From the tension peak values for Case 3 presented in Table 5.1, the results for $SM^{4.74}$ and $SM^{0.84}$ overpredicted $\overline{T}$ [5] by 1.46% and 1.23% respectively, while the $MSM^{4.74}$ results overpredicted $\overline{T}$ [5] by 1.20%. The $SM_7^{4.74}$ results underpredicted $\overline{T}$ [5] by 0.36%.

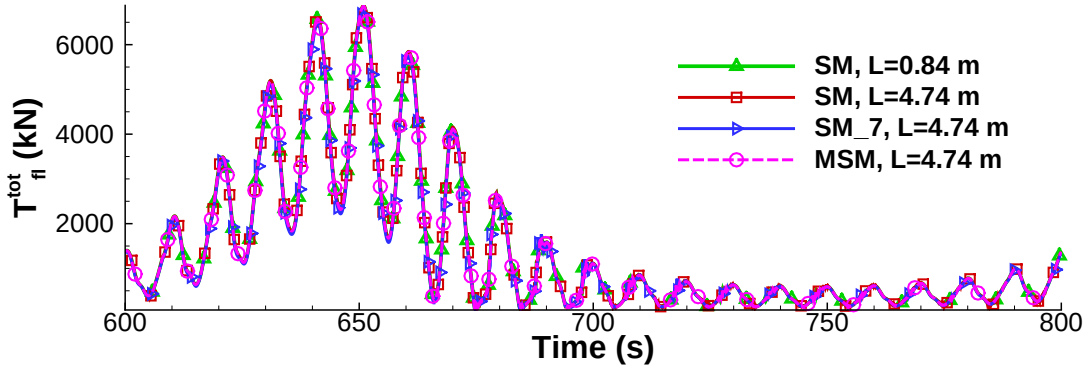

Figure 5.5: Fairlead tension time series for Case 3 for time window (600 s $\leq t \leq$ 800 s).

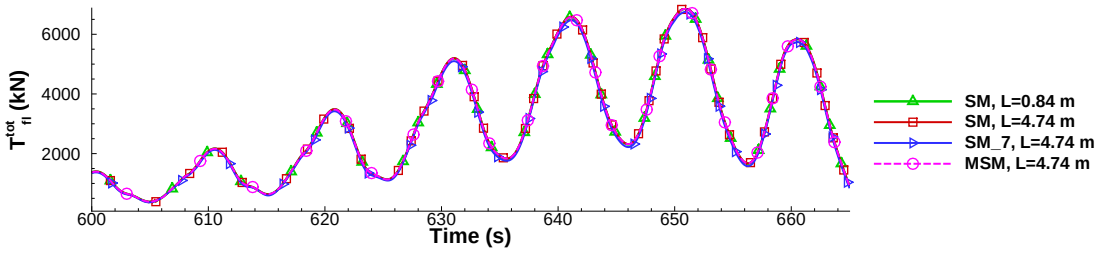

(a) Fairlead tension time histories for Case 3 with time window (600 s $\leq t \leq$ 665 s).

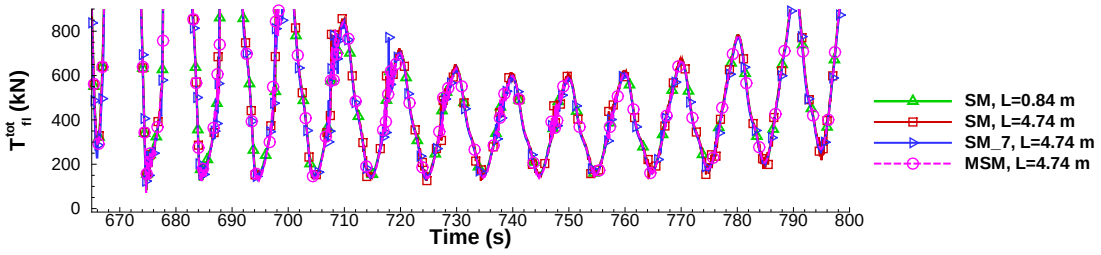

(b) Fairlead tension time histories for Case 3 with time window (665 s $\leq t \leq$ 800 s).

Figure 5.6: Fairlead tension time histories for Case 3 with SM, SM_7, MSM seabed models and 4.74 m and 0.84 m-element discretisations.

Figure 5.5 presents the fairlead tension time history for one oscillation period (600 s $\leq t \leq$ 800 s) in Case 3. The tension fluctuations do not occur between 600 s to 665 s for all models and discretisations, as presented in Figure 5.6a, due to the low nodal grounding velocities and grounding angles shown respectively in

Figures 5.7a and 5.8a. Between 665 s and 800 s, the fluctuations appear at various points in time, as presented in Figure 5.6b, with some variability between the models. From 665 s to 750 s, fluctuations appear at the troughs as well as loading cycle (positive slope) of the tension results for all models, whereas between 750 s and 800 s, some fluctuations occur at the troughs of the $SM^{4.74}$ fairlead tension results and are subdued in the results for the $SM_7^{4.74}$, $SM^{0.84}$, $MSM^{4.74}$ models.

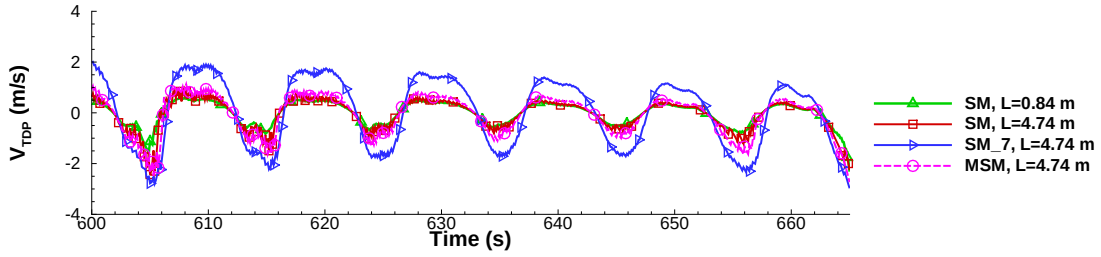

(a) Touchdown node vertical velocities for Case 3 with time window (600 s $\leq t \leq$ 665 s).

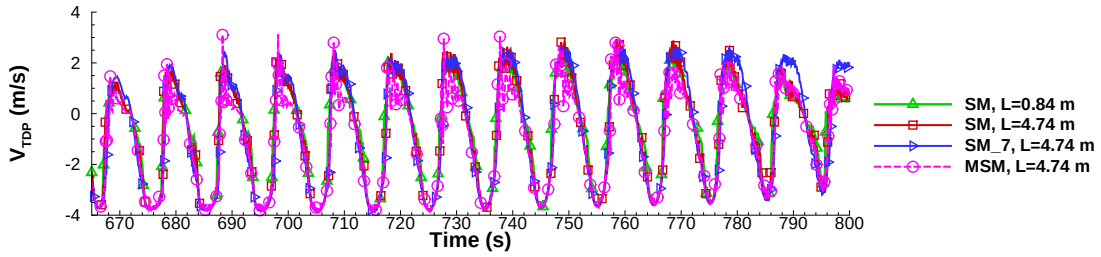

(b) Touchdown node vertical velocities for Case 3 with time window (665 s $\leq t \leq$ 800 s).

Figure 5.7: Touchdown node vertical velocities for Case 3 with SM, SM_7, MSM seabed models and 4.74 m and 0.84 m-element discretisations.

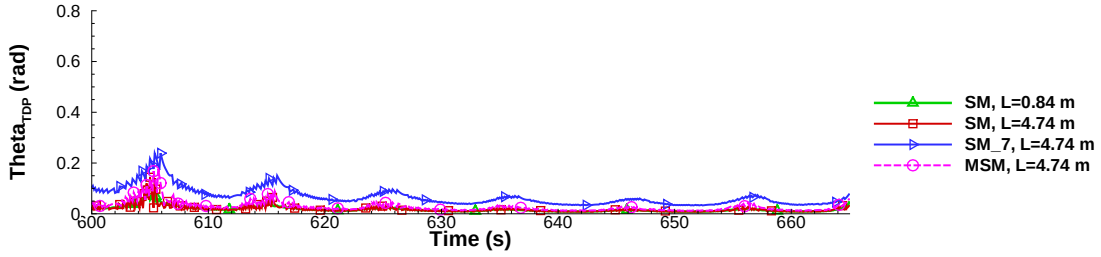

(a) Grounding element θ angles for Case 3 with time window (600 s $\leq t \leq$ 665 s).

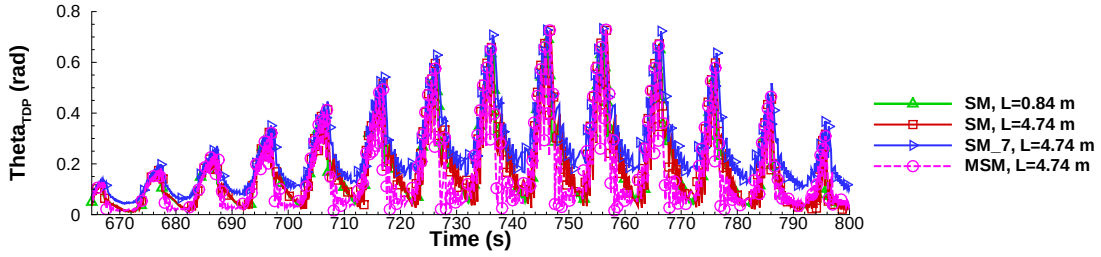

(b) Grounding element θ angles for Case 3 with time window (665 s $\leq t \leq$ 800 s).

Figure 5.8: Grounding element θ angles for Case 3 with SM, SM_7, MSM seabed models and 4.74 m and 0.84 m-element discretisations.

The characteristics for the some of the tension fluctuations in Case 3 differ from Case 1 in that these fluctuations are observed during the loading cycle, and are preceded by significant fluctuations at the troughs of the time series. The tension at the trough is close to zero, indicating that the fairlead tension is close to being slack. The strains in the line during the development of the tension fluctuations at one of the troughs at $t = 726.0$ s is presented in Table 5.9, and illustrates that a large segment of the line is under significant compression for all the models and discretisations used.

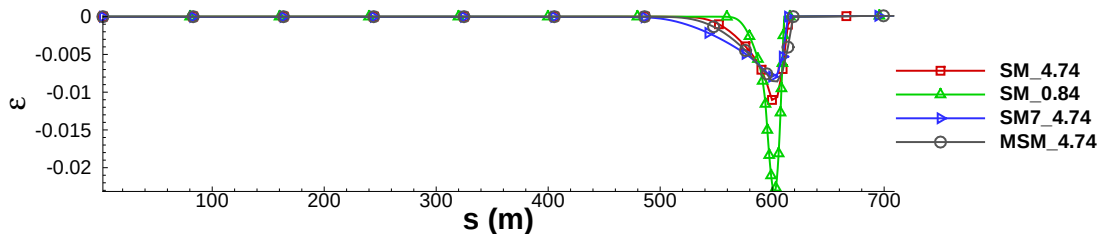

Figure 5.9: Strain distributions at $t = 726.0$ s for Case 3 during development of tension fluctuations.

At this point, a distinction is made between the tension fluctuations that occur in all the models between 665 s and 750 s, and those that occur in the $SM^{4.74}$ model from 750 s to 800 s. The former occurs due to the occurrence of snap loading, and is characterised by two waves of tensions fluctuations or shocks; the first occurs during rapid line unloading when line tension falls precipitously and parts of the line goes slack in the vicinity of the touchdown point, followed by a second wave of fluctuations that occur when the line is loaded again and the part of the line under compression returns to a tensioned state, which leads to the propagation of shock waves.

The occurrence of snap events has been demonstrated experimentally by Hsu et al.[153] and Azcona et al.[88]. The analytical shock condition proposed by Triantafyllou and Bliek [114] and experimentally verified by Gobat and Grosenbaugh [115] states that cable unloading and loading shocks develop when the condition in Equation (5.17) is met,

$$\left|\frac{\mathrm{d}X_{TDP}}{\mathrm{d}t}\right| \geq \sqrt{\frac{T_{TDP}}{m}} \tag{5.17}$$

where X_{TDP} is the position of the touchdown point, T_{TDP} is the touchdown point tension, and m is the mass per unit length of the line, and the left and right hand

sides respectively refer to the touchdown point and transverse wave speeds. In the present study, the touchdown point speed is approximated by the time rate of change of s_{TDP}, while T_{TDP} is approximated with the horizontal component of the fairlead tension following [115].

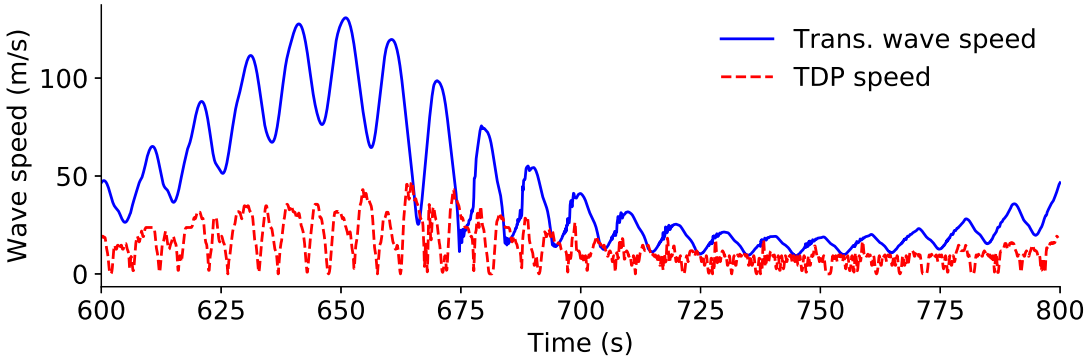

Figure 5.10: Touchdown point and transverse wave speeds for Case 3 during time window 600 s $\leq t \leq$ 800 s.

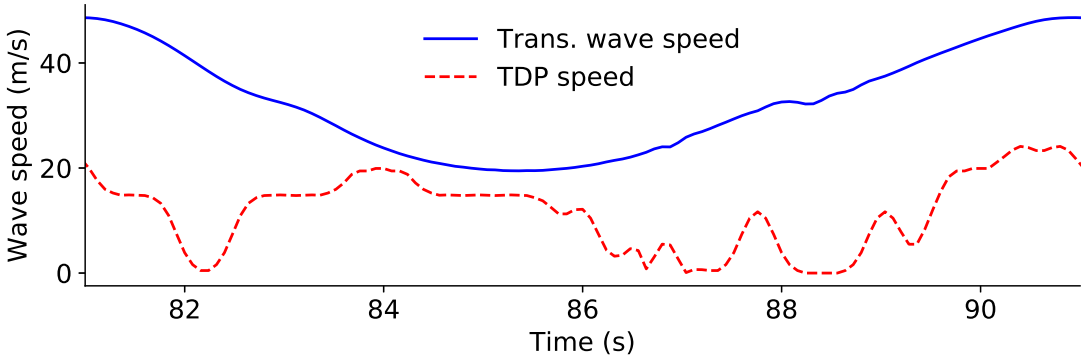

Figure 5.11: Touchdown point and transverse wave speeds for Case 1 during time window 81 s $\leq t \leq$ 91 s.

The touchdown point and transverse wave speeds in Cases 3 and 1 are shown in Figures 5.10 and 5.11 respectively. Figure 5.10 shows the occurrence of the touchdown point speed exceeding the transverse wave speed between 665 s and 750 s, which corresponds to the occurrence of snap load tension fluctuations that comprise of line unloading and loading shocks. Between 750 s and 800 s, the touchdown point speed is lower than the transverse wave speed in Case 3. Hence, the tension fluctuations that occur in the $SM^{4.74}$ tension results (see Figure 5.2) are not due to snap loading shocks. This is further illustrated in Figure 5.11 which shows that the touchdown point speed never exceeds the transverse wave speeds and hence not fulfilling the shock condition, even though there are fluctuations occurring in the tension.

The tension fluctuations occurring in the $SM^{4.74}$ model in Case 1, as well as between 750 s and 800 s in Case 3, are caused by nodal grounding. Unlike the snap loading shocks, which may occur when touchdown point velocities and θ angles are relatively low, as shown in Figures 5.7a and 5.8a respectively, and the fairlead tension approaches zero, the nodal grounding tension fluctuations occur when grounding velocities and θ angles are comparatively higher, as presented in Figures 5.7b and 5.8b respectively, and the line does not become slack. Parts of the line in the vicinity of the touchdown point may become slack during nodal grounding, which generates strain discontinuities, however, the magnitude of the negative strains are lower than what occurs in snap loading situations. The MSM model is effective in mitigating the nodal grounding tension fluctuations, but not the snap load tension shocks.

Case 4 is a biharmonic fairlead excitation in the surge direction with a maximum displacement of 18.0 m of the fairlead node from the initial position. For Case 4, Table 5.1 shows that the peak tensions with $SM^{4.74}$ and $SM^{0.84}$, and MSM models underpredict $\overline{T}$ [5] by under 1.8%, while the $SM_7^{4.74}$ model underpredicts $\overline{T}$ by approximately 2%.

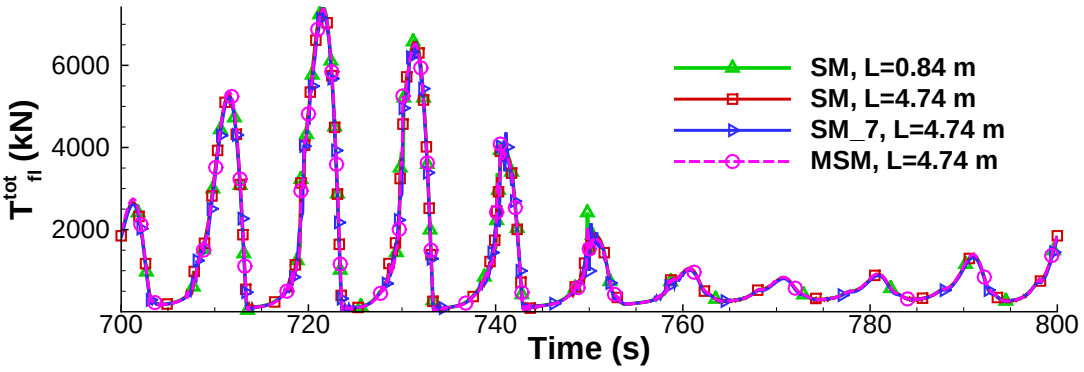

Figure 5.12: Fairlead tension time histories in Case 4 during (700 s $\leq t \leq$ 800 s).

Table 5.13 presents the touchdown point and transverse wave speeds in Case 4 and illustrates that the snap loading shock condition [114] is met between 700 s and 760 s. From 760 s to 800 s, the touchdown point speed is lower than the transverse wave speed. Figures 5.12 and 5.14a respectively show the tension time histories for Case 4 for one period of fairlead motion and a close-up view during the time window (700 s $\leq t \leq$ 760 s) when snap load shocks occur. During 700 s $\leq t \leq$ 760 s, even though the shock condition is not met, tension fluctuations appear in the results for the $SM^{4.74}$ model, but are significantly reduced in the

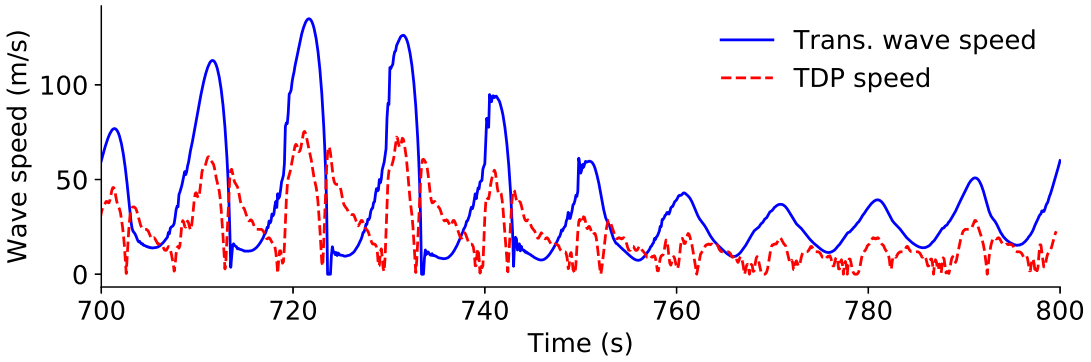

Figure 5.13: Touchdown point and transverse wave speeds for Case 4 during (700 s $\leq$ $t \leq$ 800 s).

$SM^{0.84}$ and $SM_7^{4.74}$ and $MSM^{4.74}$ models. As was in Case 3, the tension fluctuations occurring during 760 s $< t \leq$ 800 s are due to the occurrence of nodal grounding. As shown in the tension histories for the $SM^{0.84}$, $SM_7^{4.74}$ and $MSM^{4.74}$ models, this type of fluctuations can be mitigated by refining the nodal density and judiciously modifying the seabed force coefficients.

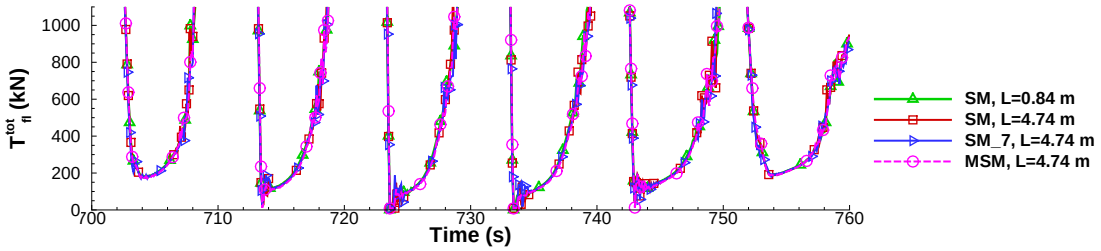

(a) Fairlead tension time histories for Case 4 with time window (700 s $\leq t \leq$ 750 s).

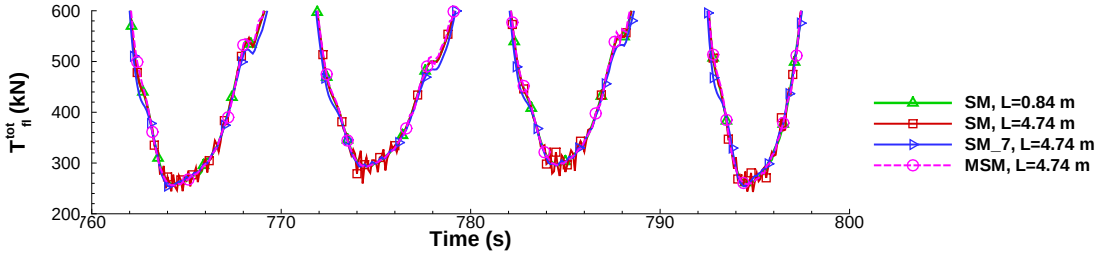

(b) Fairlead tension time histories for Case 4 with time window (750 s $\leq t \leq$ 800 s).

Figure 5.14: Fairlead tension time histories for Case 4 with SM, SM_7, MSM seabed models and 4.74 m and 0.84 m-element discretisations.

Figures 5.15 and 5.16 respectively show the touchdown node vertical velocity and θ angles during the two aforementioned time windows in Case 4. It is observed from Figure 5.16a that in the time window (700 s $\leq t \leq$ 760 s) during which snap loading fluctuations occur, the θ angles were under 0.3 rad, and in general lower than the θ angles in the time window (760 s $< t \leq$ 800 s) during which

nodal grounding fluctuations occur, presented in Figure 5.16b. An exception for this trend occurred at 756 s, when the θ angle exceeds 0.3 rad. Comparing Figures 5.15a and 5.15b, it is observed that the maximum grounding velocities in the time windows (700 s $\leq t \leq$ 760 s) and (760 s $< t \leq$ 800 s) are of comparable magnitudes approaching 4 m/s.

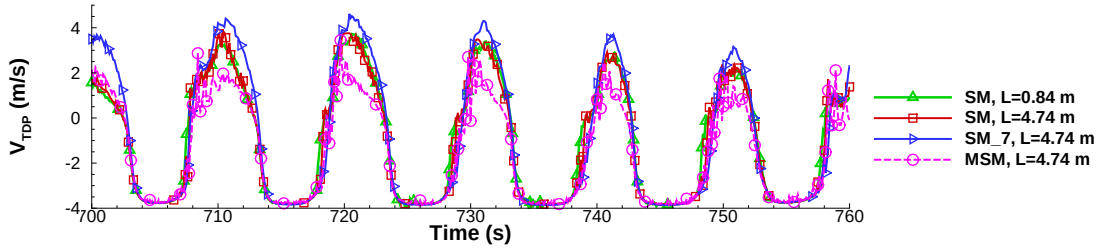

(a) Touchdown node vertical velocities for Case 4 during (700 s $\leq t \leq$ 750 s).

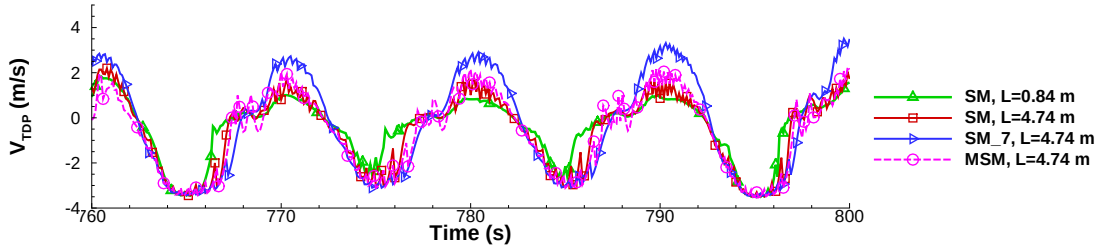

(b) Touchdown node vertical velocities for Case 4 during (750 s $\leq t \leq$ 800 s).

Figure 5.15: Touchdown node vertical velocities for Case 4 with SM, SM_7, MSM seabed models and 4.74 m and 0.84 m-element discretisations.

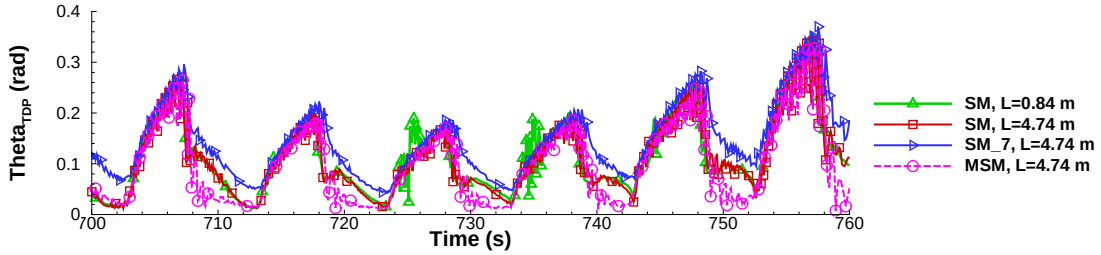

(a) Grounding element θ angles for Case 4 during (700 s $\leq t \leq$ 750 s).

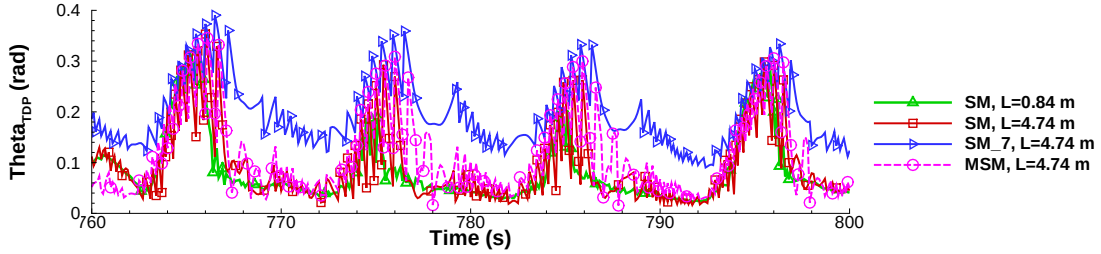

(b) Grounding element θ angles for Case 4 during (750 s $\leq t \leq$ 800 s).

Figure 5.16: Grounding element θ angles for Case 4 with SM, SM_7, MSM seabed models and 4.74 m and 0.84 m-element discretisations.

The grounding velocity and θ angle at $t = 786$ s, which are approximately 3 m/s and 0.3 rad respectively, are compared with the grounding velocities and θ angles at $t = 756$ s, respectively 3.75 m/s and 0.35 rad, and are therefore higher than necessary to induce nodal grounding fluctuations. However, due to the snap load shock condition being met at 756 s, the more severe fluctuations arising from the alternating slack and taut tension states were preeminent.

5.2.2 Deep water environment

A multi-segment, chain-wire rope-chain line with structural parameters enumerated in Figure A.2 is used in the present deep water case, with a water depth of 914.0 m. The pretension is 1200 kN, and the initial line geometry is shown in Figure 5.17. The fairlead excitation for Case 4 with parameters listed in Figure B.2 is used in this case. Comparisons are made between the SM, SM_7 and MSM models for the in-house code and Orcaflex (using the deep water seabed coefficient set presented in Figure C.1), with element sizes of 8.0 m and 4.0 m.

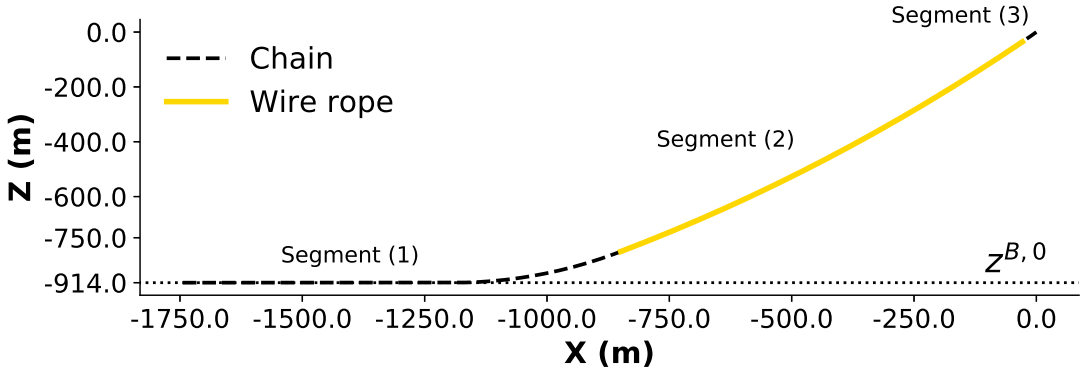

Figure 5.17: Initial static line geometry for multisegment mooring line.

The fairlead tension time series for one low frequency oscillation period of 100 s is included in Figure 5.18, while the touchdown point and transverse wave speeds are plotted in Figure 5.19. The results from Orcaflex and the in-house code are in good agreement, as evident in Figure 5.18, with a maximum difference in the peak tension of 30 kN, or 1.2%, with no noticeable phase difference in the time histories. The peak tensions from the in-house code using the SM, SM_7 and MSM models for the 8.0 m and 4.0 m element discretisations differ by a maximum of 24 kN or 0.95%.

Figure 5.19 shows that the tension shock conditions are met in the time window 700 s $\leq t \leq$ 800 s. However, in contrast to the shallow water cases presented in Section 5.2.1, the tension fluctuations in the deep water case are less pronounced. There are spikes in the SM_7 tension results at the local tension peaks at 730.5 s, 740.5 s, 750.5 s, 760.5 s and 770.5 s but these are small in magnitude.

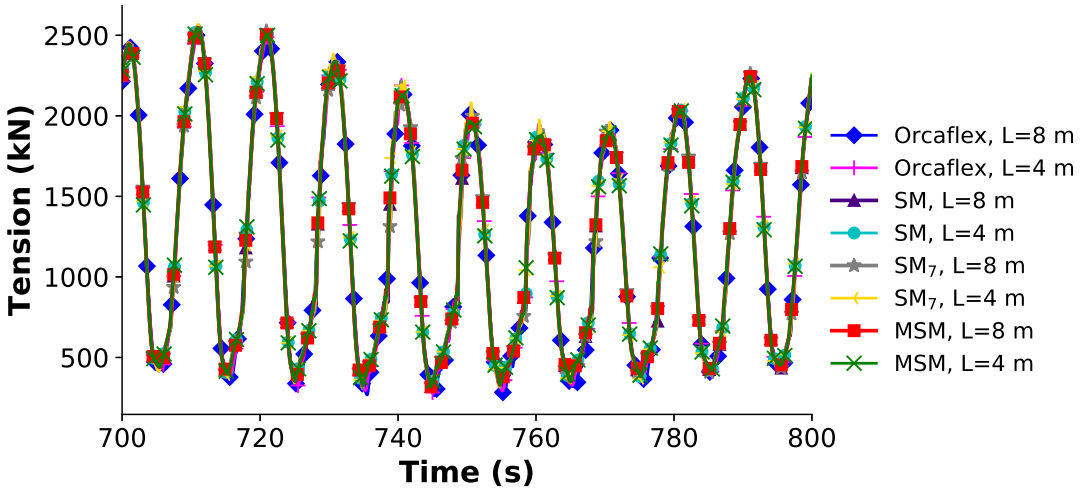

Figure 5.18: Fairlead tension time histories for Orcaflex and in-house code using SM, SM_7 and MSM seabed models for multisegmented line in deep water with Case 4 fairlead excitation during time window (700 s $\leq t \leq$ 800 s).

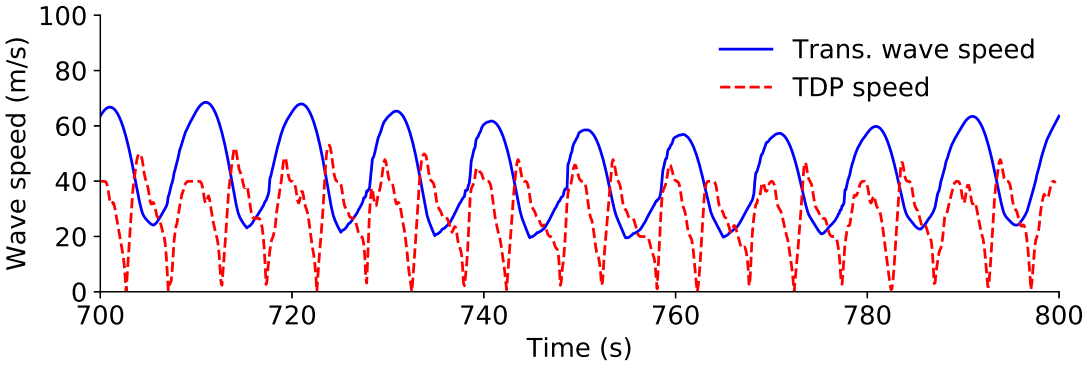

Figure 5.19: Touchdown point and transverse wave speeds for deep water case during time window (700 s $\leq t \leq$ 800 s).

Figure 5.20 shows the strain distribution in the mooring line over one such tension shock cycle (744.67 s $\leq t \leq$ 748.38 s) during which a section of the line goes slack and subsequently returns to a tensioned state. The location of line section in compression is in the vicinity of the touchdown point. As is typical of slack line tension shocks, the magnitude of the compressive strain during the snap load cycle in the present case is significantly more severe than the negative strains associated

with tension fluctuations arising from nodal grounding (see Figure 3.11a). The large strain gradients present thus generate propagating stress waves. The absence of large fluctuations in the fairlead tension is likely due to the significant physical separation between the source of the stress waves at the touchdown point and the fairlead. In the present deep water case, the distance between the fairlead and the line section under compression is approximately 1550 m, whereas in the shallow water Cases 1 and 3, the distances is considerable shorter at 160 m and 100 m, as shown in Figures 3.11a and 5.9 respectively. It is likely due to this larger separation distance that the travelling stress waves have been attenuated significantly due to fluid and line structural damping when they arrive at the fairlead.

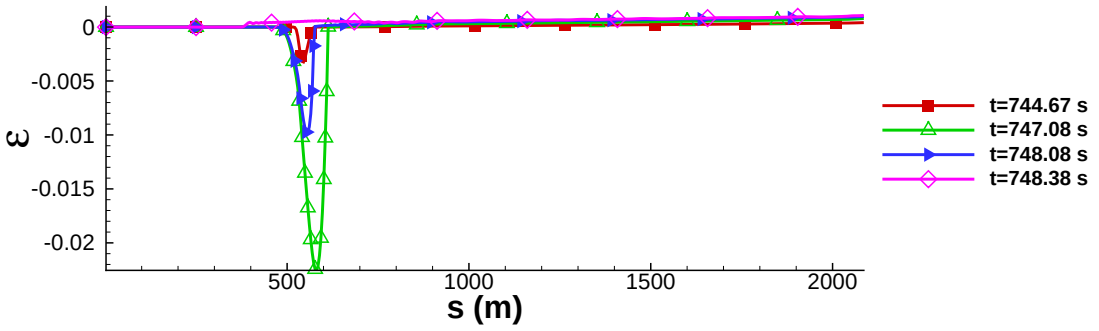

Figure 5.20: Strain distribution during slack and snap loading with time window (700 s $\leq$ $t \leq$ 800 s).

5.2.3 Effect of line discretisation on Modified Spring-Mattress seabed model coefficients

In Section 5.2.1, the proposed Modified spring-mattress (MSM) model, with coefficients for $N^{B,c}$ and $\zeta^{B,a}$ both set to 1.0 for the 4.74 m element line, was shown to be effective at reducing the severity of the tension fluctuations caused by nodal grounding. The fairlead tension results for Cases 1, 3, and 4 of the shallow water cases, using the same coefficient set of the MSM model with element sizes of 8.0 m, 4.74 m, 2.85 m and 2.03 m, are shown in Figures 5.21, 5.22, and 5.23 respectively. For the time periods during which tension fluctuations have occurred, 84.0 s $\leq t \leq$ 87.0 s in Case 1, 750.0 s $\leq t \leq$ 800.0 s in Case 3 and 760.0 s $\leq t \leq$ 800.0 s in Case 4, disparities in the severity of the reduced tension fluctuations are small between the different discretisations. Hence, the same coefficient set is shown to be applicable

and effective for a range of discretisations, which may be required for nodal density convergence studies.

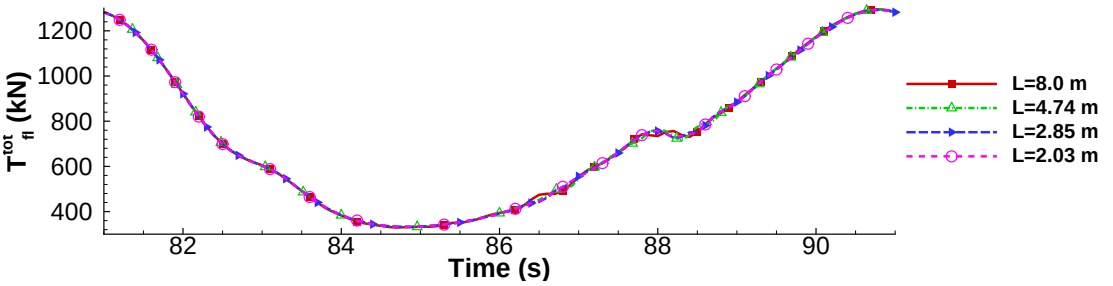

Figure 5.21: Fairlead tension time histories with MSM model ($N^{B,c}$=$\zeta^{B,a}$=1.0) and element lengths of 8.0 m, 4.74 m, 2.85 m and 2.03 m for Case 1.

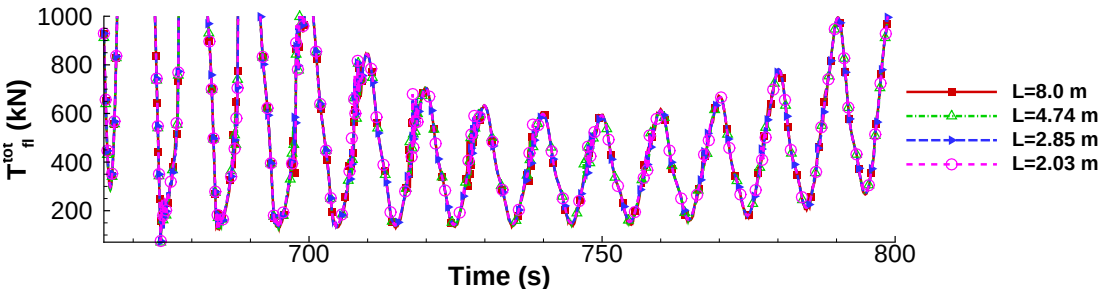

Figure 5.22: Fairlead tension time histories with MSM model ($N^{B,c}$=$\zeta^{B,a}$=1.0) and element lengths of 8.0 m, 4.74 m, 2.85 m and 2.03 m for Case 3.

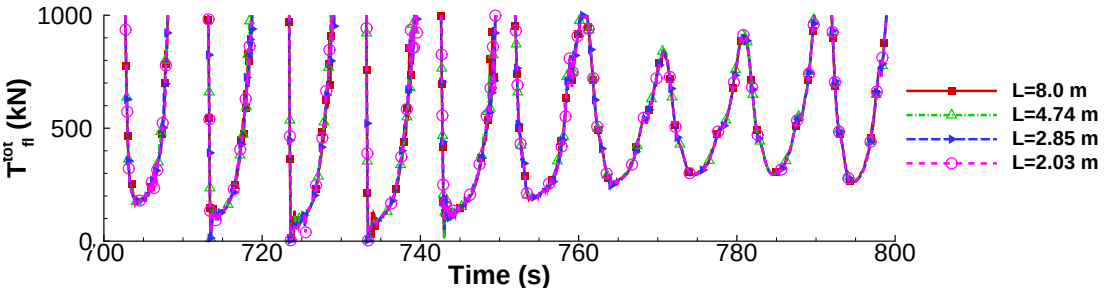

Figure 5.23: Fairlead tension time histories with MSM model ($N^{B,c}$=$\zeta^{B,a}$=1.0) and element lengths of 8.0 m, 4.74 m, 2.85 m and 2.03 m for Case 4.

5.2.4 Summary of findings from shallow and deepwater test cases

Tension fluctuations arise from either line impact with the seabed and slack-snap load cycles. In both situations, negative strain zones may form in the vicinity of the touchdown point and is the source of the propagating stress waves that appear

as fluctuations in the fairlead tension time history. The tension fluctuations are more pronounced in shallow water environments due to the close proximity of the touchdown zone to the fairlead in comparison with deep water cases. For deeper water environments, where distances from the touchdown point to the fairlead are further, the stress waves have to travel longer distances and thus undergo more damping before they arrive at the fairlead.

The tension time histories of the three test cases presented in Figures 5.2, 5.5, and 5.12 suggest that reducing the element size is an effective way to reduce the spurious tension fluctuations due to line-seabed interactions. The element size required depends on the environmental excitation and the grounding velocities of the nodes.

Increasing the seabed thickness coefficient $N^{B,c}$ and thereby reducing the vertical reaction spring stiffness, as well as reducing the vertical damping coefficient $\zeta^{B,d}$ in the SM model are also effective methods to mitigate the nodal grounding tension fluctuations. However, the peak tension results shown in Table 5.1 suggest that using required $N^{B,c}$ and $\zeta^{B,d}$ values tend to reduce peak tensions, leading to less conservative results for line tensions. This has an effect of line overload failure predictions.

The deviations of peak tension from $\overline{T}$ for Cases 1, 3 and 4, with the SM_7 coefficient set, are between -3.73% and -0.36% (underprediction), while the peak tension deviation from $\overline{T}$ with the SM coefficient set is between -0.98% (underprediction) and 1.46% (overprediction). With the MSM model, the peak tension deviation from $\overline{T}$ is between -1.77% and 1.2%. Hence, the SM coefficient set provides the most conservative line tension predictions, followed by the MSM model and SM_7 coefficient set.

The MSM model, while providing slightly less conservative maximum tension predictions compared to the SM model, is able to significantly reduce the tension fluctuations caused by line-seabed impact. The peak tensions calculated by the MSM model is also more conservative compared to the SM_7 coefficient set while providing similar effectiveness in the mitigation of the tension fluctuations. The MSM model achieves this primarily through a higher-order formulation of the vertical reaction force that calculates the reaction force based on the embedment depth of the half elements bounding a node. The application of an added mass force also

lowers the natural frequencies of line section that is in contact with the seabed and further reduces the tension fluctuations. However, a drawback is that the embedment depth of the grounding nodes may be overestimated.

The proposed Modified Spring-Mattress (MSM) model uses the coefficient set given in Table C.2 and its effectiveness in reducing the severity of the tension fluctuations arising from nodal grounding for a range of fairlead excitation frequencies and magnitudes, particularly in shallow water conditions, was shown in Section 5.2.1.

Finally, the recommended values for the artificial added mass, $\zeta^{B,a}$, seabed thickness $N^{B,c}$ coefficients in the MSM model, are both 1.0 and are generally applicable to different line materials and discretisations.

5.3 Chapter closure

A Modified Spring-Mattress model that calculates the vertical reaction force based on the orientation and elevation of the elements bounding a node was presented. This allows a more gradual application of the seabed vertical force without defining a large seabed force cutoff elevation as required in the conventional spring-mattress model. The definition of an artificial added mass force also acts to reduce the natural frequencies of the line section in contact with the seabed. The model was able to avoid the fairlead tension fluctuations for the severe excitation test cases when used together with a relatively coarse line discretisation, while also providing more conservative estimates of the peak line tensions compared with the spring-mattress model applied with the force coefficients required to adequately mitigate the tension fluctuations. The recommended values for the force coefficients in the proposed model were also given and are generally applicable to different line materials, discretisations and environments.

Chapter 6

Conclusion and Recommended Future Work

The motivation for this research is to investigate the behavior of discrete mooring line numerical models during severe seabed impact conditions. Particularly, it was noticed that tension results from a widely used commercial software tended to exhibit curious fluctuations when line grounding occurs. To conduct a comprehensive investigation of the contributing factors and circumstances that lead to this behavior, and subsequently make fundamental modifications to calculation methods, it was not feasible to rely solely on commercial software. Therefore a dynamic mooring line numerical model was developed in order to have full control over modelling approaches and numerical methods and parameters. A review of the investigations, findings and contributions of this work are presented in Section 6.1. Areas of future work are suggested in Section 6.2.

6.1 Thesis summary and conclusions

6.1.1 Key findings

The dynamic behavior of a mooring line under several fairlead excitation cases of varying severity was investigated with a commercial software and an in-house code. It was shown that the magnitudes of the periodic fairlead excitations was less of a contributing factor to the tension fluctuations than their frequencies, as evidenced

by the results from the pure slow-drift and wave-frequency excitations; even though the magnitude of the single harmonic slow-drift motions was significantly larger that the single harmonic wave-frequency motion, the former did not cause tension fluctuations.

The two conditions that are required for the production of the tension fluctuations are firstly, high nodal grounding velocities, and secondly, large strain gradients in the line model. The discrete nature of numerical mooring line models, consisting of spring-damper elements, is susceptible to numerical errors caused by rapid seabed impact. The nodal grounding velocities are directly related to the fairlead motion velocity. Even within the same excitation profile, the tendency to produce tension fluctuations was directly correlated to the instantaneous fairlead velocity. High nodal grounding velocities lead to the rapid increase of seabed forces, which is modelled by a stiff spring. This arrests the downward motion of the grounding node during the unloading cycle of the fairlead excitation period, while the suspended nodes continue on a downward motion towards the seabed. This leads to formation of localised low strain or slack regions in the vicinity of the touchdown point. These large strain gradients directly translate to unbalanced nodal tension forces which cause large nodal accelerations and motions that propagate outwards from the touchdown zone as shock waves.

As the shock waves travel along the line, they are damped by the dissipative forces, namely the internal structural damping forces, as well as hydrodynamic drag. Hence, the longer the length of the line between the touchdown zone, where the shock waves originate, and the fairlead is, the greater the attenuation of the shocks waves is before they arrive at the fairlead. Hence, for deep water simulations, the effects of the tension shocks due to nodal grounding can be insignificant, while it can be rather severe in shallow water conditions.

A secondary contributing factor to the production of large strain gradients is the orientation of a grounding element as it makes contact with the seabed. Larger grounding angles increase the likelihood of the creation of low strain regions and large strain gradients, particularly if the grounding velocities are significant. In the limit of the grounding angle being zero as it impacts the seabed, in effect the condition of an element being perfectly horizontal, the seabed force model will not cause the element length to contract, and thus avoids the creation of a low strain region. In contrast, if an element is perfectly vertical, then the occurrence of a

low strain region at the touchdown point is very high if the suspended part of the mooring line continues on a descending trajectory.

Potential solutions for circumventing the creation of the propagating shock waves were identified; namely, they are local mesh refinement close to the touchdown zone, and modifications to the widely used spring-mattress seabed force model to reduce the tendency of discretised line models to produce large strain gradients during nodal grounding. In addition to an improved understanding of the causal factors for the tension fluctuations, the development of these solution methods are the contributions of this research.

6.1.2 Contributions

6.1.2.1 Dual-rate, adaptive discretisation method for mooring line dynamics modelling

This solution approach is premised on the hypothesis (see Section 1.3) that mesh refinement is an effective means of suppressing the production of tension shock waves, and its subsequent verification, as discussed in Section 3.2.2. It was determined that refinement of the nodal density is required in the vicinity of the touchdown zone. Converged peak tension results were obtainable with such a spatial discretisation scheme. In addition, the effects of tension shock waves were effectively removed from the tension time series. However, such a discretisation scheme also gives rise to a stiff system of equations of motion for time integration. This was the motivation for the development of a dual-rate time integration approach, presented in Section 4.1, in which different time-steps were used for the time-marching of the line sections consisting of different element lengths and thus imposed different time-step limits. The results of such a time integration scheme showed good agreement with a monolithic time integration approach. A method was also presented in Section 4.1.2 to determine the optimal time-step ratio between the latent (coarse mesh) and active partitions (fine mesh), based on the evaluation of numerical stability requirements of the base integration scheme and the total simulation time.

In situations where a significant section of a mooring line experiences liftoff and grounding on the seabed will require an enlarged refined mesh region, which necessarily incurs a higher computational cost. Hence, in order for the dual-rate integration method to be computationally efficient for a wide range of dynamic conditions, an adaptive discretisation method, presented in Section 4.2, was developed so that the refined mesh is limited only to a small section of the line which is the touchdown zone in this work.

6.1.2.2 Modified Spring-Mattress model

The spring-mattress model is widely applied to model the seabed in dynamic mooring models due to its generality and efficiency. However, as was demonstrated in this research, the conventional approach tends to produce large strain gradients during nodal grounding. The development of the improved spring-mattress model, presented in Section 5.1, follows from the hypothesis (see Section 1.3) that a higher-order seabed force model which accounts for the discrete nature of the line structural model is a potential solution for reducing line-seabed impact shocks. In the proposed model, the vertical reaction force is calculated based on the orientation and elevation of the elements bounding a node. Hence the seabed force on an element is calculated from the length extent and depth of embedment of the element relative to the seabed elevation instead of considering only the position of individual nodes, allowing for a more gradual application of the vertical seabed reaction force without defining a large seabed force cutoff elevation as required in the conventional spring-mattress model.

Another feature of the improved spring-mattress model is the definition of an artificial added mass force also acts to reduce the natural frequencies of the line section in contact with the seabed. This was inspired by the concept of hydrodynamic added mass, and motivated by a requirement to dampen the vibrations of nodes experiencing large spatial and temporal changes in applied forces. There are force coefficients to be specified in the improved spring-mattress model, however, the results indicate that a single set of coefficients is generally applicable for different line materials, discretisations and environments.

6.2 Future work

Based on the work that has been performed in this research, some suggested areas for future research is proposed as follows:

1. The Modified Spring-Mattress model currently neglects bending and torsional effects. It can be improved upon to account for line bending and torsional effects so that it can be applied to pipeline and riser models.

2. The force coefficients for the proposed spring-mattress model works well for the given line material and discretisations under a wide range of excitation conditions. A wider investigation using different line materials, water depths, and discretisations could be conducted to ascertain that the coefficients are generally applicable. A procedure for the determination of suitable force coefficients for a particular set of simulation conditions can then be devised.

3. In the hybrid fine/coarse discretisation scheme, there may be potential for the size of the refined segment to the reduced. A smaller refined segment reduces the computational load of time integration, but might require an increased number of discretisation switches. Hence, a trade-off study will be helpful to refine the discretisation methodology.

4. It was shown that the element grounding angle is a factor which influences the likelihood of the production of large strain gradients, and that lower grounding angles are less likely to cause them. For a catenary line, there are line sections which are more prone to experiencing large grounding angles than others. Hence, it is possible that the level of mesh refinement required for different line sections, from the perspective of mitigating the effect of tension shocks, are different. This will allow coarser elements to be used in line sections where smaller elements are not necessary during nodal grounding.

5. The use of different line materials and discretisations along a mooring line gives rise to different time constants for different sections. The potential for applying a multi-rate time integration method to the mooring line, and the efficiency gains of such an approach, requires further investigation. In this work, a staggered approach was used for the time integration of the latent and active partitions. A concurrent approach, such as the scheme proposed

by Kaværno and Rentrop [144] or the Multi-rate Partitioned Runge-Kutta method presented by G*ü*nther et al. [137], may be suitable for a multi-rate time integration approach in which there are multiply-linked partitions. Another fully concurrent approach using explicit Runge-Kutta schemes is that presented by Grote et al. [143].

6. To provide a more comprehensive evaluation of the performance of the dual-rate time-integration procedure presented in Chapter 4.1, a comparison with implicit methods such as the Generalized-α [154], Newmark-β [155] and Wilson-θ [156] can be performed. In terms of computational efficiency, the superior stability characteristic of implicit methods allows larger time-steps to be used, at the cost of higher computational cost per time-step due to the iterative solution procedure performed within each time-step. In general, as noted by Belytschko [157], time-integration of coupled components, which can consist of stiff and non-stiff partitions, may be achieved with different approaches. Belytschko enumerates these procedures as explicit-explicit, explicit-implicit and implicit-implicit schemes. An example of an explicit-explicit method is the the procedure discussed in Chapter 4.1, in which explicit methods and different time-steps are applied in separate partitions. In the explicit-implicit approach, the stiff and non-stiff components are integrated with implicit and explicit integration schemes respectively with the same time-step in both partitions. Finally, in an implicit-implicit approach, different matrix solving procedures are implemented applied in each partition within an iteration loop. With the exception of the work performed by Thomas [112], little attention has been given to the analysis of monolithic time-integration procedures applied to mooring line dynamics. Furthermore, there appears to be a gap in existing literature on the application of multi-rate integration procedures for time-domain analysis of mooring lines.

Appendix A

Line Structural Parameters

Table A.1: Single-segment line structural parameters.

Parameter	Data
Material Type	Chain
Line length (m)	711.3
Stiffness, EA (MN)	1690
Axial structural damping ratio	0.08
Mass per unit length (kg/m)	365.72
Wet weight per unit length (kN/m)	3202
Normal Drag coefficient, C_d^ν	3.2
Axial Drag coefficient, C_d^τ	0.6
Normal added mass coefficient, C_a^ν	1.6
Axial added mass coefficient, C_a^τ	0.2
Diameter, D (m)	0.14
Structural damping ratio, ζ^S	0.08
Element size (m)	8.0

Table A.2: Multi-segment line structural parameters.

Parameter	Seg. 1	Seg. 2	Seg. 3
Material Type	Chain	Wire	Chain
Segment length (m)	914.4	1127.8	45.7
Stiffness, EA (MN)	794	690	794
Mass per unit length (kg/m)	147.08	41.38	147.08
Wet weight per unit length (kN/m)	1379.80	343.23	1379.80
Normal Drag coefficient, C_d^ν	2.4	1.2	2.4
Axial Drag coefficient, C_d^τ	1.15	0.008	1.15
Normal added mass coefficient, C_a^ν	1.0	1.0	1.0
Axial added mass coefficient, C_a^τ	0.5	0.0	0.5
Diameter, D (m)	0.089	0.089	0.089
Structural damping ratio, ζ^S	0.08	0.08	0.08

Appendix B

Prescribed Fairlead Motion Parameters

B.1 Prescribed fairlead position and velocity functions

$$\mathbf{r}(t) = R_{ramp}(t) \sum_{i=1}^{3} \left[r_i^{WF} \sin\left(\frac{2\pi t}{T_i^{WF}} + \phi_i^{WF} \right) + r_i^{LF} \sin\left(\frac{2\pi t}{T_i^{LF}} + \phi_i^{LF} \right) \right] \hat{\mathbf{e}}_i \tag{B.1}$$

$$\dot{\mathbf{r}}(t) = R_{ramp}(t) \sum_{i=1}^{3} \left[\frac{2\pi r_i^{WF}}{T_i^{WF}} \cos\left(\frac{2\pi t}{T_i^{WF}} + \phi_i^{WF} \right) + \frac{2\pi r_i^{LF}}{T_i^{LF}} \cos\left(\frac{2\pi t}{T_i^{LF}} + \phi_i^{LF} \right) \right] \hat{\mathbf{e}}_i \tag{B.2}$$

B.2 Prescribed fairlead position and velocity function coefficients

Table B.1: Prescribed fairlead motion profiles for validation cases without seabed contact.

Case	r_1^{WF} (m)	T_1^{WF} (s)	ϕ_1^{WF} (rad)	r_2^{WF} (m)	T_2^{WF} (s)	ϕ_2^{WF} (rad)	r_3^{WF} (m)	T_3^{WF} (s)	ϕ_3^{WF} (rad)
1	5.4	10.0	0.0	-	-	-	-	-	-
2	-	-	-	-	-	-	5.4	10.0	0.0
3	3.0	10.0	1.4	3.0	10.0	3.8	3.0	10.0	5.4

Table B.2: Prescribed fairlead motion profiles for evaluation for cases with nodal grounding.

Case	r_1^{WF} (m)	T_1^{WF} (s)	ϕ_1^{WF} (rad)	r_3^{WF} (m)	T_3^{WF} (s)	ϕ_3^{WF} (rad)	r_1^{LF} (m)	T_1^{LF} (s)	ϕ_1^{LF} (rad)	r_3^{LF} (m)	T_3^{LF} (s)	ϕ_3^{LF} (rad)
1	5.4	10.0	0.0	-	-	-	-	-	-	-	-	-
2	-	-	-	-	-	-	10.0	100.0	0.0	-	-	-
3	-	-	-	5.4	10.0	0.0	20.0	200.0	0.0	-	-	-
4	8.0	10.0	0.0	-	-	-	10.0	100.0	0.0	-	-	-

Appendix C

Force Coefficients for Seabed Models

Table C.1: Seabed model coefficients for Orcaflex.

Parameter	Shallow water	Deep water
Water depth (m)	82.5	914.0
Vertical stiffness (kN/m/m^2)	131.95	348.00
Shear stiffness (kN/m/m^2)	131.95	348.00
Horizontal friction coefficient	0.74	0.74

Table C.2: Seabed model coefficients in spring mattress (SM) and modified spring mattress (MSM) models for in-house code.

Model	$\zeta^{B,d}$	$\zeta^{B,f,t}$	$\zeta^{B,f,N}$	$\mu^{B,f,t}$	$\mu^{B,f,N}$	$N^{B,c}$	$\zeta^{B,a}$
SM	1.0	1.0	1.0	0.74	0.74	1.0	0.0
SM_1	1.0	1.0	1.0	0.74	0.74	5.0	0.0
SM_2	1.0	1.0	1.0	0.74	0.74	10.0	0.0
SM_3	1.0	1.0	1.0	0.74	0.74	15.0	0.0
SM_4	1.0	1.0	1.0	0.74	0.74	20.0	0.0
SM_5	0.0	1.0	1.0	0.74	0.74	5.0	0.0
SM_6	0.0	1.0	1.0	0.74	0.74	10.0	0.0
SM_7	0.0	1.0	1.0	0.74	0.74	15.0	0.0
SM_8	0.0	1.0	1.0	0.74	0.74	20.0	0.0
MSM	0.15	1.0	1.0	0.74	0.74	1.0	1.0

Bibliography

[1] O.M. Faltinsen. *Sea Loads on Ships and Offshore Structures*. Cambridge, New York: Cambridge University Press, 1990. ISBN 0521458706. doi: 9780521458702.

[2] J.M.J. Journée and W .W. Massie. *Offshore Hydromechanics*. 2001. doi: 10.1016/S0013-4686(01)00879-9. Last accessed April 2015.

[3] Sigrid Leyendecker and Sina Ober-Blöbaum. A Variational Approach to Multirate Integration for Constrained Systems. In Jean-Claude Samin and Paul Fisette, editors, *Multibody Dynamics*, pages 97–121. Basel, Switzerland: Springer Nature Switzerland AG, 2013. ISBN 9789400754041. doi: 10.1007/978-94-007-5404-1.

[4] DNV-GL. Global Performance Analysis of Deepwater Floating Structures (DNV-RP-F205), 2010. URL `https://rules.dnvgl.com/docs/pdf/DNV/codes/docs/2009-04/RP-F205.pdf`. Last accessed August 2015.

[5] D. T. Brown and S. A. Mavrakos. Comparative study on mooring line dynamic loading. *Marine Structures*, 12:131–151, 1999. doi: 10.1016/S0951-8339(99)00011-8.

[6] U.S. Energy Information Agency. *International Energy Outlook 2014*. 2014. ISBN 0160920663. doi: EIA-0484(2013). URL `http://www.eia.gov/forecasts/ieo/pdf/0484(2013).pdf`. Last accessed April 2015.

[7] Chor Foon Tang, Bee Wah Tan, and Ilhan Ozturk. Energy consumption and economic growth in Vietnam. *Renewable and Sustainable Energy Reviews*, 54:1506–1514, 2016. ISSN 13640321. doi: 10.1016/j.rser.2015.10.083.

[8] Yabo Zhao and Shaojian Wang. The Relationship between Urbanization, Economic Growth and Energy Consumption in China: An Econometric Perspective Analysis. *Sustainability*, 7(5):5609–5627, 2015. ISSN 2071-1050. doi: 10.3390/su7055609.

[9] Muhammad Azam, Abdul Khan, B. Bakhtyar, and Chandra Emirullah. The causal relationship between energy consumption and economic growth in the ASEAN-5 countries. *Renewable and Sustainable Energy Reviews*, 47:732–745, 2015. ISSN 03014215. doi: 10.1016/j.enpol.2012.08.034.

[10] British Petroleum. BP Technology Outlook, 2015. URL `https://www.bp.com/technologyoutlook`. Last accessed December 2015.

[11] Åsa Waldo. Offshore wind power in Sweden-A qualitative analysis of attitudes with particular focus on opponents. *Energy Policy*, 41:692–702, 2012. ISSN 03014215. doi: 10.1016/j.enpol.2011.11.033.

[12] Maarten Wolsink. Wind power implementation: The nature of public attitudes: Equity and fairness instead of 'backyard motives'. *Renewable and Sustainable Energy Reviews*, 11(6):1188–1207, 2007. ISSN 13640321. doi: 10.1016/j.rser.2005.10.005.

[13] S Butterfield and Palm Beach. Future for Offshore Wind Energy in the United States. Technical report, 2004. URL `https://www.nrel.gov/docs/fy04osti/36313.pdf`. Last accessed August 2015.

[14] Dominique Roddier, Christian Cermelli, Alexia Aubault, and Alla Weinstein. WindFloat: A floating foundation for offshore wind turbines. *Journal of Renewable and Sustainable Energy*, 2:1–34, 2010. ISSN 19417012. doi: 10.1063/1.3435339.

[15] Jason M. Jonkman. Dynamics of offshore floating wind turbines-model development and verification. *Wind Energy*, 12(5):459–492, 2009. ISSN 10954244. doi: 10.1002/we.347.

[16] Simon Philippe Breton and Geir Moe. Status, plans and technologies for offshore wind turbines in Europe and North America. *Renewable Energy*, 34 (3):646–654, 2009. ISSN 09601481. doi: 10.1016/j.renene.2008.05.040.

[17] Bret Bosma. *On the Design, Modeling, and Testing of Ocean Wave Energy Converters*. PhD thesis, Oregon State University, Oregon, USA, 2013.

[18] A. Muetze and J. G. Vining. Ocean Wave Energy Conversion - A Survey. In *Conference Record of the 2006 IEEE Industry Applications Conference Forty-First IAS Annual Meeting*, pages 1410–1417, Tampa, Florida, USA, 2006. doi: 10.1109/IAS.2006.256715.

[19] Balwinder Rangi and Ben Wilby. Floating Production Systems Expenditure To Total USD 81 Billion From 2015 to 2019. *Oil and Gas Facilities*, (April 2015):14–17, 2015. Last accessed October 2015.

[20] M. Iannuzzi. Environmentally assisted cracking (EAC) in oil and gas production. In V S Raja and Tetsuo Shoji, editors, *Stress Corrosion Cracking*, pages 570–607. Cambridge, UK: Woodhead Publishing, Cambridge, 1st edition, 2011. ISBN 9780857093769. doi: 10.1533/9780857093769.4.570.

[21] David T. Brown. Mooring Systems. In S. Chakrabarti, editor, *Handbook of Offshore Engineering*, chapter 8, pages 663–707. New York, USA: Elsevier Science, 2005.

[22] Chris Jenman. Mixing Dynamic Positioning And Moorings. In *Annual Conference of the Dynamic Positioning Committee*, pages 1–13, Houston, Texas, USA, 2005.

[23] Judy Murray. Conventional Mooring Reaches Deeper, 2008. URL `http://www.intermoor.com/information-center-23/technical-articles-26/conventional-mooring-reaches-deeper-106`. Last accessed October 2015.

[24] Hubert Faÿ. Mooring and Dynamic Positioning. In *Dynamic Positioning Systems: Principles, Design and Applications*, pages 163–168. Paris, France: Editions Technip, 1990.

[25] James Brekke. Drilling and Production Risers. In Subrata K Chakrabarti, editor, *Handbook of Offshore Engineering*, chapter 9. New York, USA: Elsevier Science, 1st edition, 2005.

[26] Subrata K Chakrabarti. Ocean Environment. In Subrata K Chakrabarti, editor, *Handbook of Offshore Engineering*, chapter 3. New York, USA: Elsevier Science, 1st edition, 2005.

[27] Christian Aage. The ITTC Specialist Committee on Deep Water Mooring, Written Discussion. In *Proceedings of the 22nd International Towing Tank Conference, ITTC '99*, pages 707–799, Seoul, Korea, 2000.

[28] H. Ormberg and K. Larsen. Coupled analysis of floater motion and mooring dynamics for a turret-moored ship. *Applied Ocean Research*, 20:55–67, 1998. ISSN 01411187. doi: 10.1016/S0141-1187(98)00012-1.

[29] Y. M. Low and R S Langley. Understanding the dynamic coupling effects in deep water floating structures using a simplified model. *Journal of Offshore Mechanics and Arctic Engineering-Transactions of the Asme*, 130(3), 2008. ISSN 08927219. doi: 10.1115/1.2904951.

[30] Halvor Lie, Zhen Gao, and Torgeir Moan. Mooring Line Damping Estimation by a Simplified Dynamic Model. In *Proceedings of the 26th International Conference on Offshore Mechanics and Arctic Engineering*, San Diego, California, USA, 2007. ISBN 0791842673. doi: 10.1115/OMAE2007-29155.

[31] DNV-GL. Environmental Conditions and Environmental Loads (DNV-RP-C205), 2010. URL `https://rules.dnvgl.com/docs/pdf/dnv/codes/docs/2010-10/rp-c205.pdf`. Last accessed October 2015.

[32] K. E. Kaasen. Time Domain Model Representations of Standard Wind Gust Spectra. In *Proceedings of the 9th International Offshore and Polar Engineering Conference*, pages 74–78, Brest, France, 1999.

[33] Minoo Patel. Fluid loading on offshore structures. In *Dynamics of offshore structures*, chapter 5, pages 174–214. Oxford, United Kingdom: Butterworth-Heinemann, 1st edition, 1989. ISBN 978-0-408-01074-0. doi: 10.1016/B978-0-408-01074-0.50008-2.

[34] J.A. Pinkster. *Low frequency second order wave exciting forces on floating structures*. PhD thesis, Delft University of Technology, Delft, Netherlands, 1980.

[35] C.H. Lee. WAMIT theory manual, 1995. URL `https://www.wamit.com/Publications/tmanual.pdf`. Last accessed May 2016.

[36] M. H. Kim, B. J. Koo, R. M. Mercier, and E. G. Ward. Vessel/mooring/riser coupled dynamic analysis of a turret-moored FPSO compared with OTRC

experiment. *Ocean Engineering*, 32(14-15):1780–1802, 2005. ISSN 00298018. doi: 10.1016/j.oceaneng.2004.12.013.

[37] S. Ma and M. H. Kim. Forces on a SPM Offloading Tanker in Shallow Water. *Journal of Offshore Mechanics and Arctic Engineering*, 131(November 2009): 1–6, 2015. doi: 10.1115/1.3160519.

[38] T. Duarte and J. N. A. Sarmento. Effects of Second-Order Hydrodynamic Forces on Floating Offshore Wind Turbines. In *Proceedings of the AIAA Science and Technology Forum and Exposition*, National Harbor, Maryland, USA, 2014.

[39] A. J. Hermans. Low-frequency second-order wave-drift forces and damping. *Journal of Engineering Mathematics*, 35:181–198, 1999.

[40] M. S. Triantafyllou. Cable Dynamics for Offshore Applications. In J. B. Herbich, editor, *Developments in Offshore Engineering: Wave Phenomena and Offshore Topics*, chapter 6, pages 256–294. Houston, Texas, USA: Gulf Publishing Company, 1998.

[41] Dong-sheng Qiao and Jin-ping Ou. Truncated Model Tests for Mooring Lines of a Semi-Submersible Platform and Its Equivalent Compensated Method. *Journal of Marine Science and Technology*, 22(2):125–136, 2014. doi: 10.6119/JMST-013-0108-1.

[42] Gerard Van Oortmerssen. Forces Related to Motions of Moored Ships/ Analytical Methods of Moored Ship Motions. In *Advances in Berthing and Mooring of Ships and Offshore Structures*, pages 265–281. Kluwer Academic Publishers, 1988.

[43] S Brynjolfsson and JW Leonard. Response of guyed offshore towers to stochastic loads : time domain vs frequency domain. *Engineering Structures*, 10:106–116, 1988.

[44] Z Ran, M. H. Kim, and W. Zheng. Coupled dynamic analysis of a moored spar in random waves and currents (time-domain versus frequency-domain analysis). *Journal of Offshore Mechanics and Arctic Engineering-Transactions of the Asme*, 121(3):194–200, 1999.

[45] Chiruvai P. Vendhan. Coupled dynamics of deepwater structures: issues and challenges. *Ships and Offshore Structures*, pages 37–41, 2014. ISSN 1744-5302. doi: 10.1080/17445302.2014.944334.

[46] B. Teng and Y. C. Li. The Linearization of Drag Force and the Error Estimation of Line Force Spectrum. *Coastal Engineering*, 14:173–183, 1990.

[47] Ove T. Gudmestad and Jerome J. Connor. Linearization methods and the influence of current on the nonlinear hydrodynamic drag force. *Applied Ocean Research*, 5(4):184–194, 1983.

[48] R.S. Langley. The linearisation of three dimensional drag force in random seas with current. *Applied Ocean Research*, 6(3):126–131, 1984. ISSN 01411187. doi: 10.1016/0141-1187(84)90001-4.

[49] Riaan van 't Veer. Application of linearized Morison load in pipe lay stinger design. In *Proceedings of the 27th International Conference on Offshore Mechanics and Arctic Engineering*, pages 1–10, Estoril, Portugal, 2008.

[50] Y. M. Low and R. S. Langley. Time and frequency domain coupled analysis of deepwater floating production systems. *Applied Ocean Research*, 28(6): 371–385, 2006. ISSN 01411187. doi: 10.1016/j.apor.2007.05.002.

[51] Yungang Liu and Lars Bergdahl. Frequency-domain dynamic analysis of cables. *Engineering Structures*, 19(6):499–506, 1997. ISSN 01410296. doi: 10.1016/S0141-0296(96)00091-0.

[52] Yungang Liu and Lars Bergdahl. Influence of current and seabed friction on mooring cable response: Comparison between time-domain and frequency-domain analysis. *Doktorsavhandlingar vid Chalmers Tekniska Hogskola*, 19 (1447):945–953, 1998. ISSN 0346718X. doi: 10.1016/S0141-0296(97)00176-4.

[53] Y. M. Low and R. S. Langley. A hybrid time/frequency domain approach for efficient coupled analysis of vessel/mooring/riser dynamics. *Ocean Engineering*, 35:433–446, 2008. ISSN 00298018. doi: 10.1016/j.oceaneng.2008.01.001.

[54] API. Design and Analysis of Stationkeeping Systems for Floating Structures (API-RP-2SK). Technical report, American Petroleum Institute, 2005.

[55] William C. Webster. Mooring-induced damping. *Ocean Engineering*, 22(6): 571–591, 1995. ISSN 00298018. doi: 10.1016/0029-8018(94)00027-5.

[56] E. Huse and Matsumoto K. Practical Estimation of Mooring Line Damping. In *Proceedings of the 20th Offshore Technology Conference*, Richardson, Texas, USA, 1988. doi: doi.org/10.4043/5676-MS.

[57] Yungang Liu and Lars Bergdahl. Improvement on Huse's Model for Estimating Mooring Cable Induced Damping. In *Proceedings of the 17th OMAE Conference*, Lisbon, Portugal, 1998.

[58] C. Bauduin and Mamoun N. A Contribution on Quasi-Static Mooring Damping. *Journal of Offshore Mechanics and Arctic Engineering*, 122(May 2000): 125–133, 2015.

[59] J. E. W. Wichers and R. H. M. Huijsmans. The contribution of hydrodynamic damping induced by mooring chains on low frequency vessel motions. In *Proceedings of the 20th Offshore Technology Conference*, Houston, Texas, 1990. doi: doi.org/10.4043/6218-MS.

[60] D. T. Brown, G. J. Lyons, and H. M. Lin. Advances in Mooring Line Damping. *Underwater Technology*, 21(2):5–11, 1995.

[61] Tianhui Fan. Dynamic effects of equivalent truncated mooring systems for a semi-submersible platform. *Brodogradnja/Shipbilding*, 65(4), 2014.

[62] Tianhui Fan, Dongsheng Qiao, and Jinping Ou. Innovative approach to design truncated mooring system based on static and damping equivalent. *Ships and Offshore Structures*, 9(6), 2015. doi: 10.1080/17445302.2013.867631.

[63] Madjid Karimirad. Effect of Aerodynamic and Hydrodynamic Damping on Dynamic Response of a Spar Type Floating Wind Turbine. In *Proceedings of the European Wind Energy Conference 2010*, Warsaw, Poland, 2010.

[64] J. M. Heurtier, P. Le Buhan, Fontaine E., C. Le Cunff, F. Biolley, and C. Berhault. Coupled Dynamic Response of Moored FPSO with Risers. In *Proceedings of the 11th International Offshore and Polar Engineering Conference, Stavanger, Norway*, 2001.

[65] Matthew Hall and Andrew Goupee. Validation of a lumped-mass mooring line model with DeepCwind semisubmersible model test data. *Ocean Engineering*, 104:590–603, 2015. ISSN 00298018. doi: 10.1016/j.oceaneng.2015.05.035.

[66] H. J. J. van den Boom. Dynamic Behaviour of Mooring Lines. In *Proceedings of the 4th International Conference on Behaviour of Offshore Structures*, Delft, Netherlands, 1985.

[67] Cecile Melis, Philippe Jean, and Pedro Vargas. Out-of-Plane Bending Testing of Chain Links. In *Proceedings of the 24th International Conference on Offshore Mechanics and Arctic Engineering*, Halkidiki, Greece, 2005. doi: 10.1115/OMAE2005-67353.

[68] J. R. M. De Sousa, M. Q. De Siqueira, and G. B Ellwanger. Numerical Analysis of Wire Ropes Considering Coupled Extensional and Torsional Behaviour. In *Proceedings of the 11th International Offshore and Polar Engineering Conference*, Stavanger, Norway, 2001.

[69] M Masciola, J Jonkman, and A Robertson. Implementation of a Multisegmented, Quasi-Static Cable Model. In *Proceedings of the 23rd International Ocean and Polar Engineering Conference*, Alaska, USA, 2013.

[70] Y T Chai, K S Varyani, and N D P Barltrop. Semi-analytical quasi-static formulation for three-dimensional partially grounded mooring system problems. *Ocean Engineering*, 29(6):627–649, 2002. ISSN 00298018. doi: 10.1016/S0029-8018(01)00038-5.

[71] Thomas S. Walton and Harry Polachek. Calculation of transient motion of submerged cables. *Mathematics of Computation*, (14):27–46, 1960. ISSN 0025-5718. doi: http://dx.doi.org/10.1090/S0025-5718-1960-0116470-5.

[72] H. Polachek, T. S. Walton, R. Mejia, and C. Dawson. Transient motion of an elastic cable immersed in a fluid. *Mathematics of Computation*, 17(81):60–63, 1963. ISSN 00255718, 10886842. URL `http://www.jstor.org/stable/2003734`.

[73] Tai Pil Ha. *Frequency and time domain motion and mooring analyses for a FPSO operating in deep water*. PhD thesis, University of Newcastle upon Tyne, Newcastle upon Tyne, United Kingdom, 2011.

[74] Zong-yu Chang, Yuan-guang Tang, Hua-jun Li, Jian-ming Yang, and Lei Wang. Analysis for the deployment of single-point mooring buoy system based on multi-body dynamics method. *China Ocean Engineering*, 26(3): 495–506, aug 2012. ISSN 0890-5487. doi: 10.1007/s13344-012-0037-x.

[75] V.J. Kurian, M.A. Yassir, C.Y. Ng, and I.S. Harahap. Nonlinear dynamic analysis of multi-component mooring lines incorporating line-seabed interaction. *Research Journal of Applied Sciences, Engineering and Technology*, 6 (8):1428–1445, 2013. ISSN 20407459.

[76] M Masciola, J Jonkman, and A Robertson. Extending the Capabilities of the Mooring Analysis Program: A Survey of Dynamic Mooring Line Theories for Integration into FAST. In *Proceedings of the 33rd International Conference on Ocean, Offshore and Arctic Engineering*, San Francisco, California, USA, 2014.

[77] C. Gatti-Bono and Perkins N. C. Numerical Simulations of Cable/seabed Interaction. *International Journal of Offshore and Polar Engineering*, 14 (02), 2004.

[78] Bradley J Buckham. *Dynamics Modelling of Low-Tension Tethers for Submerged Remotely Operated Vehicles*. PhD thesis, University of Victoria, Victoria, British Columbia, Canada, 1997.

[79] Shan Huang and Dracos Vassalos. A numerical method for predicting snap loading of marine cables. *Applied Ocean Research*, 15:235–242, 1993.

[80] S Huang and D Vassalos. Dynamics of small-sagged taut-slack marine cables. *Computers & Structures*, 58(3):557–562, 1996.

[81] D. L. Garrett. Dynamic Analysis of Slender Rods. *Journal of Energy Resources Technology*, 104(4):302, 1982. ISSN 01950738. doi: 10.1115/1.3230419.

[82] Robert D. Cook, David S. Malkus, Michael E. Plesha, and R. J. Witt. *Concept and Applications of Finite Element Analysis*. New Jersey, USA: John Wiley and Sons, Inc., 4th edition, 2002. ISBN 978-0-471-35605-9.

[83] D.L. Garrett. Coupled analysis of floating production systems. *Ocean Engineering*, 32(7):802–816, may 2005. ISSN 00298018. doi: 10.1016/j.oceaneng.2004.10.010.

[84] Arcandra Tahar and M. H. Kim. Coupled-dynamic analysis of floating structures with polyester mooring lines. *Ocean Engineering*, 35(17-18):1676–1685, 2008. ISSN 00298018. doi: 10.1016/j.oceaneng.2008.09.004.

[85] Haifei Chen, Sipeng Xu, and Haiyan Guo. Nonlinear analysis of flexible and steel catenary risers with internal flow and seabed interaction effects. *Journal of Marine Science and Application*, 10(2):156–162, 2011. ISSN 1671-9433. doi: 10.1007/s11804-011-1055-4.

[86] Min Dong Yang, Bin Teng, Long Fei Xiao, De Zhi Ning, Zhong Min Shi, and Yan Qu. Full time-domain nonlinear coupled dynamic analysis of a truss spar and its mooring/riser system in irregular wave. *Science China Physics, Mechanics and Astronomy*, 57(1):152–165, 2014. ISSN 1674-7348. doi: 10.1007/s11433-013-5273-4.

[87] John W Leonard and John H Nath. Comparison of finite element and lumped parameter methods for oceanic cables. *Engineering Structures*, 3:153–167, 1981.

[88] Jose Azcona, Xabier Munduate, Leo Gonzalez, and Tor A. Nygaard. Experimental validation of a dynamic mooring lines code with tension and motion measurements of a submerged chain. *Ocean Engineering*, 129(July 2015): 415–427, 2017. ISSN 00298018. doi: 10.1016/j.oceaneng.2016.10.051.

[89] C.M. Ablow and S. Schechter. Numerical simulation of undersea cable dynamics. *Ocean Engineering*, 10(6):443–457, 1983.

[90] F Milinazzo, M I Wilkie, and S A Latchman. An efficient algorithm for simulating the dynamics of towed cable systems. *Ocean Engineering*, 14(6): 513–526, 1987.

[91] J. I. Gobat. *The Dynamics of Geometrically Compliant Mooring Systems*. Phd thesis, Massechusetts Institute of Technology, Massachusetts, USA and Woods Hole Oceanographic Institution, Massachusetts, USA, 2000.

[92] J. I. Gobat and M. A. Grosenbaugh. WHOI Cable v2.0: Time Domain Numerical Simulation of Moored and Towed Oceanographic Systems. Technical report, Woods Hole Oceanographic Institution, 2000.

[93] J. J. Burgess. Bending Stiffness in an Undesea Cable Deployment. In *International Offshore and Polar Engineering Conference*, volume 2, pages 308–315, 1992. ISBN 1880653001.

[94] Stefanos A. Katifeoglou and Ioannis K. Chatjigeorgiou. Dynamic interaction of catenary risers with the seafloor. *Applied Ocean Research*, 38(2012):1–15, 2012. ISSN 01411187. doi: 10.1016/j.apor.2012.06.001. URL `http://dx.doi.org/10.1016/j.apor.2012.06.001`.

[95] Lin Chen, Biswajit Basu, and Søren R.K. Nielsen. A coupled finite difference mooring dynamics model for floating offshore wind turbine analysis. *Ocean Engineering*, 162(April):304–315, 2018. ISSN 00298018. doi: 10.1016/j.oceaneng.2018.05.001.

[96] C. G. Koh, Y. Zhang, and S. T. Quek. Low Tension Cable Dynamics: Numerical and Experimental Studies. *Journal of Engineering Mechanics*, 125 (3):347–354, 1999. ISSN 1098-6596. doi: 10.1017/CBO9781107415324.004.

[97] Ricky Thethi. Soil Interaction Effects on Simple Catenary Riser Response. In *Proceedings of the Deepwater Pipeline & Riser Technology Conference*, Houston, Texas, 2001.

[98] Ali Nakhaee and Jun Zhang. Trenching effects on dynamic behavior of a steel catenary riser. *Ocean Engineering*, 37(2-3):277–288, 2010. ISSN 0029-8018. doi: 10.1016/j.oceaneng.2009.10.005. URL `http://dx.doi.org/10.1016/j.oceaneng.2009.10.005`.

[99] Xiaowei Feng, Susan Gourvenec, and David White. Load capacity of caisson anchors exposed to seabed trenching. *Ocean Engineering*, (171):181–192, 2019.

[100] S Dutta, B Hawlader, and R Phillips. Numerical investigation of dynamic embedment of offshore pipelines. In *Proceedings of the 18th International Conference on Soil Mechanics and Geotechnical Engineering*, pages 2347–2350, 2006.

[101] C Gaudin and D J White. New centrifuge modelling techniques for investigating seabed pipeline behaviour Modélisation en centrifugeuse du comportement des pipelines sous-marins. In *Proceedings of the 17th International Conference on Soil Mechanics and Geotechnical Engineering*, number 1991, pages 448–451, 2009. ISBN 9781607500315. doi: 10.3233/978-1-60750-031-5-448.

[102] Bithin Ghorai and Santiram Chatterjee. Influences of strain rate and soil remoulding on initial break-out resistance of deepwater on-bottom pipelines

Soil heave. *Computers and Geotechnics*, 91:82–92, 2017. ISSN 0266-352X. doi: 10.1016/j.compgeo.2017.07.006. URL `http://dx.doi.org/10.1016/j.compgeo.2017.07.006`.

[103] M Randolph and Peter Quiggin. Non-linear hysteretic seabed model for catenary pipeline contact. *International Conference on Offshore Mechanics and Arctic Engineering*, pages 1–10, 2009. doi: 10.1115/OMAE2009-79259. URL `http://proceedings.asmedigitalcollection.asme.org/proceeding.aspx?articleid=1623566`.

[104] D J White and C Y Cheuk. Modelling the soil resistance on seabed pipelines during large cycles of lateral movement. *Marine Structures*, 21:59–79, 2008. doi: 10.1016/j.marstruc.2007.05.001.

[105] R. Ghadimi. A simple and efficient algorithm for the static and dynamic analysis of flexible marine risers. *Computers & Structures*, 29:541–555, 1988.

[106] J. I. Gobat and M. A. Grosenbaugh. Time-domain numerical simulation of ocean cable structures. *Ocean Engineering*, 33(10):1373–1400, 2006. ISSN 00298018. doi: 10.1016/j.oceaneng.2005.07.012.

[107] Ltd Orcina. Orcaflex, 2016. URL `https://www.orcina.com/SoftwareProducts/OrcaFlex/`. Last accessed April 2018.

[108] MARIN. aNyMoor, 2014. URL `https://mods.marin.nl/display/ANYMOOR`. Last accessed April 2018.

[109] I.K. Chatjigeorgiou and S. A. Mavrakos. Assessment of bottom-cable interaction effects on mooring line dynamics. In *Proceedings of the 17th International Conference on Offshore Mechanics and Arctic Engineering*, Lisbon, Portugal, 1998.

[110] T. R. Goodman and J. P. Breslin. Statics and Dynamics of Anchoring Cables in Waves. *Journal of Hydronautics*, 10(4):113–120, 1976. ISSN 0022-1716. doi: 10.2514/3.63057.

[111] S. A. Mavrakos, V. J. Papazoglou, M. S. Triantafyllou, and J. Hatjigeorgiou. Deep Water Mooring Dynamics. *Marine Structures*, 9(2):181–209, 1996. ISSN 09518339. doi: 10.1016/0951-8339(94)00019-O.

[112] D. O. Thomas. *A Numerical Investigation of Time Schemes Applied to the Dynamic Solution of Mooring Lines*. PhD thesis, University of Newcastle upon Tyne, Newcastle upon Tyne, UK, 1993.

[113] Fei Wang, Guo Liang Huang, De Heng Deng, and Xing Hua Tu. A study on dynamic response of cable-seabed interaction. *Journal of Shanghai Jiaotong University (Science)*, 14 E(4):443–449, 2009. ISSN 10071172. doi: 10.1007/s12204-009-0443-2.

[114] M. S. Triantafyllou, A. Bliek, and H. Shin. Dynamic Analysis as a Tool for Open-Sea Mooring System Design. *SNAME Transactions*, 93:303–324, 1985.

[115] J. I. Gobat and M. A. Grosenbaugh. Dynamics in the Touchdown Region of Catenary Moorings. *International Journal of Offshore and Polar Engineering*, 11(4), 2001.

[116] Toshio Nakajima, Seizo Motora, and Masataka Fujino. On the dynamic analysis of multi-component mooring lines. In *Proceedings of the 14th Offshore Technology Conference*, Houston, Texas, USA, 1982.

[117] D. O. Thomas and G. E. Hearn. Deepwater mooring line dynamics with emphasis on seabed interference effects. In *Proceedings of the 26th Offshore Technology Conference*, Houston, Texas, USA, 1994. doi: doi.org/10.4043/7488-MS.

[118] P.A. Ong and Sergio Pellegrino. Modelling of seabed interaction in frequency domain analysis of mooring cables. In *Proceedings of the 22nd International Conference on Offshore Mechanics and Arctic Engineering*, pages 1–10, Cancun, Mexico, 2003.

[119] Long Yu and Jia Hua Tan. Numerical investigation of seabed interaction in time domain analysis of mooring cables. *Journal of Hydrodynamics*, 18(4): 424–430, 2006. ISSN 10016058. doi: 10.1016/S1001-6058(06)60115-7.

[120] R.B Gorden, M. G. Brown, and E.M. Allen. Mooring Integrity Management: A State-of-the-Art Review. In *Proceedings of the Offshore Technology Conference*, Houston, Texas, 2014. doi: doi.org/10.4043/25134-MS.

[121] Nobel Denton Europe Ltd. FPSO Mooring System Integrity Study (A3792/01/NDE/APC). Technical report, Nobel Denton, Aberdeen, UK,

2002. URL `http://www.ukooa.co.uk/issues/fpso/docs/mainstudy.pdf`. Last accessed October 2016.

[122] J. R. Morison. The Force Distribution Exerted by Surface Waves on Piles. Technical report, University of California, Berkeley, California, 1953.

[123] J S Butcher. *Numerical Methods for Ordinary Differential Equations*. John Wiley & Sons, Ltd, 3 edition, 2016. ISBN 9781119121503.

[124] G.D. Hahn. A modified Euler method for dynamic analyses. *International Journal for Numerical Methods in Engineering*, 32(March 1990):943–955, 1991. ISSN 00295981.

[125] E. Miletics and G. Molnárka. Implicit extension of Taylor series method with numerical derivatives for initial value problems. *Computers & Mathematics with Applications*, 50(7):1167–1177, 2005. ISSN 08981221. doi: 10.1016/j.camwa.2005.08.017.

[126] J. A. Nelder and R. Mead. A Simplex Method for Function Minimization. *The Computer Journal*, 7(4):308–313, 1965. doi: 10.1093/comjnl/7.4.308.

[127] Singiresu Rao. *Mechanical Vibrations*. Prentice Hall, New York, NY, USA, 5th edition, 2011. ISBN 9780132128193.

[128] Leping Yang, Qingbin Zhang, Ming Zhen, and Haitao Liu. *Dynamics and Design of Space Nets for Orbital Capture*. Tsinghua University Press, Beijing, 2017. ISBN 9783662540626.

[129] Matthew Hall, Brad Buckham, and Curran Crawford. Evaluating the importance of mooring line model fidelity in floating offshore wind turbine simulations. In *Proceedings of the 33rd International Conference on Ocean, Offshore and Arctic Engineering*, number October 2013, pages 1835–1853, San Francisco, California, USA, 2014. doi: doi.org/10.1002/we.1669.

[130] Johannes Palm, Claes Eskilsson, and Lars Bergdahl. An hp-adaptive discontinuous Galerkin method for modelling snap loads in mooring cables An hp -adaptive discontinuous Galerkin method for modelling snap loads in mooring cables. *Ocean Engineering*, 144:266–276, 2017. ISSN 0029-8018. doi: 10.1016/j.oceaneng.2017.08.041.

[131] W. K. Liu and T. Belytschko. Mixed-time implicit-explicit finite elements for transient analysis. *Computers & Structures*, 15(4):445–450, 1982. ISSN 00457949. doi: 10.1016/0045-7949(82)90079-7.

[132] Liu Wing Kam, Ted Belytschko, and Zhang Yi Fei. Implementation and accuracy of mixed-time implicit-explicit methods for structural dynamics. *Computers & Structures*, 19(4):521–530, 1984.

[133] Isidoro Miranda, Robert M Ferencz, and Thomas J R Hughes. An improved implicit-explicit time integration method of structural dynamics. *Earthquake Engineering and Structure Dynamics*, 18(5435505), 1989.

[134] E. D. Sotelino. A concurrent explicit-implicit algorithm in structural dynamics. *Computers & Structures*, 51(2):181–190, 1994.

[135] C. W. Gear and D. R. Wells. Multirate linear multistep methods. *BIT Numerical Mathematics*, 24(4):484–502, 1984. ISSN 00063835. doi: 10.1007/BF01934907.

[136] Pak Wing Fok. A Linearly Fourth Order Multirate Runge–Kutta Method with Error Control. *Journal of Scientific Computing*, 66(1):177–195, 2016. ISSN 08857474. doi: 10.1007/s10915-015-0017-4.

[137] M. Günther, Anne Kværnø, and P. Rentrop. Multirate Partitioned Runge-Kutta Methods. *BIT Numerical Mathematics*, 41(3):504–514, 2001. ISSN 00063835. doi: 10.1023/A:1021967112503.

[138] M. Günther and P. Rentrop. Multirate ROW methods and latency of electric circuits. *Applied Numerical Mathematics*, 13(1-3):83–102, 1993. ISSN 01689274. doi: 10.1016/0168-9274(93)90133-C.

[139] C Engstler and C Lubich. Multirate extrapolation methods for differential equations with different time scales. *Computing*, 58(1997):173–185, 1997. ISSN 0010-485X. doi: 10.1007/BF02684438.

[140] Martin Arnold. Multi-Rate Time Integration for Large Scale Multibody System Models. In Peter Eberhard, editor, *Proceedings of the IUTAM Symposium on Multiscale Problems in Multibody System Contacts: Proceedings of the IUTAM Symposium*, pages 1–10. Stuttgart, Germany, 2007. ISBN 978-1-4020-5981-0. doi: 10.1007/978-1-4020-5981-0_1.

[141] Siddhartha S Shome, Edward J Haug, and Laurent O Jay. Dual-Rate Integration Using Partitioned Runge-Kutta Methods for Mechanical Systems with Interacting Subsystems. *Mechanics Based Design of Structures and Machines*, 32(3):253–282, 2004. doi: 10.1081/LMBD-200027930.

[142] Johnny Chang, Scott Ploen, Garett Sohl, and Bryan Martin. Parallel Multi-Step/Multi-Rate Integration of Two-Time Scale Dynamic Systems. In *AIAA Modeling and Simulation Technologies Conference and Exhibit*, Providence, Rhode Island, USA, 2004. ISBN 978-1-62410-074-1. doi: 10.2514/6.2004-5162.

[143] Marcus J. Grote, Michaela Mehlin, and Teodora Mitkova. Runge-Kutta Based Explicit Local Time Stepping Methods for Wave Propagation. *SIAM Journal on Scientific Computing*, 37(2):A747–A775, 2015.

[144] A Kværnø and P Rentrop. Low order multirate Runge-Kutta methods in electric circuit simulation [Preprint], 1999. URL `http://citeseerx.ist.psu.edu/viewdoc/summary?doi=10.1.1.9.3084`. Last accessed April 2018.

[145] Andreas Bartel. Multirate ROW methods of mixed type for circuit simulation. *Scientific Computing in Electrical Engineering*, 18(1):241–249, 2001.

[146] Chee Meng Low, Eddie Yin Kwee Ng, Srikanth Narasimalu, and Kie Hian Chua. Multirate Timestepping For Mooring Line Dynamics. In *Proceedings of the Offshore Technology Conference Brazil*, Rio de Janeiro, Brazil, 2017. doi: doi.org/10.4043/28041-MS.

[147] M. J. D. Powell. A Direct Search Optimization Method That Models the Objective and Constraint Functions by Linear Interpolation. In Susana Gomez and Jean-Pierre Hennart, editors, *Advances in Optimization and Numerical Analysis*, pages 51–67. Springer Netherlands, Dordrecht, Netherlands, 1994. doi: 10.1007/978-94-015-8330-5_4.

[148] Alan Miller. Constrained optimization by linear approximation routine in Fortran 90, 2000. URL `http://wp.csiro.au/alanmiller/`. Last accessed March 2018.

[149] F. N. Fritsch. PCHIP Final Specifications. Technical report, Lawrence Livermore Laboratory, Livermore, California, USA, 1982.

[150] John Burkardt. ASA047 Nelder-Mead Minimization, 2008. URL `https://people.sc.fsu.edu/{~}jburkardt/f_src/asa047/asa047.html`. Last accessed June 2018.

[151] Orcina. Orcaflex Seabed Friction Coefficients. URL `https://www.orcina.com/SoftwareProducts/OrcaFlex/Documentation/Help/Content/html/LineTypes,FrictionData.htm`. Last accessed October 2016.

[152] Chee Meng Low, Eddie Yin Kwee Ng, Srikanth Narasimalu, Frank Lin, and Youngkook Kim. Numerical modelling of seabed impact effects on chain and small diameter mooring cables. *Applied Ocean Research*, 80:248–277, 2018. ISSN 0141-1187. doi: 10.1016/j.apor.2018.09.010.

[153] Wei Ting Hsu, Krish P. Thiagarajan, and Lance Manuel. Extreme mooring tensions due to snap loads on a floating offshore wind turbine system. *Marine Structures*, 55:182–199, 2017. ISSN 09518339. doi: 10.1016/j.marstruc.2017.05.005.

[154] J. Chung and G. M. Hulbert. A Time Integration Algorithm for Structural Dynamics With Improved Numerical Dissipation: The Generalized-α Method. *Journal of Applied Mechanics*, 60(2):371, 1993. ISSN 00218936. doi: 10.1115/1.2900803. URL `http://cat.inist.fr/?aModele=afficheN{&}cpsidt=4808978{%}5Cnhttp://appliedmechanics.asmedigitalcollection.asme.org/article.aspx?articleid=1410995{%}5Cnhttp://www.mendeley.com/research/time-integration-algorithm-structural-dynamics-improved-numerical-dissipati`

[155] N.M. Newmark. A Method of Computation for Structural Dynamics, 1959. ISSN 0044-7951.

[156] E.L. Wilson, I. Farhoomand, and K.J. Bathe. Nonlinear dynamic analysis of complex structures. *Earthquake engineering & structural dynamics*, 1(March 1972):241–252, 1973. ISSN 00988847. doi: 10.1002/eqe.4290010305.

[157] T. Belytschko, H.J. Yen, and R. Mullen. Mixed Methods for Time Integration. *Computer Methods in Applied Mechanics and Engineering*, 17:259–275, 1979.

List of Publications

The following is a list of publications that have resulted from the current thesis:

1. C. M. Low, E. Y. K. Ng, S. Narasimalu, F. Lin, Y. Kim, Numerical modelling of seabed impact effects on chain and small diameter mooring cables, Applied Ocean Research 80 (2018) 248-277. doi:10.1016/ j.apor.2018.09.010. URL doi.org/10.1016/j.apor.2018.09.010

2. C. M. Low, E. Y. K. Ng, S. Narasimalu, Y. Kim, K. H. Chua, Adaptive Discretisation and Dual-rate Time-stepping of Mooring Cable Dynamics, *Ocean Engineering*. (Under Review)

3. C. M. Low, E. Y. K. Ng, S. Narasimalu, K. H. Chua, Multirate Timestepping For Mooring Line Dynamics. In *Proceedings of the Offshore Technology Conference Brazil*, Rio de Janeiro, Brazil, 2017. doi:10.4043 /28041-MS.